UCLA
UCLA Electronic Theses and Dissertations

Title

Programmable RNA Condensates

Permalink

https://escholarship.org/uc/item/8zn0b59k

ISBN

9798189298660

Author

Li, Shiyi

Publication Date

2026-08-31

Peer reviewed|Thesis/dissertation

eScholarship.org Powered by the California Digital Library
University of California

UNIVERSITY OF CALIFORNIA

Los Angeles

Programmable RNA Condensates

A dissertation submitted in partial satisfaction of the

requirements for the degree Doctor of Philosophy in Bioengineering

by

Shiyi Li

2026

© Copyright by

Shiyi Li

2026

ABSTRACT OF THE DISSERTATION

Programmable RNA Condensates

by

Shiyi Li

Doctor of Philosophy in Bioengineering

University of California, Los Angeles, 2026

Professor Elisa Franco, Chair

Artificial biomolecular condensates have emerged as powerful tools for controlling cellular behavior. Here we introduce methods to build artificial condensates via annealing, co-transcription, and within living mammalian cells by designing modular RNA motifs composed of a single short RNA strand. These condensates emerge spontaneously, creating RNA-rich compartments that remain separated from their surrounding environment. The RNA sequences include stem–loop domains that fold as the RNA is transcribed and then condense in the nucleus and cytoplasm through loop–loop interactions. These sequences can be optimized and diversified, enabling the generation of distinct, non-mixing condensate populations and the programmable

control of their subcellular localization. The RNA motifs can also be modified to recruit small molecules, proteins and RNA molecules in a sequence-specific manner to the RNA-rich phase. By introducing RNA linkers, we can build condensates with multiple sub-compartments, whose organization can be controlled by tuning the linker stoichiometry. These artificial condensates provide a versatile platform for studying and manipulating molecular functions inside living cells.

The dissertation of Shiyi Li is approved.

Song Li

Irene Chen

Yen-Chih Lin

Elisa Franco, Committee Chair

University of California, Los Angeles

2026

CONTENTS

LIST OF FIGURES

LIST OF TABLES

ACKNOWLEDGEMENTS

First and foremost, I would like to thank my advisor, Dr. Elisa Franco. I started my Ph.D. questioning what I was capable of and being driven largely by survival anxiety. You gave me not only academic support, but also your time, patience, and thoughtful guidance, allowing me to grow both as a researcher and as a person. You are my mentor in every sense, showing me what it means to be a researcher who is passionate and genuine about science, and a gentle yet strong female figure who cares deeply about both her career and her family. You made my Ph.D. journey far more meaningful than simply earning a degree.

I would also like to thank my committee members, Dr. Song Li, Dr.s Neil Y.C. Lin, and Dr. Irene Chen for your valuable feedback and warm support throughout my Ph.D. journey.

I am also grateful to all my lab mates and collaborators. In particular, I want to thank Annie, who trained me on all the protocols; Neil and Alex, who introduced me to the world of cell culture; and Doug and Wen, who answered my desperate cold email and pulled me out of the nightmare of failed cloning. Special thanks also go to all my mentees, Eric, Yuna, Kevin, Madison, and Diego. Mentoring you has brought me tremendous fulfillment, and a new understanding of what leadership truly means. Thank you for letting me witness and be part of your growth.

I also want to thank my boyfriend, Derek. You showed me that a happy, connected, and continuously growing relationship is real and achievable. To my climbing friends, especially Wesley and Yuhang, and to my Japanese classmates, thank you for bringing color and joy to my Ph.D. life. And to my lifelong friends from middle

school, high school, and college, thank you for all the conversations and trips that have filled my life with happiness and energy.

Finally, I would like to thank my parents. There will always be people with whom I can share my achievements and happiness, but only with my parents have I always felt safe to share every breakdown and tear. I would not be where I am today without you. I am incredibly lucky to be your daughter and to have always been unconditionally loved by both of you.

Chapter 1, in full, is a reprint of the material as it appears in *Nature Communications* 15, no. 1 (2024): 6244. Stewart, Jaimie Marie, Shiyi Li, Anli A. Tang, Melissa Ann Klocke, Martin Vincent Gobry, Giacomo Fabrini, Lorenzo Di Michele, Paul WK Rothemund, and Elisa Franco. Named “Modular RNA motifs for orthogonal phase separated compartments." CC BY 4.0. The dissertation author is the co-first author of this paper.

Chapter 2, in full, is a reprint of the material as it appears in *Nature Nanotechnology* (2026): 1-10. Shiyi Li, Yuna Kim, Kevin Wang, Eric John Payson, Anli A. Tang, Maria Villalba Nieto, Dino Osmanovic *et al*. Named "Programmable artificial RNA condensates in mammalian cells." CC BY 4.0. The dissertation author is the first author of this paper.

Financial support was provided by the University of California, Los Angeles and Eli and Edythe Broad Center of Regenerative Medicine and Stem Cell Research Rose Hills Foundation Innovator Grant; NIH 1R35GM155833, the Alfred Sloan Foundation through award G-2021-16831 and G-2024-22575, and NSF through FMRG: Bio award 2134772, CAREER award 1938194, and BBSRC-NSF/BIO award 2020039.

VITA / BIOGRAPHICAL SKETCH

2021 Bachelor of Science in Biomedical Engineering, Shanghai Jiao Tong University

PUBLICATIONS

Shiyi Li, Yuna Kim, Kevin Wang, Eric John Payson, Anli A. Tang, Maria Villalba Nieto, Dino Osmanovic *et al*. "Programmable artificial RNA condensates in mammalian cells." *Nature Nanotechnology* (2026): 1-10.

Stewart, Jaimie Marie†, **Shiyi Li**†, Anli A. Tang†, Melissa Ann Klocke, Martin Vincent Gobry, Giacomo Fabrini, Lorenzo Di Michele, Paul WK Rothemund, and Elisa Franco. "Modular RNA motifs for orthogonal phase separated compartments." *Nature Communications* 15, no. 1 (2024): 6244.

Fabrini, Giacomo, Nada Farag, Sabrina Pia Nuccio, **Shiyi Li**, Jaimie Marie Stewart, Anli A. Tang, Reece McCoy *et al*. "Co-transcriptional production of programmable RNA condensates and synthetic organelles." *Nature Nanotechnology* 19, no. 11 (2024): 1665-1673.

Tang, Anli A., Martin Vincent Gobry, **Shiyi Li**, Ebbe Sloth Andersen, and Elisa Franco. "Switchable RNA motifs for dynamic transcriptional control of RNA condensates." *Nucleic Acids Research* 53, no. 12 (2025): gkaf497.

Elisa Franco, **Shiyi Li**, Annie Tang. METHODS FOR BUILDING ARTIFICIAL RNA ORGANELLES IN LIVING CELLS. Provisional Application Serial No. 63/679,560, filed on Aug 5, 2024.

Elisa Franco, **Shiyi Li**, Annie Tang. SINGLE STRANDED RNA MOTIFS FOR IN VITRO COTRANSCRIPTIONAL PRODUCTION OF ORTHOGONAL PHASE SEPARATED CONDENSATES. Provisional Application Serial No. 63/588,142, filed on October 5, 2023

1 Chapter 1: Modular RNA motifs for orthogonal phase separated compartments

Adapted, with permission from Stewart, Jaimie Marie, Shiyi Li, Anli A. Tang, Melissa Ann Klocke, Martin Vincent Gobry, Giacomo Fabrini, Lorenzo Di Michele, Paul WK Rothemund, and Elisa Franco. "Modular RNA motifs for orthogonal phase separated compartments." *Nature Communications* 15, no. 1 (2024): 6244.

1.1 Introduction

The discovery of membrane-less organelles is transforming our understanding of cellular biology and disease[1]. These organelles, also known as biomolecular condensates, arise when mixtures of nucleic acids and proteins segregate into spatially separated phases due to specific and non-specific (electrostatic and hydrophobic) molecular interactions[2]. Condensation broadly describes the formation of viscoelastic aggregates, and in biology, it is typically associated with a phase transition of mixtures of both RNA and proteins[2,3] that is driven by the interaction of intrinsically disordered domains (IDRs) of proteins[4], protein-RNA interactions[5] or RNA-RNA interactions[6]. Distinct, immiscible condensates—here termed “orthogonal condensates” — arise through variations of the chemical identity and interactions of the protein and RNA components from which the condensates are composed. The prevailing model is that orthogonal condensates enable the spatial and temporal control of chemical components and biochemical reactions. In general, the greater the number of

orthogonal condensates that can be created, the greater the number of distinct biochemical functions that can be performed. In cells there are dozens of functionally distinct condensates[7], that are involved in diverse gene regulation processes[8], cellular stress[9], and neurodegenerative diseases such as Alzheimer's Disease and ALS[10]. The development of libraries of synthetic, orthogonal condensates would allow for the engineering of coordinated systems of controllable microcompartments with distinct functions matching the complexity of living systems.

As sequence-programmable biopolymers, proteins and RNA have all shown promise as building blocks of artificial condensates. A fundamental design principle used in these investigations has been to introduce weak, non-specific, homotypic interactions that are thought to be essential for phase separation. This was made possible by engineering proteins to include IDRs present in naturally condensing proteins like FUS and SUMO proteins[11–14]. Similarly, artificial RNA condensates have been demonstrated using long molecules featuring expanded repeats of short sequences, which are found in nuclear foci associated with neurological diseases[15,16]. While IDRs and short repeats introduce multivalency, they also introduce promiscuous molecular interactions, thereby limiting the possibility of building coexisting yet immiscible condensates with distinct identities and tunable properties. An alternative approach has been pioneered through nanostructured DNA motifs that form condensates thanks to localized interactions whose specificity is achieved by rationally designed base-pairing[17–19]. Star-shaped DNA motifs have successfully been used to build coexisting but immiscible orthogonal condensates with programmable phase transitions[17,19,20].

Taking inspiration from the success of DNA nanostar condensates, and using techniques from RNA nanotechnology[21,22] we have designed and synthesized both multi-stranded and single-stranded RNA motifs that phase separate into orthogonal condensates. With the aid of computational models predicting RNA-RNA interactions, we demonstrate a suite of star-shaped RNA motifs, or nanostars, that generate RNA-dense droplets thanks to designed base-pairing domains, either linear sticky-ends or kissing loops, at the tip of their arms (**Fig. 1-1**). As shown in DNA nanostar analogs, this strategy makes it possible to obtain phase transitions by controlling nanostar affinity (determined by sequence and length of the base-pairing domains) and valency (determined by the number of arms)[17,18,23]. We adapt RNA nanostars to include an array of RNA aptamer domains that bind to small molecules and peptides, producing an expandable library of modular motifs that yield condensates with the capacity to recruit and segregate client molecules. Finally, we show that single-stranded RNA nanostars fold and produce condensates co-transcriptionally[24], and could serve as genetically encoded building blocks to make RNA organelles with desired biophysical features and with the capacity to concentrate molecular targets. This feature is immediately applicable to building organelles in synthetic cells, as demonstrated in a companion paper by Fabrini *et al*[25].

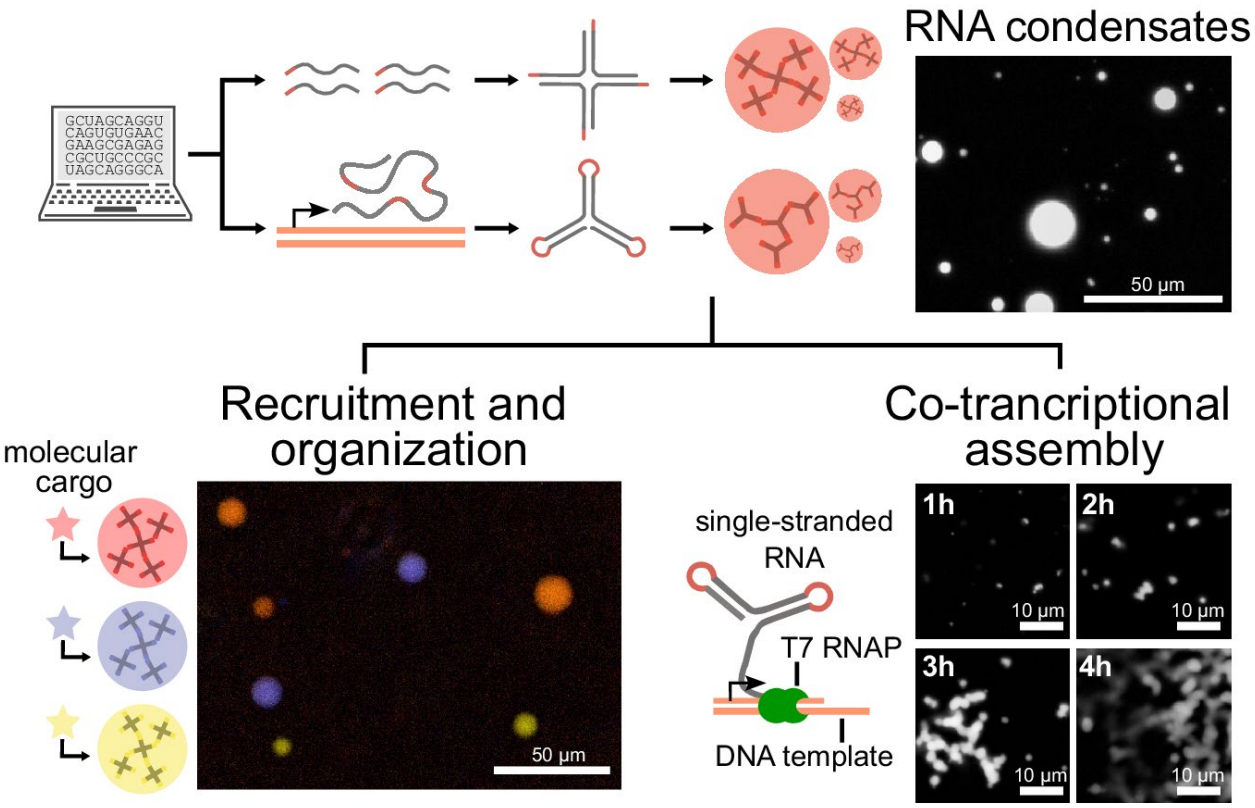

Figure 1-1. Engineering synthetic RNA condensates for orthogonal separation, molecular recruitment, and co-transcriptional assembly.

We demonstrate the design and formation of RNA condensates from rationally designed multi-stranded and single-stranded RNA nanostars. These condensates have the capacity to recruit and organize molecules, and single-stranded motifs yield condensates co-transcriptionally. Scale bars: top right and bottom left, 50 μm; bottom right, 10 μm.

1.2 Results

1.2.1 Condensates emerge from rationally designed multi-stranded RNA motifs interacting via sticky-ends

We begin by demonstrating RNA nanostars assembled from multiple RNA strands, a design that takes inspiration from DNA nanostars interacting via linear sticky-ends[18] (**Fig. 1-2a**). In our designs, arm sequences are distinct, but each arm presents

the same palindromic sticky-end that controls nanostar affinity. We built several four-arm variants, labeled 4m1, 4m2, etc., where “m” denotes the multi-stranded nature of the constructs, “4” is the number of arms, and the final number denotes the sticky-end variant. The sequences of 15-nucleotide (nt) arms and their sticky-ends were optimized using NUPACK[26] to prevent repeats and unwanted interactions. To improve flexibility, we included unpaired adenines at the nanostar core and at the base of the sticky-ends[27]. To produce condensates, RNA was first transcribed *in vitro* and spin-column purified. Denaturing Polyacrylamide Gel Electrophoresis (PAGE) confirms the production of transcripts of the expected length, and a small amount of truncated products **Fig. 1-10**). Purified RNA was suspended in 40 mM HEPES, 100 mM KCl, 500 mM NaCl, which we will refer to as “assembly buffer”, and thermally treated by a melt and hold protocol (**Fig. 1-2b**). The initial heating phase at 70 °C denatures unspecific binding and releases any structures from kinetic trapping. Nanostars form during the temperature drop from 70 °C to 50 °C, and condensates form during the 12-h long hold at 50 °C. Native PAGE of annealed samples including at least two of the participating strands shows the formation of complexes that migrate slowly or do not enter the wells (**Fig. 1-11**). Additional hold temperatures and buffer conditions were screened in the Supplementary Information file (**Fig. 1-7** to **Fig. 1-9**). Samples were stained with 1X SYBR gold for imaging.

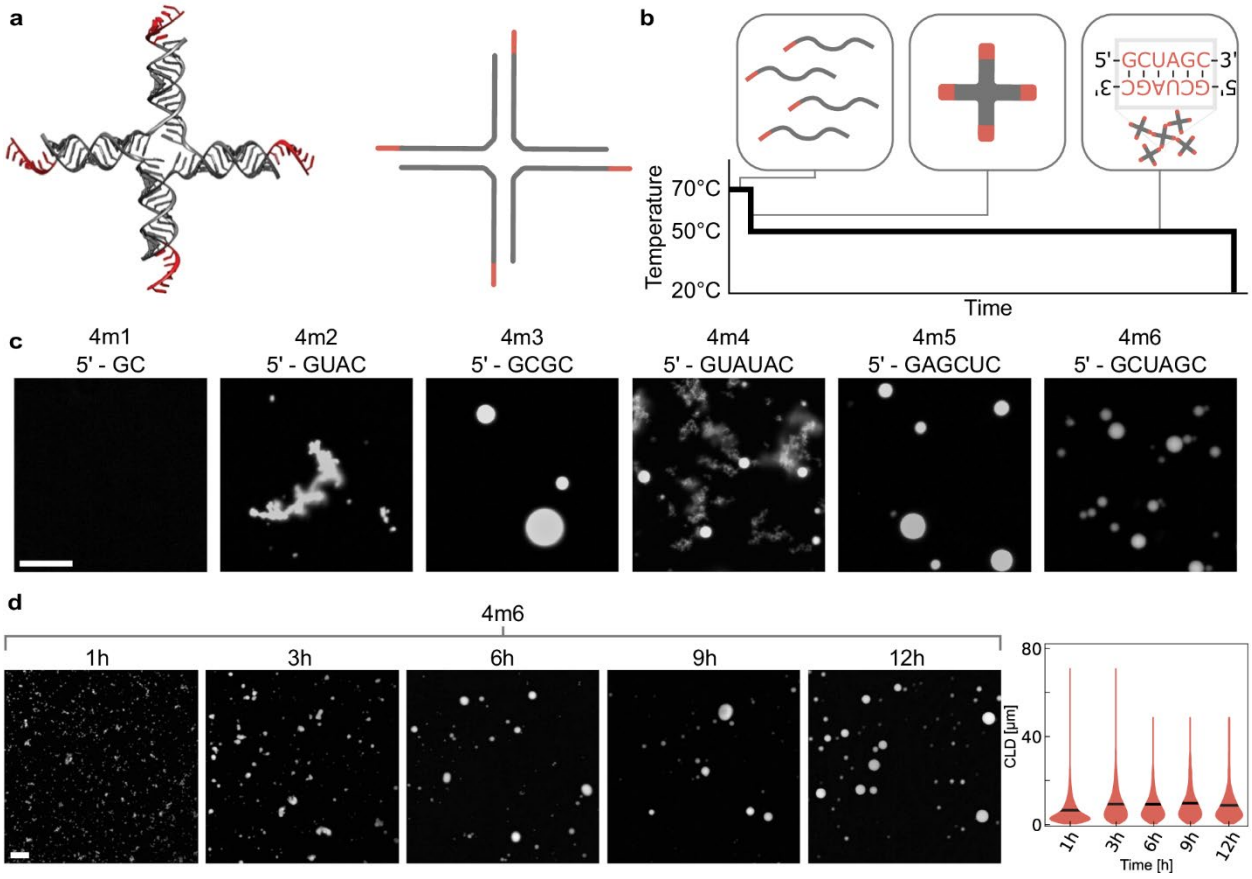

Figure 1-2. Multi-stranded RNA nanostars yield condensates of variable size and morphology.

a PDB rendering and 2D representation of a multi-stranded RNA nanostar. **b** We use a "melt and hold" thermal annealing that sequentially promotes RNA denaturation (left), nanostar assembly (middle), and nanostar-nanostar interactions (right) that yield condensates. **c** Condensate morphology depends on the sequence and length of nanostar sticky-ends. **d** Growth of multi-stranded condensates (4m6) formed in 40 mM HEPES/100 mM KCl/500 mM NaCl and sampled for imaging over a 12-h incubation period. Right: condensate growth during incubation is confirmed by the image chord length distributions (CLD); black lines indicate the mean. Samples were stained with SYBR Gold and imaged. Images are representative of data collected in three replicates. Violin plots in (d) pool data from one sample, imaged 14 times. Scale bars: 40 µm.

We found that 4–6 nt long sticky-ends yield condensates of varying morphology, including round droplets, aggregates of slowly fusing droplets, and “cloudy” aggregates (**Fig. 1-2c**). In contrast, no condensates formed in the absence of sticky-ends or with 2 nt long sticky-ends unless excess salt was added[27] (**Fig. 1-2c** and **Fig. 1-12**). We observed the presence of aggregates in sticky-ends with high UA content. This can not be simply explained thermodynamically, given the higher free energy (ΔG) of the sticky-end (**Table 1-1**); but likely due to the formation of UAUA or U quartet/tetrads[28–31]. We tested the influence of the cold temperature on variant 4m5, finding that lower hold temperatures (40–45 °C) yield aggregates, while temperatures in the range of 46–65 °C produce spherical assemblies; a 70 °C hold eliminates condensation (**Fig. 1-7**). Condensates persist at high KCl concentrations (**Fig. 1-8**), and the addition of MgCl2 alters their melting temperature (**Fig. 1-9**).

We tracked the condensation of variant 4m6 during the temperature hold, finding large condensates after 3–6 h of incubation (**Fig. 1-2d**). The average size of condensates increases during the hold step, as shown via chord length distribution (CLD) analysis[32–35] (**Fig. 1-2d**, right, and **Method 1.4.7**). Chords are generated from binary masks of epifluorescence images, by measuring the intersections between straight lines and regions corresponding to condensates. CLDs are an expedient method to obtain information about the length scale of condensates regardless of their shape, which varies from spheres to aggregated networks depending on the nanostar design and assembly conditions. Fluorescence recovery after photobleaching (FRAP) experiments show no recovery at room temperature, and minimal recovery at 50 °C (**Fig. 1-13**), indicating gel-like behavior.

1.2.2 Loop-loop interactions enable condensation of single-stranded RNA motifs

A requirement for potentially producing RNA nanostars in living cells is that they form at constant temperature. To achieve this, we developed RNA nanostars comprising a single strand rather than several distinct molecules. In these designs, sticky-ends are replaced by kissing loop (KL) domains placed at the end of consecutive stems that serve as nanostar arms (**Fig. 1-3a**). Like in the multi-stranded designs, the arm sequences are distinct to minimize misfolding but all KLs on a particular nanostar are identical. Given our goal of co-transcriptional formation, we decided to minimize transcript length and include only three consecutive arms, the lowest valency for condensation. Stem sequences were adapted from design 4m6, eliminating one of the arms. We started by testing the palindromic wild-type Human Immunodeficiency Virus (HIV) KL sequence (GCGCGC, variant termed 3sWT, where “s” denotes the single-stranded nature of the design and “3” the number of arms), and we also developed variants with non-palindromic sticky-ends (3sα-ζ), each including 2 distinct nanostars (**Fig. 1-3b**). First, we characterized the condensation of our designs using RNA transcribed by T7 polymerase, spin-column purified, and annealed with our melt and hold protocol in our assembly buffer.

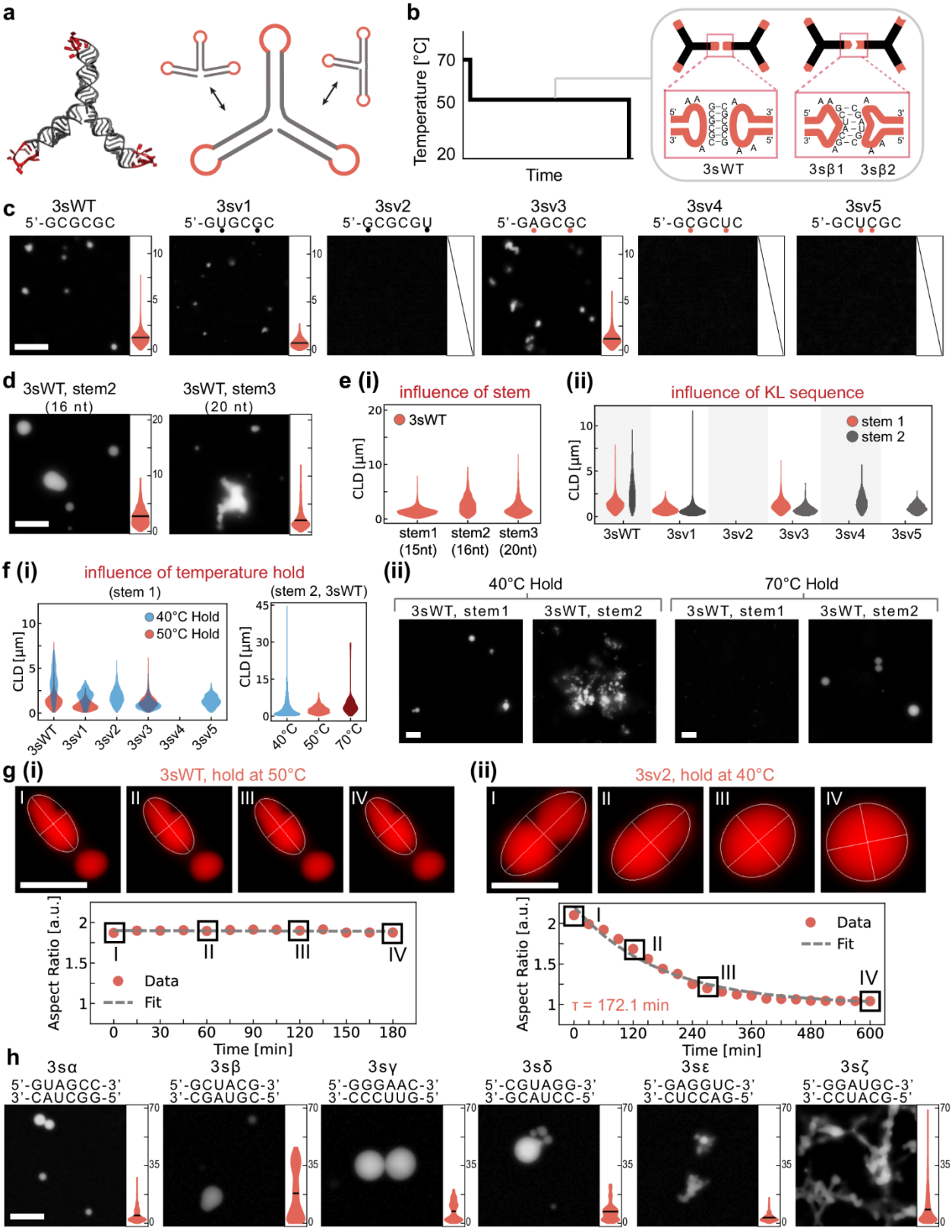

Figure 1-3. Condensates generated by single-stranded RNA nanostars.

a PDB and 2D representation of a single-stranded RNA nanostar. **b** Melt and hold thermal annealing protocol; one-nanostar systems with palindromic KL (left) and two-nanostar systems with non-palindromic KL (right) condense during the hold phase. **c** Example images and violin plots of the chord length distribution (CLD) of condensates formed by nanostars differing by KL. Black dots indicate wobble pairs. Orange dots indicate mismatches. **d** Example images and CLD of condensates forming under different nanostar stems. **e** Influence of the stem sequence and length: (i) longer stems yield larger condensates; (ii) changing stem sequence impacts condensate formation and morphology across KL variants (**f**) (i) The hold temperature influences formation of stem1 variants; (ii) example images comparing 3sWT-stem1 and 3sWT-stem2 under a 40° and 70 °C hold. **g** Top: epifluorescence micrographs demonstrating coalescence of droplets from variant 3sWT-stem 1, held at 50 °C (i) and variant 3sv2-stem 1, held at 40 °C. Bottom: Time-dependent change in aspect ratios of condensates (orange dots), computed as the major and minor axes ratio from the best-fit-ellipses. Dashed lines are exponential fits of function $1 + Ae^{(-t/\tau)}$. **h** Two-nanostar systems produce condensates of varying morphology, as captured by violin plots of the CLD. All experiments were replicated at least three times; images are representative examples. Violin plots pool data from three independent replicates. Scale bars: 10 μm.

We found that condensate formation occurs robustly across designs, although it is influenced by KL and stem sequences. The 3sWT nanostars yield abundant condensates that continue to grow throughout the hold step of the annealing protocol (**Fig. 1-16**). Condensate formation can be disrupted by replacing one KL with a polyadenine domain (**Fig. 1-17**): this indicates that KL interactions, rather than stem-stem interactions, are the primary drivers for phase separation. We then tested 5 variants of the WT KL (dubbed 3sv1-v5) with mismatches or wobble pairs that modulate the probability of KL dimerization and therefore change the nanostar affinity (**Fig. 1-3c** and **Fig. 1-18**). The selection and naming order of these variants is based on the

dimerization capacity of the KL sequences taken from the HIV-1 dimer linker structure, as reported in literature[36]. Condensates are observed with the WT, v1, and v3 variants, yielding similar CLDs, but not with variants v2, v4, and v5: these outcomes are consistent with previous dimerization studies[36]. While KL v2 is expected to dimerize, it did not yield condensates likely due to the high hold temperature and the lack of divalent cations in our assembly buffer. Denaturing PAGE of purified RNA samples shows the presence of expected transcription products, as well as truncated products of consistent length across variants (**Fig. 1-19**). These truncated products appear to hinder condensation, as they increase the critical concentration for droplet formation when compared to gel extracted RNA samples that exclude the truncated products (**Fig. 1-20**). Native PAGE of annealed samples show retention in the wells, confirming the presence of large, stable aggregates (**Fig. 1-21**).

Next, we examined the influence of stem sequence and length on condensate formation. We built nanostars with a 16-nt “stem 2” variant whose sequence is adapted from a well-known design for three-arm DNA nanostars17, and a 20-nt “stem 3” variant designed using NUPACK. We obtain condensates with both stem variants with the WT KL (**Fig. 1-3d**), and longer arms correlate with larger condensate size, an effect also observed with DNA nanostars[37] (**Fig. 1-3e (i)**). When combining stem 2 with different KL variants, we find that variants v4 and v5 yield condensates (**Fig. 1-3e (ii)**) pointing to the fact that the stem-mediated interactions may play a role in condensation under the melt and hold protocol. This role cannot be simply explained thermodynamically, given the similar ΔG of stem 1 and stem 2 formation (NUPACK estimates $\Delta G = -67.45$ kcal/mol for stem 1 and $\Delta G = -68.53$ kcal/mol for stem 2 at 50 °C, with comparable GC content

flanking the KL). The stem sequences flanking the KL and flanking the NS core may create kinetic effects as they influence bond mobility, and could participate in domain swapping[38]. Interestingly, we also found that variant 3sv2 yields condensate when combined with longer stem 3 (**Fig. 1-18**), while it does not with shorter stems 1 and 2 (**Fig. 1-3e(ii)**). Our results indicate that the stem length and sequence have major effects on the propensity of nanostars to form condensates: a model capturing these coupled effects could be obtained through further systematic experiments combined with molecular dynamics simulations[39].

The choice of hold temperature significantly influences condensation (**Fig. 1-3f**). For stem 1 variants, a 40 °C hold facilitates condensation when compared to a 50 °C hold: as shown in **Fig. 1-3f(i)**, variants 3sv2 and 3sv5 form condensates at 40 °C but do not at 50 °C, and variants 3sWT and 3sv1 form larger droplets at 40 °C when compared to 50 °C (example microscopy images are in **Fig. 1-18**). All stem 2 variants, except 3sv2, yield condensates under a 50 °C hold (**Fig. 1-3e(ii)** and **Fig. 1-18**). Strikingly, variant 3sWT-stem2 forms condensates even with a 70 °C hold, likely due to interactions enabled by partial stem melting (**Fig. 1-3f(i)** and **(ii)**).

To quantify the mobility of nanostars in the dense phase, we performed Fluorescence Recovery After Photobleaching (FRAP) experiments for variants 3sWT at 50 °C and 3sv2 at 40 °C (**Fig. 1-22**). Nanostars were fluorescent-tagged by doping 1% of CY3-UTP during transcription. No significant recovery was observed over five minutes. To study the kinetics of condensate fusion, we estimated the inverse capillary velocity η/γ, where η is the viscosity and γ is the surface tension (**Fig. 1-3g** and **Fig. 1-23**). Variant 3sWT showed no fusion throughout the 3-h incubation at 50 °C (**Fig. 1-3g**,

left). Variant 3sv2 slowly fused over 10 hours and the example condensate shows a relaxation constant τ = 172 minutes. We find η/γ = 57.81 min μm^{-1} (**Fig. 1-23**), which is significantly larger when compared to natural and artificial biomolecular condensates[40–43] as well as artificial DNA condensates[44]. Collectively, this evidence suggests that single-stranded nanostar condensates are viscous, like multi-stranded nanostars. Finally, lateral confocal projections showed no significant wetting of condensates on the glass slide surface (**Fig. 1-24**).

The addition of $MgCl_2$ to the assembly buffer alters the observed phase transitions. In this case, also 3sWT-stem1 nanostars yield condensates under a 70 °C hold, and variant 3sv2-stem1 also produces condensates under a 50 °C hold (**Fig. 1-25**). Other variants produce more non-spherical condensates when compared with the standard assembly buffer including monovalent cations (**Fig. 1-25**). This behavior is consistent with the fact that divalent cations like $MgCl_2$ generally stabilize nucleic acid assemblies[45], and may increase the affinity of KL nanostars that otherwise do not condense[46]. At the same time, $MgCl_2$ can promote aggregation and kinetic trapping[47], altering condensate viscosity. This is an important consideration because $MgCl_2$ is typically required for *in vitro* transcription, and is a ubiquitous component in protocols for DNA or RNA self-assembly.

Finally, we tested 6 more RNA nanostar variants (3sα-ζ) each comprising two distinct nanostars (e.g., 3sα1, 3sα2) with non-palindromic KL designed to be complementary (**Fig. 1-3h**). By adopting non-palindromic sequences, we can expand by 64-fold the theoretical sequence design space of a 6 nucleotide KL domain. With the melt and hold protocol and our assembly buffer, we found that all two-nanostar variants

generated condensates with variable size and morphology (**Fig. 1-3h**). While individual nanostars (e.g., 3sα1) have the potential to multimerize as they carry identical stems, they fail to produce any condensate except for variant 3sε1, which we attribute to partial self-complementarity of the KL domains (**Fig. 1-26**). Native PAGE shows that two-nanostar samples are retained in the well, consistent with the formation of condensates. When only one nanostar out of the two is present, the sample migrates in the well and generates a few bands likely to be multimers forming due to stem-stem interactions (**Fig. 1-21**). These findings indicate that stem-mediated RNA multimerization can occur but is not the primary driver of condensation, unlike what proposed in the recent literature[6,48].

In summary, our data shows that changes in KL and stem length and sequences all influence condensation. KL with more than 4 base pairs is likely to yield condensation, depending on the overall strength of their interaction (**Fig. 1-27**), which is influenced by non-canonical base pairing, stacking, and secondary and tertiary structure[6].

1.2.3 Orthogonal RNA condensates can be programmed to recruit guest molecules

We next demonstrate the potential of RNA nanostars to capture client molecules and recruit them to the RNA-dense phase. We focus on condensates produced through the melt-and-hold protocol using purified RNA.

A major advantage of multi-stranded nanostars is that only one of the strands needs to be modified for the inclusion of aptamers, so we began by appending client recruitment domains (aptamers) at the tip of one of the arms of variants 4m3, 4m5, and 4m6 (upstream of the 5’ end of the sticky-end). We first validated this idea through

fluorescent light-up aptamers (FLAPs) known as Red Broccoli (appended to variant 4m6, Corn (4m5), and Orange Broccoli (4m3), which all bind to fluorophore 3,5-difluoro-4-hydroxybenzylidene imidazolinone-2-oxime (DFHO) but each results in a distinct emission spectrum (**Fig. 1-4a**, **Fig. 1-14**). (For ease of visualization, we depict FLAPs using the secondary structure predicted by NUPACK[26], which does not capture their complex 3D tertiary structure[49]). Because these variants were designed to maximize orthogonality, we expected each nanostar to form distinct condensates that do not mix with the others. Through microscopy, we first verified that these nanostars yield condensates when assembled in isolation in the presence of DFHO (**Fig. 1-14**), and then that they do not mix when assembled simultaneously. To quantitatively assess the degree of condensate mixing we plotted a histogram of the arctangent of the pixel intensity ratio FITC/Cy3 (**Fig. 1-4a**, bottom right, and **Fig. 1-28**). The histogram peaks of control samples (individually assembled nanostars) are consistent with those of samples including mixed nanostars, indicating that the aptamers are not colocalized. These histograms highlight that although our nanostars are designed to remain de-mixed, the excitation and emission spectra of the FLAPs have some overlap (Orange Broccoli 513/562 nm, Red Broccoli 518/582 nm, and Corn 505/545 nm)[49]. Further, Orange Broccoli and Red Broccoli have a high degree of sequence similarity, where mutation at nucleotide position 71 is hypothesized to be the key cause of the difference in fluorescence emission[49,50]. Finally, differences in fluorescence intensity are likely due to the difference in the KD of DFHO (Orange Broccoli ~230 nM, Red Broccoli ~206 nM, and Corn ~70 nM[49,50]).

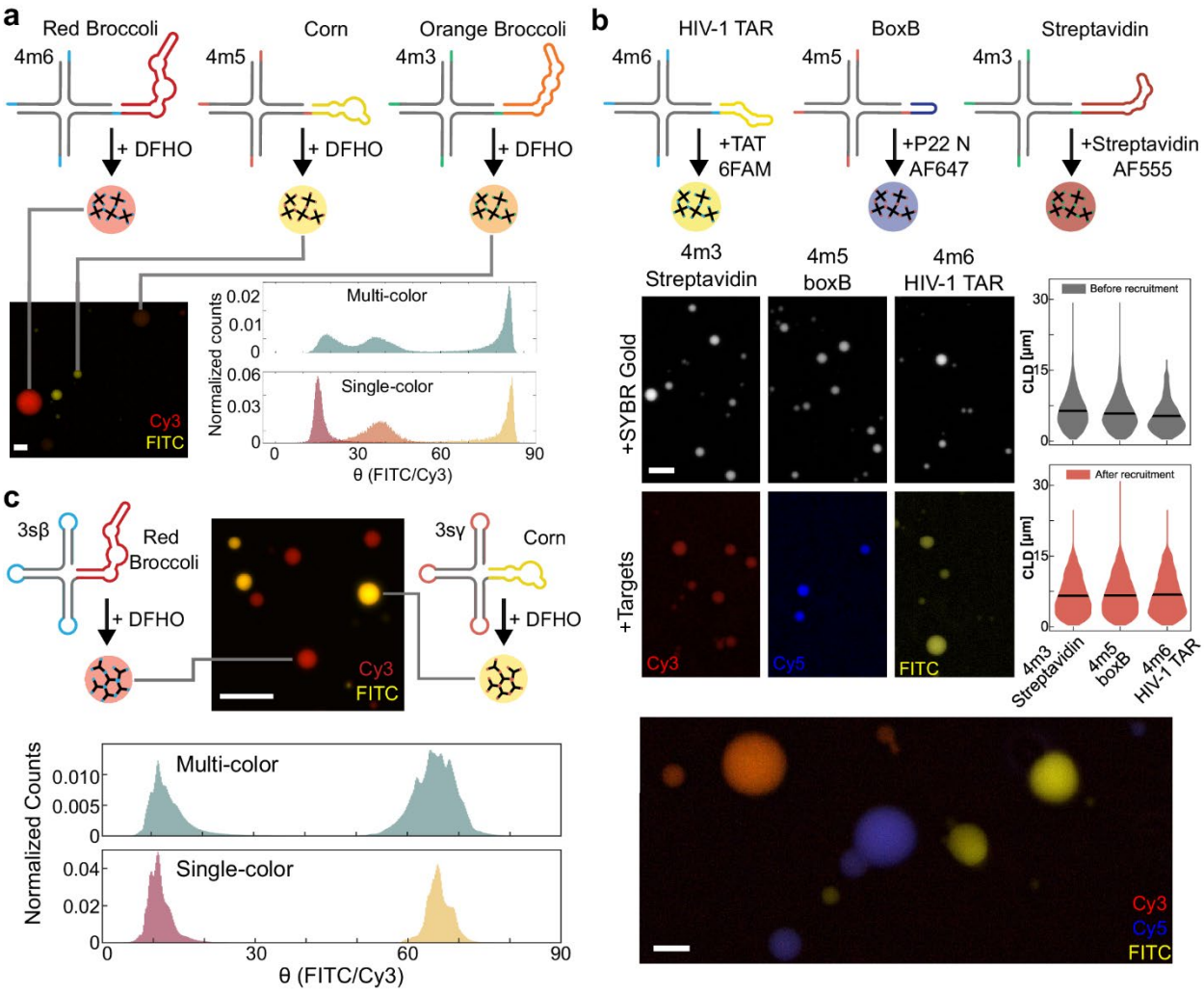

Figure 1-4. Sequence-orthogonal RNA nanostars produce distinct condensates that recruit clients specifically and remain demixed.

a Multi-stranded sequence-orthogonal nanostars modified to include FLAPs. When annealed in one pot they produce distinct RNA condensates that do not mix. Condensates were imaged in both FITC and Cy3 channels; each pixel's FITC/Cy3 ratio was mapped to an angle θ and histogrammed. Histogram peaks for nanostars annealed individually align with those of nanostars annealed together. **b** Top: Nanostars including aptamer domains that recruit streptavidin, P22 N peptide, and TAT peptide guests. Middle: Example images and violin plots of the CLD for condensates before and after recruitment of peptides. Black line indicates the mean. Bottom: Nanostars were designed to be sequence-orthogonal, thus their one-pot assembly with fluorescently labeled clients shows their recruitment and

compartmentalized into specific condensates (red, blue, and yellow). **c** Sequence-orthogonal single-stranded RNA motifs pairs (two nanostar systems, 3sβ and 3sγ), modified to include Corn and Red Broccoli fluorogenic aptamers. The peaks of the FITC/Cy3 angle histogram for nanostars annealed individually align with the peaks of nanostars annealed together. Experiments were done in triplicates; images provide representative examples. Violin plots and histograms pool data from all replicates. Scale bars: 20 μm.

Next, we show that our RNA condensates can recruit client peptides to the dense phase. For this purpose, we replaced FLAPs with peptide and protein binding domains: we considered a streptavidin binding aptamer (appended to nanostar variant 4m3), boxB RNA that binds P22 N peptide (appended to nanostar variant 4m5), and TAR RNA that binds TAT peptide (appended to nanostar variant 4m6)[51–53], shown in **Fig. 1-4B**. We selected these peptides for their versatility: the streptavidin-biotin pair is widely used for purification and localization assays[54]; the P22 bacteriophage N peptide is a strong binder for its aptamer boxB, and is useful for RNA colocalization studies[55]; finally, Tat bound to its aptamer is a strong transcriptional regulator involved in HIV replication[56]. Strands including aptamers were doped into the mixture of unmodified strands at a ratio of 1:4 (25%). We verified that each peptide binding nanostar yields condensates when assembled individually, and it successfully recruits its client; after peptide recruitment, condensates become on average larger (**Fig. 1-4b**, bottom). Undesired cross-binding of targets to their non-cognate aptamer occurs only for TAT, due to its positively charged amino acid residues that cause non-specific binding to negatively charged RNA (**Fig. 1-15**). Overall, our orthogonal RNA nanostars partition the fluorescently labeled peptides into distinct compartments that do not mix.

Finally, we confirmed that also single-stranded RNA nanostars can recruit client molecules. We selected orthogonal two-nanostar variants 3sβ and 3sγ and we modified them to include FLAPs binding DFHO (Red Broccoli and Corn, respectively) as an additional arm (25% FLAP-modified strands in the mix). We observed the formation of condensates of distinct colors upon annealing nanostars together (**Fig. 1-4c**, **Fig. 1-29**). We verified that these condensates do not mix through our quantitative image analysis (computation of the arctangent of FITC/Cy3 intensity ratio for each pixel, **Fig. 1-28**), which shows aligned histogram peaks when purified nanostars are annealed separately or together (**Fig.1-4c**, bottom).

1.2.4 Co-transcriptional formation of RNA condensates

We finally demonstrate that single-stranded RNA nanostars produce condensates co-transcriptionally at 37 °C, in the absence of thermal annealing (**Fig. 1-5a**). Tandem stem-loops fold based on local RNA interactions so they are expected to form stable structures as they are being transcribed under isothermal conditions[57]. We transcribed nanostars using linear templates under the control of the T7 bacteriophage promoter, using a high-yield *in vitro* transcription buffer that includes components required for transcription and 10 mM NaCl, 30 mM $MgCl_2$, and 2 mM spermidine[58] (see "Methods"). For these experiments, we selected variant 3sv2-stem1 (**Fig. 1-5a**), which produces abundant spherical condensates when purified and thermally treated with a 40 °C hold, as well as in the presence of $MgCl_2$ (**Fig. 1-18 and 1-25**). We observed large condensates (stained with SYBR Gold) within 1–2 hours of nanostar transcription (**Fig. 1-5b**), which corresponds to an estimated RNA concentration of 2 μM (**Fig. 1-30**). The amount of RNA produced correlates with average condensate size, measured

through the mean-chord length (μCLD), and both double within the first 3 hours; larger aggregates can be obtained by increasing the DNA template concentration (**Fig. 1-31**). The number of condensates only slightly decreases over time, which suggests that our reaction conditions promote condensate growth primarily by monomer addition, rather than fusion, while nanostars are being transcribed (**Fig. 1-5b**). FRAP of condensate produced during transcription shows no recovery over the observation window (**Fig. 1-32**). We also tested the co-transcriptional assembly of the two-nanostar variant 3sβ, which similarly produces aggregates that grow rapidly into a slowly fusing network (**Fig. 1-5c**, d); 3sβ1 or 3sβ2 transcribed individually do not form condensates (**Fig. 1-33**). Native PAGE confirms the formation of large aggregates in the two-nanostar sample, and some multimerization for 3sβ1 or 3sβ2, as observed on purified and annealed samples (**Fig. 1-34**). We found that the amount of monovalent and divalent cations (NaCl and $MgCl_2$) in the transcription buffer has significant effects on co-transcriptional formation, as shown in control experiments involving the two-nanostar variant 3sβ (**Fig. 1-35**); buffers included in commercial kits may fail to yield condensates if they do not include sufficient cation levels. We expect that co-transcriptional condensates can be obtained using other nanostar variants that produce condensates from purified RNA with the melt and 40 °C hold protocol (**Fig. 1-3f**, **Fig. 1-18**).

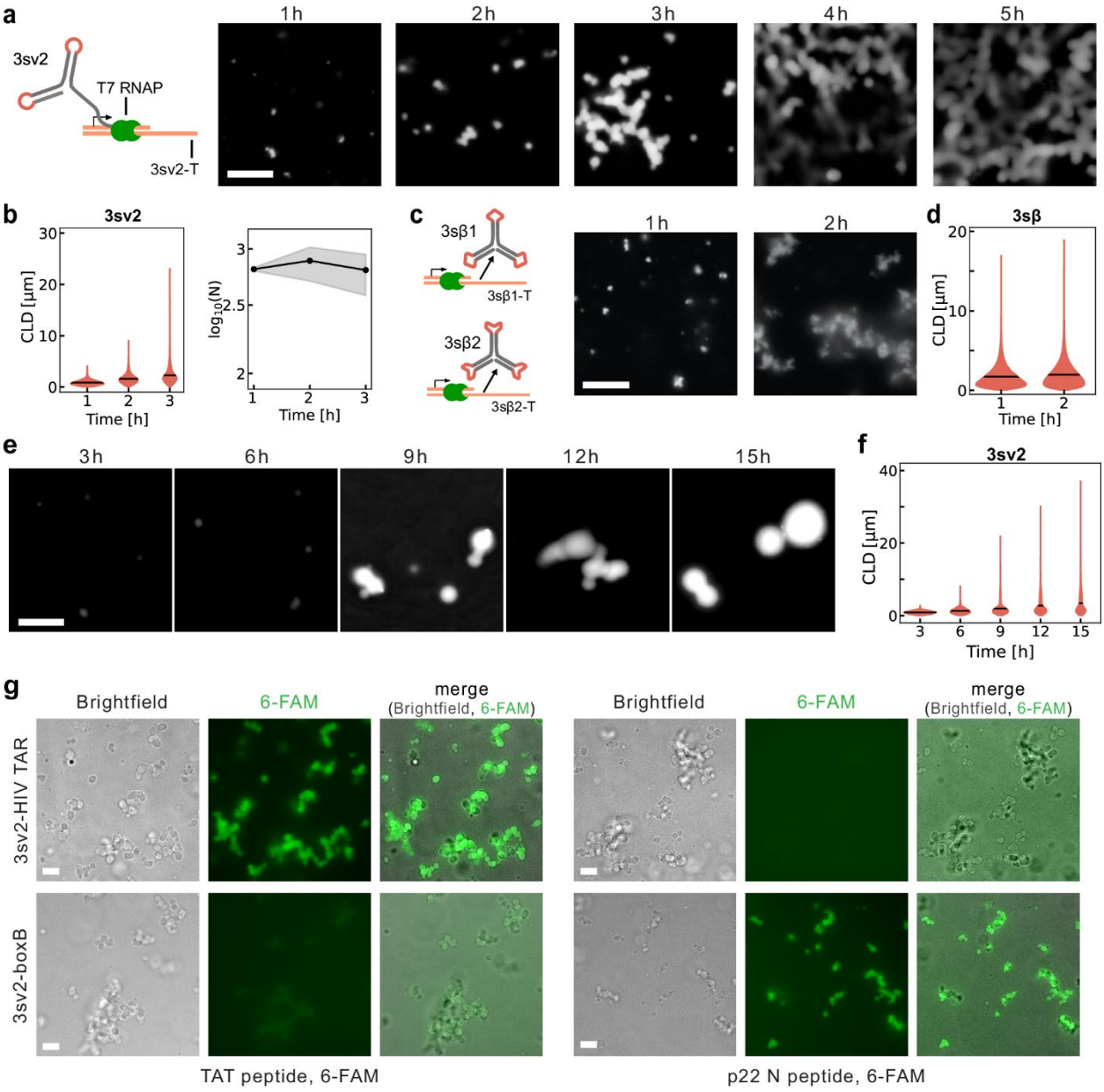

Figure 1-5. co-transcriptional, isothermal formation of single-stranded RNA nanostars and peptide recruitment.

a Scheme shows transcription and co-transcriptional folding of motif 3sv2; example images show condensate formation in T7 *in vitro* transcription reaction sampled at different time points. **b** Temporal evolution of the CLD (left) and number (N, right) of 3sv2 nanostars. Black lines indicate the mean chord length from $n = 3$ at given time points. **c** Scheme shows transcription and co-transcriptional folding of motif pairs 3sβ1 and 3sβ2; example images show 3sβ condensate growth in T7 *in vitro* transcription

reaction. **d** Temporal evolution of the CLD of 3sβ condensates. Black lines indicate the mean chord length from n = 3 at given time points. (**e**) Example images show 3sv2 condensate growth in a cell-free PURExpress® reaction. **f** Temporal evolution of the CLD of 3sv2 condensate in PURExpress®. Black lines indicate the mean chord length from *n* = 3 at given time points. **g** Brightfield and fluorescence microscopy images show specific peptide recruitment to condensates formed co-transcriptionally after 2-hour incubation. 3sv2 nanostars were modified to include TAR (top) or boxB (bottom) aptamer, recruiting either TAT or p22 N peptide labeled with 6-FAM. Peptides are added at the beginning of transcription. Experiments were done in triplicates; images are representative examples. Scale bars: 10 μm.

co-transcriptionally produced RNA condensates could be useful as membrane-less organelles that can spontaneously recruit proteins. To demonstrate that this is immediately feasible in cell-free systems, we verified that nanostar 3sv2-stem1 could produce condensates when transcribed using PURExpress®, a commercial kit for cell-free protein synthesis[59]. The production of large condensates appears slow in PURExpress® when compared to a high-yield transcription kit, as evidenced by example images of **Fig. 1-5d** and by the μCLD shown in **Fig. 1-5f**. Condensate growth rate may be increased by using larger amounts of DNA template or of RNA polymerase. After several hours, PURExpress® samples form very large, spherical condensates when compared to high-yield *in vitro* transcription conditions; this difference may be due to the presence of translation components of the PURExpress® kit (**Fig. 1-36**). Finally, we modified 3sv2-stem1 to recruit p22 N and TAT peptides using their corresponding aptamers (boxB and TAR, respectively) and demonstrated that these peptides are recruited to the condensates co-transcriptionally. We incubated peptides and DNA templates for 2 h in high-yield transcription buffer, and we verified the correct, specific

recruitment of peptides to the dense phase (**Fig. 1-5g**). No qualitative difference is observed if peptides are added 2 h after the start of transcription (**Fig. 1-37**).

1.3 Discussion

We have demonstrated the design and synthesis of modular RNA nanostars for phase separation. We showed that both multi-stranded and single-stranded nanostars robustly form condensates in standard buffers commonly adopted in nanotechnology applications, in the absence of binding partners. We focused on two protocols, (1) transcribing and purifying RNA strands, then performing a temperature treatment consisting of a denaturing step and a long temperature hold, or (2) co-transcriptional assembly. We examined how condensation is influenced by various nanostar design features and extrinsic factors such as ionic conditions and temperature. Further, we have programmed orthogonal condensates to recruit and organize small molecules and peptides, thus mimicking the ability of biological condensates to recruit clients[60]. Our strategy is modular, and may lead to the development of libraries of orthogonal condensates recruiting diverse clients. Multi-stranded and single-stranded RNA nanostars offer different advantages depending on the downstream application or purpose. Owing to the ease in designing linear sticky-ends and hybridizing domains, the affinity and valency of multi-stranded nanostars can be easily tuned, making it possible to build RNA condensates with a broad range of biophysical properties that should be comparable to those demonstrated for similar DNA condensates[19,20,27]. Further, this design allows for the modular introduction of RNA or DNA strands with distinct functionalities, including client recruitment and adaptation to chemical or physical inputs

that are relevant for developing therapeutic, multifunctional biomaterials[61]. Single-stranded nanostars produce condensates isothermally under physiological conditions, making them immediately useful as RNA organelles that can be produced in artificial cells, as demonstrated in a parallel study[25]. We are evaluating whether these constructs can be genetically encoded in living cells.

A distinguishing feature of our RNA condensates is that they are formed through compact, nanostructured motifs designed using short sequences that are optimized to fold as desired. Previous work has shown the emergence of coacervates from unstructured RNA homopolymers in the presence of polymeric cations that are not necessary in our system[62–64]. RNA strands assembling into pure RNA hydrogels have been identified via SELEX[65], however, this approach does not offer a clear design strategy to modularly adapt the condensing motifs as easily as with RNA nanostars. Recent work demonstrated that liquid RNA droplets can be produced inside cells through long RNA molecules featuring short sequence repeats (CAG/CUG)[15,16,66]. By fusing the CAG-repeats to recruitment domains, it was possible to demonstrate compositional control of RNA droplets both in bacteria and in mammalian cells[15,16]. Intracellular RNA condensates were also obtained via homodimerization of two different RNA aptamer repeats[67], which remain demixed forming up to two types of orthogonal compartments inside cells. In these exciting achievements, sequence repeats are an expedient strategy to introduce multivalency, but it is not clear this approach can yield a scalable number of orthogonal condensates.

A simplified working model of RNA nanostars suggests that we can determine their affinity, valency, and size by changing the sticky ends/kissing loops, number of

arms, and arm length. However, we still lack a clear picture of how different combinations of these parameters affect phase transitions and condensation kinetics. Further, some of these parameters mutually couple in ways that are difficult to predict; for example, changes in the stem sequence can have an impact on the nanostar affinity if they affect the folding of the interaction domains, and these effects are sensitive to temperature and ionic conditions. The influence of combinations of design changes could be predicted by coarse-grained models that capture the interactions among nanostars[68,69], and should be validated against systematic experiments characterizing phase diagrams and growth rates of nanostar condensates. These models could accelerate the design of customized RNA condensates while minimizing experimental burden. Finally, while we have demonstrated modular recruitment of small molecules and peptides, we expect limitations in which classes of molecules of proteins are recruited by RNA nanostars with specificity. RNA aptamers can be promiscuous, for example TAR RNA is known to bind positively charged arginine[70]. Further, arbitrary RNA domains may non-specifically recruit amino acid sequences; for example, positively charged peptides naturally tend to bind to the negatively charged backbone of RNA, regardless of sequence specificity (like we observed with TAT protein). We expect that, in complex biological samples, various RNA-binding proteins could bind non-specifically to our artificial condensates and possibly compromise their formation. Another challenge is that some recruitment motifs could introduce misfolding or remodeling of the secondary structure of co-transcriptionally produced single-stranded nanostars. Design methods developed for RNA origami may provide valuable lessons toward enhancing the robustness and functionalities of RNA nanostars[71].

Orthogonal, customizable micron-sized compartments made with RNA may find clinical and industrial applications for purification, diagnostics, and therapeutic treatments. RNA condensates with the capacity to selectively sequester binding targets may be useful for separating crude mixtures of molecules or low-volume clinical samples. The incorporation of stimuli-responsive domains in RNA nanostars could make it possible to develop sensors and diagnostic tools, and further engineering may allow this platform to serve as a smart drug delivery system capable of encapsulating and releasing therapeutic molecules. Lastly, we envision that single-stranded RNA nanostars may be used to produce functional RNA organelles in living cells and potentially control cellular processes.

1.4 Methods

Sequences, detailed methods, and additional experiments are included in the Supplementary Table and Supplementary Information file.

1.4.1 Sequence design

The RNA strands were designed and optimized using the NUPACK design tool using scripts reported in Supplementary Note 1[26]. Aptamer sequences were selected from previous studies[49,50]. The Corn aptamer was modified from previous work 3 by adding GG to the 5’ end and CC to the 3’ end to ensure transcription. Red Broccoli and Orange Broccoli aptamers were modified from 2 to include flanking sequences GUAUGUGG at the 5’ end and CCCACAUAC at the 3’ end, which surround conserved fluorogen-binding sequences and broccoli bridging sequences. The boxB RNA

sequence that binds P22 N peptide and HIV-1 Tat aptamer that binds Tat peptide was taken from previous work[72,73]. The streptavidin binding aptamer was modified from previous work[51] by adding a G at the 5' end and a C at the 3' end to ensure transcription. Aptamer sequences were appended to the 5'- sticky end of the S1 strand of a given motif. The secondary structure of the motif with aptamer modification was analyzed using NUPACK to ensure that the secondary structure of the motif and aptamer was similar to the fold of the individual modules. Three-armed single-stranded RNA nanostars (3 s) were designed by combining distinct arm sequences with several kissing loop variants. Stem 1 sequences were adapted from the multi-stranded motifs (4 m); stem 2 sequences were adapted from the design by Sato *et al*. for DNA nanostars[17]; stem 3 sequences were designed using NUPACK. Two of the three spacers between arms include two unpaired adenines, and the other is a nick, allowing the motif to have flexible configurations. All KLs are nine nucleotides long and include a six-nt interaction sequence flanked by three unpaired adenine residues, two upstream and one downstream of the interaction sequence (5'-AA…A-3'). KL variants used for the one-nanostar motifs were adapted from the HIV-1 palindromic KL sequence[36]. Each variant was obtained by introducing a single-base substitution in the six nt interaction domain of the wild type KL (5'-GCGCGC). KL for two-nanostar motifs were designed de novo to function as pairs (heterodimers). All sequences for the two-nanostar design include four GC pairs and two AU pairs to ensure similar bond stabilities. Fluorogenic aptamer sequences identical to the multi-stranded designs were adopted from literature[49,50]. The expected folding of each design was confirmed using NUPACK26. All sequences are listed in **Table 1-2** and **1-3**.

1.4.2 RNA synthesis

RNA strands for multi-stranded nanostars were transcribed from PAGE purified DNA templates, including a T7 promoter, purchased from Integrated DNA Technologies. Lyophilized DNA was resuspended in nuclease-free water. RNA strands for single-stranded nanostars were transcribed from standard desalt DNA templates, purchased from Integrated DNA Technologies as Lab Ready. DNA templates were annealed in 1X TE/50 mM NaCl from 90 °C to RT at −1 °C/min. RNA strands were individually transcribed *in vitro* using the AmpliScribe T7-Flash transcription (ASF3507, Biosearch Technologies) kit from DNA templates following the manufacturer's protocol. RNA strands were then purified using Amicon Ultra 10 K 0.5 ml centrifugal filters (UFC501096) and 1X TE buffer and centrifuging three times at 14,000 g. For multi-stranded nanostars, each strand was transcribed from a fully double-stranded DNA template, including the T7 promoter. For single-stranded nanostars, we used single-stranded non-coding DNA templates annealed to a 21-nt complement including the promoter region and a 4 nt sealing domain (5'-GCGC). We estimated the concentration of purified RNA using Nanodrop 2000c from measurements of absorption at 260 nm and the extinction coefficient provided by the manufacturer.

1.4.3 Condensate preparation

Condensates made from purified RNA (multi-stranded or single-stranded nanostars) were formed in our assembly buffer: 40 mM HEPES, 100 mM KCl, 500 mM NaCl. Strands were thermally annealed in an Eppendorf Mastercycler using a melt and hold protocol which includes a melt at 70 °C for 10 minutes, followed by 12 hours of incubation at specified temperatures, and by a quick drop to 20 °C for 5 minutes before

imaging. For multi-stranded nanostars, we used purified RNA strands each at equimolar concentrations (5 μM). Strands including aptamer sequences were added at 1.25 μM concentration (25% doping). For single-stranded nanostars, we used purified RNA at an estimated 5 μM concentration. For two-nanostar condensates we used purified RNA with each nanostar at 5 μM concentration; thus, the total RNA concentration in these experiments was doubled. For two-nanostar motif experiments using fluorogenic RNA aptamers, aptamers-containing strands were added at a 25% doping. Condensates formed from motifs without aptamer were imaged with 1X SYBR Golding staining (S11494, Thermofisher). Dye was added 5 minutes after cooling to 20 °C. Condensates formed from aptamer-appended motifs were stained with DFHO (Lucerna Technologies). DFHO stock was stored in DMSO at a concentration of 10 mM. DFHO staining solution was prepared by diluting DFHO stock in HEPES buffer with a final concentration of 1 mM DFHO and 40 mM HEPES. Samples were imaged immediately after staining.

1.4.4 Preparation of peptide and protein targets

Fluorescent peptides were synthesized by either LifeTein, LLC or GenScript. Fluorophores were added to the N-terminal, AlexaFluor647 for P22 N peptide, and 6-FAM for TAT peptide. For co-transcriptional experiments, both N peptide and TAT were labeled with 6-FAM. Peptide synthesis was guaranteed a purity of ≥95% with standard Trifluoroacetic acid (TFA) removal (Final TFA Counterion % <10%. Lyophilized peptide was resuspended in 10 mM HEPES with a molarity of ~350 μM and stored at 5 °C. Streptavidin, Alexa Fluor™ 555 conjugate was purchased from Thermo Fisher Scientific at 2 mg/ml concentration, with a molarity of ~35 μM. Streptavidin conjugate was diluted

with 10 mM HEPES and stored at 5 °C. For multi-stranded nanostars, peptides were added to the samples after the melt-and-hold step. For single-stranded nanostars, peptides were added at the beginning of co-transcription.

1.4.5 Co-transcriptional production of condensates

Condensates produced during transcription of single-stranded RNA nanostars were formed using DNA templates prepared as described under “RNA synthesis”. RNA strands were transcribed *in vitro* at 37 °C using 7.5% (v/v) T7 polymerase from the AmpliScribe T7-Flash transcription kit (ASF3507, Biosearch Technologies), and transcription buffer prepared in-house: 40 mM of Tris-HCl, 10 mM of NaCl, 30 mM $MgCl_2$, 2 mM spermidine, 7.5 mM each NTP, 10 mM DTT. For the sequence-orthogonal single-stranded RNA nanostars (two-nanostar system), the RNA strands were transcribed *in vitro* under the same conditions, with the exception of the NaCl and $MgCl_2$ concentrations, which were adjusted to 20 mM each. When using the PURExpress® kit (E6800S, New England Biolabs), we adhered to the manufacturer’s protocol and incubated our sample at 37 °C. Unless otherwise specified, we used a final concentration of 10 nM DNA template for the *in vitro* transcription; we used 10 ng DNA for the cell-free PURExpress® reaction.

1.4.6 Fluorescence microscopy

Condensates produced from multi-stranded motifs were obtained with an Olympus BX-UCB upright fluorescence microscope using a 20x air objective. We used filtersets Cy3 (Chroma Filter Set Exciter D540/25x EX Dichroic Q565lp BS Emitter D620/60 m EM), Cy5 (Chroma Filter Set Exciter HQ620/60x EX Dichroic Q660LP BS Emitter HQ700/75 m EM), and FITC (Chroma Filter Set Exciter D480/30x EX Dichroic

Q505lp BS Emitter D535/40 m EM), with a standard exposure time of 100 ms for samples stained with SYBR gold, 500 ms for samples with DFHO or fluorescent peptides and proteins. Condensates produced from single-stranded motifs were imaged using a Nikon Eclipse TI-E inverted microscope using a 60x oil immersion objective. SYBR gold-stained samples were detected using the FITC channel (ex 455−485 nm/em 510−545 nm) with an exposure time of 100 ms. DFHO-stained samples were detected in both the FITC channel with an exposure time of 200 ms, and in the Cy3 channel (ex 512−552 nm/em 565−615 nm) with an exposure time of 100 ms. Peptide recruiting condensates, which contain 6-FAM labeled peptides, were imaged using the FITC channel (ex 455−485 nm/em 510−545 nm); exposure time was set to 500 ms, except for the samples including 3sv2-TAT nanostars and TAT peptide, in which exposure was set at 100 ms. For samples stained with SYBR Gold, 1X SYBR gold was used after thermal treatment. For samples with DFHO, 50 μM DFHO in 2 mM HEPES buffer was used before thermal treatment (for multi-stranded nanostars) and after thermal treatment (for single-stranded nanostars). For lateral confocal projections, samples were annealed using the melt-and-hold protocol and stained with 1x SYBR Gold, and imaged under a 60x objective on a Nikon Ti-2 microscope with an NLS5+ camera. Z-stack images were captured with a thickness of 0.3 μm.

1.4.7 Image processing and visualization

All fluorescence images were pre-processed in FIJI (ImageJ). All codes are provided as indicated in the code availability. Raw images were background subtracted, contrast-enhanced, and converted to a binary mask. For condensate number analysis, objects smaller than 6 px2 were considered noise and excluded. Condensate numbers

were measured by FIJI and recorded. To gather information on condensate size, we measured chord length distributions (CLD)[32–35] from the binary masks using a Python3 script based on PoreSpy, which relies on Scipy and Skimage. Violin plots were generated using a Python3 script based on Seaborn. All experimental replicates were pooled into a single violin plot. Means were computed across three technical replicates. To determine whether our nanostars including distinct fluorogenic aptamers produce condensates that mix or do not mix, we built pixel intensity histograms from fluorescence microscopy images (**Fig. 1-4** and **Fig. 1-28**). This was done because upon DFHO staining, both Corn and Red Broccoli aptamers can be detected in the FITC channel and the Cy3 channel, albeit with varying intensity, since the Corn aptamer emission peak is 545 nm, and the Red Broccoli emission peak is 582 nm. Histograms were generated from the coordinate angles calculated from every pixel within the regions of interest. Additional details on image processing and visualization are provided in Supplementary Note 2.

1.4.8 Denaturing Polyacrylamide Gel Electrophoresis

Gel pre-mix was prepared by adding 42 g of urea to nanopure water, the mixture was then heated until the urea completely dissolved. This mixture was allowed to cool to room temperature, and then a 40% (v/v) 19:1 acrylamide/bis-acrylamide solution was added in the appropriate volume for the desired percentage (final volume 100 mL). 8 mL of pre-mix was added in appropriate ratios with TBE and nanopure water, ammonium persulfate (APS), and tetramethylethylenediamine (TEMED) to start polymerization. Gels were cast in 8 × 8 cm, 1 mm thick disposable mini gel cassettes (Thermo Scientific, #NC2010) and allowed to polymerize for 30 minutes to 2 h before electrophoresis.

Samples and low-range ssRNA ladder (NEB, N0364S) were prepared by mixing individual strands with denaturing RNA loading dye (NEB, B0363S), then heated at 90 °C for 10 minutes and immediately placed on ice. After curing, the gel was pre-run in a 1X TBE buffer for 30 minutes. Gels were run at room temperature at 100 V in 1X TBE unless otherwise noted. After electrophoresis, the gels were stained in 1xSYBR Gold Nucleic Acid Gel Stain and then imaged using the iBright™ FL1500 Imaging for multi-stranded nanostars and using the Bio-Rad Gel Imaging Systems for single-stranded nanostar.

1.4.9 Non-denaturing Polyacrylamide Gel Electrophoresis

40% solution of 19:1 acrylamide/bis-acrylamide, TAE, APS, and TEMED were added together at appropriate concentrations for the desired polyacrylamide percentage, then cast in 8 × 8 cm, 1 mm thick disposable mini gel cassettes (Thermo Scientific, #NC2010) and allowed to polymerize for at least 2 h before electrophoresis. Samples were prepared by annealing in our assembly buffer (40 mM HEPES/100KCl/500 mM NaCl) in 1:1 stoichiometric ratios. Gels were run at 4 °C at 120 V in 1X TBE buffer. After electrophoresis gels were stained in SYBR Gold Nucleic Acid Gel Stain or ethidium bromide and then imaged using the iBright™ FL1500 Imaging for multi-stranded nanostars and using the Bio-Rad Gel Imaging Systems for single-stranded

1.4.10 Fluorescence recovery after photobleaching (FRAP)

RNA was transcribed by adding 1% of CY3-labeled UTP (ENZ-42505) to the transcription mix. Co-transcribed samples were diluted 10 times with 1x transcription buffer after transcription to reduce background fluorescence. Samples were loaded into

a house-made chamber and sealed with epoxy (Gorilla, 5-minute set) for imaging. Imaging was done every 5 seconds for 30 seconds before bleaching and every 5 seconds for 5 minutes after bleaching. Bleaching was done with a 488 nm laser, at 50 ms exposure for multi-stranded nanostars and 200 ms exposure for single-stranded nanostars. Images were processed to eliminate the influence of horizontal drifting using the SIFT algorithm[74]. Normalized pixel intensity within ROIs was exported and recovery was calculated as

$$(I_{bleach,t}/I_{bleach,\max})/(I_{unbleach,t}/I_{unbleach,max})$$

where *I* denotes the mean pixel intensity among the bleached or unbleached area, *t* denotes the time point, max denotes the highest pixel intensity within the area among all time points. Images are plotted as mean ± error bar from N = 3.

1.4.11 Condensate fusion

Samples were purified, annealed, stained with 1x SYBR Gold, then loaded into an observation chamber and sealed with epoxy as described above. Imaging was done every 15 minutes for 4 hours under the FITC channel. Each fusion event was identified manually and segmented using Otsu thresholding. The binary mask was then labeled to extract the centroid position, major and minor axis lengths, and orientation. Best-fit-ellipses were generated based on the extracted data. The aspect ratio was calculated as the major-to-minor axes ratio and used for further analysis. A detailed description of image analysis and Python packages used is in Supplementary Note 2, Data Processing for time-dependent coalescence.

1.4.12 Statistics & Reproducibility

For peptide recruitment samples using multi-stranded nanostars, size analysis of each condition was performed using data from n = 3 and fields of view (FOV) = 10, for incubation over time samples of multi-stranded nanostars, size analysis of each time point was performed using data from one experimental replicate and FOV = 14. For single-stranded nanostars, n = 3 is applied unless specified. Each experiment with purified RNA includes FOV = 7; formation of orthogonal Corn/Red Broccoli-tagged condensates includes FOV = 10; each co-transcription experiment includes FOV = 11; each PurExpress co-transcription experiment includes FOV = 11. Images with very strong background noise, making data processing impossible are excluded. To ensure the same sample sizes, the final number of images for the experiment depends on the group with the minimum processable data.

1.4.13 Code availability

Image analysis was done using publicly available packages as described in the Supplementary Methods. Custom code is available at: https://github.com/FrancoLabUCLA/Stewart-Li-Tang-2024-Nat-Commun.

1.5 References

1. Shin, Y. & Brangwynne, C. P. Liquid phase condensation in cell physiology and disease. *Science* **357**, eaaf4382 (2017).
2. Hyman, A. A., Weber, C. A. & Jülicher, F. Liquid-liquid phase separation in biology. *Annu. Rev. Cell Dev. Biol.* **30**, 39–58 (2014).
3. Alberti, S. Phase separation in biology. *Curr. Biol.* **27**, R1097–R1102 (2017).

4. Kato, M., Zhou, X. & McKnight, S. L. How do protein domains of low sequence complexity work? *RNA* **28**, 3–15 (2022).
5. Rhine, K., Vidaurre, V. & Myong, S. RNA Droplets. *Annu. Rev. Biophys.* **49**, 247–265 (2020).
6. Bevilacqua, P. C., Williams, A. M., Chou, H.-L. & Assmann, S. M. RNA multimerization as an organizing force for liquid-liquid phase separation. *RNA* **28**, 16–26 (2022).
7. Courchaine, E. M., Lu, A. & Neugebauer, K. M. Droplet organelles? *EMBO J.* **35**, 1603–1612 (2016).
8. Hirose, T., Ninomiya, K., Nakagawa, S. & Yamazaki, T. A guide to membraneless organelles and their various roles in gene regulation. *Nat. Rev. Mol. Cell Biol.* **24**, 288–304 (2023).
9. Alberti, S. & Hyman, A. A. Biomolecular condensates at the nexus of cellular stress, protein aggregation disease and ageing. *Nat. Rev. Mol. Cell Biol.* **22**, 196–213 (2021).
10. Alberti, S. & Dormann, D. Liquid-liquid phase separation in disease. *Annu. Rev. Genet.* **53**, 171–194 (2019).
11. Schuster, B. S. & others. Controllable protein phase separation and modular recruitment to form responsive membraneless organelles. *Nat. Commun.* **9**, 2985 (2018).
12. Reinkemeier, C. D., Girona, G. E. & Lemke, E. A. Designer membraneless organelles enable codon reassignment of selected mRNAs in eukaryotes. *Science* **363**, eaaw2644 (2019).

13. Dai, Y. & others. Programmable synthetic biomolecular condensates for cellular control. *Nat. Chem. Biol.* **19**, 518–528 (2023).

14. van der Lee, R. & others. Classification of intrinsically disordered regions and proteins. *Chem. Rev.* **114**, 6589–6631 (2014).

15. Jain, A. & Vale, R. D. RNA phase transitions in repeat expansion disorders. *Nature* **546**, 243–247 (2017).

16. Guo, H. & others. Spatial engineering of E. coli with addressable phase-separated RNAs. *Cell* **185**, 3823-3837.e23 (2022).

17. Sato, Y., Sakamoto, T. & Takinoue, M. Sequence-based engineering of dynamic functions of micrometer-sized DNA droplets. *Sci. Adv.* **6**, eaba3471 (2020).

18. Biffi, S. & others. Phase behavior and critical activated dynamics of limited-valence DNA nanostars. *Proc. Natl. Acad. Sci. U. S. A.* **110**, 15633–15637 (2013).

19. Jeon, B.-J., Nguyen, D. T. & Saleh, O. A. Sequence-Controlled adhesion and microemulsification in a two-phase system of DNA liquid droplets. *J. Phys. Chem. B* **124**, 8888–8895 (2020).

20. Gong, J., Tsumura, N. & Sato, Y. Computational DNA droplets recognizing miRNA sequence inputs based on liquid-liquid phase separation. *Adv. Funct. Mater.* **32**, 2270206 (2022).

21. Chworos, A. & others. Building programmable jigsaw puzzles with RNA. *Science* **306**, 2068–2072 (2004).

22. Guo, P. The emerging field of RNA nanotechnology. *Nat. Nanotechnol.* **5**, 833–842 (2010).

23. Conrad, N., Chang, G., Fygenson, D. K. & Saleh, O. A. Emulsion imaging of a DNA nanostar condensate phase diagram reveals valence and electrostatic effects. *J. Chem. Phys.* **157**, 234203 (2022).

24. McRae, E. K. S. & others. Structure, folding and flexibility of co-transcriptional RNA origami. *Nat. Nanotechnol.* **18**, 808–817 (2023).

25. Fabrini, G. & others. Co-transcriptional production of programmable RNA condensates and synthetic organelles. *bioRxiv* https://doi.org/10.1101/2023.10.06.561174 (2024) doi:10.1101/2023.10.06.561174.

26. Zadeh, J. N. & others. NUPACK: analysis and design of nucleic acid systems. *J. Comput. Chem.* **32**, 170–173 (2011).

27. Nguyen, D. T. & Saleh, O. A. Tuning phase and aging of DNA hydrogels through molecular design. *Soft Matter* **13**, 5421–5427 (2017).

28. Xiao, C.-D., Ishizuka, T. & Xu, Y. Antiparallel RNA G-quadruplex formed by human telomere RNA containing 8-bromoguanosine. *Sci. Rep.* **7**, 6695 (2017).

29. Cheong, C. & Moore, P. B. Solution structure of an unusually stable RNA tetraplex containing G- and U-quartet structures. *Biochemistry* **31**, 8406–8414 (1992).

30. Gu, J., Wang, J. & Leszczynski, J. Hydrogen bonding in 5-bromouracil-adenine-5-bromouracil-adenine (T+AT+A) tetrads. *J. Phys. Chem. B* **108**, 9277–9286 (2004).

31. Falkenberg, C. V., Blinov, M. L. & Loew, L. M. Pleomorphic ensembles: formation of large clusters composed of weakly interacting multivalent molecules. *Biophys. J.* **105**, 2451–2460 (2013).

32. Levitz, P. Off-lattice reconstruction of porous media: critical evaluation, geometrical confinement and molecular transport. *Adv. Colloid Interface Sci.* **76–77**, 71–106 (1998).

33. Levitz, P. Toolbox for 3D imaging and modeling of porous media: relationship with transport properties. *Cem. Concr. Res.* **37**, 351–359 (2007).

34. Testard, V., Berthier, L. & Kob, W. Influence of the glass transition on the liquid-gas spinodal decomposition. *Phys. Rev. Lett.* **106**, 125702 (2011).

35. Di Michele, L. & others. Multistep kinetic self-assembly of DNA-coated colloids. *Nat. Commun.* **4**, 2007 (2013).

36. Clever, J. L., Wong, M. L. & Parslow, T. G. Requirements for kissing-loop-mediated dimerization of human immunodeficiency virus RNA. *J. Virol.* **70**, 5902–5908 (1996).

37. Agarwal, S., Osmanovic, D., Klocke, M. A. & Franco, E. The growth rate of DNA condensate droplets increases with the size of participating subunits. *ACS Nano* **16**, 11842–11851 (2022).

38. Zhang, F. & others. Function of hexameric RNA in packaging of bacteriophage φ29 DNA in vitro. *Mol. Cell* **2**, 141–147 (1998).

39. Stoev, I. D. & others. On the role of flexibility in linker-mediated DNA hydrogels. *Soft Matter* **16**, 990–1001 (2020).

40. Brangwynne, C. P. & others. Germline P granules are liquid droplets that localize by controlled dissolution/condensation. *Science* **324**, 1729–1732 (2009).

41. Brangwynne, C. P., Mitchison, T. J. & Hyman, A. A. Active liquid-like behavior of nucleoli determines their size and shape in Xenopus laevis oocytes. *Proc. Natl. Acad. Sci. U. S. A.* **108**, 4334–4339 (2011).

42. Elbaum-Garfinkle, S. & others. The disordered P granule protein LAF-1 drives phase separation into droplets with tunable viscosity and dynamics. *Proc. Natl. Acad. Sci. U. S. A.* **112**, 7189–7194 (2015).

43. Alshareedah, I. & others. Interplay between short-range attraction and long-range repulsion controls reentrant liquid condensation of ribonucleoprotein-RNA complexes. *J. Am. Chem. Soc.* **141**, 14593–14602 (2019).

44. Jeon, B.-J. & others. Salt-dependent properties of a coacervate-like, self-assembled DNA liquid. *Soft Matter* **14**, 7009–7015 (2018).

45. Dey, S. & others. DNA origami. *Nat. Rev. Methods Primer* **1**, 1–24 (2021).

46. Wadsworth, G. M. & others. RNAs undergo phase transitions with lower critical solution temperatures. *Nat. Chem.* **15**, 1693–1704 (2023).

47. Rossi-Gendron, C. & others. Isothermal self-assembly of multi-component and evolutive DNA nanostructures. *Nat. Nanotechnol.* https://doi.org/10.1038/s41565-023-01468-2 (2023) doi:10.1038/s41565-023-01468-2.

48. Poudyal, R. R., Sieg, J. P., Portz, B., Keating, C. D. & Bevilacqua, P. C. RNA sequence and structure control assembly and function of RNA condensates. *RNA* **27**, 1589–1601 (2021).

49. Song, W. & others. Imaging RNA polymerase III transcription using a photostable RNA-fluorophore complex. *Nat. Chem. Biol.* **13**, 1187–1194 (2017).

50. Filonov, G. S., Song, W. & Jaffrey, S. R. Spectral tuning by a single nucleotide controls the fluorescence properties of a fluorogenic aptamer. *Biochemistry* **58**, 1560–1564 (2019).

51. Leppek, K. & Stoecklin, G. An optimized streptavidin-binding RNA aptamer for purification of ribonucleoprotein complexes identifies novel ARE-binding proteins. *Nucleic Acids Res.* **42**, e13 (2014).

52. Austin, R. J., Xia, T., Ren, J., Takahashi, T. T. & Roberts, R. W. Differential modes of recognition in N peptide-boxB complexes. *Biochemistry* **42**, 14957–14967 (2003).

53. Yamaoki, Y., Nagata, T., Mashima, T. & Katahira, M. Development of an RNA aptamer that acquires binding capacity against HIV-1 Tat protein via G-quadruplex formation in response to potassium ions. *Chem. Commun.* **53**, 7056–7059 (2017).

54. Dundas, C. M., Demonte, D. & Park, S. Streptavidin-biotin technology: improvements and innovations in chemical and biological applications. *Appl. Microbiol. Biotechnol.* **97**, 9343–9353 (2013).

55. Ma, H. & others. Multiplexed labeling of genomic loci with dCas9 and engineered sgRNAs using CRISPRainbow. *Nat. Biotechnol.* **34**, 528–530 (2016).

56. Rizzuti, M., Nizzardo, M., Zanetta, C., Ramirez, A. & Corti, S. Therapeutic applications of the cell-penetrating HIV-1 Tat peptide. *Drug Discov. Today* **20**, 76–85 (2015).

57. Lai, D., Proctor, J. R. & Meyer, I. M. On the importance of cotranscriptional RNA structure formation. *RNA* **19**, 1461–1473 (2013).

58. Milburn, S. C., Goldrick, M. & Winkler, M. Compositions and methods for increasing the yields of in vitro RNA transcription and other polynucleotide synthetic reactions. (1993).

59. Shimizu, Y. & others. Cell-free translation reconstituted with purified components. *Nat. Biotechnol.* **19**, 751–755 (2001).

60. Banani, S. F., Lee, H. O., Hyman, A. A. & Rosen, M. K. Biomolecular condensates: organizers of cellular biochemistry. *Nat. Rev. Mol. Cell Biol.* **18**, 285–298 (2017).

61. Guo, P. & Afonin, K. A. *RNA Nanotechnology and Therapeutics*. (CRC Press, 2022).

62. Boeynaems, S. & others. Spontaneous driving forces give rise to protein-RNA condensates with coexisting phases and complex material properties. *Proc. Natl. Acad. Sci.* **116**, 7889–7898 (2019).

63. Cakmak, F. P., Choi, S., Meyer, M. O., Bevilacqua, P. C. & Keating, C. D. Prebiotically-relevant low polyion multivalency can improve functionality of membraneless compartments. *Nat. Commun.* **11**, 5949 (2020).

64. Choi, S., Meyer, M. O., Bevilacqua, P. C. & Keating, C. D. Phase-specific RNA accumulation and duplex thermodynamics in multiphase coacervate models for membraneless organelles. *Nat. Chem.* **14**, 1110–1117 (2022).

65. Huang, Z., Kangovi, G. N., Wen, W., Lee, S. & Niu, L. An RNA aptamer capable of forming a hydrogel by self-assembly. *Biomacromolecules* **18**, 2056–2063 (2017).

66. Xue, Z. & others. Targeted RNA condensation in living cells via genetically encodable triplet repeat tags. *Nucleic Acids Res.* **51**, 8337–8347 (2023).

67. Wu, J. & others. Self-assembly of intracellular multivalent RNA complexes using dimeric corn and beetroot aptamers. *J. Am. Chem. Soc.* **144**, 5471–5477 (2022).

68. Locatelli, E., Handle, P. H., Likos, C. N., Sciortino, F. & Rovigatti, L. Condensation and demixing in solutions of DNA nanostars and their mixtures. *ACS Nano* **11**, 2094–2102 (2017).

69. Xing, Z., Ness, C., Frenkel, D. & Eiser, E. Structural and linear elastic properties of DNA hydrogels by coarse-grained simulation. *Macromolecules* **52**, 504–512 (2019).

70. Tao, J. & Frankel, A. D. Specific binding of arginine to TAR RNA. *Proc. Natl. Acad. Sci. U. S. A.* **89**, 2723–2726 (1992).

71. Geary, C., Grossi, G., McRae, E. K. S., Rothemund, P. W. K. & Andersen, E. S. RNA origami design tools enable cotranscriptional folding of kilobase-sized nanoscaffolds. *Nat. Chem.* **13**, 549–558 (2021).

72. Tan, R. & Frankel, A. D. Structural variety of arginine-rich RNA-binding peptides. *Proc. Natl. Acad. Sci. U. S. A.* **92**, 5282–5286 (1995).

73. Yamamoto, R. & others. A novel RNA motif that binds efficiently and specifically to the Ttat protein of HIV and inhibits the trans-activation by Tat of transcription in vitro and in vivo. *Genes Cells* **5**, 371–388 (2000).

74. Linear Stack Alignment with SIFT. (2012).

75. Dzuricky, M., Rogers, B. A., Shahid, A., Cremer, P. S. & Chilkoti, A. De novo engineering of intracellular condensates using artificial disordered proteins. *Nat. Chem.* **12**, 814–825 (2020).

76. Ji, R. *et al.* RNA Condensate as a Versatile Platform for Improving Fluorogenic RNA Aptamer Properties and Cell Imaging. *J. Am. Chem. Soc.* **146**, 4402–4411 (2024).

77. Banani, S. F. & others. Compositional control of phase-separated cellular bodies. *Cell* **166**, 651–663 (2016).

78. Li, P. & others. Phase transitions in the assembly of multivalent signalling proteins. *Nature* **483**, 336–340 (2012).

79. Stewart, J. M. *et al.* Modular RNA motifs for orthogonal phase separated compartments. *Nat. Commun.* **15**, 6244 (2024).

80. Fabrini, G. *et al.* Co-transcriptional production of programmable RNA condensates and synthetic organelles. *Nat. Nanotechnol.* **19**, 1665–1673 (2024).

81. Litke, J. L. & Jaffrey, S. R. Highly efficient expression of circular RNA aptamers in cells using autocatalytic transcripts. *Nat. Biotechnol.* **37**, 667–675 (2019).

82. Tan, E., Chin, C. S. H., Lim, Z. F. S. & Ng, S. K. HEK293 Cell Line as a Platform to Produce Recombinant Proteins and Viral Vectors. *Front. Bioeng. Biotechnol.* **9**, 796991 (2021).

83. DuBridge, R. B. & others. Analysis of mutation in human cells by using an Epstein-Barr virus shuttle system. *Mol. Cell. Biol.* https://doi.org/10.1128/mcb.7.1.379-387.1987 (1987) doi:10.1128/mcb.7.1.379-387.1987.

84. Bereiter, R. & others. Engineering covalent small molecule-RNA complexes in living cells. *Nat. Chem. Biol.* https://doi.org/10.1038/s41589-024-01801-3 (2025) doi:10.1038/s41589-024-01801-3.

85. Johansson, H. E., Liljas, L. & Uhlenbeck, O. C. RNA recognition by the MS2 phage coat protein. *Semin. Virol.* **8**, 176–185 (1997).

86. Li, X., Wu, J. & Jaffrey, S. R. Engineering fluorophore recycling in a fluorogenic RNA aptamer. *Angew. Chem. Int. Ed.* **133**, 24355–24363 (2021).

87. Chen, X. & others. Visualizing RNA dynamics in live cells with bright and stable fluorescent RNAs. *Nat. Biotechnol.* **37**, 1287–1293 (2019).

88. Molliex, A. & others. Phase separation by low complexity domains promotes stress granule assembly and drives pathological fibrillization. *Cell* **163**, 123–133 (2015).

89. Feric, M. & others. Coexisting liquid phases underlie nucleolar subcompartments. *Cell* **165**, 1686–1697 (2016).

90. Parker, D. M., Tauber, D. & Parker, R. G3BP1 promotes intermolecular RNA-RNA interactions during RNA condensation. *Mol. Cell* **85**, 571–584 (2025).

91. Zhou, W.-Y. & others. Circular RNA: metabolism, functions and interactions with proteins. *Mol. Cancer* **19**, 172 (2020).

92. Fischer, J. W., Busa, V. F., Shao, Y. & Leung, A. K. L. Structure-mediated RNA decay by UPF1 and G3BP1. *Mol. Cell* **78**, 70–84 (2020).

93. Yu, H. & others. HSP70 chaperones RNA-free TDP-43 into anisotropic intranuclear liquid spherical shells. *Science* **371**, eabb4309 (2021).

94. Timney, B. L. & others. Simple rules for passive diffusion through the nuclear pore complex. *J. Cell Biol.* **215**, 57–76 (2016).

95. Arzt, M. & others. LABKIT: labeling and segmentation toolkit for big image data. *Front. Comput. Sci.* **4**, 777728 (2022).

96. Lee, D. S. W. & others. Size distributions of intracellular condensates reflect competition between coalescence and nucleation. *Nat. Phys.* **19**, 586–596 (2023).

97. Cawte, A. D., Unrau, P. J. & Rueda, D. S. Live cell imaging of single RNA molecules with fluorogenic Mango II arrays. *Nat. Commun.* **11**, 1283 (2020).

98. Udono, H. & others. Programmable computational RNA droplets assembled via kissing-loop interaction. *ACS Nano* **18**, 15477–15486 (2024).

99. Agarwal, S., Osmanovic, D., Dizani, M., Klocke, M. & Franco, E. Dynamic control of DNA condensation. *Nat. Commun.* **15**, 1915 (2024).

100. Malouf, L. & others. Sculpting DNA-based synthetic cells through phase separation and phase-targeted activity. *Chem* https://doi.org/10.1016/j.chempr.2023.10.004 (2023) doi:10.1016/j.chempr.2023.10.004.

101. Roden, C. & Gladfelter, A. S. RNA contributions to the form and function of biomolecular condensates. *Nat. Rev. Mol. Cell Biol.* **22**, 183–195 (2021).

102. Garcia-Jove Navarro, M. & others. RNA is a critical element for the sizing and the composition of phase-separated RNA-protein condensates. *Nat. Commun.* **10**, 3230 (2019).

103. Bose, M., Rankovic, B., Mahamid, J. & Ephrussi, A. An architectural role of specific RNA-RNA interactions in oskar granules. *Nat. Cell Biol.* **26**, 1934–1942 (2024).

104. Langdon, E. M. & others. mRNA structure determines specificity of a polyQ-driven phase separation. *Science* **360**, 922–927 (2018).

105. Welles, R. M. & others. Determinants that enable disordered protein assembly into discrete condensed phases. *Nat. Chem.* **16**, 1062–1072 (2024).

106. Kim, T. H. & others. Phospho-dependent phase separation of FMRP and CAPRIN1 recapitulates regulation of translation and deadenylation. *Science* **365**, 825–829 (2019).

107. Dai, Y., You, L. & Chilkoti, A. Engineering synthetic biomolecular condensates. *Nat. Rev. Bioeng.* **1**, 466–480 (2023).

108. Kim, J. & Franco, E. RNA nanotechnology in synthetic biology. *Curr. Opin. Biotechnol.* **63**, 135–141 (2020).

109. Rostain, W. Engineering of RNA sensors and actuators in living cells. (University of Warwick, 2017).

110. Filonov, G. S., Moon, J. D., Svensen, N. & Jaffrey, S. R. Broccoli: rapid selection of an RNA mimic of green fluorescent protein by fluorescence-based selection and directed evolution. *J. Am. Chem. Soc.* **136**, 16299–16308 (2014).

111. Dunn, K. W., Kamocka, M. M. & McDonald, J. H. A practical guide to evaluating colocalization in biological microscopy. *Am. J. Physiol.-Cell Physiol.* **300**, C723–C742 (2011).

112. Yang, E. *et al.* Elucidation of TRIM25 ubiquitination targets involved in diverse cellular and antiviral processes. *PLOS Pathog.* **18**, e1010743 (2022).

113. Huang, S. *et al.* Positive selection analyses identify a single WWE domain residue that shapes ZAP into a more potent restriction factor against alphaviruses. *PLOS Pathog.* **20**, e1011836 (2024).

1.6 Supplementary Information

1.6.1 Supplementary Notes

SUPPLEMENTARY NOTES 1

The RNA strands were designed and optimized using the NUPACK Design tool with the script shown below[26]. A target secondary structure was denoted by DU+ notation. Sticky ends or kissing loops were pre-selected and noted as a design restraint as well as certain repeat nucleotide sequences. We used the default energy parameters from Serra and Turner, 1995 in 1M Na^+ [26].

NUPACK script for multi-stranded motif strand design:

---

material = rna

temperature[C] = 25.0 # optional units: C (default) or K

trials = 3

sodium[M] = 1.0 # optional units: M (default), mM, uM, nM, pM

dangles = some

target structure using DU+ notation

#5' SE

structure msmotif = U7 D15 (U2 D15 (+ U7) U2 D15 (+ U7) U2 D15 (+ U7) U2)

```
# sequence domains

domain A2 = AA


#input sticky-end sequence

domain SE = GCUAGCA

domain S4 = N15

domain S3 = N15

domain S2 = N15

domain S1 = N15


# thread sequence domains onto target structures

#5' SE

msmotif.seq = SE S1 A2 S2 SE S2* A2 S3 SE S3* A2 S4 SE S4* A2 S1*


# specify stop conditions for normalized ensemble defect

# default: 1.0 (percent) for each target structure

msmotif.stop = 1.0


# prevent sequence patterns
```

prevent = AAAA, CCCC, GGGG, UUUU, KKKKKK, MMMMMM, RRRRRR, SSSSSS, WWWWWW, YYYYYY

NUPACK script for single-stranded motif stem design:

---

material = rna1999

temperature = 37

trials = 10

structure NS= U1D20 U9 U2 D20 U9 U2 D20 U9

domain arm1= N20AAGCGCGCAN20AA

domain arm2= N20AAGCGCGCAN20AA

domain arm3= N20AAGCGCGCAN20

NS.seq = arm1 arm2 arm3

prevent = AAAA, CCCC, GGGG, UUUU, KKKKKK, MMMMMM, RRRRRR, SSSSSS, WWWWWW, YYYYYY

Supplementary Note 2

Pre-processing

Images affected by strong background noise making it impossible to process, and images that are defocused, or have overlap FOV were discarded.

All multi-stranded nanostar images for quantification were processed in FIJI (ImageJ) using a custom macro implementing the following pipeline: Images were

thresholded using a custom macro implementing the following pipeline: contrast enhancement (5% pixels saturated), background subtraction with white top-hat morphological filters (element=disk, radius=20), denoising via Gaussian Blur (sigma=2), and background subtraction with a rolling ball radius of 25-50 pixels.

For single-stranded nanostars, all black-and-white fluorescence images in figures were processed in FIJI (ImageJ) using a custom macro implementing the following pipeline: calibration, contrast enhancement (10% pixels saturated), denoising via Gaussian Blur (sigma = 1.5), and background subtraction with rolling ball method (radius = 1, for extremely large droplets radius = 10). Images for peptide recruitment were thresholded with LUT window (5000, 10000) (16-bit) for the brightfield channel and at (10000,65535) for 6FAP-tagged peptides. Brightfield channel images were inverted to a black background before merging.

Segmentation

In peptide recruitment experiments using multi-stranded nanostars, we used the MaxEntropy method for thresholding. Masks were generated from the CY3 channel for the Streptavidin-binding motif, the CY5 channel for the P22-binding motif, and FITC channel images for TAT-binding motifs. For single-stranded nanostars, we used the Moment method for thresholding. All masks were saved as TIFF files for further analysis.

Chord Length Distribution (CLD) analysis

All chords mentioned in the paper are applied and calculated by functions from the Python package Porespy, particularly Porespy.filters.apply_chords, using the built-in

method. In short, chords are applied as lines with fixed space (in our case, 1 pixel) within the area of interest in both the x and y directions. Objects touching the edges of the FOV are excluded (trim_edges = False). Chord lengths are then calculated as the number of pixels of each line and calibrated to micrometers.

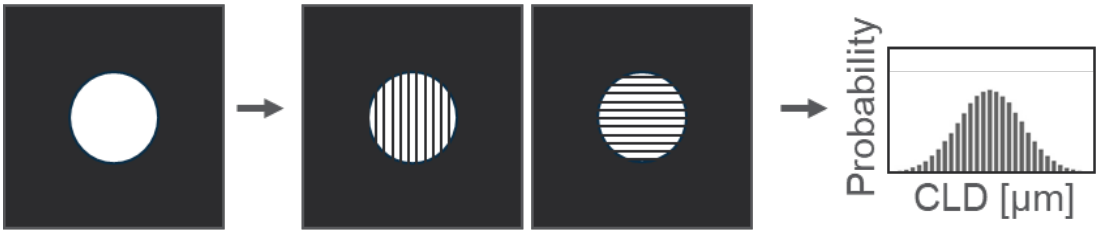

Figure 1-6. Chord Length Distribution (CLD) analysis.

The resulting Numpy arrays are saved in NPY format via Numpy. Each sample's resulting chord lengths, along x and y and across all FOVs, are pooled together, and saved into new arrays. The reported means are calculated as mean(mean_sample1, mean_sample2, mean_sample3).

CONDENSATE NUMBER ANALYSIS

Objects smaller than 6 px2 (about 0.3 µm2) were considered as noise and excluded. Droplet numbers were autogenerated by FIJI - Measure and recorded.

COORDINATE ANGLE MAPPING

To determine whether our nanostars including distinct fluorogenic aptamers produce condensates that mix or do not mix, we built pixel intensity histograms from fluorescence microscopy images (**Fig. 1-4**). This was done because upon DFHO staining, both Corn and Red Broccoli aptamers can be detected in the FITC channel and the Cy3 channel, albeit with varying intensity, since Corn aptamer Emmax = 545 nm, and Red Broccoli Emmax = 582 nm2. Images were processed to obtain the intensity of each pixel within segmented regions of interest in each channel (FITC and

Cy3) and computing the angle of their coordinates in a plane with an x-axis corresponding to the CY3 channel intensity and with a y-axis corresponding to the FITC channel intensity, as sketched in **Fig. 1-28**. A line was drawn from the projected point to the origin, and the angle between this line and the x-axis was referred to as the coordinate angle. Finally, we generated a histogram based on the coordinate angles calculated from every pixel within the regions of interest.

It is important to note that although both Corn and Red Broccoli rely on the formation of G-quadruplexes to bind their fluorophore, Red Broccoli forms an intramolecular core-binding region, while Corn forms homodimer where fluorophores bind dimer interfaces2,9. This aptamer-directed dimerization is present in addition to designed KL-directed interactions, and results in the formation of structures other than spherical droplets for Corn-appended nanostars (**Fig. 1-29**, indicated by white arrow). These structures can be distinguished based on their non-spherical shape and were excluded from histogram generation according to their region labels.

As a control, we prepared separate samples including condensates from nanostars including Corn or Red Broccoli individually. The expectation is that if the nanostars are orthogonal, the histogram peaks measured when Corn and Red Broccoli condensates are produced in the same sample would be aligned with those of the separately annealed controls. If any mixing occurs due to the nanostar interactions, then a shift of the peaks (indicating mixing with a specific stoichiometry) or a uniform distribution (indicating mixing following a random stoichiometry) would be observed.

Subsequent processing was performed using a Python3 script. For each FOV, we generated a mask by applying a Gaussian blur (sigma = 5) and gamma

enhancement (gamma = 0.5) to the CY3 channel image, thresholding it using the Otsu method, skeletonizing it to generate seeds, and growing it using a watershed transformation. For each pixel within the masks, pixel intensities for CY3, FITC channels, and the region labels were extracted into three columns and saved in a .csv file. We manually excluded regions with unfocused droplets and non-spherical, cloudy condensates. Finally, we used a Python script to read and concatenate the data of 10 FOV into a single .csv file. The calculation of coordinate angles and histogram plotting is described below (Data visualization).

DATA VISUALIZATION

Violin plots were generated using a Python3 script based on Seaborn. For three NPY files storing chord length information of three repeats, the script loads the files, calibrates chord length into μm, and pools them into one array as the input dataset for violin plots. Cut = 0 was applied to ensure that the kernel density estimation doesn't exceed the data range. As for kernel density estimation for the violin plots, data was normalized to have the same area of the violins (scale = 'area'). The coordinate angle histogram was generated using a Matlab script. The script loaded .csv files in which we recorded the pixel intensity of FITC and Cy3 channels of regions of interest (condensates). The background was eliminated by subtracting the smallest value of each channel. Each row of the resulting array contained the background-subtracted pixel intensities of both channels for each pixel within the droplet region. The coordinate angle for each pixel was calculated as arctan (FITC intensity/Cy3 intensity). Histograms were normalized to have the unitary area.

Data processing for FRAP

Images are first processed to eliminate the influence of horizontal drifting using the SIFT algorithm (https://imagej.net/plugins/linear-stack-alignment-with-sift) with default parameters and no interpolation. Then, a spherical ROI was drawn at the bleached area and an ROI of the same size was generated on the surrounding unbleached droplets and used as controls. Normalized pixel intensity within both ROIs was exported and recovery was calculated as

$$(I_{bleach,t}/I_{bleach,\max})/(I_{unbleach,t}/I_{unbleach,max}) \quad (1)$$

where I denote mean pixel intensity among the area, t denotes a certain time point, max denotes the highest pixel intensity within the area among all time points.

Data processing for time-dependent coalescence

Images were stacked and aligned using the Registration plugin - Linear stack alignment with SIFT to correct horizontal drifting. Then images are enhanced with saturation = 5% and background subtracted with rolling ball radius = 9 for display. Seven fusion events were found and manually cropped from the epifluorescence images, exported as TIFF files, and imported into Python. For each fusion event, condensates were segmented using Otsu unsupervised thresholding as implemented in skimage.filters.threshold_otsu. The binarized image was then labeled using skimage.measure.label, which associates a different label to each segmented object. Associated geometrical properties, including centroid position, major and minor axis lengths, and orientation, were extracted via skimage.measure.regionprops_table. The Characteristic length (lc) of condensates at the initial frame was measured manually in ImageJ using the ROI tool and calculated as the mean of the two droplets' radii. For

time points following contact, the Aspect Ratio was computed as the ratio between the major and the minor axis length of the best-fit ellipse and appended to a list. Time constants were obtained by fitting the Aspect Ratio vs time profiles with a single exponential decay with the formula using scipy.optimize.curve_fit, where a and τ_c are fitting parameters. Finally, computed time constants were linearly fitted against the pre-fusion characteristic droplet size (Characteristic Length, lc) using scipy.stats.linregress, yielding the inverse capillary velocity as the fit slope. Linear regression parameters (mean ± standard error), R2, and p-value with respect to the null hypothesis (H0) of null slope are as follows: slope = 3468.64±1892.93, intercept: 2228.90±6195.51, R2 = 0.63, p-value = 0.126.Add your text here and indent the first line of all new paragraphs. All text is double spaced. All text and hyperlinks must be the same font, same font size (10-12pt), and in black colored text. All text must be the same justification, like left justified or fully justified. All text, figures/tables, captions, and equations must fit within the 1-inch margins.

1.6.2 Supplementary Figures

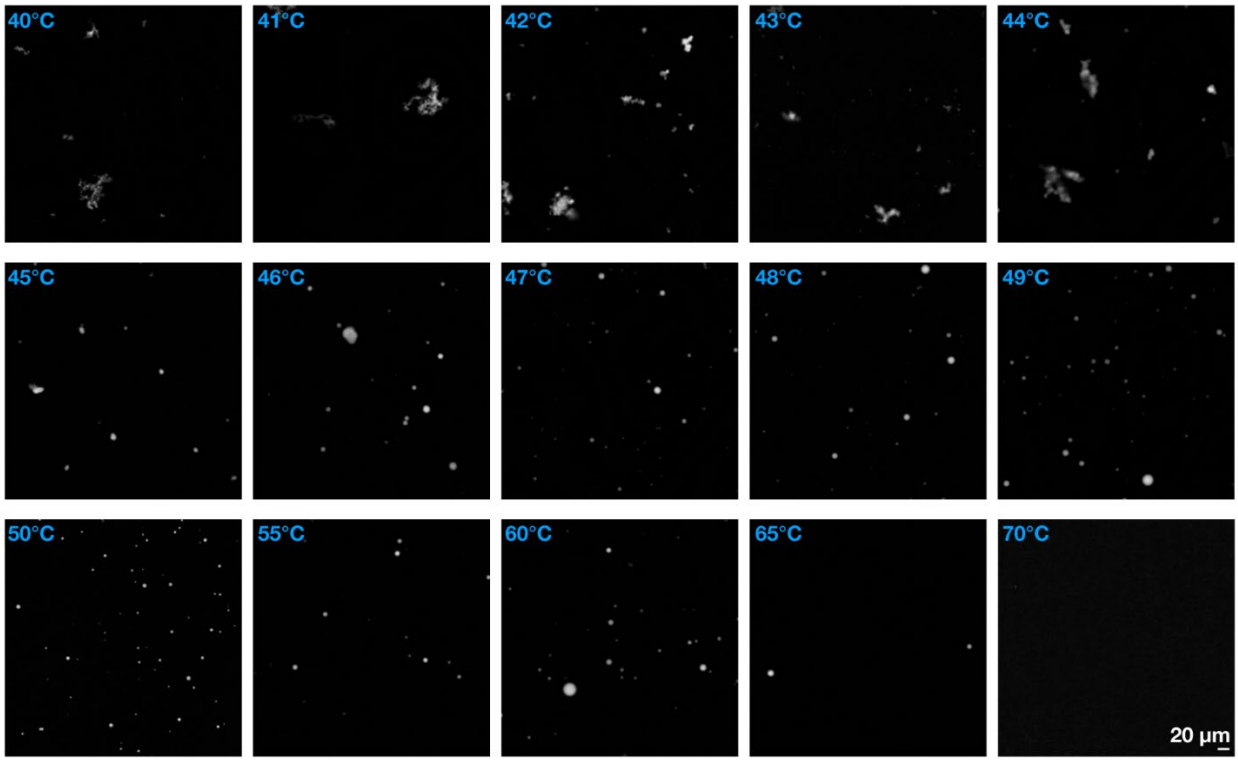

Figure 1-7. 12-hour incubation over variable temperatures of multi-stranded condensates.

Multi-stranded condensates (4m5) were annealed with our annealing protocol that includes a melt phase (70°C for 10 min) and hold phase (temperature between 40°C-70°C 12h) protocol. Strands were annealed in our assembly buffer (40 mM HEPES/100KCl/500 mM NaCl). Samples were stained with SYBR Gold and imaged. Experiments were repeated three times, n=3; here we provide representative images.

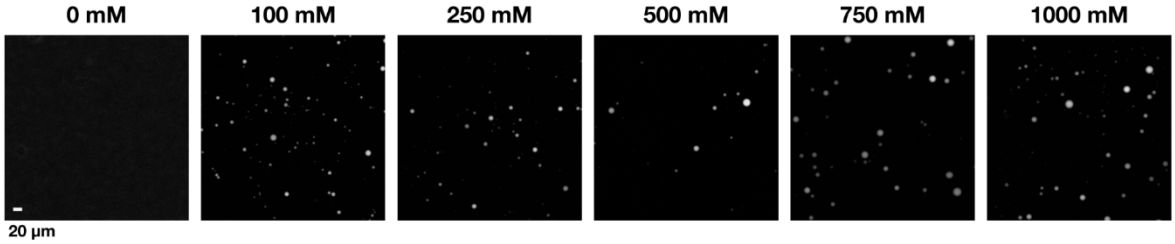

Figure 1-8. Potassium titrations of multi-stranded condensates.

Nanostars (4m6) were assembled in 40 mM HEPES and a variable KCl concentration. All samples underwent a thermal treatment of a 70°C denaturing steep for 10 minutes, then incubated at 50°C for 12 hours, then a quick cool to room temperature. Liquid-like condensate formation begins at 100 mM KCl and maintains droplet-like morphology through 1000 mM KCl. Samples were stained with SYBR Gold and imaged. Experiments were repeated three times, n=3; here we provide representative images.

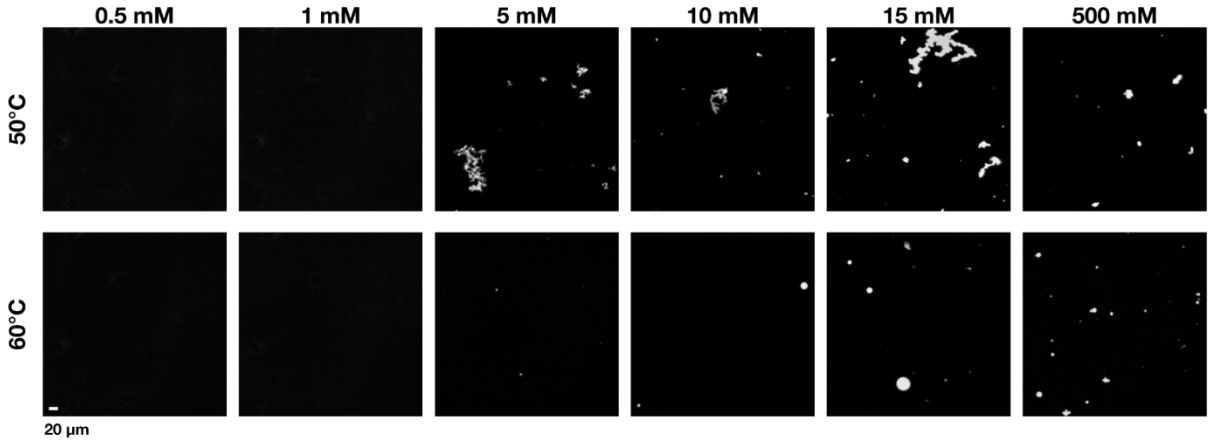

Figure 1-9. Magnesium titrations of multi-stranded condensates.

Nanostars (4m6) were assembled in 40 mM HEPES and a variable Magnesium concentration. Under the protocol using equimolar purified RNA strands that form an RNA motif via thermal treatment of a 70°C denaturing step for 10 minutes, then incubating at 50°C for 12 hours, then a quick cool to room temperature, the addition of Magnesium causes gel formation, starting at 5 mM. As expected, the addition of Magnesium changes the melting temperature of the condensates, in which we observe droplet-like assemblies when we raise to a 12-hour incubation step from 50°C to 60°C around 15 mM Magnesium. Samples were stained with SYBR Gold for imaging. Experiments were repeated three times, n=3; here we provide representative images.

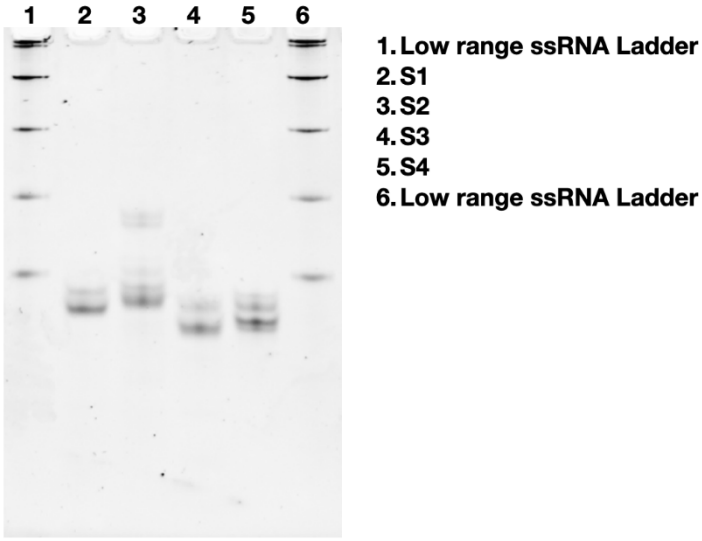

Figure 1-10. 10% denaturing polyacrylamide gel of RNA strands S1, S2, S3, and S4 from design 4m6 with sticky-end sequence 5'-GCUAGC.

RNA was produced from *in vitro* T7 transcription and purified by Amicon 10K 0.5 mL centrifugal filters. Experiments were repeated three times, n=3. Target strand sizes are 39 NT, however, shorter and longer products are present which may contribute to the unwanted formation of assemblies.

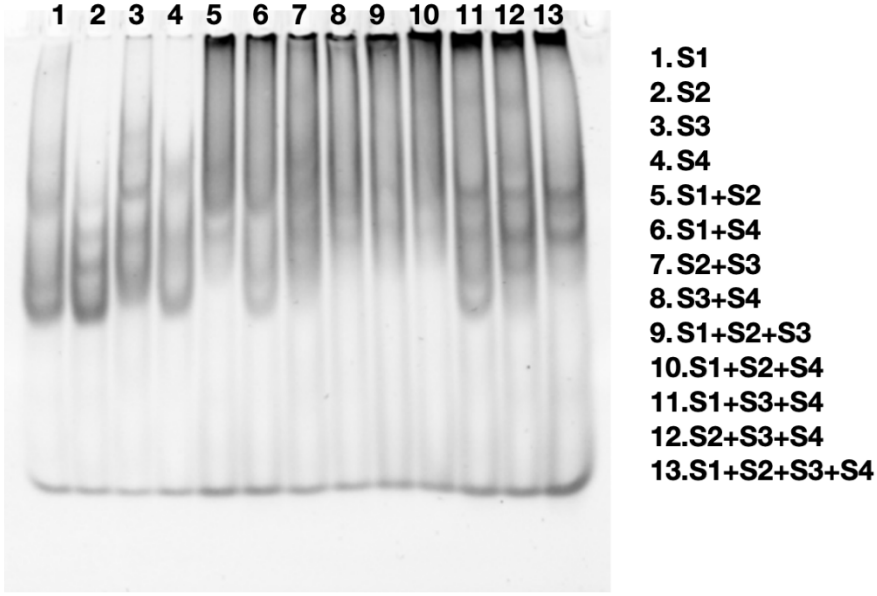

Figure 1-11. 12% non-denaturing polyacrylamide gel of RNA strands S1, S2, S3, and S4 from design 4m6 with sticky-end sequence 5'-GCUAGC.

RNA was produced from *in vitro* T7 transcription and purified by Amicon 10K 0.5 mL centrifugal filters (as mentioned in Supplementary Section 1.2.1). Samples were annealed either individually (lanes 1-4) or in equimolar concentrations (lanes 5-13). Experiments were replicated twice, n = 2. Individual strands (lanes 1-4) form secondary structures as indicated by multiple bands. Two interacting strands (lanes 5-8) annealed together form large structures as evidenced by large complexes that are present in the wells and smears. S1+S2 produces the largest amount of sample stuck in the well for two interacting strands. Three interacting strands (lanes 9-12) and the complete NS sample (lane 13) present greater prominent bands in comparison to the two-strand samples. Samples that are present in the wells may occur due to palindromic sequences that make it possible for long chains to form. Smears may also be present due to erroneous transcription products that form unwanted assemblies.

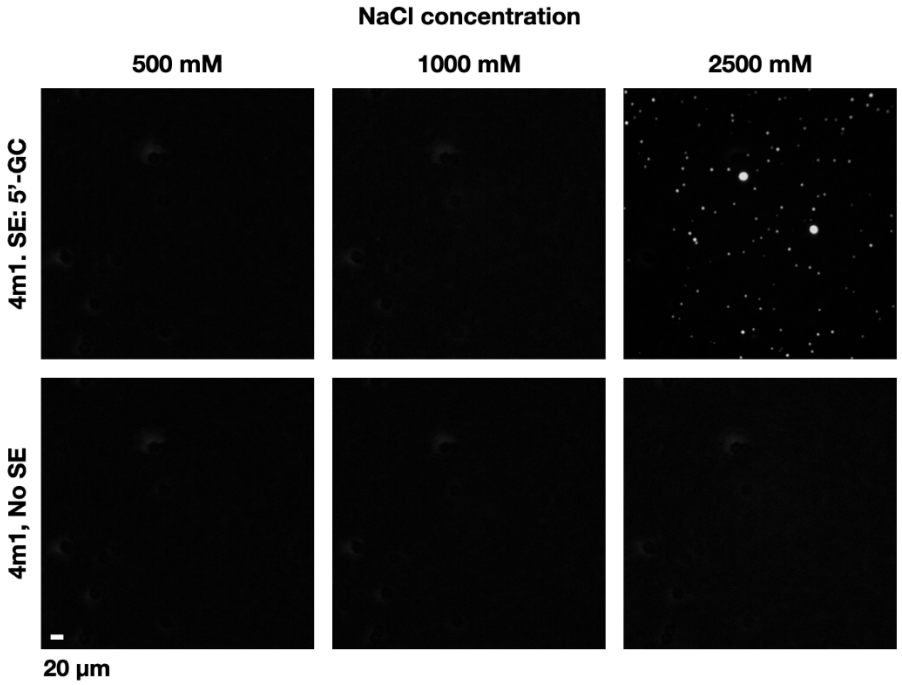

Figure 1-12. NaCl titrations using multi-stranded nanostars with and without 2nt sticky ends.

Nanostar with 2nt 5'-GC (4m1) required 40 mM HEPES/100 mM KCl and increased NaCl concentration to form via a thermal treatment of a 70°C denaturing step for 10 minutes, then incubating at 50°C for 12 hours. RNA nanostars without sticky-ends (4m1) do not form in comparable buffer and temperature conditions. Samples were stained and imaged with SYBR Gold. Experiments were repeated three times, n=3; here we provide representative images.

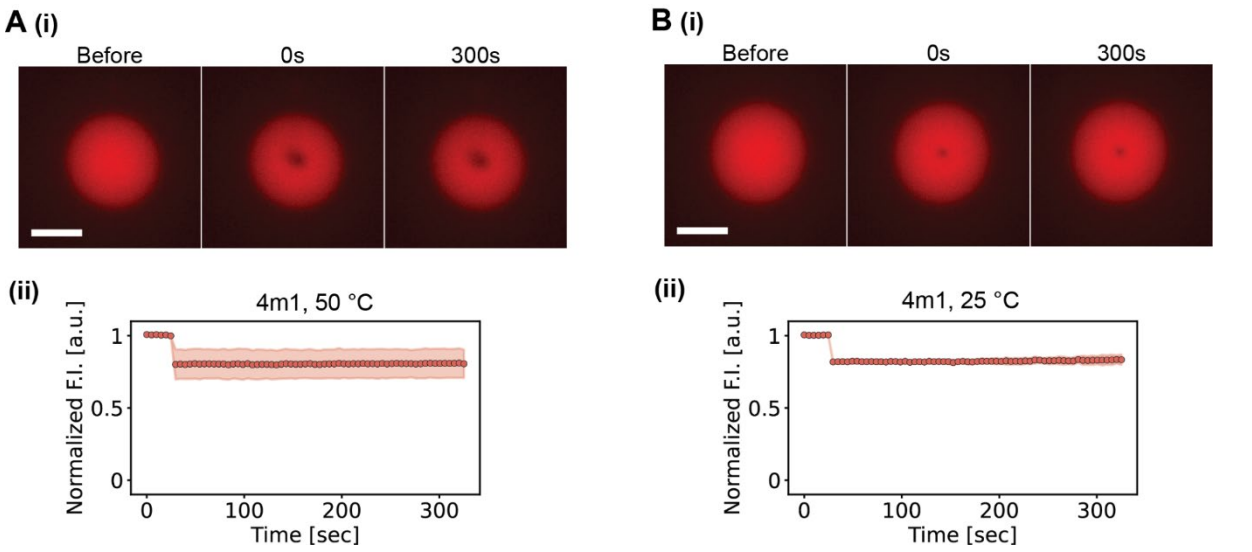

Figure 1-13. Fluorescence recovery after photobleaching (FRAP) analysis of condensate formed from multi-stranded nanostar treated with melt-and-hold protocol showed little recovery.

RNA was transcribed with 1% of CY3 tagged UTP and purified with size exclusion columns before imaging. Condensates were annealed with the heal-and-hold protocol and imaged at 50°C (for A) or at room temperature (for B). Orange dots indicate mean intensity at the corresponding time point. Shaded areas indicate standard error. Mean and standard error were calculated from 3 FOVs each belonging to one replicate. Scale bar, 10 μm.

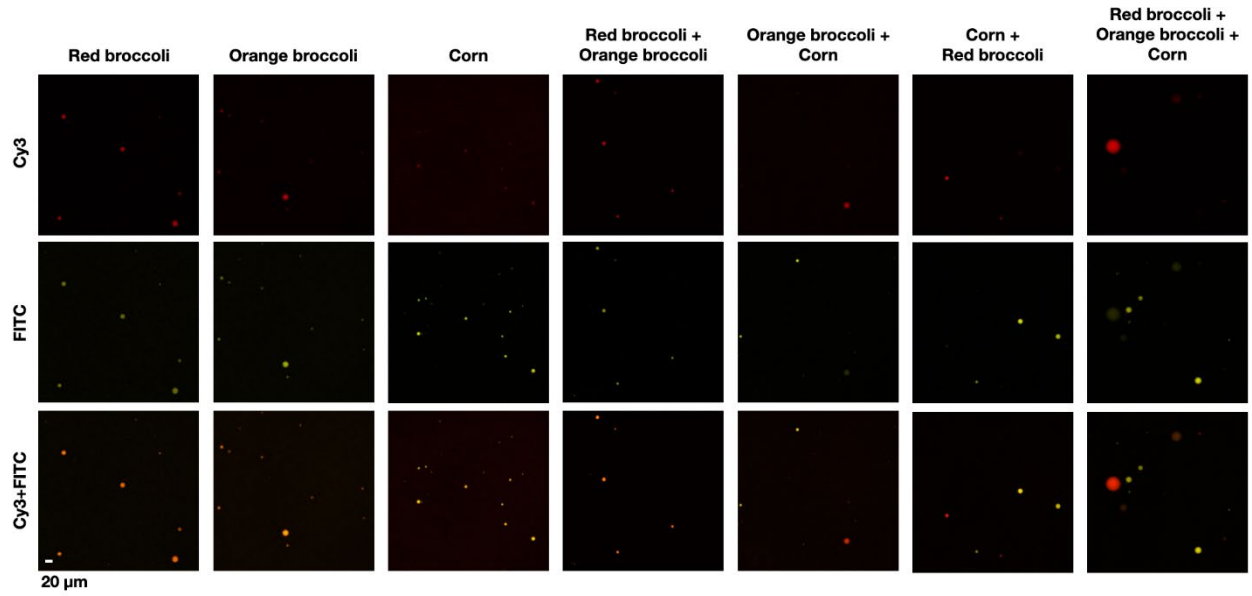

Figure 1-14. Condensates with fluorogenic aptamers.

RNA nanostars 4m3, 4m5, and 4m6 with Orange Broccoli, Corn, and Red Broccoli aptamers respectively, formed as single, double, and triple condensate systems in 40 mM HEPES, 100 mM KCl, 500 mM NaCl. Condestes were thermally treated by a quick 70°C melt followed by a 12h-long hold 50°C. Condensates were imaged using single filter channels Cy3 and FITC and showing the resulting overlay of filters Cy3 and FITC. Experiments were repeated three times, n=3; here we provide representative images.

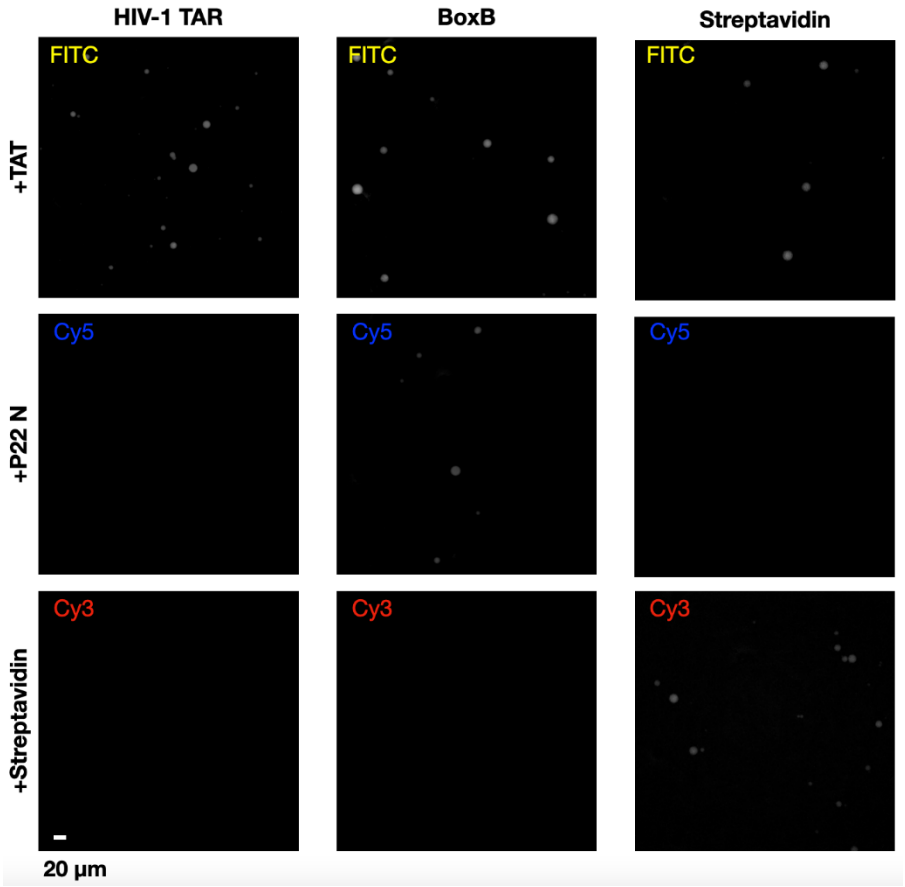

Figure 1-15. Recruitment of peptides and protein of multistranded condensates.

Fluorescence microscopy data of multistranded condensates 4m6 with TAR RNA, 4m5 with boxB RNA, and 4m3 with streptavidin binding aptamer in the presence of individual targets TAT peptide labeled with 6FAM, P22 N peptide labeled with AF647, and streptavidin protein labeled with AF555. Experiments were repeated three times, n=3; here we provide representative images. The positive charge of TAT peptide due to the rich arginine content causes indiscriminate binding to negatively charged RNA. Scale bar, 20 µm.

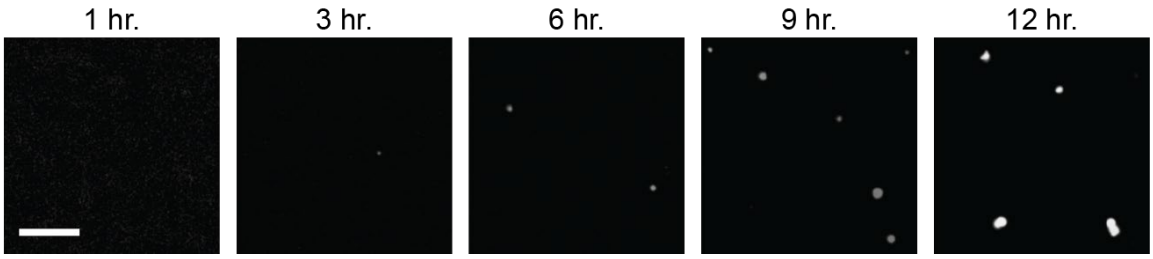

Figure 1-16. Condensate growth during incubation at 50°C.

We tracked the growth of our three-arm single-stranded nanostar 3sWT-stem1 during the hold step. The annealing mixture was aliquot into five samples, initiated simultaneously, and imaged at different time points. Condensates were stained with SYBR Gold and imaged. Images are enhanced for brightness and contrast with the same treatment for displaying. Experiments were repeated three times, n=3; here we provide representative images. Scale bar, 10 μm.

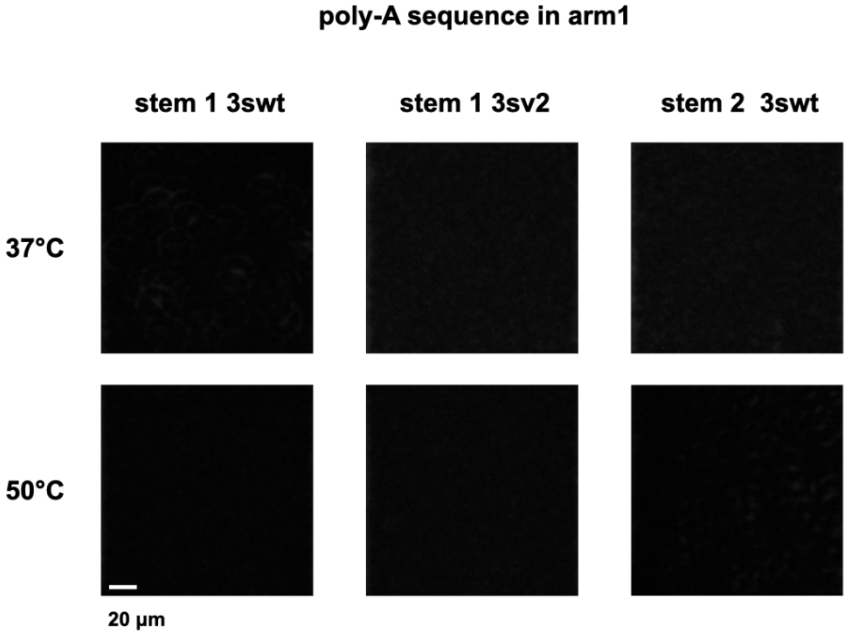

Figure 1-17. Single-stranded nanostar variants with one of the three WT KLs replaced with the poly-A sequence formed no condensate.

After the melt step, nanostars were incubated at 37°C or 50°C for 12h and cooled to 20°C before imaging. Samples were stained with SYBR Gold for imaging. Experiments were repeated three times, n=3; here we provide representative images. Scale bar, 20 μm.

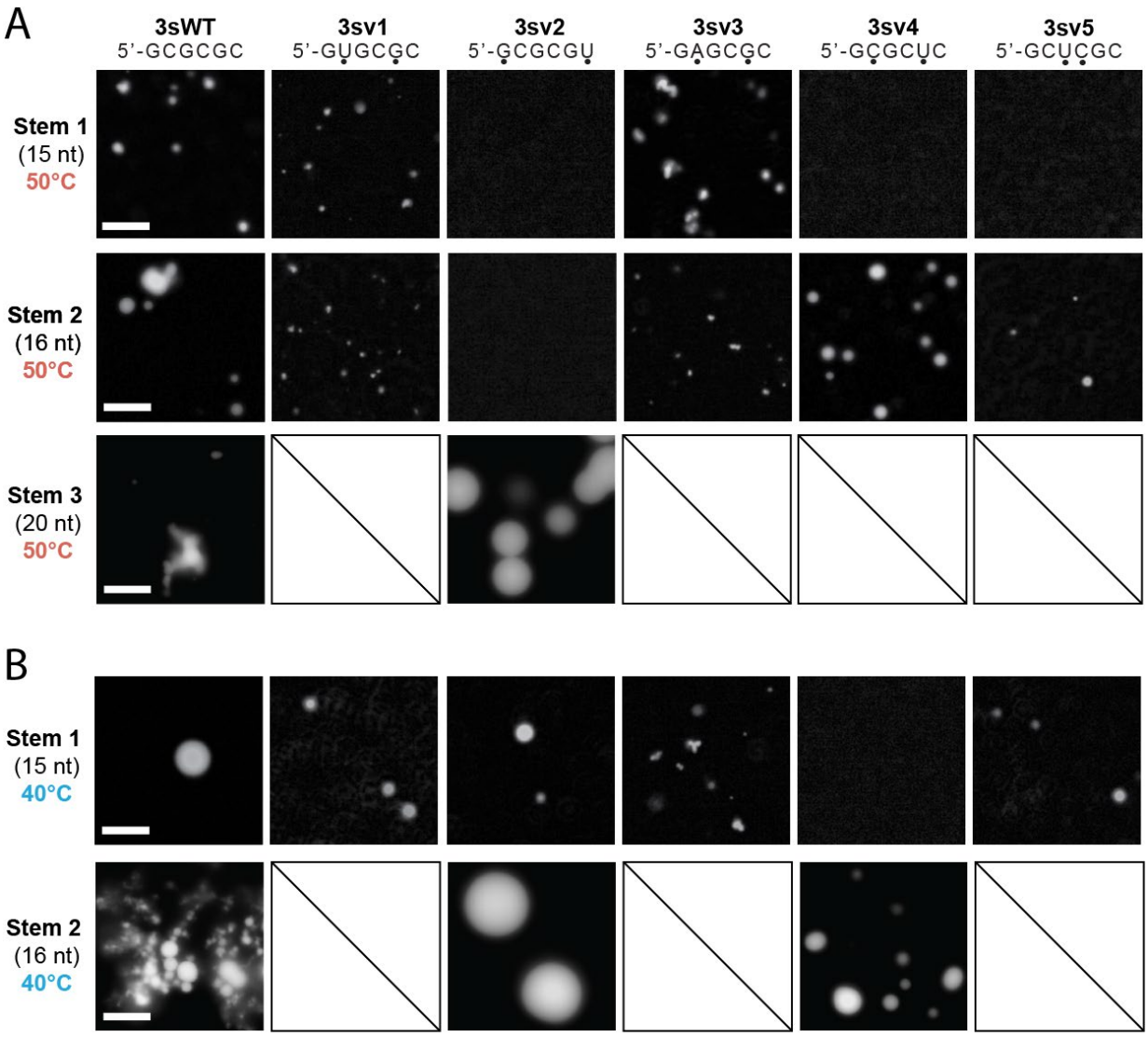

Figure 1-18. Overview of fluorescence microscopy images for single nanostar designs.

A) Condensates assembly from three types of stems and six types of self-complementary kissing loops that had no (3sWT) or two (all variants) mismatches (indicated by dots) with a 50°C hold. Stems have different lengths and sequences. B) Condensates assemble with a 40°C hold. All variants were assembled from purified RNA using our assembly buffer and the melt and hold annealing protocol (10 min at 70°C followed by 12 h hold at specified temperature), and stained with SYBR Gold for imaging. Experiments were done in n=3; here we provide representative images. Scale bar, 10 μm.

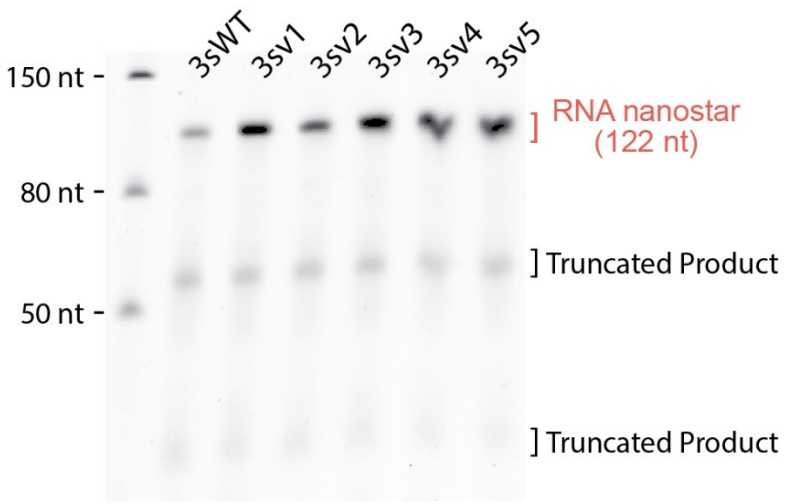

Figure 1-19. Purified RNA Transcribed by T7 polymerase includes truncated product.

In an 8% denaturing polyacrylamide gel, RNA purified from transcription products by T7 polymerase exhibited a major band corresponding to the desired stem 1 RNA nanostars, alongside two minor bands representing truncated products. The single-stranded regions of the DNA templates fold into nanostar structures, as predicted by NUPACK, while the formation of stem-loop structures causes early transcription termination due to polymerase dissociation. The gel was stained with 1x SYBR Gold. The gel was repeated at least five times with consistent results.

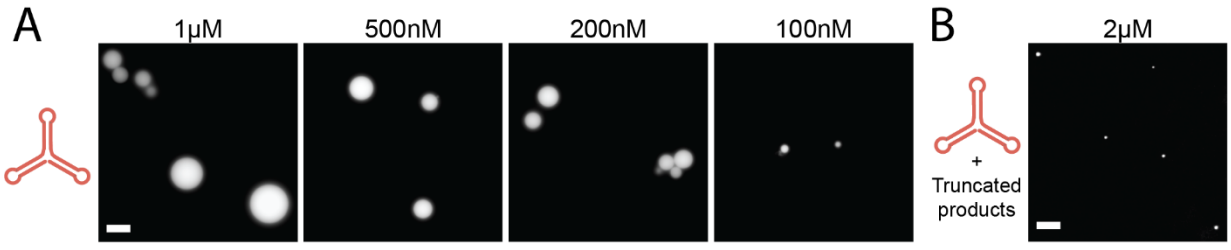

Figure 1-20. The critical concentration for condensation is influenced by the presence of truncated transcription products.

A) Variant 3sv2, stem 1 was transcribed, size-exclusion-column purified, and gel extracted. Condensates form at concentrations as low as 100 nM. B) Variant 3sv2, stem 1 was transcribed and size-exclusion-column purified, but not gel extracted. In the presence of truncated products, only tiny

condensates can form at 2 μM. All samples were treated by the melt-and-hold protocol with a hold temperature at 40°C in our assembly buffer, and were stained with 1x SYBR Gold for imaging. Experiments were repeated three times, n=3; here we provide representative images. Scale bar, 10 μm.

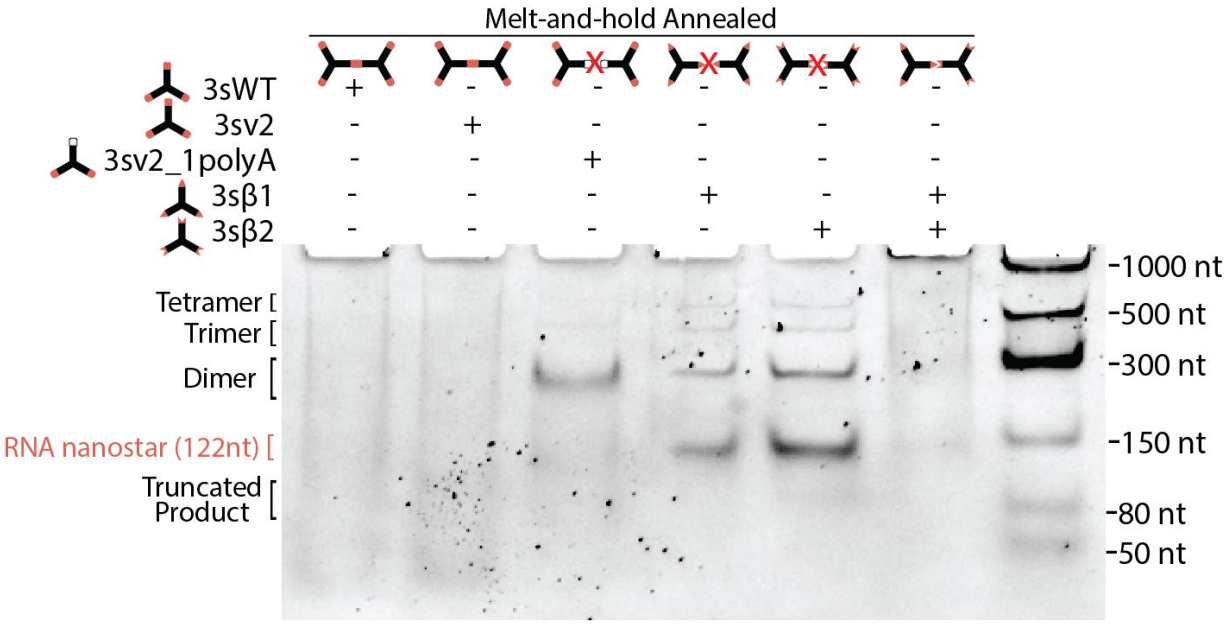

Figure 1-21. Folding and interaction between single-stranded RNA treated with melt-and-hold protocol.

In 8% native polyacrylamide gels, folded nanostars migrate slower than single-stranded RNA ladders. This characteristic is known for structured RNA. nanostars with palindromic kissing loops form complexes manifest as smears that cannot pass through the gel. Eliminating one kissing loop by changing it to poly A (5'-AAAAAA) dissociates the complex and generates predominantly dimers. The gel was stained with 1x SYBR Gold. The gel was repeated twice with consistent results.

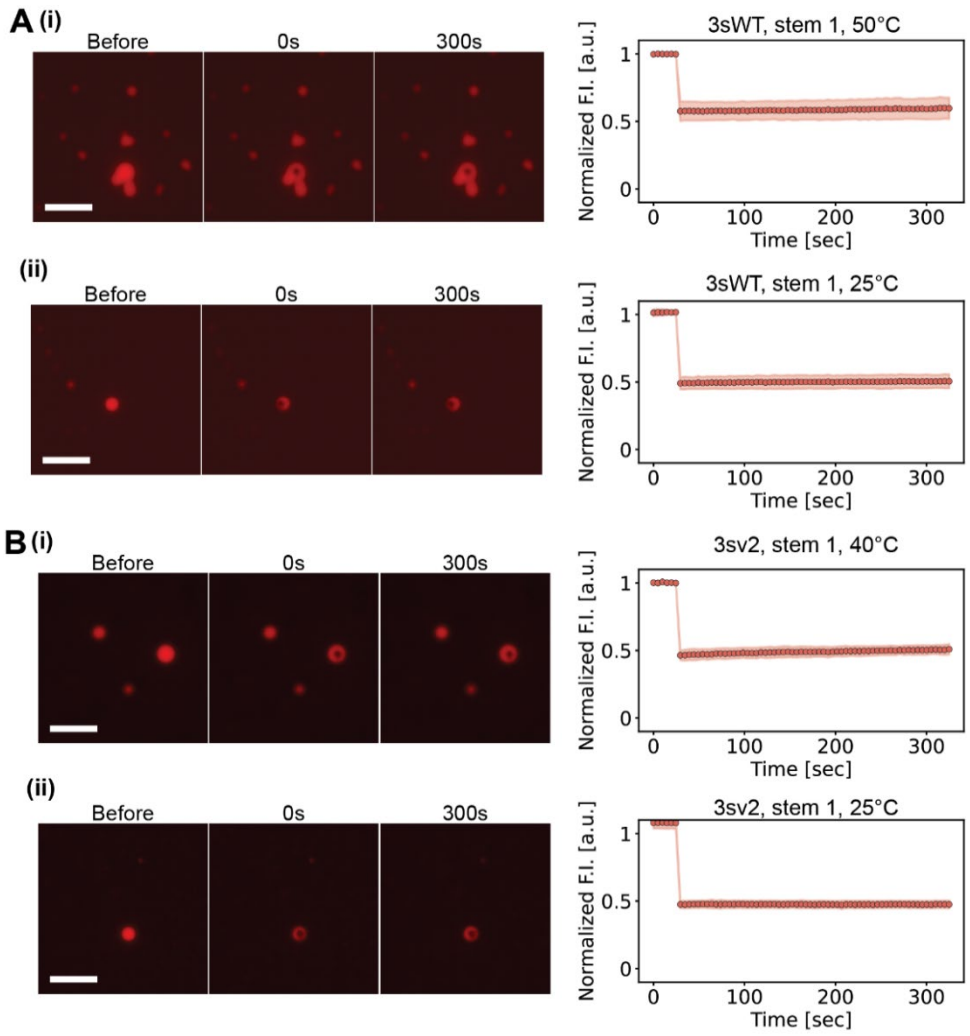

Figure 1-22. Fluorescence recovery after photobleaching (FRAP) analysis of condensate formed from single-stranded nanostar treated with melt-and-hold protocol and co-transcribed showed little recovery.

RNA was transcribed with 1% of CY3 tagged UTP and purified with size exclusion columns before imaging. Condensates were annealed with the heal-and-hold protocol and imaged at 50°C (**A (i)**, for variant 3sWT) or 40°C (**B(i)**, for variant 3sv2) or at room temperature (**A(ii)** and **B(ii)**). Orange dots indicate mean intensity at the corresponding time point. Shaded areas indicate standard error. Mean and standard error were calculated from 3 FOVs each belonging to a single replicate. Scale bar, 10 μm.

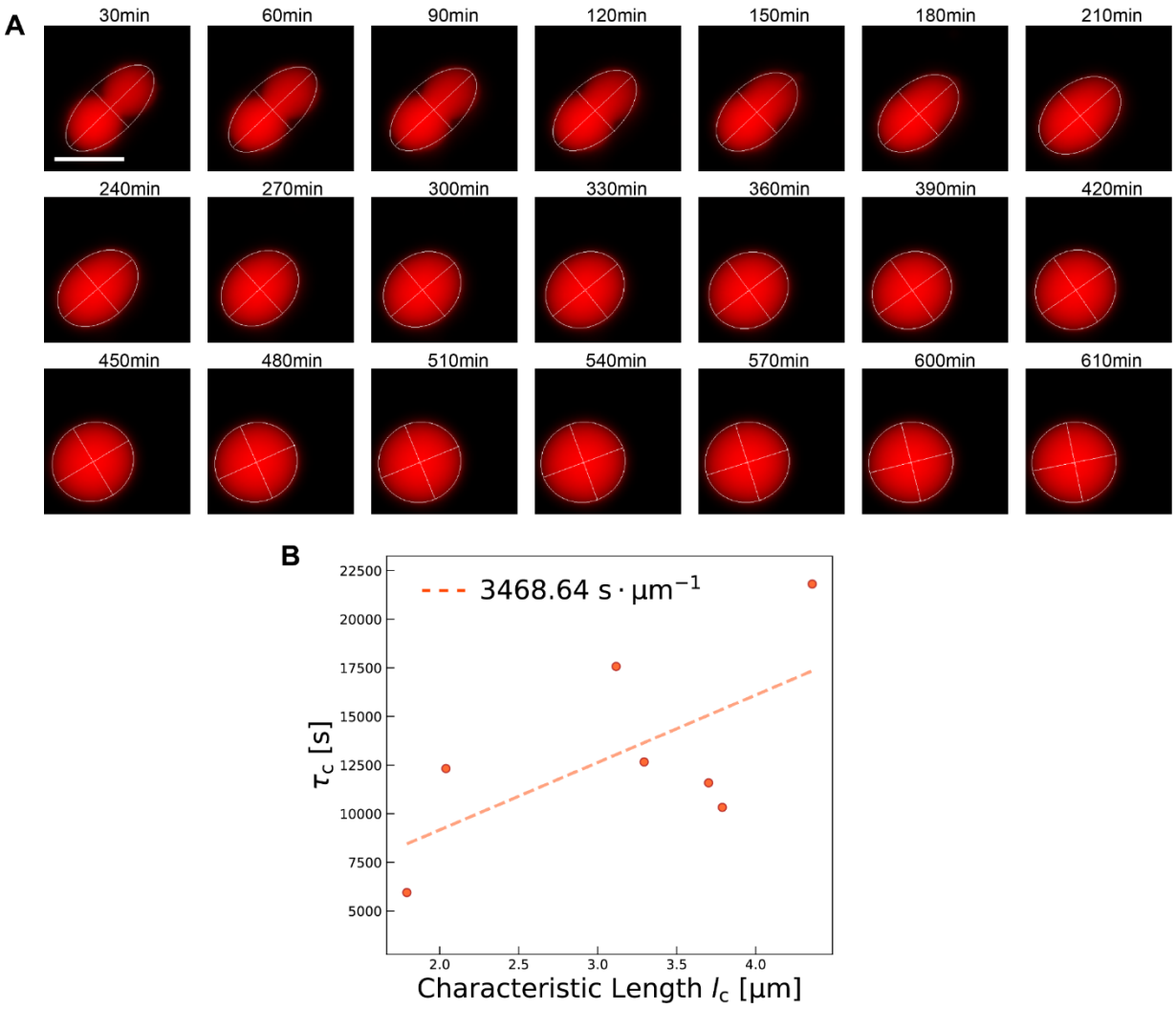

Figure 1-23. Time-dependent coalescence of 3sv2 holding at 40 °C.

(**A**) A coalescence event of 3sv2 droplets. (**B**) The time constant (*τc*) against the characteristic length (lc). Linear regression yields the inverse capillary velocity, μ/γ based on seven coalescence events from one sample. R^2 and p-value for the null hypothesis (H_0) of null slope are as follows: slope = 3468.64±1892.93, intercept: 2228.90±6195.51, R^2 = 0.63, p-value = 0.126. The characteristic length was calculated as the mean of two droplets at the beginning of a coalescence event. RNA was transcribed, column purified, and annealed following the melt-and-hold protocol. Condensates are stained with 1x SYBR Gold and imaged in a sealed chamber. Images are processed with SIFT for stack alignment to correct horizontal drifting. Data is extracted from one field of view from one experimental replicate. Scale bar, 10 μm.

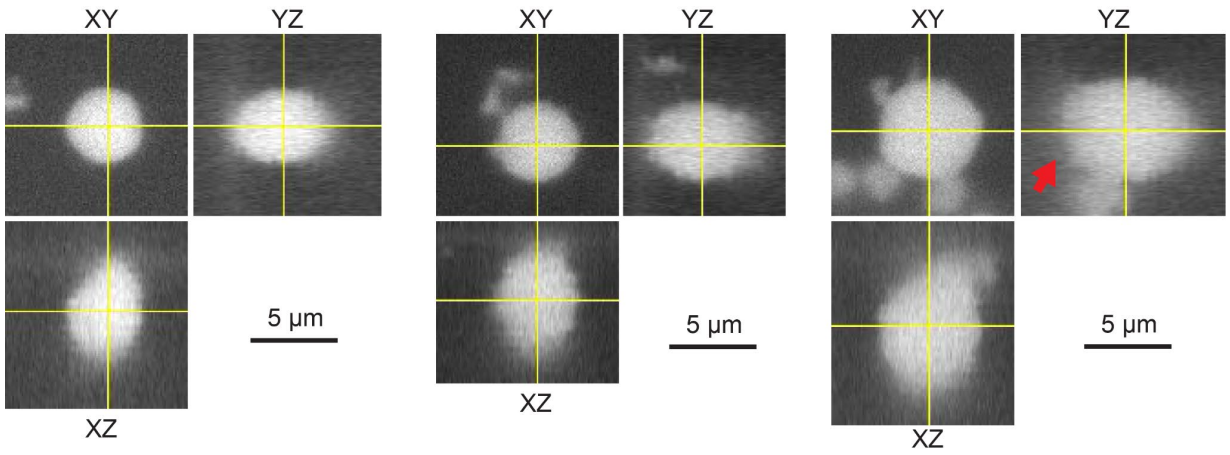

Figure 1-24. Orthogonal views of confocal images of condensates demonstrate sedimentation of condensates on the glass slide surface with no significant deformation or wetting of the surface.

Variant 3sv2, stem 1 was annealed following the melt-and-hold protocol by held at 40°C. The red arrow indicated one droplet where slight wetting of the surface was observed. Samples are stained with 1x SYBR Gold. The extension of droplets on the z-axis direction could be attributed to photonic leakage of confocal imaging. Data is extracted from three fields of view from one sample. Scale bar, 5 μm.

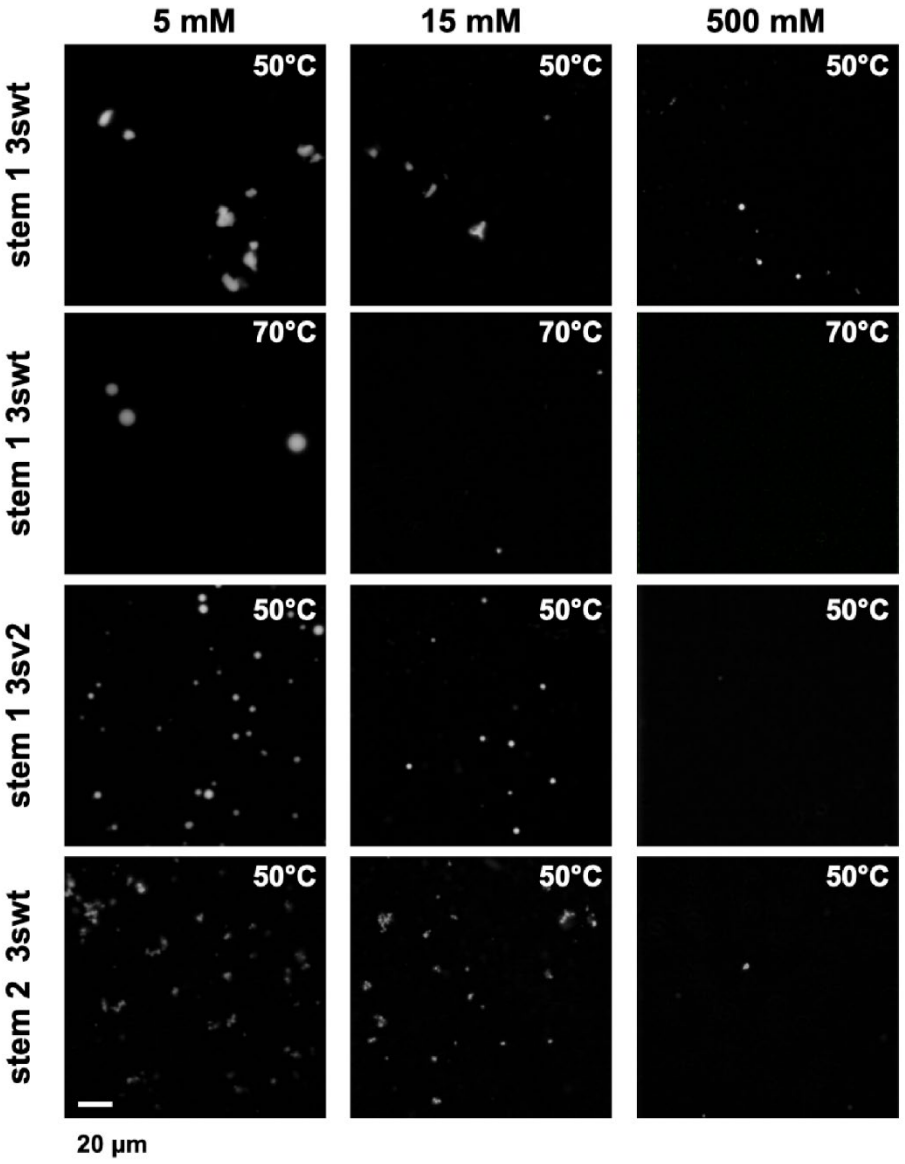

Figure 1-25. Condensate formation at different magnesium conditions. Fluorescence micrographs showing condensate morphology of three motifs in the presence of 40 mM HEPES and a variable $MgCl_2$ concentration.

Condensates were annealed at 50°C for 12h and cooled to 20°C before imaging. Samples were stained with SYBR Gold for imaging. Experiments were repeated three times, n=3; here we provide representative images. Scale bar, 20 µm.

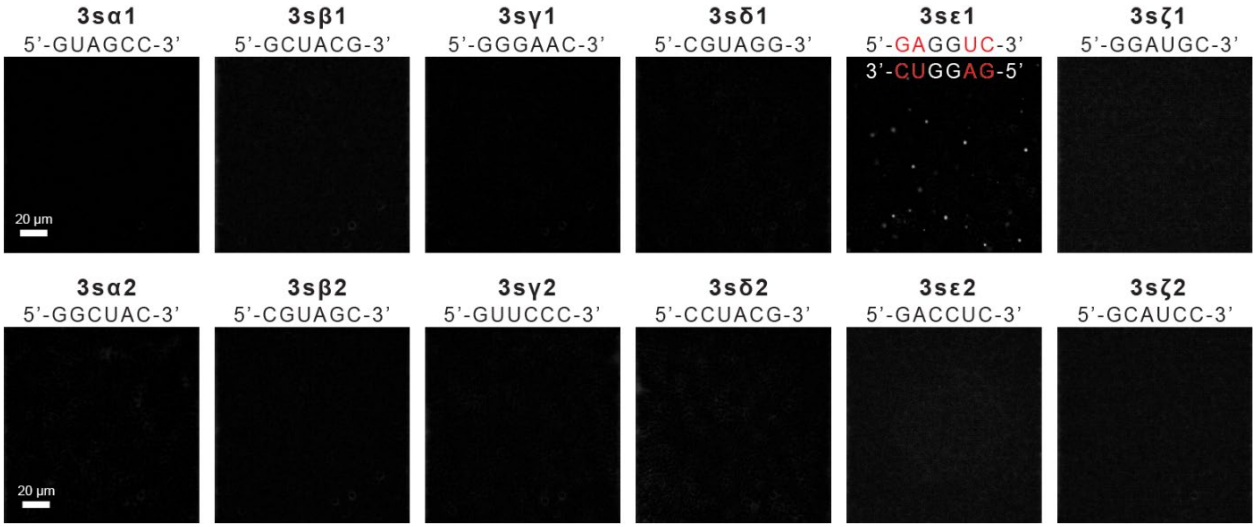

Figure 1-26. Condensates do not form when annealing individual components of the two nanostar designs.

Motifs have identical stems, and these results indicate that stem-stem interactions do not determine condensate formation. Only variant 3sε1 form condensates; the KL of this variant includes two guanine pairs surrounded by a total of four complementary base pairs, confirming that mismatches within kissing loops can be tolerated and still yield condensates. However, condensation is sensitive to the type of substitution and to the position of mismatches within kissing loops. Experiments were repeated three times, n=3; here we provide representative images. Scale bar, 20 μm.

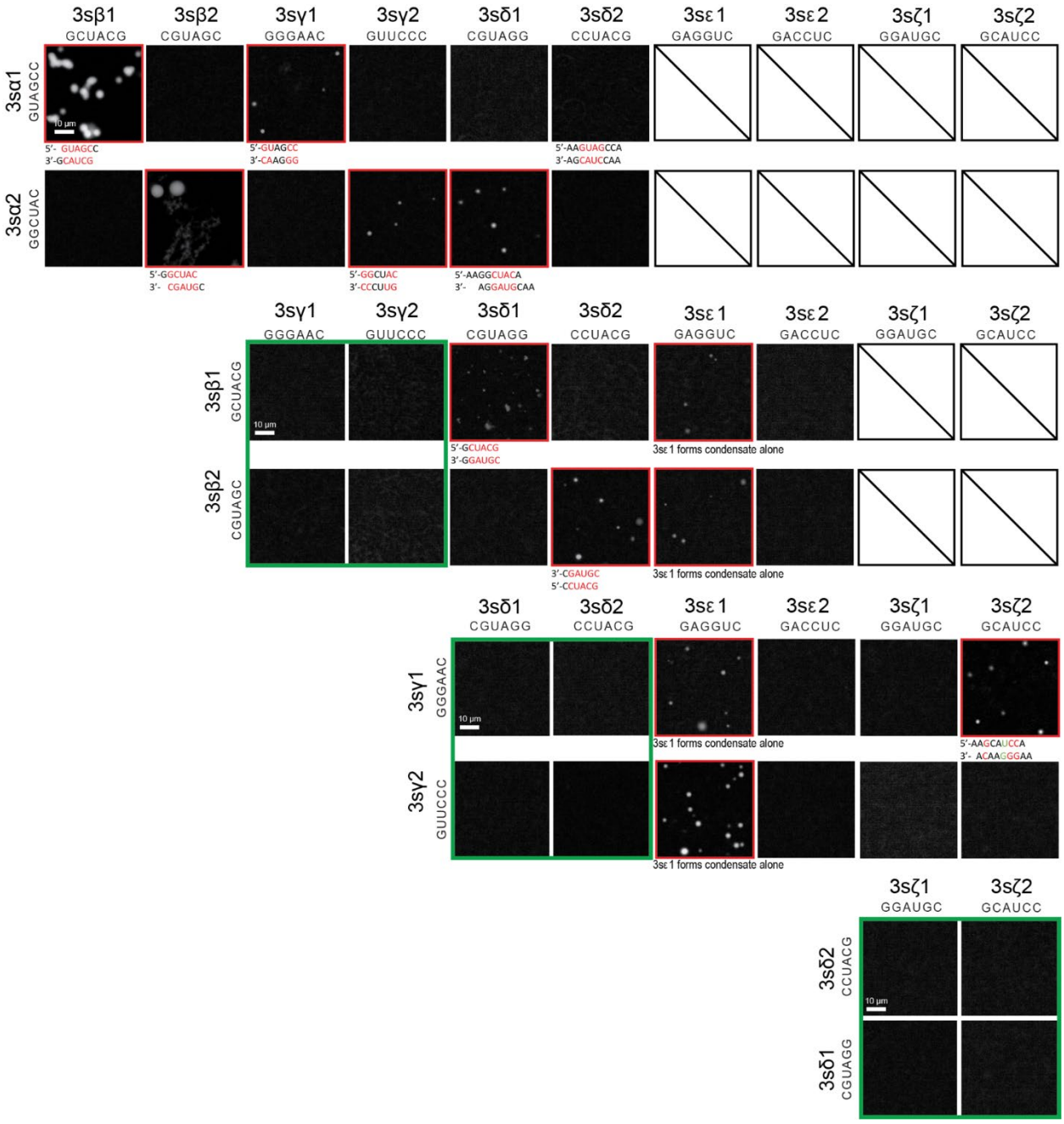

Figure 1-27. Cross orthogonality between two nanostar condensates.

Each box includes representative microscopy images of samples prepared by annealing (melt and hold at 50°C) two nanostars that are part of different nanostar-generating condensates. The name and sequence are marked to the left of each row and at the top of each column. Pairs that produce condensates are highlighted in red. Possible sequence base pairings are highlighted in red underneath images. Pairs that are fully orthogonal are in green. Pair 3sβ and 3sγ are used for orthogonality

demonstrations in Fig. 1-4C. Pair 3sζ fails as it generates gel-like networks which do not match our goal of generating liquid-like droplets (see Fig. 3H in the manuscript). Pair 3sε fails as nanostar 3sε1 yields condensates on its own (Supplementary Figure 20). Experiments were repeated three times, n=3; here we provide representative images. Scale bar, 10 μm.

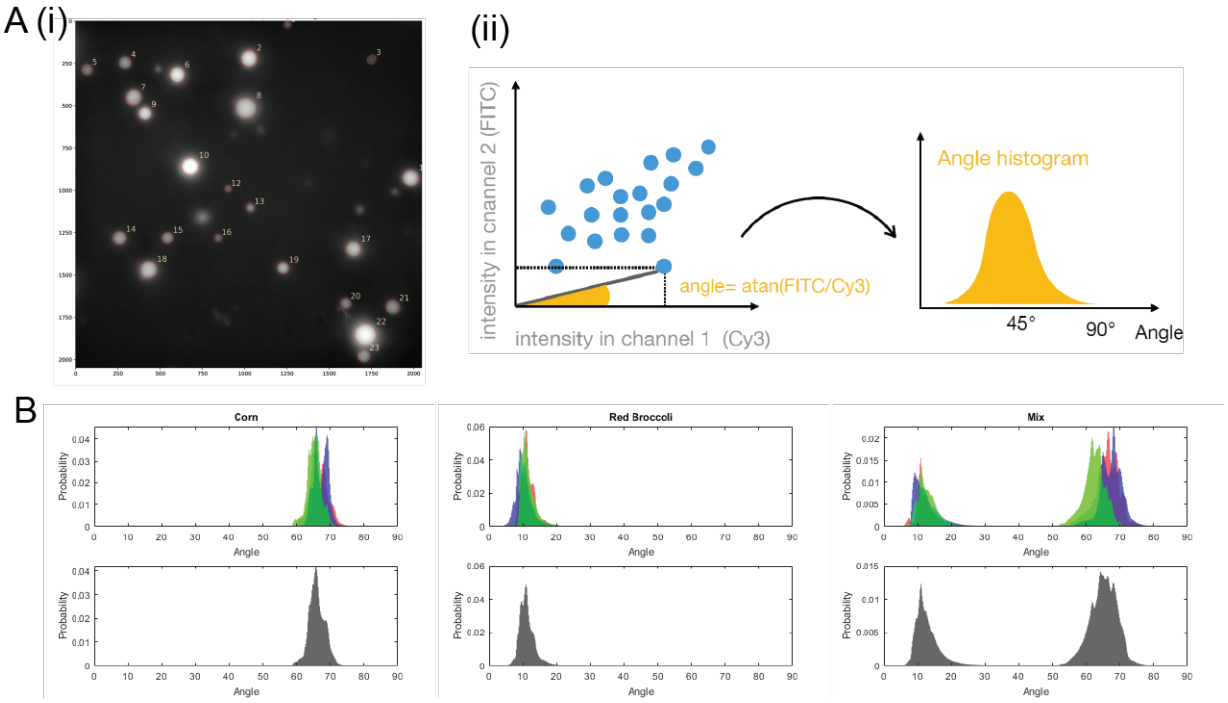

Figure 1-28. Coordinate angle mapping workflow and results for each sample.

(A) (i) Example of an overlay of fluorescent image and labeled regions that were drawn from corresponding binary mask. We extracted pixel intensities in the CY3 and FITC channels within these labeled regions (circled in red). (ii) For each pixel, a coordinate angle was calculated as arctan (FITC_intensity/CY3_intensity). A histogram of coordinate angles was generated for each sample (FOV = 10). (B) Histograms of n = 3 samples (top panel, in red, green, and blue) and sum of the three (bottom panel, in gray) for 3sγ_Corn, 3sβ_Red Broccoli, and one-pot annealing of the two. The skewing towards smaller angles (for Corn) and bigger angles (for Red Broccoli) were due to saturated pixels in the FITC channel (for Corn) or CY3 channel (for Red Broccoli). Total RNA concentration doubled in mixed annealing, resulting in bigger droplets and more saturation, thus increasing the skewing of peaks towards the middle.

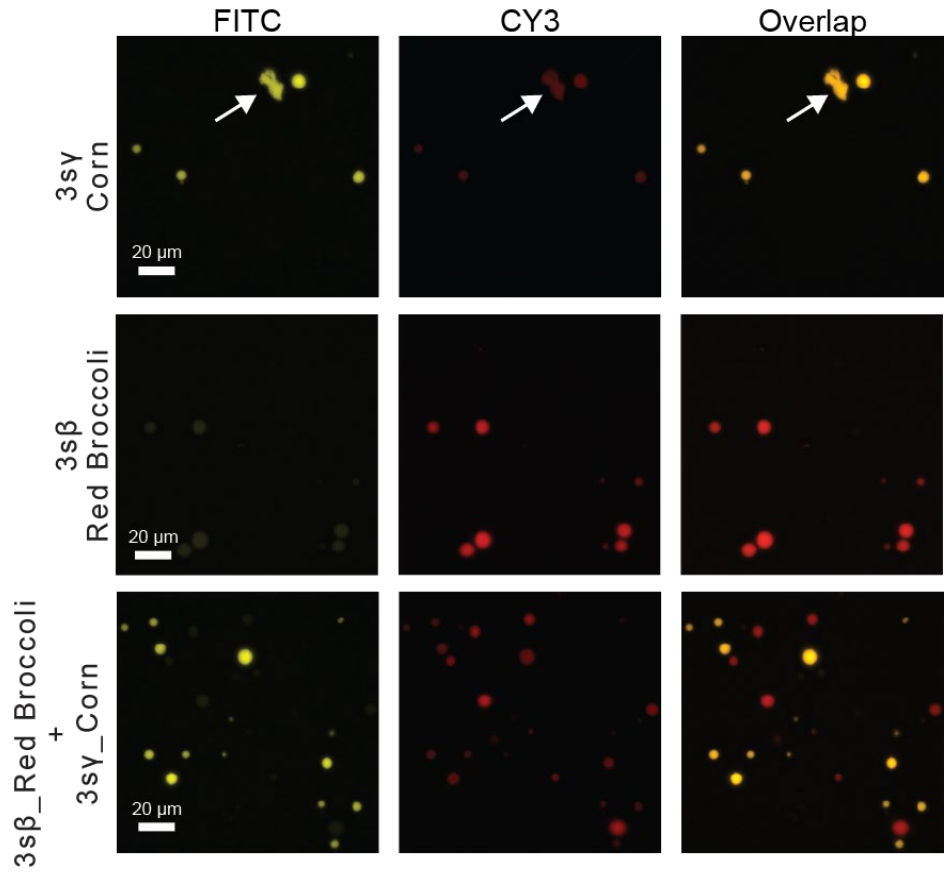

Figure 1-29. Example images of individually and simultaneously annealed two nanostar condensates that include fluorogenic aptamers.

Rows 1 and 2 from the top are individually annealed nanostars, row 3 shows example images of simultaneously annealed nanostars. The nanostars include 25% of aptamer-appended strands. White arrows point at non-spherical condensates whose formation may be driven by the dimerization of Corn aptamers. Experiments were repeated three times, n=3; images are representative examples.

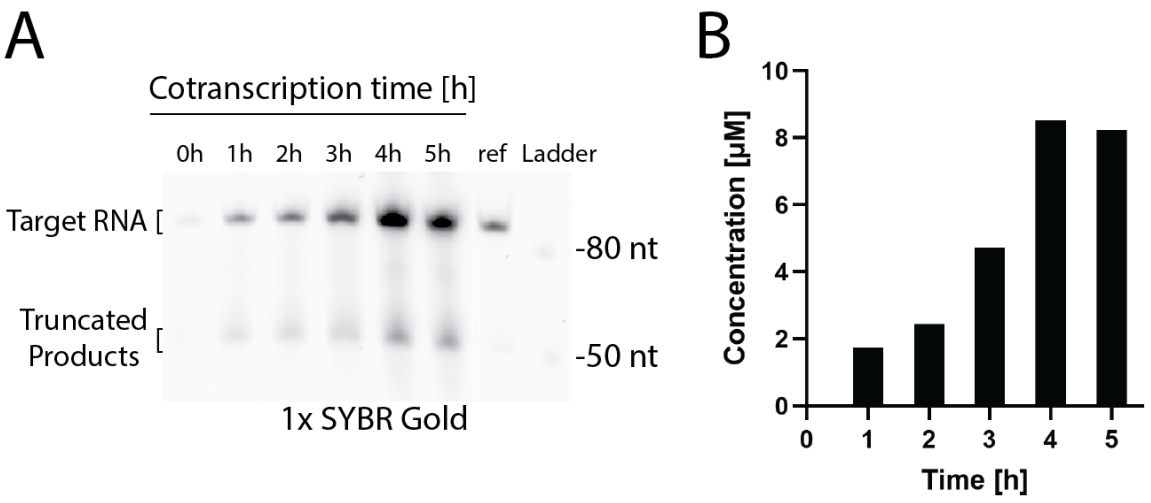

Figure 1-30. Estimation of RNA co-transcription rate.

A) 8% Denaturing PAGE gel; the reference strand (3sv2, gel extracted) is alongside products of transcription, terminated after 5 hours by adding DNase I. Transcription protocol is consistent with the one used to produce condensates (10nM DNA template, high-yield transcription buffer). The concentration of reference strands was measured using a Nanodrop2000c spectrophotometer as absorption at 260 nm and calculated following the method outlined in Section 1.4.2. Transcription samples were diluted 25 times with water, and 2µL of each sample was loaded. Reference strands were loaded at concentrations of 100 nM in the well (left, totaling 0.2 pmol). Gel electrophoresis for this experiment was performed once. B) The co-transcription rate of RNA was calculated based on data from panel A (n=1). The total pixel intensity of bands corresponding to the target product (122 nt) was extracted and calibrated to the concentration of the reference strand.

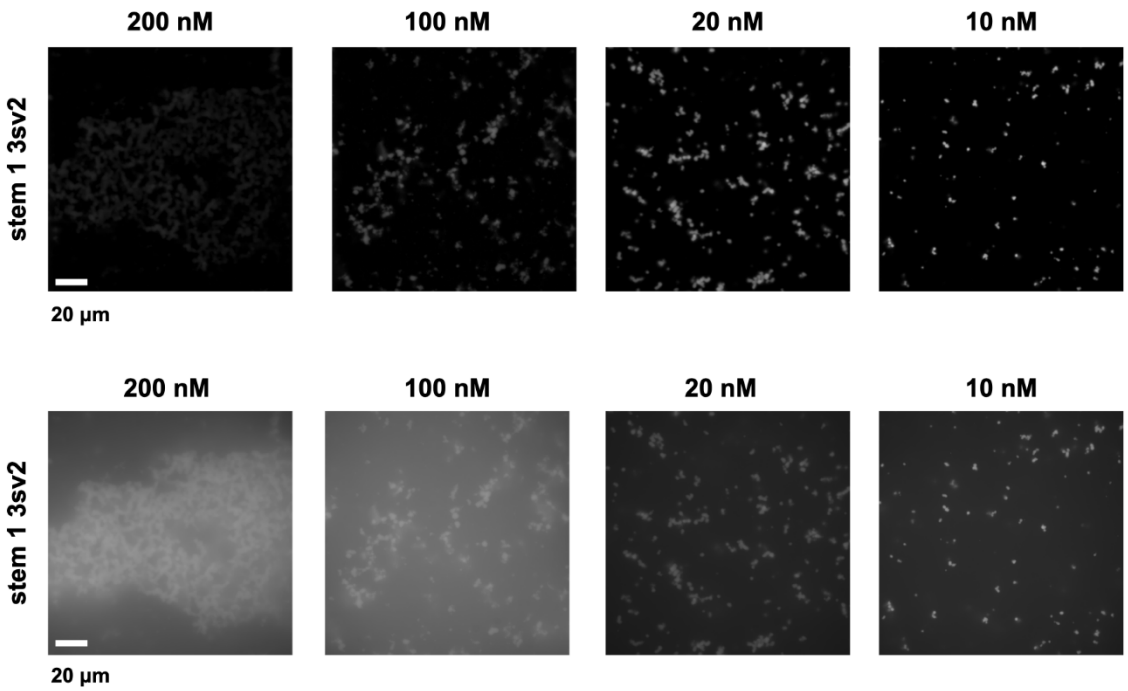

Figure 1-31. DNA template titration for co-transcription experiments.

Fluorescence micrographs at 2h timepoint showing co-transcriptional condensate formation with a variable final DNA template concentration. Experiments were repeated three times, n=3; images are representative examples. Scale bar, 20 µm.

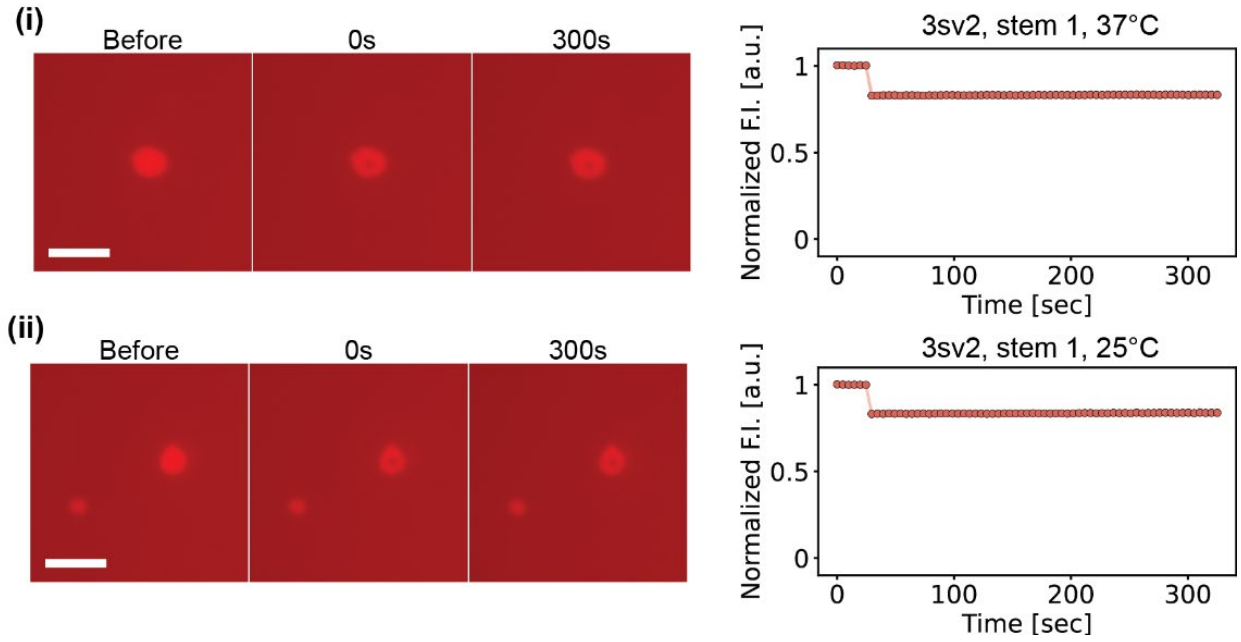

Figure 1-32. Fluorescence recovery after photobleaching (FRAP) analysis of condensate formed from co-transcription of single-stranded nanostar showed little recovery.

Condensates were co-transcribed with 1% CY3-labeled UTP, diluted 10 times with 1x co-transcription buffer to reduce background fluorescence, and imaged at 37°C (i) or at room temperature (ii). Orange dots indicate mean intensity at the corresponding time point. Mean and standard error were calculated from 3 FOVs each belonging to one experimental replicate; we obtained a remarkably low standard error, which confirms the lack of recovery.

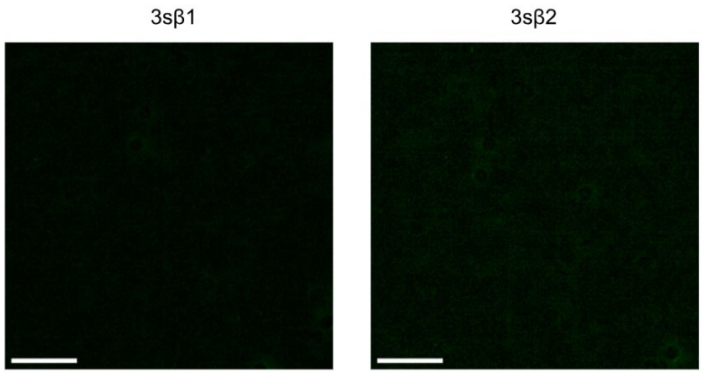

Figure 1-33. Individual nanostars with non-palindromic KL cannot form condensates co-transcriptionally.

Fluorescence micrographs at 1h timepoint showing no co-transcriptional condensate formation for either nanostar when transcribed alone. Experiments were repeated three times, n=3; images are representative examples. Scale bar, 10 μm.

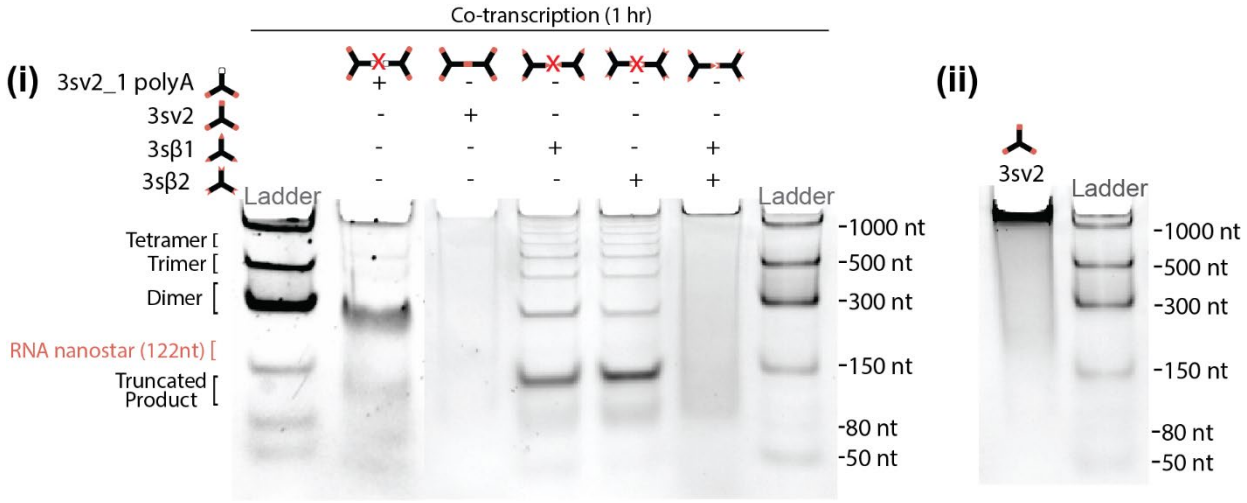

Figure 1-34. Co-transcriptional folding and interaction between single-stranded RNA.

(i) In 8% native polyacrylamide gels, nanostars with palindromic kissing loops form complexes that manifest as smears that cannot pass through the gel. Eliminating one kissing loop by changing it to poly A (5'-AAAAAA) dissociates the complex and generates predominantly dimers. **(ii)** Increased loading of 3sv2 demonstrates apparent retention of RNA in wells. The gel was stained with 1x SYBR Gold. The gel was repeated twice with consistent results.

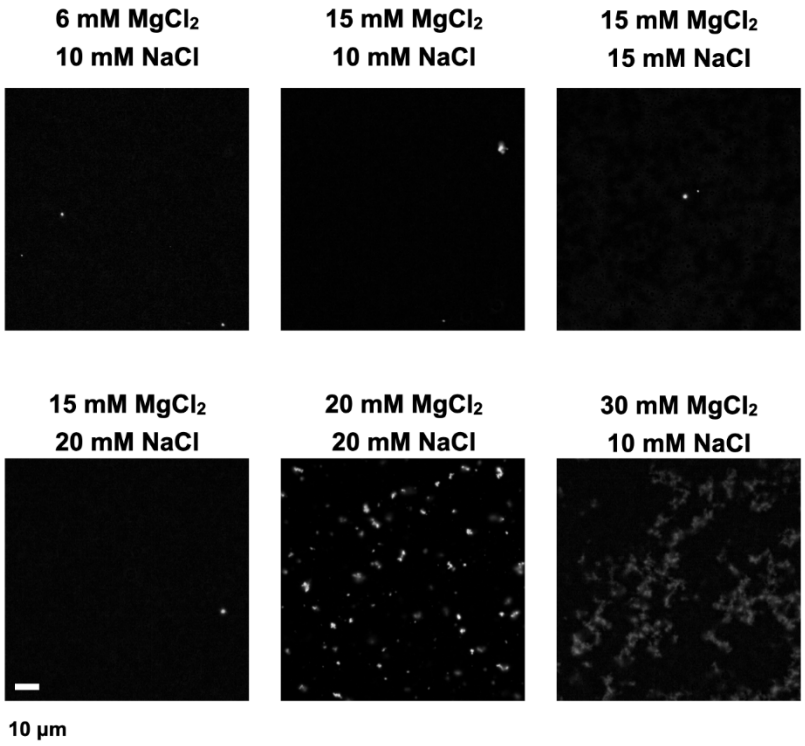

Figure 1-35. Magnesium and sodium titration for co-transcription experiments of the two-nanostar system (3sβ).

Fluorescence micrographs at 1h timepoint showing co-transcriptional condensate formation with various $MgCl_2$ and NaCl concentrations. Each template is added at 10 nM. Reaction conditions are consistent with those listed in section 1.3.2. Experiments were repeated three times, n=3; images are representative examples. Scale bar, 10 µm.

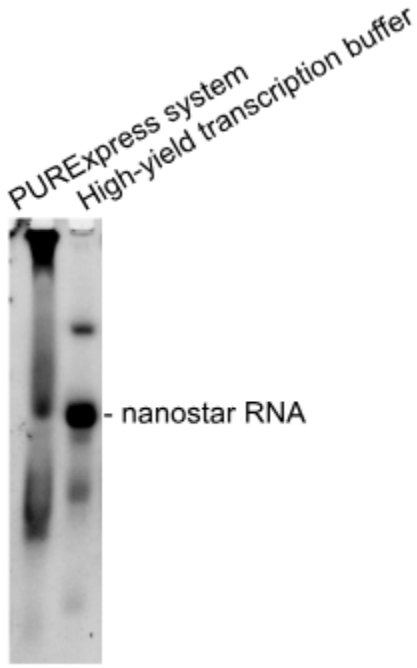

Figure 1-36. Nanostar RNA (stem 1 3sv2) transcribed with the PURExpress system or the high-yield transcription buffer.

In 8% native polyacrylamide gels, nanostars that were transcribed from the PurExpress system (left lane) had more byproducts than the ones that were transcribed with the high-yield transcription buffer (right lane). DNase I was used to stop the transcription after 3 hours of incubation at 37°C. The 8% denaturing polyacrylamide gel was stained with 1x SYBR Gold. The gel was repeated twice with consistent results.

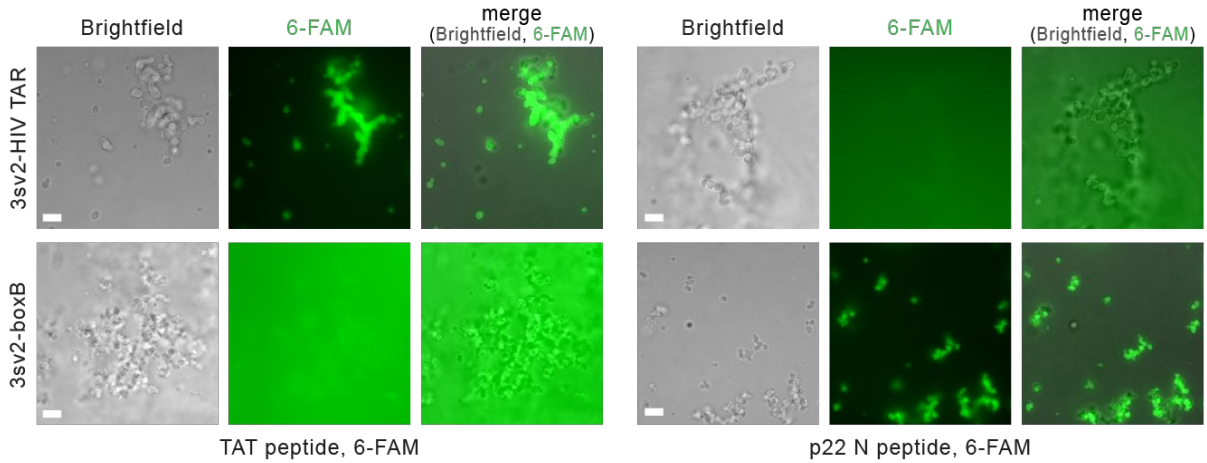

Figure 1-37. Adding peptides after transcription.

3sv2 nanostars were modified to include TAR (top) or boxB (bottom) aptamer, recruiting either TAT or p22 N peptide labeled with 6-FAM. No significant difference between condensate growth was observed compared with adding peptide at the beginning of transcription (Fig. 1-5G), indicating minimal interference of peptide on condensation. Experiments were repeated three times, n=3; images are representative examples. Scale bars: 10 μm.

1.6.3 Supplementary Tables

Table 1-1. NUPACK ΔG calculations of sticky-end duplexes at 25°C using rna95 (NUPACK3) parameters, some dangles (NUPACK3) ensemble, and 1M Na^+.

5' SE sequence duplex	ΔG (kcal/mol)
GC	-2.12
GCGC	-8.17
GUAC	-4.5
GAGCUC	-11.43
GUAUAC	-6.96
GCUAGC	-11.17

Table 1-2. Multi-stranded motif sequences.

RNA sequences for four arm multi-stranded motif		**Sequence**
4m1,No SE	S1	5'-GGUGAACAGUAUGCGAAGCGGAAGUGUGCGGA
	S2	5'-CAAUCUAGGUCUGCCAACGCAUACUGUUCACC
	S3	5'-GAGUCUACAGGCGCAAAGGCAGACCUAGAUUG
	S4	5'-UCCGCACACUUCCGCAAUGCGCCUGUAGACUC
4m1,SE:5'-GC	S1	5'-GCAGGUGAACAGUAUGCGAAGCGGAAGUGUGCGGA
	S2	5'-GCACAAUCUAGGUCUGCCAACGCAUACUGUUCACC
	S3	5'-GCAGAGUCUACAGGCGCAAAGGCAGACCUAGAUUG
	S4	5'-GCAUCCGCACACUUCCGCAAUGCGCCUGUAGACUC
4m2,SE:5'-GUAC	S1	5'-GUACAGGUCAGUGUGAACGCAAGCGAGAGCGCUGCCC
	S2	5'-GUACAGGGCAGCGCUCUCGCAAGCGUAUCACUACACC
	S3	5'-GUACAGGUGUAGUGAUACGCAAGCGAUGAACGUAGGG
	S4	5'-GUACACCCUACGUUCAUCGCAAGCGUUCACACUGACC

4m3,SE:5'-GCGC	S1	5'-GCGCAUCCACGGCGUGUCGCAAGACGCCGACGCGUCG
	S2	5'-GCGCAGUCGGGAUAUACCGGAAGCGACACGCCGUGGA
	S3	5'-GCGCAAGUCCACAGUGGCGCAACCGGUAUAUCCCGAC
	S4	5'-GCGCACGACGCGUCGGCGUCAAGCGCCACUGUGGACU
	S1_Orange_Broccoli	5'-GUAUGUGG **GAGACGGUCGGGUCC** AGAUAUUCGUAUCUGUCGAGUAG *C* **GUGUGGGCUC** CCACAUACGCGCAUCCACGGCGUGUCGCAAGACGCCGACGCGUCG
	S1_Streptavidin	5'-GAUGCGGCCGCCGACCAGAAUCAUGCAAGUGCGUAAGAUAGUCGCGGGUCGGCGGCCGCAUCGCGCAUCCACGGCGUGUCGCAAGACGCCGACGCGUCG
4m4,SE:5'-GUAUAC	S1	5'-GUAUACAGGUCAGUGUGAACGCAAGCGAGAGCGCUGCCC
	S2	5'-GUAUACAGGGCAGCGCUCUCGCAAGCGUAUCACUACACC
	S3	5'-GUAUACAGGUGUAGUGAUACGCAAGCGAUGAACGUAGGG
	S4	5'-GUAUACACCCUACGUUCAUCGCAAGCGUUCACACUGACC
4m5,SE:5'-GAGCUC	S1	5'-GAGCUCAGAGUCUCUGGUCGCCAAGCUUAUCGGACACUG
	S2	5'-GAGCUCAAGUAGGCACAUCAGCAAGGCGACCAGAGACUC
	S3	5'-GAGCUCAUGCGUGGAGACAACGAAGCUGAUGUGCCUACU
	S4	5'-GAGCUCACAGUGUCCGAUAAGCAACGUUGUCUCCACGCA
	S1_Corn	5'-GGCGCGAGGAAGGAGGUCUGAGGAGGUCACUGCGCCGAGCUCAGAGUCUCUGGUCGCCAAGCUUAUCGGACACUG
	S1_P22	5'-GGUGCGCUGACAAAGCGCGCCGAGCUCAGAGUCUCUGGUCGCCAAGCUUAUCGGACACUG
4m6,SE:5'-GCUAGC	S1	5'-GCUAGCAGGUCAGUGUGAACGCAAGCGAGAGCGCUGCCC
	S2	5'-GCUAGCAGGGCAGCGCUCUCGCAAGCGUAUCACUACACC
	S3	5'-GCUAGCAGGUGUAGUGAUACGCAAGCGAUGAACGUAGGG
	S4	5'-GCUAGCACCCUACGUUCAUCGCAAGCGUUCACACUGACC
	S1_Red_Broccoli	5'-GUAUGUGG **GAGACGGUCGGGUCC** AGAUAUUCGUAUCUGUCGAGUAG *U* **GUGUGGGCUC** CCACAUACGCUAGCAGGUCAGUGUGAACGCAAGCGAGAGCGCUGCCC
	S1_TAT	5'-GGAGCUUGAUCCCGGAAACGGUCGAUCGCUCCGCUAGCAGGUCAGUGUGAACGCAAGCGAGAGCGCUGCCC

RNA sequences for three arm multi-stranded motif		**Sequence**
3m1,SE: 5'-GCUAGC	S1	5'-GCUAGCAGGUCAGUGUGAACGCAAGCGAGAGCGCUGCCC
	S2	5'-GCUAGCAGGGCAGCGCUCUCGCAAGCGUAUCACUACACC
	S3	5'-GCUAGCAGGUGUAGUGAUACGCAAGCGUUCACACUGACC
	S1_Red_Broccoli	5'-GUAUGUGGGAGACGGUCGGGUCCAGAUAUUCGUAUCUGUCGAGUAGUGUGUGGGCUCCCACAUACGCUAGCAGGUCAGUGUGAACGCAAGCGAGAGCGCUGCCC

DNA template sequences for four arm multi-stranded motif		**Sequence**
4m1,SE:5'-GC	S1 (NT/T)	5'-CTAATACGACTCACTATAGCAGGTGAACAGTATGCGAAGCGGAAGTGTGCGGA / 5'-TCCGCACACTTCCGCTTCGCATACTGTTCACCTGCTATAGTGAGTCGTATTAG
	S2 (NT/T)	5'-CTAATACGACTCACTATAGCACAATCTAGGTCTGCCAACGCATACTGTTCACC / 5'-GGTGAACAGTATGCGTTGGCAGACCTAGATTGTGCTATAGTGAGTCGTATTAG
	S3 (NT/T)	5'-CTAATACGACTCACTATAGCAGAGTCTACAGGCGCAAAGGCAGACCTAGATTG / 5'-CAATCTAGGTCTGCCTTTGCGCCTGTAGACTCTGCTATAGTGAGTCGTATTAG
	S4 (NT/T)	5'-CTAATACGACTCACTATAGCATCCGCACACTTCCGCAATGCGCCTGTAGACTC / 5'-GAGTCTACAGGCGCATTGCGGAAGTGTGCGGATGCTATAGTGAGTCGTATTAG
4m2,SE:5'-GUAC	S1 (NT/T)	5'-CTAATACGACTCACTATAGTACAGGTCAGTGTGAACGCAAGCGAGAGCGCTGCCC / 5'-GGGCAGCGCTCTCGCTTGCGTTCACACTGACCTGTACTATAGTGAGTCGTATTAG

	S2 (NT/T)	5'-CTAATACGACTCACTATAGTACAGGGCAGCGCTCTCGCAAGCGTATCACTACACC / 5'-GGTGTAGTGATACGCTTGCGAGAGCGCTGCCCTGTACTATAGTGAGTCGTATTAG
	S3 (NT/T)	5'-CTAATACGACTCACTATAGTACAGGTGTAGTGATACGCAAGCGATGAACGTAGGG / 5'-CCCTACGTTCATCGCTTGCGTATCACTACACCTGTACTATAGTGAGTCGTATTAG
	S4 (NT/T)	5'-CTAATACGACTCACTATAGTACACCCTACGTTCATCGCAAGCGTTCACACTGACC / 5'-GGTCAGTGTGAACGCTTGCGATGAACGTAGGGTGTACTATAGTGAGTCGTATTAG
4m3,SE:5'-GCGC	S1(NT/T)	5'-CTAATACGACTCACTATAGCGCATCCACGGCGTGTCGCAAGACGCCGACGCGTCG / 5'-CGACGCGTCGGCGTCTTGCGACACGCCGTGGATGCGCTATAGTGAGTCGTATTAG
	S2(NT/T)	5'-CTAATACGACTCACTATAGCGCAGTCGGGATATACCGGAAGCGACACGCCGTGGA / 5'-TCCACGGCGTGTCGCTTCCGGTATATCCCGACTGCGCTATAGTGAGTCGTATTAG
	S3(NT/T)	5'-CTAATACGACTCACTATAGCGCAAGTCCACAGTGGCGCAACCGGTATATCCCGAC / 5'-GTCGGGATATACCGGTTGCGCCACTGTGGACTTGCGCTATAGTGAGTCGTATTAG
	S4(NT/T)	5'-CTAATACGACTCACTATAGCGCACGACGCGTCGGCGTCAAGCGCCACTGTGGACT / 5'-AGTCCACAGTGGCGCTTGACGCCGACGCGTCGTGCGCTATAGTGAGTCGTATTAG
	S1_Orange_Broccoli(NT/T)	5'-CTAATACGACTCACTATAGTATGTGGGAGACGGTCGGGTCCAGATATTCGTATCTGTCGAGTAGCGTGTGGGCTCCCACATACGCGCATCCACGGCGTGTCGCAAGACGCCGACGCGTCG / 5'-CGACGCGTCGGCGTCTTGCGACACGCCGTGGATGCGCGTATGTGGGAGCC

		CACACGCTACTCGACAGATACGAATATCTGGACCCGACCGTCTCCCACATACTATAGTGAGTCGTATTAG
	S1_Streptavidin(NT/T)	5'-CTAATACGACTCACTATAGATGCGGCCGCCGACCAGAATCATGCAAGTGCGTAAGATAGTCGCGGGTCGGCGGCCGCATCGCGCATCCACGGCGTGTCGCAAGACGCCGACGCGTCG / 5'-CGACGCGTCGGCGTCTTGCGACACGCCGTGGATGCGCGATGCGGCCGCCGACCCGCGACTATCTTACGCACTTGCATGATTCTGGTCGGCGGCCGCATCTATAGTGAGTCGTATTAG
4m4,SE:5'-GUAUAC	S1 (NT/T)	5'-CTAATACGACTCACTATAGTATACAGGTCAGTGTGAACGCAAGCGAGAGCGCTGCCC / 5'-GGGCAGCGCTCTCGCTTGCGTTCACACTGACCTGTATACTATAGTGAGTCGTATTAG
	S2 (NT/T)	5'-CTAATACGACTCACTATAGTATACAGGGCAGCGCTCTCGCAAGCGTATCACTACACC / 5'-GGTGTAGTGATACGCTTGCGAGAGCGCTGCCCTGTATACTATAGTGAGTCGTATTAG
	S3 (NT/T)	5'-CTAATACGACTCACTATAGTATACAGGTGTAGTGATACGCAAGCGATGAACGTAGGG / 5'-CCCTACGTTCATCGCTTGCGTATCACTACACCTGTATACTATAGTGAGTCGTATTAG
	S4 (NT/T)	5'-CTAATACGACTCACTATAGTATACACCCTACGTTCATCGCAAGCGTTCACACTGACC / 5'-GGTCAGTGTGAACGCTTGCGATGAACGTAGGGTGTATACTATAGTGAGTCGTATTAG
4m5,SE:5'-GAGCUC	S1(NT/T)	5'-CTAATACGACTCACTATAGAGCTCAGAGTCTCTGGTCGCCAAGCTTATCGGACACTG / 5'-CAGTGTCCGATAAGCTTGGCGACCAGAGACTCTGAGCTCTATAGTGAGTCGTATTAG
	S2(NT/T)	5'-CTAATACGACTCACTATAGAGCTCAAGTAGGCACATCAGCAAGGCGACCAGAGACTC / 5'-GAGTCTCTGGTCGCCTTGCTGATGTGCCTACTTGAGCTCTATAGTGAGTCGTATTAG
	S3(NT/T)	5'-CTAATACGACTCACTATAGAGCTCATGCGTGGAGACAACGAAGCTGATGTGC

		CTACT / 5'-AGTAGGCACATCAGCTTCGTTGTCTCCACGCATGAGCTCTATAGTGAGTCGTATTAG
	S4(NT/T)	5'-CTAATACGACTCACTATAGAGCTCACAGTGTCCGATAAGCAACGTTGTCTCCACGCA / 5'-TGCGTGGAGACAACGTTGCTTATCGGACACTGTGAGCTCTATAGTGAGTCGTATTAG
	S1_Corn(NT/T)	5'-CTAATACGACTCACTATAGGCGCGAGGAAGGAGGTCTGAGGAGGTCACTGCGCCGAGCTCAGAGTCTCTGGTCGCCAAGCTTATCGGACACTG / 5'-CAGTGTCCGATAAGCTTGGCGACCAGAGACTCTGAGCTCGGCGCAGTGACCTCCTCAGACCTCCTTCCTCGCGCCTATAGTGAGTCGTATTAG
	S1_P22(NT/T)	5'-CTAATACGACTCACTATAGGTGCGCTGACAAAGCGCGCCGAGCTCAGAGTCTCTGGTCGCCAAGCTTATCGGACACTG / 5'-CAGTGTCCGATAAGCTTGGCGACCAGAGACTCTGAGCTCGGCGCGCTTTGTCAGCGCACCTATAGTGAGTCGTATTAG
4m6,SE:5'-GCUAGC	S1(NT/T)	5'-CTAATACGACTCACTATAGCTAGCAGGTCAGTGTGAACGCAAGCGAGAGCGCTGCCC / 5'-GGGCAGCGCTCTCGCTTGCGTTCACACTGACCTGCTAGCTATAGTGAGTCGTATTAG
	S2(NT/T)	5'-CTAATACGACTCACTATAGCTAGCAGGGCAGCGCTCTCGCAAGCGTATCACTACACC / 5'-GGTGTAGTGATACGCTTGCGAGAGCGCTGCCCTGCTAGCTATAGTGAGTCGTATTAG
	S3(NT/T)	5'-CTAATACGACTCACTATAGCTAGCAGGTGTAGTGATACGCAAGCGATGAACGTAGGG / 5'-CCCTACGTTCATCGCTTGCGTATCACTACACCTGCTAGCTATAGTGAGTCGTATTAG
	S4(NT/T)	5'-CTAATACGACTCACTATAGCTAGCACCCTACGTTCATCGCAAGCGTTCACACTGACC / 5'-GGTCAGTGTGAACGCTTGCGATGAACGTAGGGTGCTAGCTATAGTGAGTCGTATTAG
	S1_Red_Broccoli(NT/T)	5'-CTAATACGACTCACTATAGTATGTGGGAGACGGTCGGGTCCAGATATTCGTATCTGTCGAGTAGTGTGTGGGCTCCCACATACGCTAGCAGGTCAGTGTGAAC

		GCAAGCGAGAGCGCTGCCC / 5'-GGGCAGCGCTCTCGCTTGCGTTCACACTGACCTGCTAGCGTATGTGGGAGCCCACACACTACTCGACAGATACGAATATCTGGACCCGACCGTCTCCCACATACTATAGTGAGTCGTATTAG
	S1_TAT(NT/T)	5'-CTAATACGACTCACTATAGGAGCTTGATCCCGGAAACGGTCGATCGCTCCGCTAGCAGGTCAGTGTGAACGCAAGCGAGAGCGCTGCCC / 5'-GGGCAGCGCTCTCGCTTGCGTTCACACTGACCTGCTAGCGGAGCGATCGACCGTTTCCGGGATCAAGCTCCTATAGTGAGTCGTATTAG

DNA template sequences for three arm multi-stranded motif		**Sequence**
3m1,SE: 5'-GCUAGC	S1(NT/T)	5'-CTAATACGACTCACTATAGCTAGCAGGTCAGTGTGAACGCAAGCGAGAGCGCTGCCC / 5'-GGGCAGCGCTCTCGCTTGCGTTCACACTGACCTGCTAGCTATAGTGAGTCGTATTAG
	S2(NT/T)	5'-CTAATACGACTCACTATAGCTAGCAGGGCAGCGCTCTCGCAAGCGTATCACTACACC / 5'-GGTGTAGTGATACGCTTGCGAGAGCGCTGCCCTGCTAGCTATAGTGAGTCGTATTAG
	S3(NT/T)	5'-CTAATACGACTCACTATAGCTAGCAGGTGTAGTGATACGCAAGCGTTCACACTGACC / 5'-GGTCAGTGTGAACGCTTGCGTATCACTACACCTGCTAGCTATAGTGAGTCGTATTAG
	S1_Red_Broccoli(NT/T)	5'-CTAATACGACTCACTATAGTATGTGGGAGACGGTCGGGTCCAGATATTCGTATCTGTCGAGTAGTGTGTGGGCTCCCACATACGCTAGCAGGTCAGTGTGAACGCAAGCGAGAGCGCTGCCC / 5'-GGGCAGCGCTCTCGCTTGCGTTCACACTGACCTGCTAGCGTATGTGGGAGCCCACACACTACTCGACAGATACGAATATCTGGACCCGACCGTCTCCCACATACTATAGTGAGTCGTATTAG

Table 1-3. Single-stranded motif sequences.

RNA sequences for single-stranded motif		Sequence
Single motif, stem1	3swt	5'-GGCGAGAGCGCUGCCCAAGCGCGCAGGGCAGCGCUCUCGCAAGCGAUGAACGUAGGGAAGCGCGCACCCUACGUUCAUCGCAAGCGUUCACACUGACCAAGCGCGCAGGUCAGUGUGAACGC
	3sv1	5'-GGCGAGAGCGCUGCCCAAGUGCGCAGGGCAGCGCUCUCGCAAGCGAUGAACGUAGGGAAGUGCGCACCCUACGUUCAUCGCAAGCGUUCACACUGACCAAGUGCGCAGGUCAGUGUGAACGC
	3sv2	5'-GGCGAGAGCGCUGCCCAAGCGCGUAGGGCAGCGCUCUCGCAAGCGAUGAACGUAGGGAAGCGCGUACCCUACGUUCAUCGCAAGCGUUCACACUGACCAAGCGCGUAGGUCAGUGUGAACGC
	3sv3	5'-GGCGAGAGCGCUGCCCAAGAGCGCAGGGCAGCGCUCUCGCAAGCGAUGAACGUAGGGAAGAGCGCACCCUACGUUCAUCGCAAGCGUUCACACUGACCAAGAGCGCAGGUCAGUGUGAACGC
	3sv4	5'-GGCGAGAGCGCUGCCCAAGCGCUCAGGGCAGCGCUCUCGCAAGCGAUGAACGUAGGGAAGCGCUCACCCUACGUUCAUCGCAAGCGUUCACACUGACCAAGCGCUCAGGUCAGUGUGAACGC
	3sv5	5'-GGCGAGAGCGCUGCCCAAGCUCGCAGGGCAGCGCUCUCGCAAGCGAUGAACGUAGGGAAGCUCGCACCCUACGUUCAUCGCAAGCGUUCACACUGACCAAGCUCGCAGGUCAGUGUGAACGC
	3sv2_TAT	5'-GCGAGAGCGCUGCCCAAGCGCGUAGGGCAGCGCUCUCGCAAGCGAUGAACGUAGGGAAGCGCGUACCCUACGUUCAUCGCAAGCGUUCACACUGACCAAGCGCGUAGGUCAGUGUGAACGCAAGGAGCUUGAUCCCGGAAACGGUCGAUCGCUCC
	3sv2_BoxB	5'-GCGAGAGCGCUGCCCAAGCGCGUAGGGCAGCGCUCUCGCAAGCGAUGAACGUAGGGAAGCGCGUACCCUACGUUCAUCGCAAGCGUUCACACUGACCAAGCGCGUAGGUCAGUGUGAACGCAAGGUGCGCUGACAAAGCGCGCC
	3swt	5'-GGUCGUAGCAUCGCACCAAGCGCGCAGGUGCGAUGCUACGACAACAGUGA

Single motif, stem2		GGACGGAAGUAAGCGCGCAACUUCCGUCCUCACUGAACAACCACGCCUGUCCAAAGCGCGCAUGGACAGGCGUGGUUG
	3sv1	5'-GUCGUAGCAUCGCACCAAGUGCGCAGGUGCGAUGCUACGACAACAGUGAGGACGGAAGUAAGUGCGCAACUUCCGUCCUCACUGAACAACCACGCCUGUCCAAAGUGCGCAUGGACAGGCGUGGUUG
	3sv2	5'-GGUCGUAGCAUCGCACCAAGCGCGUAGGUGCGAUGCUACGACAACAGUGAGGACGGAAGUAAGCGCGUAACUUCCGUCCUCACUGAACAACCACGCCUGUCCAAAGCGCGUAUGGACAGGCGUGGUUG
	3sv3	5'-GUCGUAGCAUCGCACCAAGAGCGCAGGUGCGAUGCUACGACAACAGUGAGGACGGAAGUAAGAGCGCAACUUCCGUCCUCACUGAACAACCACGCCUGUCCAAAGAGCGCAUGGACAGGCGUGGUUG
	3sv4	5'-GGUCGUAGCAUCGCACCAAGCGCUCAGGUGCGAUGCUACGACAACAGUGAGGACGGAAGUAAGCGCUCAACUUCCGUCCUCACUGAACAACCACGCCUGUCCAAAGCGCUCAUGGACAGGCGUGGUUG
	3sv5	5'-GUCGUAGCAUCGCACCAAGCUCGCAGGUGCGAUGCUACGACAACAGUGAGGACGGAAGUAAGCUCGCAACUUCCGUCCUCACUGAACAACCACGCCUGUCCAAAGCUCGCAUGGACAGGCGUGGUUG
Single motif, stem3	3sWT	5'-GCGACGUGUUACGGCGAGGCAAGCGCGCAGCCUCGCCGUAACACGUCGCAAGGCGGAACGGACCUCGGCUCAAGCGCGCAGAGCCGAGGUCCGUUCCGCCAAGCUCCGCUCCCAGUGGGCUCAAGCGCGCAGAGCCCACUGGGAGCGGAGC
Poly-A control	3swt, stem1	5'-GCGAGAGCGCUGCCCAAAAAAAAAGGGCAGCGCUCUCGCAAGCGAUGAACGUAGGGAAGCGCGCACCCUACGUUCAUCGCAAGCGUUCACACUGACCAAGCGCGCAGGUCAGUGUGAACGC
	3sv2, stem1	5'-GCGAGAGCGCUGCCCAAAAAAAAAGGGCAGCGCUCUCGCAAGCGAUGAACGUAGGGAAGCGCGUACCCUACGUUCAUCGCAAGCGUUCACACUGACCAAGCGCGUAGGUCAGUGUGAACGC
	3swt, stem2	5'-GGUCGUAGCAUCGCACCAAAAAAAAAGGUGCGAUGCUACGACAACAGUGAGGACGGAAGUAAGCGCGCAACUUCCGUCCUCACUGAACAACCACGCCUGUCCAAAGCGCGCAUGGACAGGCGUGGUUG

Double motif, stem1	3sα1	5'- GCGAGAGCGCUGCCCAAGUAGCCAGGGCAGCGCUCUCGCAAGCGAUGAAC GUAGGGAAGUAGCCACCCUACGUUCAUCGCAAGCGUUCACACUGACCAAG UAGCCAGGUCAGUGUGAACGC
	3sα2	5'- GCGAGAGCGCUGCCCAAGGCUACAGGGCAGCGCUCUCGCAAGCGAUGAAC GUAGGGAAGGCUACACCCUACGUUCAUCGCAAGCGUUCACACUGACCAAG GCUACAGGUCAGUGUGAACGC
	3sβ1	5'- GCGAGAGCGCUGCCCAAGCUACGAGGGCAGCGCUCUCGCAAGCGAUGAAC GUAGGGAAGCUACGACCCUACGUUCAUCGCAAGCGUUCACACUGACCAAG CUACGAGGUCAGUGUGAACGC
	3sβ2	5'- GCGAGAGCGCUGCCCAACGUAGCAGGGCAGCGCUCUCGCAAGCGAUGAAC GUAGGGAACGUAGCACCCUACGUUCAUCGCAAGCGUUCACACUGACCAAC GUAGCAGGUCAGUGUGAACGC
	3sβ1_Red Broccoli	5'- GCGAGAGCGCUGCCCAAGCUACGAGGGCAGCGCUCUCGCAAGCGAUGAAC GUAGGGAAGCUACGACCCUACGUUCAUCGCAAGCGUUCACACUGACCAAG CUACGAGGUCAGUGUGAACGCAAGUUGGGAGACGGUCGGGUCCAGAUAUU CGUAUCUGUCGAGUAGUGUGUGGGCUCCCAAC
	3sγ1	5'- GCGAGAGCGCUGCCCAAGGGAACAGGGCAGCGCUCUCGCAAGCGAUGAAC GUAGGGAAGGGAACACCCUACGUUCAUCGCAAGCGUUCACACUGACCAAG GGAACAGGUCAGUGUGAACGC
	3sγ2	5'- GCGAGAGCGCUGCCCAAGUUCCCAGGGCAGCGCUCUCGCAAGCGAUGAAC GUAGGGAAGUUCCCACCCUACGUUCAUCGCAAGCGUUCACACUGACCAAG UUCCCAGGUCAGUGUGAACGC
	3sγ1_Corn	5'- GCGAGAGCGCUGCCCAAGGGAACAGGGCAGCGCUCUCGCAAGCGAUGAAC GUAGGGAAGGGAACACCCUACGUUCAUCGCAAGCGUUCACACUGACCAAG GGAACAGGUCAGUGUGAACGCAAGGCGCGAGGAAGGAGGUCUGAGGAGG UCACUGCGCC
	3sδ1	5'- GCGAGAGCGCUGCCCAACGUAGGAGGGCAGCGCUCUCGCAAGCGAUGAAC GUAGGGAACGUAGGACCCUACGUUCAUCGCAAGCGUUCACACUGACCAAC GUAGGAGGUCAGUGUGAACGC
	3sδ2	5'- GCGAGAGCGCUGCCCAACCUACGAGGGCAGCGCUCUCGCAAGCGAUGAAC

		GUAGGGAACCUACGACCCUACGUUCAUCGCAAGCGUUCACACUGACCAAC CUACGAGGUCAGUGUGAACGC
	3sε1	5'- GCGAGAGCGCUGCCCAAGAGGUCAGGGCAGCGCUCUCGCAAGCGAUGAAC GUAGGGAAGAGGUCACCCUACGUUCAUCGCAAGCGUUCACACUGACCAAG AGGUCAGGUCAGUGUGAACGC
	3sε2	5'- GCGAGAGCGCUGCCCAAGACCUCAGGGCAGCGCUCUCGCAAGCGAUGAAC GUAGGGAAGACCUCACCCUACGUUCAUCGCAAGCGUUCACACUGACCAAG ACCUCAGGUCAGUGUGAACGC
	3sζ1	5'- GCGAGAGCGCUGCCCAAGGAUGCAGGGCAGCGCUCUCGCAAGCGAUGAAC GUAGGGAAGGAUGCACCCUACGUUCAUCGCAAGCGUUCACACUGACCAAG GAUGCAGGUCAGUGUGAACGC
	3sζ2	5'- GCGAGAGCGCUGCCCAAGCAUCCAGGGCAGCGCUCUCGCAAGCGAUGAAC GUAGGGAAGCAUCCACCCUACGUUCAUCGCAAGCGUUCACACUGACCAAG CAUCCAGGUCAGUGUGAACGC

DNA template sequences for single-stranded motif, with a GCGC zip and T7 promoter		**Sequence (Non-template (NT)/Template (T) strand)**
Single motif, stem1	3swt	NT: 5'- GCGCTAATACGACTCACTATAGGCGAGAGCGCTGCCCAAGCGCGCAGGGCA GCGCTCTCGCAAGCGATGAACGTAGGGAAGCGCGCACCCTACGTTCATCGC AAGCGTTCACACTGACCAAGCGCGCAGGTCAGTGTGAACGC T: 5'- GCGTTCACACTGACCTGCGCGCTTGGTCAGTGTGAACGCTTGCGATGAACGT AGGGTGCGCGCTTCCCTACGTTCATCGCTTGCGAGAGCGCTGCCCTGCGCG CTTGGGCAGCGCTCTCGCCTATAGTGAGTCGTATTAGCGC
	3sv1	NT: 5'- GCGCTAATACGACTCACTATAGGCGAGAGCGCTGCCCAAGTGCGCAGGGCA GCGCTCTCGCAAGCGATGAACGTAGGGAAGTGCGCACCCTACGTTCATCGC AAGCGTTCACACTGACCAAGTGCGCAGGTCAGTGTGAACGC T: 5'- GCGTTCACACTGACCTGCGCACTTGGTCAGTGTGAACGCTTGCGATGAACGT

		AGGGTGCGCACTTCCCTACGTTCATCGCTTGCGAGAGCGCTGCCCTGCGCA CTTGGGCAGCGCTCTCGCCTATAGTGAGTCGTATTAGCGC
	3sv2	NT: 5'- GCGCTAATACGACTCACTATAGGCGAGAGCGCTGCCCAAGCGCGTAGGGCA GCGCTCTCGCAAGCGATGAACGTAGGGAAGCGCGTACCCTACGTTCATCGC AAGCGTTCACACTGACCAAGCGCGTAGGTCAGTGTGAACGC T: 5'- GCGTTCACACTGACCTACGCGCTTGGTCAGTGTGAACGCTTGCGATGAACGT AGGGTACGCGCTTCCCTACGTTCATCGCTTGCGAGAGCGCTGCCCTACGCG CTTGGGCAGCGCTCTCGCCTATAGTGAGTCGTATTAGCGC
	3sv3	NT: 5'- GCGCTAATACGACTCACTATAGGCGAGAGCGCTGCCCAAGAGCGCAGGGCA GCGCTCTCGCAAGCGATGAACGTAGGGAAGAGCGCACCCTACGTTCATCGC AAGCGTTCACACTGACCAAGAGCGCAGGTCAGTGTGAACGC T: 5'- GCGTTCACACTGACCTGCGCTCTTGGTCAGTGTGAACGCTTGCGATGAACGT AGGGTGCGCTCTTCCCTACGTTCATCGCTTGCGAGAGCGCTGCCCTGCGCT CTTGGGCAGCGCTCTCGCCTATAGTGAGTCGTATTAGCGC
	3sv4	NT: 5'- GCGCTAATACGACTCACTATAGGCGAGAGCGCTGCCCAAGCGCTCAGGGCA GCGCTCTCGCAAGCGATGAACGTAGGGAAGCGCTCACCCTACGTTCATCGC AAGCGTTCACACTGACCAAGCGCTCAGGTCAGTGTGAACGC T: 5'- GCGTTCACACTGACCTGAGCGCTTGGTCAGTGTGAACGCTTGCGATGAACGT AGGGTGAGCGCTTCCCTACGTTCATCGCTTGCGAGAGCGCTGCCCTGAGCG CTTGGGCAGCGCTCTCGCCTATAGTGAGTCGTATTAGCGC
	3sv5	NT: 5'- GCGCTAATACGACTCACTATAGGCGAGAGCGCTGCCCAAGCGCTCAGGGCA GCGCTCTCGCAAGCGATGAACGTAGGGAAGCGCTCACCCTACGTTCATCGC AAGCGTTCACACTGACCAAGCGCTCAGGTCAGTGTGAACGC 5'- GCGTTCACACTGACCTGCGAGCTTGGTCAGTGTGAACGCTTGCGATGAACGT AGGGTGCGAGCTTCCCTACGTTCATCGCTTGCGAGAGCGCTGCCCTGCGAG CTTGGGCAGCGCTCTCGCCTATAGTGAGTCGTATTAGCGC
	3sv2_TAT	NT: 5'- GCGCTAATACGACTCACTATAGCGAGAGCGCTGCCCAAGCGCGTAGGGCAG CGCTCTCGCAAGCGATGAACGTAGGGAAGCGCGTACCCTACGTTCATCGCA AGCGTTCACACTGACCAAGCGCGTAGGTCAGTGTGAACGCAAGGAGCTTGAT CCCGGAAACGGTCGATCGCTCC T: 5'- GGAGCGATCGACCGTTTCCGGGATCAAGCTCCTTGCGTTCACACTGACCTAC GCGCTTGGTCAGTGTGAACGCTTGCGATGAACGTAGGGTACGCGCTTCCCTA

		CGTTCATCGCTTGCGAGAGCGCTGCCCTACGCGCTTGGGCAGCGCTCTCGC TATAGTGAGTCGTATTAGCGC
	3sv2_Box B	NT: 5'- GCGCTAATACGACTCACTATAGCGAGAGCGCTGCCCAAGCGCGTAGGGCAG CGCTCTCGCAAGCGATGAACGTAGGGAAGCGCGTACCCTACGTTCATCGCA AGCGTTCACACTGACCAAGCGCGTAGGTCAGTGTGAACGCAAGGTGCGCTG ACAAAGCGCGCC T: 5'- GGCGCGCTTTGTCAGCGCACCTTGCGTTCACACTGACCTACGCGCTTGGTCA GTGTGAACGCTTGCGATGAACGTAGGGTACGCGCTTCCCTACGTTCATCGCT TGCGAGAGCGCTGCCCTACGCGCTTGGGCAGCGCTCTCGCTATAGTGAGTC GTATTAGCGC/
Single motif, stem2	3swt	NT: 5'- GCGCTAATACGACTCACTATAGGTCGTAGCATCGCACCAAGCGCGCAGGTG CGATGCTACGACAACAGTGAGGACGGAAGTAAGCGCGCAACTTCCGTCCTC ACTGAACAACCACGCCTGTCCAAAGCGCGCATGGACAGGCGTGGTTG T: 5'- CAACCACGCCTGTCCATGCGCGCTTTGGACAGGCGTGGTTGTTCAGTGAGG ACGGAAGTTGCGCGCTTACTTCCGTCCTCACTGTTGTCGTAGCATCGCACCT GCGCGCTTGGTGCGATGCTACGACCTATAGTGAGTCGTATTAGCGC
	3sv1	5'- GCGCTAATACGACTCACTATAGTCGTAGCATCGCACCAAGTGCGCAGGTGCG ATGCTACGACAACAGTGAGGACGGAAGTAAGTGCGCAACTTCCGTCCTCACT GAACAACCACGCCTGTCCAAAGTGCGCATGGACAGGCGTGGTTG/ 5'- CAACCACGCCTGTCCATGCGCACTTTGGACAGGCGTGGTTGTTCAGTGAGGA CGGAAGTTGCGCACTTACTTCCGTCCTCACTGTTGTCGTAGCATCGCACCTG CGCACTTGGTGCGATGCTACGACTATAGTGAGTCGTATTAGCGC
	3sv2	NT: 5'- GCGCTAATACGACTCACTATAGGTCGTAGCATCGCACCAAGCGCGTAGGTGC GATGCTACGACAACAGTGAGGACGGAAGTAAGCGCGTAACTTCCGTCCTCAC TGAACAACCACGCCTGTCCAAAGCGCGTATGGACAGGCGTGGTTG T: 5'- CAACCACGCCTGTCCATACGCGCTTTGGACAGGCGTGGTTGTTCAGTGAGGA CGGAAGTTACGCGCTTACTTCCGTCCTCACTGTTGTCGTAGCATCGCACCTA CGCGCTTGGTGCGATGCTACGACCTATAGTGAGTCGTATTAGCGC
	3sv3	NT: 5'- GCGCTAATACGACTCACTATAGTCGTAGCATCGCACCAAGAGCGCAGGTGCG ATGCTACGACAACAGTGAGGACGGAAGTAAGAGCGCAACTTCCGTCCTCACT GAACAACCACGCCTGTCCAAAGAGCGCATGGACAGGCGTGGTTG T: 5'- CAACCACGCCTGTCCATGCGCTCTTTGGACAGGCGTGGTTGTTCAGTGAGGA

		CGGAAGTTGCGCTCTTACTTCCGTCCTCACTGTTGTCGTAGCATCGCACCTG CGCTCTTGGTGCGATGCTACGACTATAGTGAGTCGTATTAGCGC
	3sv4	NT: 5'- GCGCTAATACGACTCACTATAGGTCGTAGCATCGCACCAAGCGCTCAGGTGC GATGCTACGACAACAGTGAGGACGGAAGTAAGCGCTCAACTTCCGTCCTCAC TGAACAACCACGCCTGTCCAAAGCGCTCATGGACAGGCGTGGTTG T: 5'- CAACCACGCCTGTCCATGAGCGCTTTGGACAGGCGTGGTTGTTCAGTGAGGA CGGAAGTTGAGCGCTTACTTCCGTCCTCACTGTTGTCGTAGCATCGCACCTG AGCGCTTGGTGCGATGCTACGACCTATAGTGAGTCGTATTAGCGC
	3sv5	NT: 5'- GCGCTAATACGACTCACTATAGTCGTAGCATCGCACCAAGCTCGCAGGTGCG ATGCTACGACAACAGTGAGGACGGAAGTAAGCTCGCAACTTCCGTCCTCACT GAACAACCACGCCTGTCCAAAGCTCGCATGGACAGGCGTGGTTG T: 5'- CAACCACGCCTGTCCATGCGAGCTTTGGACAGGCGTGGTTGTTCAGTGAGGA CGGAAGTTGCGAGCTTACTTCCGTCCTCACTGTTGTCGTAGCATCGCACCTG CGAGCTTGGTGCGATGCTACGACTATAGTGAGTCGTATTAGCGC
Single motif, stem3	3swt	NT: 5'- GCGCTAATACGACTCACTATAGCGACGTGTTACGGCGAGGCAAGCGCGCAG CCTCGCCGTAACACGTCGCAAGGCGGAACGGACCTCGGCTCAAGCGCGCAG AGCCGAGGTCCGTTCCGCCAAGCTCCGCTCCCAGTGGGCTCAAGCGCGCAG AGCCCACTGGGAGCGGAGC T: 5'- GCTCCGCTCCCAGTGGGCTCTGCGCGCTTGAGCCCACTGGGAGCGGAGCTT GGCGGAACGGACCTCGGCTCTGCGCGCTTGAGCCGAGGTCCGTTCCGCCTT GCGACGTGTTACGGCGAGGCTGCGCGCTTGCCTCGCCGTAACACGTCGCTA TAGTGAGTCGTATTAGCGC
Poly-A control	3swt, stem1	NT: 5'- GCGCTAATACGACTCACTATAGCGAGAGCGCTGCCCAAAAAAAAAGGGCAGC GCTCTCGCAAGCGATGAACGTAGGGAAGCGCGCACCCTACGTTCATCGCAA GCGTTCACACTGACCAAGCGCGCAGGTCAGTGTGAACGC T: 5'- GCGTTCACACTGACCTGCGCGCTTGGTCAGTGTGAACGCTTGCGATGAACGT AGGGTGCGCGCTTCCCTACGTTCATCGCTTGCGAGAGCGCTGCCCTTTTTTT TTGGGCAGCGCTCTCGCTATAGTGAGTCGTATTAGCGC
	3sv2, stem1	NT: 5'- GCGCTAATACGACTCACTATAGCGAGAGCGCTGCCCAAAAAAAAAGGGCAGC GCTCTCGCAAGCGATGAACGTAGGGAAGCGCGTACCCTACGTTCATCGCAA GCGTTCACACTGACCAAGCGCGTAGGTCAGTGTGAACGC T: 5'- GCGTTCACACTGACCTACGCGCTTGGTCAGTGTGAACGCTTGCGATGAACGT

		AGGGTACGCGCTTCCCTACGTTCATCGCTTGCGAGAGCGCTGCCCTTTTTTTT TTGGGCAGCGCTCTCGCTATAGTGAGTCGTATTAGCGC
	3swt, stem2	NT: 5'- GCGCTAATACGACTCACTATAGGTCGTAGCATCGCACCAAAAAAAAAGGTGC GATGCTACGACAACAGTGAGGACGGAAGTAAGCGCGCAACTTCCGTCCTCA CTGAACAACCACGCCTGTCCAAAGCGCGCATGGACAGGCGTGGTTG T: 5'- CAACCACGCCTGTCCATGCGCGCTTTGGACAGGCGTGGTTGTTCAGTGAGG ACGGAAGTTGCGCGCTTACTTCCGTCCTCACTGTTGTCGTAGCATCGCACCT TTTTTTTTGGTGCGATGCTACGACCTATAGTGAGTCGTATTAGCGC
Double motif, stem1	3sα1	NT: 5'- GCGCTAATACGACTCACTATAGCGAGAGCGCTGCCCAAGTAGCCAGGGCAG CGCTCTCGCAAGCGATGAACGTAGGGAAGTAGCCACCCTACGTTCATCGCAA GCGTTCACACTGACCAAGTAGCCAGGTCAGTGTGAACGC T: 5'- GCGTTCACACTGACCTGGCTACTTGGTCAGTGTGAACGCTTGCGATGAACGT AGGGTGGCTACTTCCCTACGTTCATCGCTTGCGAGAGCGCTGCCCTGGCTAC TTGGGCAGCGCTCTCGCTATAGTGAGTCGTATTAGCGC
	3sα2	NT: 5'- GCGCTAATACGACTCACTATAGCGAGAGCGCTGCCCAAGGCTACAGGGCAG CGCTCTCGCAAGCGATGAACGTAGGGAAGGCTACACCCTACGTTCATCGCAA GCGTTCACACTGACCAAGGCTACAGGTCAGTGTGAACGC T: 5'- GCGTTCACACTGACCTGTAGCCTTGGTCAGTGTGAACGCTTGCGATGAACGT AGGGTGTAGCCTTCCCTACGTTCATCGCTTGCGAGAGCGCTGCCCTGTAGCC TTGGGCAGCGCTCTCGCTATAGTGAGTCGTATTAGCGC
	3sβ1	NT: 5'- GCGCTAATACGACTCACTATAGCGAGAGCGCTGCCCAAGCTACGAGGGCAG CGCTCTCGCAAGCGATGAACGTAGGGAAGCTACGACCCTACGTTCATCGCAA GCGTTCACACTGACCAAGCTACGAGGTCAGTGTGAACGC T: 5'- GCGTTCACACTGACCTCGTAGCTTGGTCAGTGTGAACGCTTGCGATGAACGT AGGGTCGTAGCTTCCCTACGTTCATCGCTTGCGAGAGCGCTGCCCTCGTAGC TTGGGCAGCGCTCTCGCTATAGTGAGTCGTATTAGCGC
	3sβ2	NT: 5'- GCGCTAATACGACTCACTATAGCGAGAGCGCTGCCCAACGTAGCAGGGCAG CGCTCTCGCAAGCGATGAACGTAGGGAACGTAGCACCCTACGTTCATCGCAA GCGTTCACACTGACCAACGTAGCAGGTCAGTGTGAACGC T: 5'- GCGTTCACACTGACCTGCTACGTTGGTCAGTGTGAACGCTTGCGATGAACGT

		AGGGTGCTACGTTCCCTACGTTCATCGCTTGCGAGAGCGCTGCCCTGCTACG TTGGGCAGCGCTCTCGCTATAGTGAGTCGTATTAGCGC
	3sβ1_Red Broccoli	NT: 5'- CTAATACGACTCACTATAGCGAGAGCGCTGCCCAAGCTACGAGGGCAGCGC TCTCGCAAGCGATGAACGTAGGGAAGCTACGACCCTACGTTCATCGCAAGCG TTCACACTGACCAAGCTACGAGGTCAGTGTGAACGCAAGTTGGGAGACGGTC GGGTCCAGATATTCGTATCTGTCGAGTAGTGTGTGGGCTCCCAAC T: 5'- GTTGGGAGCCCACACACTACTCGACAGATACGAATATCTGGACCCGACCGTC TCCCAACTTGCGTTCACACTGACCTCGTAGCTTGGTCAGTGTGAACGCTTGC GATGAACGTAGGGTCGTAGCTTCCCTACGTTCATCGCTTGCGAGAGCGCTGC CCTCGTAGCTTGGGCAGCGCTCTCGCTATAGTGAGTCGTATTAG
	3sγ1	NT: 5'- GCGCTAATACGACTCACTATAGCGAGAGCGCTGCCCAAGGGAACAGGGCAG CGCTCTCGCAAGCGATGAACGTAGGGAAGGGAACACCCTACGTTCATCGCA AGCGTTCACACTGACCAAGGGAACAGGTCAGTGTGAACGC T: 5'- GCGTTCACACTGACCTGTTCCCTTGGTCAGTGTGAACGCTTGCGATGAACGT AGGGTGTTCCCTTCCCTACGTTCATCGCTTGCGAGAGCGCTGCCCTGTTCCC TTGGGCAGCGCTCTCGCTATAGTGAGTCGTATTAGCGC
	3sγ2	NT: 5'- GCGCTAATACGACTCACTATAGCGAGAGCGCTGCCCAAGTTCCCAGGGCAG CGCTCTCGCAAGCGATGAACGTAGGGAAGTTCCCACCCTACGTTCATCGCAA GCGTTCACACTGACCAAGTTCCCAGGTCAGTGTGAACGC T: 5'- GCGTTCACACTGACCTGGGAACTTGGTCAGTGTGAACGCTTGCGATGAACGT AGGGTGGGAACTTCCCTACGTTCATCGCTTGCGAGAGCGCTGCCCTGGGAA CTTGGGCAGCGCTCTCGCTATAGTGAGTCGTATTAGCGC
	3sγ1_Corn	NT: 5'- GCGCTAATACGACTCACTATAGCGAGAGCGCTGCCCAAGGGAACAGGGCAG CGCTCTCGCAAGCGATGAACGTAGGGAAGGGAACACCCTACGTTCATCGCA AGCGTTCACACTGACCAAGGGAACAGGTCAGTGTGAACGCAAGGCGCGAGG AAGGAGGTCTGAGGAGGTCACTGCGCC T: 5'- GGCGCAGTGACCTCCTCAGACCTCCTTCCTCGCGCCTTGCGTTCACACTGAC CTGTTCCCTTGGTCAGTGTGAACGCTTGCGATGAACGTAGGGTGTTCCCTTC CCTACGTTCATCGCTTGCGAGAGCGCTGCCCTGTTCCCTTGGGCAGCGCTCT CGCTATAGTGAGTCGTATTAGCGC
	3sδ1	NT: 5'- GCGCTAATACGACTCACTATAGCGAGAGCGCTGCCCAACGTAGGAGGGCAG CGCTCTCGCAAGCGATGAACGTAGGGAACGTAGGACCCTACGTTCATCGCAA GCGTTCACACTGACCAACGTAGGAGGTCAGTGTGAACGC

		T: 5'- GCGTTCACACTGACCTCCTACGTTGGTCAGTGTGAACGCTTGCGATGAACGT AGGGTCCTACGTTCCCTACGTTCATCGCTTGCGAGAGCGCTGCCCTCCTACG TTGGGCAGCGCTCTCGCTATAGTGAGTCGTATTAGCGC
	3sδ2	NT: 5'- GCGCTAATACGACTCACTATAGCGAGAGCGCTGCCCAACCTACGAGGGCAG CGCTCTCGCAAGCGATGAACGTAGGGAACCTACGACCCTACGTTCATCGCAA GCGTTCACACTGACCAACCTACGAGGTCAGTGTGAACGC T: 5'- GCGTTCACACTGACCTCGTAGGTTGGTCAGTGTGAACGCTTGCGATGAACGT AGGGTCGTAGGTTCCCTACGTTCATCGCTTGCGAGAGCGCTGCCCTCGTAG GTTGGGCAGCGCTCTCGCTATAGTGAGTCGTATTAGCGC
	3sε1	NT: 5'- GCGCTAATACGACTCACTATAGCGAGAGCGCTGCCCAAGAGGTCAGGGCAG CGCTCTCGCAAGCGATGAACGTAGGGAAGAGGTCACCCTACGTTCATCGCAA GCGTTCACACTGACCAAGAGGTCAGGTCAGTGTGAACGC T: 5'- GCGTTCACACTGACCTGACCTCTTGGTCAGTGTGAACGCTTGCGATGAACGT AGGGTGACCTCTTCCCTACGTTCATCGCTTGCGAGAGCGCTGCCCTGACCTC TTGGGCAGCGCTCTCGCTATAGTGAGTCGTATTAGCGC
	3sε2	NT: 5'- GCGCTAATACGACTCACTATAGCGAGAGCGCTGCCCAAGACCTCAGGGCAG CGCTCTCGCAAGCGATGAACGTAGGGAAGACCTCACCCTACGTTCATCGCAA GCGTTCACACTGACCAAGACCTCAGGTCAGTGTGAACGC T: 5'- GCGTTCACACTGACCTGAGGTCTTGGTCAGTGTGAACGCTTGCGATGAACGT AGGGTGAGGTCTTCCCTACGTTCATCGCTTGCGAGAGCGCTGCCCTGAGGT CTTGGGCAGCGCTCTCGCTATAGTGAGTCGTATTAGCGC
	3sζ1	NT: 5'- GCGCTAATACGACTCACTATAGCGAGAGCGCTGCCCAAGGATGCAGGGCAG CGCTCTCGCAAGCGATGAACGTAGGGAAGGATGCACCCTACGTTCATCGCAA GCGTTCACACTGACCAAGGATGCAGGTCAGTGTGAACGC T: 5'- GCGTTCACACTGACCTGCATCCTTGGTCAGTGTGAACGCTTGCGATGAACGT AGGGTGCATCCTTCCCTACGTTCATCGCTTGCGAGAGCGCTGCCCTGCATCC TTGGGCAGCGCTCTCGCTATAGTGAGTCGTATTAGCGC
	3sζ2	NT: 5'- GCGCTAATACGACTCACTATAGCGAGAGCGCTGCCCAAGCATCCAGGGCAG CGCTCTCGCAAGCGATGAACGTAGGGAAGCATCCACCCTACGTTCATCGCAA GCGTTCACACTGACCAAGCATCCAGGTCAGTGTGAACGC T: 5'- GCGTTCACACTGACCTGGATGCTTGGTCAGTGTGAACGCTTGCGATGAACGT

		AGGGTGGATGCTTCCCTACGTTCATCGCTTGCGAGAGCGCTGCCCTGGATG CTTGGGCAGCGCTCTCGCTATAGTGAGTCGTATTAGCGC

Table 1-4. Peptide sequences.

Peptide	Amino acid sequence	Note
P22 N peptide	GNAKTRRHERRRKLAIERDTIGY	
HIV-1 TAT	SFITKALGISYGRKKRRQRRRPP QGSQTHQVSLSKQ	
Streptavidin		This product was purchased from https://www.thermofisher.com/order/catalog/product/S32355. No sequence available.

2 Chapter 2: Programmable artificial RNA condensates in mammalian cells

Adapted, with permission from Shiyi Li, Yuna Kim, Kevin Wang, Eric John Payson, Anli A. Tang, Maria Villalba Nieto, Dino Osmanovic *et al*. "Programmable artificial RNA condensates in mammalian cells." *Nature Nanotechnology* (2026): 1-10.

2.1 Introduction

Biomolecular condensates are associated with a multitude of processes in living cells, including gene expression, metabolism and diseases[9]. For this reason, there is growing interest in methods for producing artificial condensates with controllable composition, viscoelastic properties and subcellular location, as a means for manipulating cellular functions[13]. One approach to building artificial condensates is to establish weak interactions among engineered proteins that carry intrinsically disordered domains[11,75]. Similarly, RNA molecules designed to include multiple, short sequence repeats yield artificial RNA condensates[15,66,67,76]. As weak promiscuous bonds make it difficult to build condensates with a compositional identity and exclusive functions, a promising alternative approach is to take advantage of multivalent molecules with site-specific interactions[77,78].

We and others recently described *in vitro* assembly of RNA condensates from short single strands of RNA (100–200 nucleotides long) that operate as multivalent particles[79,80]. These structural motifs, termed single-stranded RNA (ssRNA) nanostars, consist of at least three stem–loops that fold during transcription, functioning as ‘arms’

(Fig. 1a). The arms interact through sequence-specific binding of their loop domains, known as kissing loops (KLs), which are typically palindromic and identical on each arm. KLs can be designed to be non-interacting, so distinct nanostars can produce condensates that do not mix[79,80]. The modular design of nanostars allows for the addition of domains for the recruitment of small molecules and proteins[79,80]. Here, we demonstrate that ssRNA nanostars can generate condensates within living mammalian cells with controlled mixing patterns, and that the interactions and localization of these condensates can be tuned by modifying the nanostar design.

2.2 Results

2.2.1 RNA nanostars produce condensates that recruit target molecules

We produced ssRNA nanostars in living cells using the Tornado expression system[81] for spontaneous RNA circularization that extends the RNA's half-life (**Fig. 2-8 and 2-9** and **Table 2-1**). We started with a nanostar design that carries three 15-nucleotide (nt) arms, each with a 6-nt KL UCGCGA (variant A), as shown in **Fig. 2-1a** (design 15nt-3A-Br). We included the Broccoli aptamer in one of the arms, to visualize the expressed RNA in cells by adding its fluorogenic ligand 3,5-difluoro-4-hydroxybenzylidene imidazolinone (DFHBI) to the media[50]. This nanostar design generates condensates during *in vitro* transcription at a constant temperature (**Fig. 2-10**), and we observed comparable structures forming in transfected HEK293T, HeLa and U-2 OS cells (**Fig. 2-1b** and **Fig. 2-11 and 2-12**). Further experiments were done in HEK293T cells, which show higher expression levels owing to the presence of the SV40 large T antigen[82,83]. Flow cytometry experiments confirmed that expression of circularized Broccoli alone results in lower granularity when compared with nanostar-

expressing cells (**Fig. 2-13**). Microscopy further confirmed diffuse fluorescence in the cytoplasm, with few puncta in the nucleus, and shells that may correspond to circularized RNA colocalized with other cellular components[81,84] (**Fig. 2-14a**). Replacement of at least one KL with a polyA sequence disrupts the formation of full droplets, although shells persist, confirming that condensation is driven by loop–loop interactions (**Fig. 2-14b**).

RNA nanostars can recruit ‘guest’ molecules through embedded aptamers. We demonstrate this using the MS2 aptamer to recruit an MCP-tagged reporter[85]. We cotransfected two plasmids into cells, one encoding the modified MS2-RNA nanostar and the other encoding the MCP-mCherry guest (**Fig. 2-1c** and **Fig. 2-15 and 2-16**), and measured the colocalization of fluorescent signals. Live-cell imaging confirmed successful mCherry recruitment into RNA condensates (**Fig. 2-1d** and **Fig. 2-17**). By contrast, nanostars lacking the MS2 domain did not affect the spatial localization of mCherry (**Fig. 2-16**).

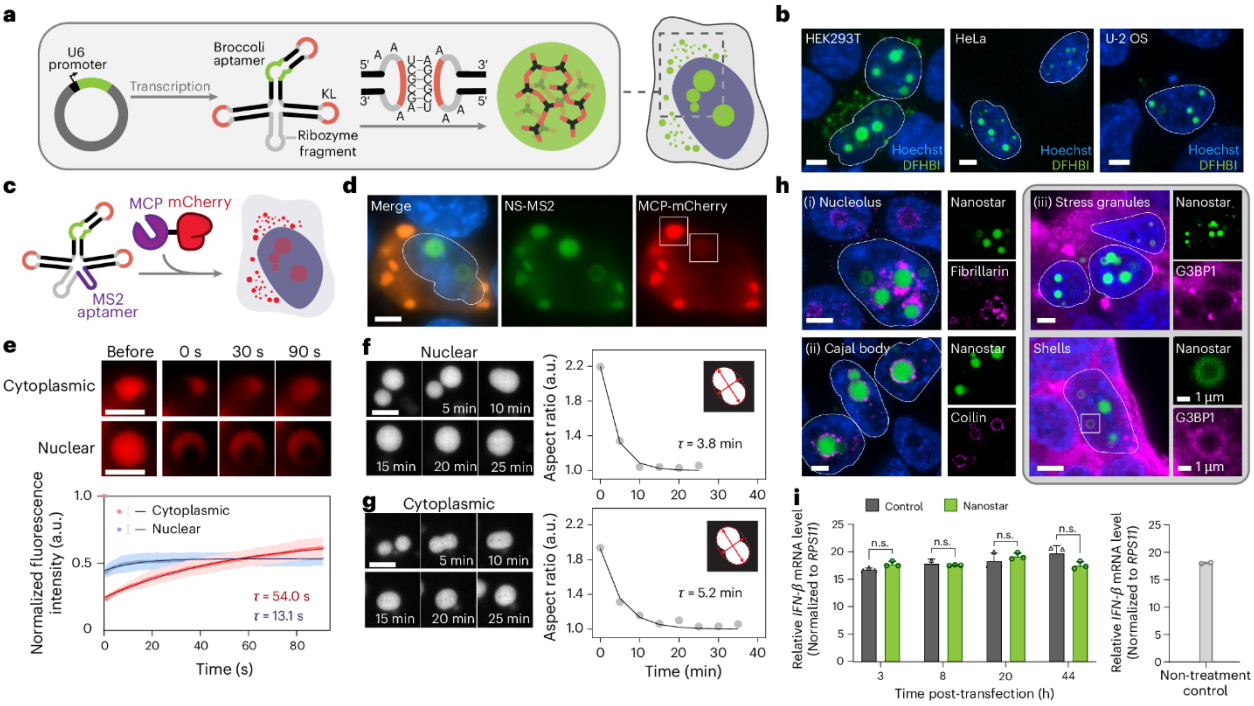

Figure 2-1. Circularized RNA nanostars generate condensates in multiple mammalian cell lines.

a, RNA nanostars were expressed in mammalian cells from transfected Tornado plasmids, yielding circularized RNA motifs that form condensates through KL interactions. **b**, Representative confocal microscopy images showing RNA condensate formation in HEK293T, HeLa and U-2 OS cells. The nuclei of condensate-expressing cells are outlined. **c**, A schematic illustrating the recruitment of MCP-mCherry to RNA nanostars through the incorporation of an MS2 aptamer as an additional arm. **d**, Split channel fluorescent images of a HEK293T cell cotransfected with MCP-mCherry and MS2-nanostar. Two representative condensates analysed by FRAP in e are highlighted. **e**, Representative fluorescence images (top) and pixel intensity profile (bottom) at different time points after photobleaching. Blue and orange dots represent the mean pixel intensity within the bleached region at each time point. Error bars indicate standard deviation. Dark blue and red lines show exponential fits with time constant τ. Means and standard deviations were calculated from three fields of view, each from an independent replicate. **f,g**, Fluorescence images (left) and time-dependent changes in aspect ratio (right) demonstrating the coalescence of nuclear (**f**) and cytoplasmic (**g**) condensates in HEK293T cells expressing Broccoli-labelled nanostars. Aspect ratios (grey dots) were calculated as the ratio of major to minor axes from best-fit ellipses. Dashed lines indicate exponential fits with decay constant τ. **h**, Colocalization of RNA

condensates with endogenous membraneless organelles in HEK293T cells. Cell nuclei (blue), RNA condensates (green) and canonical marker proteins for each indicated organelle labelled by immunostaining (magenta) are shown. **i**, Quantitative PCR analysis of IFN-beta mRNA expression in nanostar-expressing cells (green), Lipofectamine-treated cells (dark grey) and untreated cells (light grey) at the indicated time points post-transfection. Statistical analysis using two-way ANOVA followed by multiple comparison tests showed no significant difference. All cellular expression data were collected 48 h post-transfection, except for the time-lapse experiments. Images in **b** are z-projections from confocal stacks. All experiments were performed in three independent replicates, and representative images are shown. Scale bars, 5 μm. n.s., not significant.

2.2.2 Diffusivity and viscosity of RNA condensates

Using fluorescence recovery after photobleaching (FRAP), we estimated the diffusion timescale for the mCherry guest protein. Cytoplasmic condensates exhibit a recovery time constant of 54 s, while nuclear condensates show a faster but minimal recovery (**Fig. 2-1e** and **Fig. 2-18**), probably because of the lower level of mCherry, which lacks a nuclear localization signal. The abundance of mCherry correlated with higher percentage of recovery, presumably because guest-molecule recruitment hinders nanostar interactions and increases guest diffusivity (**Fig. 2-19**). FRAP analysis of nuclear and cytoplasmic condensates using Broccoli reveals faster recovery, $\tau = 7.8$ s and $\tau = 10.2$ s (**Fig. 2-20a–d**), respectively, and $\tau = 18.2$ s *in vitro* (**Fig. 2-21a**). Because small-molecule ligands bind their RNA aptamer non-covalently (Broccoli Kd $\approx$ 300 nM), the observed recovery is probably dominated by dynamic ligand exchange rather than RNA diffusion. Nuclear condensates labelled with Pepper[84,86], another fluorogenic aptamer that produces red fluorescence upon the addition of (4-((2-hydroxyethyl)(methyl)amino)-benzylidene)-cyanophenylacetonitrile 620 (HBC620),

showed distinct recovery with a larger fitted time constant of 79.5 s, consistent with a lower Kd ≈ 3.5 nM (ref. [87]) when compared with Broccoli (**Fig. 2-20e,f**).

Fusion of RNA condensates in living cells proceeded with a time constant of τ = 3.8 min for a nuclear event, and τ = 5.2 min for a cytoplasmic event (**Fig. 2-1f,g** and **Fig. 2-23 to 2-26**). Nuclear events appeared faster than cytoplasmic events, potentially reflecting differences in environment. Although faster in cells than *in vitro* (τ ≈ 16 h) (**Fig. 2-22**), the fusion of RNA condensates remains slower than that of P granules and stress granules, which relax within seconds[40,88], and is comparable to nucleolar dynamics[89]. Together, FRAP and fusion results indicate that RNA condensates are relatively viscous. We observed a nuclear 'splitting' event (**Fig. 2-26**), suggesting influence from other cellular components.

2.2.3 RNA condensates interact with nuclear organelles but do not elicit an immune response

Immunostaining for fibrillarin indicates an accumulation of RNA nanostars in the nucleolar region (**Fig. 2-1h(i)** and **Fig. 2-27a**). In these cells, fibrillarin localized at the condensate surface but remained excluded from the condensates. Some RNA nanostar variants might be favoured for nucleolar localization (**Fig. 2-27b**). Similarly, coilin aggregates on the condensates surface, suggesting the recruitment of Cajal bodies (**Fig. 2-1h(ii)** and **Fig. 2-28**). Cells producing high levels of RNA condensates showed increased stress granule formation, as indicated by G3BP1 staining (**Fig. 2-1h(iii)**, top, and **Fig. 2-29**). Colocalization of G3BP1 and nanostars was only observed in a few cells with high cytoplasmic RNA condensate formation[90,91] (**Fig. 2-29e**). In some nuclei,

G3BP1 colocalized on the outside of shells, but not with condensates (**Fig. 2-1h(iii)**, bottom, and **Fig. 2-30**). Shells were observed in other systems producing circularized RNA, indicating that they are not specific to nanostar condensates[84] (**Fig. 2-14 and 2-30**). More work is needed to determine whether stress granules in nanostar-expressing cells arise owing to specific RNA–protein interactions, or because of metabolic stress caused by elevated cytoplasmic RNA levels[90–93]. We found no colocalization with P-bodies and nuclear speckles (**Fig. 2-31**). No immunogenic response was observed in transfected cells, as indicated by comparable mRNA expression levels of interferon beta 1 (IFNB1) and the IFN-stimulated genes ISG15 and IFIT1 in cells with and without condensates (**Fig. 2-1i**, **Fig. 2-32** and **Table 2-4**).

2.2.4 RNA nanostar design determines the subcellular localization of condensates

Local concentration of nanostars is determined by the relative speed of transcription in the nucleus, export from the nucleus and degradation. These processes crucially affect condensate formation, which occurs only if the nanostar concentration exceeds a critical value C^* (ref. [2]). We illustrate this through a simple compartment model (**Fig. 2-2a**), in which nanostars are produced at a rate of R inside the nucleus, exported to the cytoplasm at a constant rate D and degraded in the cytoplasm at rate γ

$$C_n'(t) = R - DC_n(t) \quad (1)$$

$$C_c'(t) = Dv C_n(t) - \gamma C_c(t) \quad (2)$$

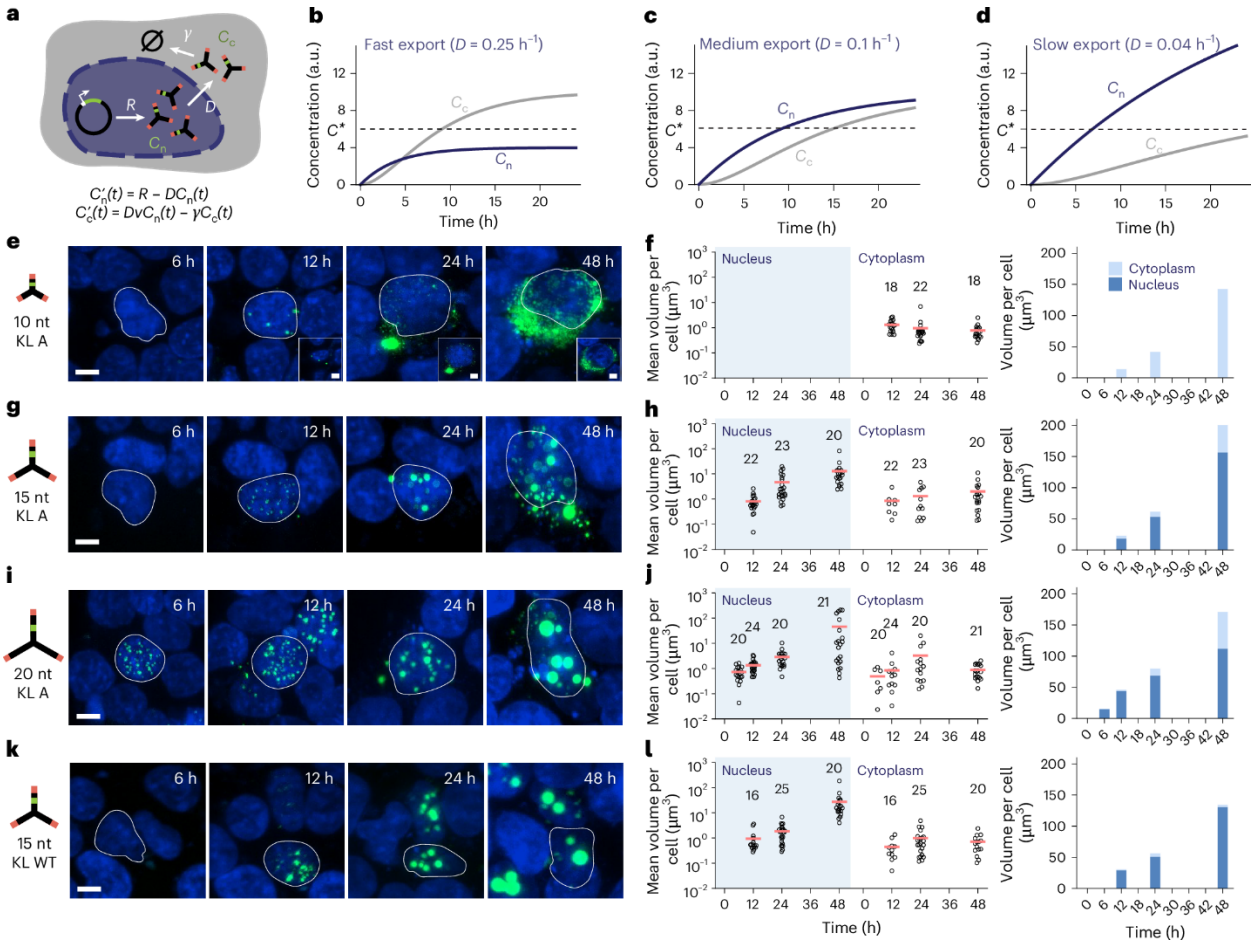

Figure 2-2. Nuclear and cytoplasmic condensate formation depends on nanostar design.

a, A model schematic depicting parameters determining nanostar concentration in the nucleus (C_n) and cytoplasm (C_c). R denotes the transcription rate, D the nuclear export rate and γ the degradation rate. v represents the nuclear-to-cytoplasm volume ratio (V_n:V_c). Ø indicates RNA degradation products. Phase separation occurs when concentration exceeds the critical concentration (C^*). **b–d**, Simulated concentration profiles for nuclear (C_n) and cytoplasmic (C_c) compartments at fast (**b**), medium (**c**) or slow (**d**) export rates (D), with other parameters held constant ($R = 1$, $\gamma = 0.2$ and $v = 2$). Faster export favours cytoplasmic accumulation, whereas slower export promotes nuclear enrichment. **e,g,i,k**, Representative confocal *z*-projections showing condensate growth over 48 h for nanostars with KL A and 10-nt (**e**), 15-nt (**g**) and 20-nt (**i**) arms, and for nanostars with KL WT and 15-nt arms (**k**). Nuclei are stained with Hoechst (blue) and nanostars with DFHBI (green). The same cell is outlined across time points for each design. Insets in e show single midplane sections confirming cytoplasmic localization. Additional midplane images

are provided in Fig. 2-36. **f,h,j,l,** Quantification of condensate formation from nanostars with KL A and 10-nt (**f**), 15-nt (**h**) and 20-nt (**j**) arms, and for nanostars with KL WT and 15-nt arms (**l**). Dot plots (left) show the temporal evolution of mean condensate volume per cell in the nucleus and cytoplasm; numbers above indicate the number of analysed cells at each time point across three independent replicates. Bar plots (right) show total condensate volume per cell averaged across analysed cells. Scale bars, 5 µm.

Here, $C'_n(t)$ and $C'_c(t)$ denote the time derivatives of the nanostar concentrations in the nucleus (Cn) and cytoplasm (C_c), v is a correction term accounting for the change in volume ratio $V_n:V_c$. The production rate R depends primarily on the amount of plasmids delivered into each cell, and the degradation rate γ should only depend on the nanostar concentration. By contrast, the export constant D, governed by the size-sensitive permeability of the nuclear pore, can be dramatically affected by structural design features of nanostars. Depending on the value of D, the critical concentration may never be reached, or can be reached at different times in the nucleus and in the cytoplasm (**Fig. 2-2b–d**). By systematically changing the nanostar size and intermolecular affinity, one could modulate where and when condensates form[94].

To test this model, we first modified the nanostar arm length (10, 15 and 20 nt)[79], and measured the nuclear and cytoplasmic volume of RNA condensates at 6, 12, 24 and 48 h post-transfection[95] (**Fig. 2-2e–j** and **Figs. 2-33 to 2-35**). We found that 10-nt arm nanostars (arm length 3.4 nm, molecular weight (MW) 56.8 kDa) form condensates exclusively in the cytoplasm as they probably diffuse quickly through the nuclear pore complex (**Fig. 2-2e,f**), demonstrating a similar behaviour as simulated in Fig. 2b. These nanostars do not colocalize with nucleoli nor with Cajal bodies (**Figs. 2-27b and 28b**). Nanostars with a 15-nt arm (arm length 5.1 nm, MW 66.3 kDa) and a 20-nt arm (arm

length 6.8 nm, MW 75.8 kDa), having sizes close to the nucleus' permeability barrier, form condensates inside the nucleus first, and the cytoplasmic fraction increases over time (**Fig. 2-2g–j**). Nanostars with 20-nt arms condensed at an earlier time point, reflecting a dependence of growth rate on nanostar size[37]. In addition to depending on arm length, the nanostar export rate could also be impacted by the rate of assembly. To test this we changed the 15-nt arm nanostar from KL A (UCGCGA) to the strongest possible variant, KL WT (GCGCGC)[36] and observed an increase in the nuclear condensate fraction (**Fig. 2-2k,l**).

We then elucidated how design parameters influence condensate localization, abundance and morphology, by systematically varying size (arm length), valency (number of arms) and avidity (KL strength) of the nanostars[37] (**Fig. 2-3**). For each variant, we measured corresponding condensate volume, number and cellular localization 48 h after transfection (**Figs. 2-36 to 40**). Consistent with **Fig. 2-2**, nanostars with 10-nt arms formed condensates only in the cytoplasm, while nanostars with 15–25-nt long arms also generated fewer and larger condensates in the nucleus (**Fig. 2-3a,b**). Next, we varied the nanostar arm number between two and four (**Fig. 2-3c,d**). Nanostars with valency less than three only formed shells. Replacing KLs with polyA sequences yielded similar effects as deleting arms (**Fig. 2-14**). Increasing arm number yielded fewer but larger condensates in the nucleus, probably due to accelerated nuclear aggregation, and correspondingly, more small puncta in the cytoplasm, probably due to enhanced nucleation. Finally, we investigated the impact of KL strength on condensate formation across four variants, with GC content spanning from 0% to 100% (**Fig. 2-3e,f** and **Table 2-2**). The strongest variant (WT, GCGCGC)

yielded large condensates in the nucleus and a higher number of smaller puncta in the cytoplasm, resembling the behaviour of the four-arm nanostar. By contrast, weak KL variants E (GUAUAC) and F (UAUAUA) primarily formed nuclear shells. Overall, larger and fewer condensates accumulated in the nucleus as we increased arm number and strength of the KLs (**Fig. 2-3g, Fig. 2-37** and **Table 2-3**).

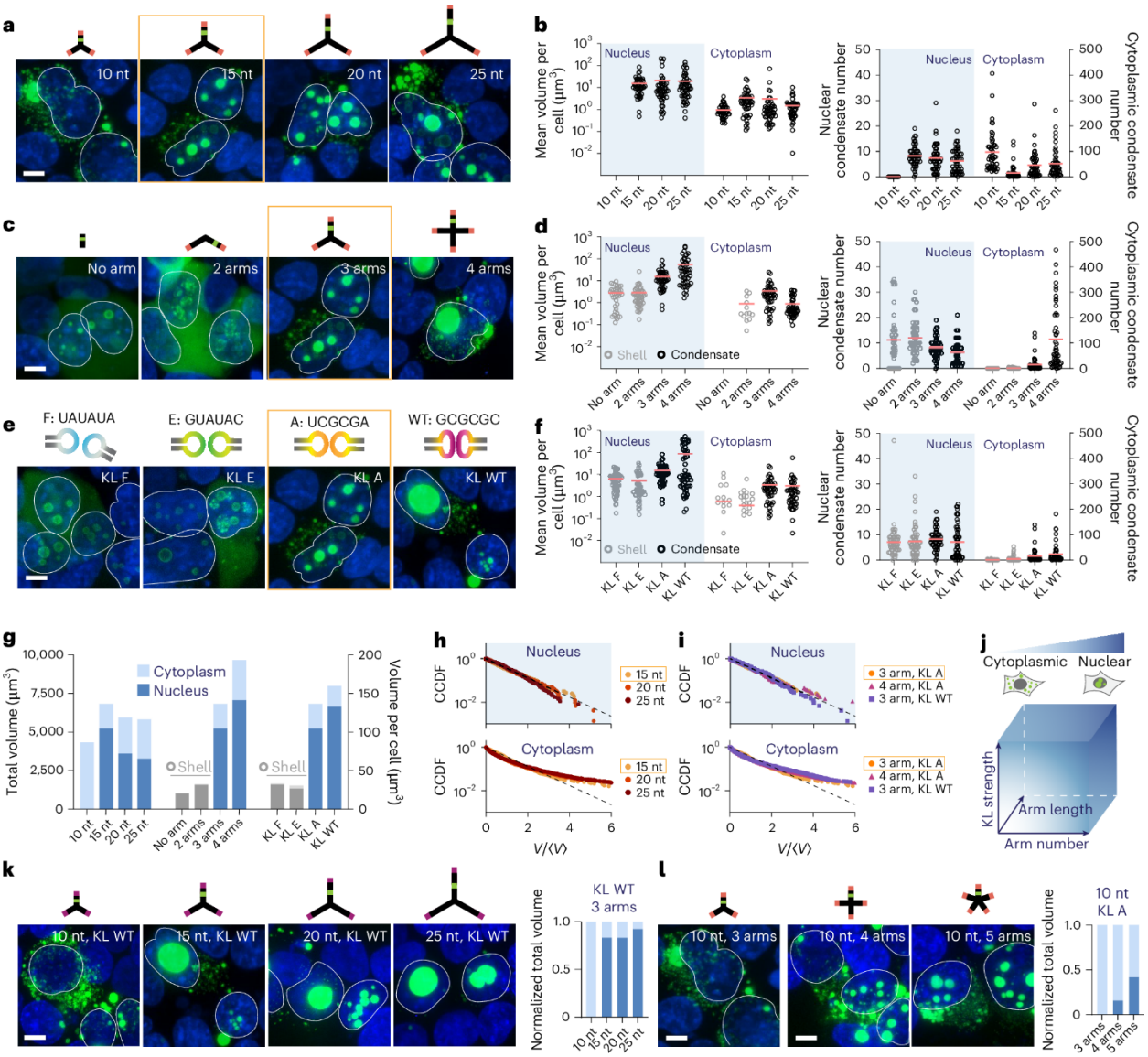

Figure 2-3. Engineering condensate volume distribution and localization through nanostar design.

a,c,e, Representative confocal z-projections showing condensates formed by RNA nanostar variants with different arm lengths (**a**), arm numbers (**c**) or KL sequences (**e**). Nuclei are stained with Hoechst (blue) and nanostars with DFHBI (green). The nuclei of condensate-expressing cells are outlined. Yellow boxes highlight the same variant across panels. **b,d,f**, Quantification of condensate formation from nanostars with different arm lengths (**b**), arm numbers (**d**) or KL sequences (**f**). Mean condensate volume per cell in the nucleus and cytoplasm (log scale) (left). Number of condensates per cell in the nucleus and cytoplasm (right). Each dot represents one cell; red lines indicate the mean. **g**, Total condensate volume across 50 analysed cells (left axis) and mean volume per cell (right axis) for the indicated designs. **h,i**, CCDFs of condensate volumes. Nuclear condensates are well described by an exponential distribution (dashed line), whereas cytoplasmic condensates exhibit sub-exponential distribution across variants differing in arm length (h), arm number or KL sequence (i). Condensates were segmented in three dimensions, normalized to the mean condensate volume of each cell, pooled across cells and plotted collectively. Each dot represents a single condensate. **j**, A schematic summarizing the relationship between nanostar design parameters and condensate localization. Increased KL strength, arm length or arm number promotes nuclear enrichment. **k,l,** Representative confocal images (left) showing enhanced nuclear localization with increased arm length (**k**) or arm number (**l**). The quantification of normalized total condensate volume from 50 cells (right) shows an increased nuclear fraction (dark blue) relative to cytoplasm (light blue). All experiments were performed in three independent replicates. Scale bars, 5 μm.

Across designs, normalized volume complementary cumulative distribution functions (CCDFs)[96] show that nuclear condensates follow an exponential distribution, while cytoplasmic condensates are sub-exponential (**Fig. 2-3h,i**). This difference may be because of faster condensate birth inside the nucleus when compared with the cytoplasm[96]. No apparent deviation in the normalized CCDF was observed across

designs. Similar trends are observed in the CCDF of condensate volume measured at different time points, from the experiments reported in **Fig. 2-2** (**Fig. 2-38**).

Overall, these results show that RNA nanostar design provides means to tune the nuclear-to-cytoplasmic distribution of condensates. The proportion of nuclear condensates increases with stronger KLs, more arms and longer arms (**Fig. 2-3j** and **Fig. 2-39**). We further validated this programmable control by (1) maximizing nuclear localization and (2) relocating cytoplasmic-only condensates into the nucleus through sequence modifications (**Fig. 2-3k,l** and **Fig. 40**). First, we introduced the KL WT to enhance interaction strength and observed almost exclusively nuclear condensates for the 25-nt nanostar (**Fig. 2-3k**). Next, we increased the arm number from three to five, reasoning that higher valency and molecular size might synergistically promote nuclear localization. As expected, 10-nt nanostars with more arms formed nuclear condensates whose size and number scaled with arm number (**Fig. 2-3l**).

Collectively, these experiments demonstrate that RNA nanostars are a robust motif for building cellular condensates, and that structural and sequence variations enable control over their localization and size. Partition coefficient analysis across all designs confirmed higher nuclear enrichment when compared with cytoplasmic condensates, while shell-forming constructs consistently displayed low partition coefficients (**Fig. 2-41**). We verified that variations to the nanostar design do not compromise their ability to recruit target proteins (**Fig. 2-42a**), but the diffusivity of guest molecules might vary following the change in the interaction of nanostars (**Fig. 2-42b**). Finally, we observed that cells expressing RNA nanostars exhibit an enlarged nucleus, probably as a consequence of increased local osmotic pressure (**Figs. 2-43 and 44**).

2.2.5 Sequence design produces diverse condensates with tunable interactions and cellular localization

RNA nanostars can be created to have diverse KL domains (**Fig. 2-4** and **Fig. 45**). First, we tested a two-nanostar system with non-palindromic, complementary KLs11 (**Fig. 2-4a**), each labelled with distinct fluorogenic aptamers, Broccoli and Pepper. No condensation was observed when only one of these two nanostars was expressed (**Fig. 2-4b**, top and middle). When both nanostars are coexpressed, condensates show colocalized Broccoli and Pepper fluorescence with a high Pearson correlation coefficient (PCC) (**Fig. 2-4b**, bottom). Distinct slopes in the fluorescence scatter plot suggest different Broccoli-to-Pepper ratios in the cytoplasm and nucleus, probably due to the influence of aptamers on nanostar folding and nuclear export speed.

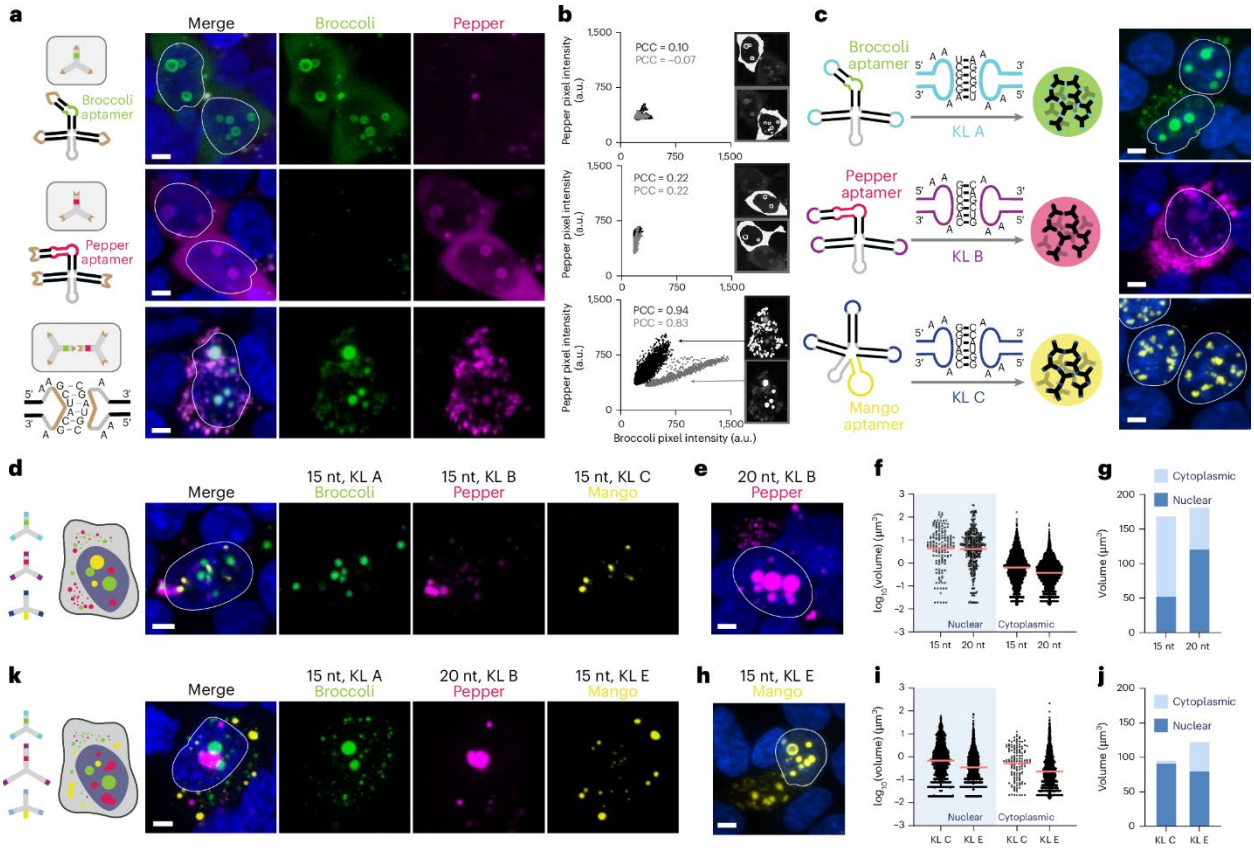

Figure 2-4. Nanostar KL sequences determine condensate miscibility.

a, A schematic of nanostars labelled with Broccoli or Pepper that interact through complementary, non-palindromic KLs. Fluorescence micrographs show condensate formation upon coexpression of both nanostars. **b**, Scatter plots of Broccoli and Pepper pixel intensities within the indicated regions of interest, with corresponding PCCs. The lower panel compares nuclear and cytoplasmic condensates, which exhibit distinct correlation patterns. **c**, A schematic of nanostars bearing KLs A, B or C, labelled with Broccoli, Pepper or Mango aptamers, and representative fluorescence images of the resulting condensates. **d**, Cotransfection of 15-nt arm nanostars carrying distinct KLs (A, B and C) produces spatially segregated condensates that do not mix. **e,h**, Confocal images of cells expressing modified nanostars with altered arm length (e, Pepper tagged) or KL strength (h, Mango tagged) to modulate subcellular localization. **f,i**, Dot plots showing the distribution of nuclear and cytoplasmic condensate volumes (log scale) forming from Pepper-tagged (**f**) or Mango-tagged (**i**) nanostars. Each dot represents one condensate; red lines indicate the mean. **g,j**, Bar charts comparing the average condensate volume

in the nucleus and cytoplasm forming from Pepper-tagged (**g**) or Mango-tagged (**j**) nanostars. **k**, Reprogrammed subcellular localization of distinct condensates using modified Pepper- and Mango-tagged nanostars while maintaining the Broccoli design. Cells were stained with Hoechst (nuclei), DFHBI (Broccoli), HBC620 (Pepper), and TO1-B (Mango). Nuclei are outlined. All experiments were performed in three independent replicates. Images are confocal z-projections. Scale bars, 5 μm.

Leveraging the sequence-specificity of loop–loop interactions, RNA nanostars can be optimized to generate distinct, non-interacting condensates. To illustrate this we designed three nanostars[80], each carrying distinct palindromic KLs (A, B and C) and different fluorogenic aptamers, Broccoli, Pepper and Mango (produces yellow fluorescence upon the addition of TO1-Biotin (TO1-B))[97]. Each nanostar generated condensates, with differences in their cellular localization depending on the aptamer reporter (**Fig. 2-4c** and **Fig. 2-46**). While the distribution of Broccoli- and Pepper-carrying nanostars remained consistent with variants described earlier, Mango-carrying nanostars with KL C primarily yielded nuclear condensates, as the Mango aptamer loop might enhance nanostar interactions and promote nuclear aggregation. Simultaneous transfection of plasmids, each carrying one of the nanostars, resulted in distinct, non-mixing condensates (**Fig. 2-4d** and **Fig. 2-47**), which maintained the subcellular localization observed when expressed individually.

Taking advantage of the design guidelines identified in **Figs. 2-2** and **2-3**, we then sought to shift the cellular localization of non-mixing condensates. To shift Pepper-tagged condensates to the nucleus, we extended the nanostar arm length from 15 nt to 20 nt. With this change, we observed a higher nuclear-to-cytoplasmic volume ratio (**Fig. 2-4e–g**). Enhancing KL strength was a less effective strategy (**Fig. 2-49a–c**). To localize

Mango-tagged nanostars more to the cytoplasm, we adopted weaker KLs, switching from design C (GGUACC) to design E (GUAUAC). This change successfully increased the cytoplasmic-to-nuclear condensate volume (**Fig. 2-4h–j**). Adopting KL F (AUAUAU) yielded only nuclear shells (**Fig 2-49d**). Cotransfection of the new plasmid triplet resulted in distinct condensates with the expected changes in subcellular distribution (**Fig. 2-4k**). Taken together, these results indicate that the principles governing the interaction specificity, morphology and cellular localization of condensates remain valid across variants; however, the efficiency in manipulating condensate properties is affected by details of nanostar and aptamer sequence.

We then demonstrated how to systematically colocalize non-mixing condensates (20 nt, KLs A and B, labelled with Broccoli and Pepper, respectively) through the production of RNA linkers carrying both KLs[19,80] (**Fig. 2-5** and **Figs. 50 and 51**). We tested two- and four-arm linkers (**Fig. 2-5a**). The colocalization level of distinct condensates depends on the ratio of the linker plasmid concentration relative to the nanostar plasmid concentration (**Fig. 2-5b**). At levels of nanostar:two-arm-linker:nanostar-plasmid ratios up to 1:3:1, nuclear Broccoli- and Pepper-carrying condensates interacted while remaining distinct, producing Janus-like morphologies (**Fig. 2-5c**, top row). At higher ratios, they completely mixed. We observed similar results for the four-arm linker (**Fig. 2-5d**, top row); however, a 1:2:1 ratio of nanostar:four-arm-linker:nanostar was sufficient to produce mixed condensates in the nucleus. Because each linker now carried twice as many arms, this result was consistent with the two-arm linker, which yielded mixed condensates at a 1:4:1 ratio. In the cytoplasm, however, two-arm linkers produced mixed condensates at lower plasmid

ratios when compared with four-arm linkers, presumably because the smaller two-arm motifs are exported faster from the nucleus and their concentrations increase more rapidly in the cytoplasm (**Fig. 2-5c,d**, bottom row).

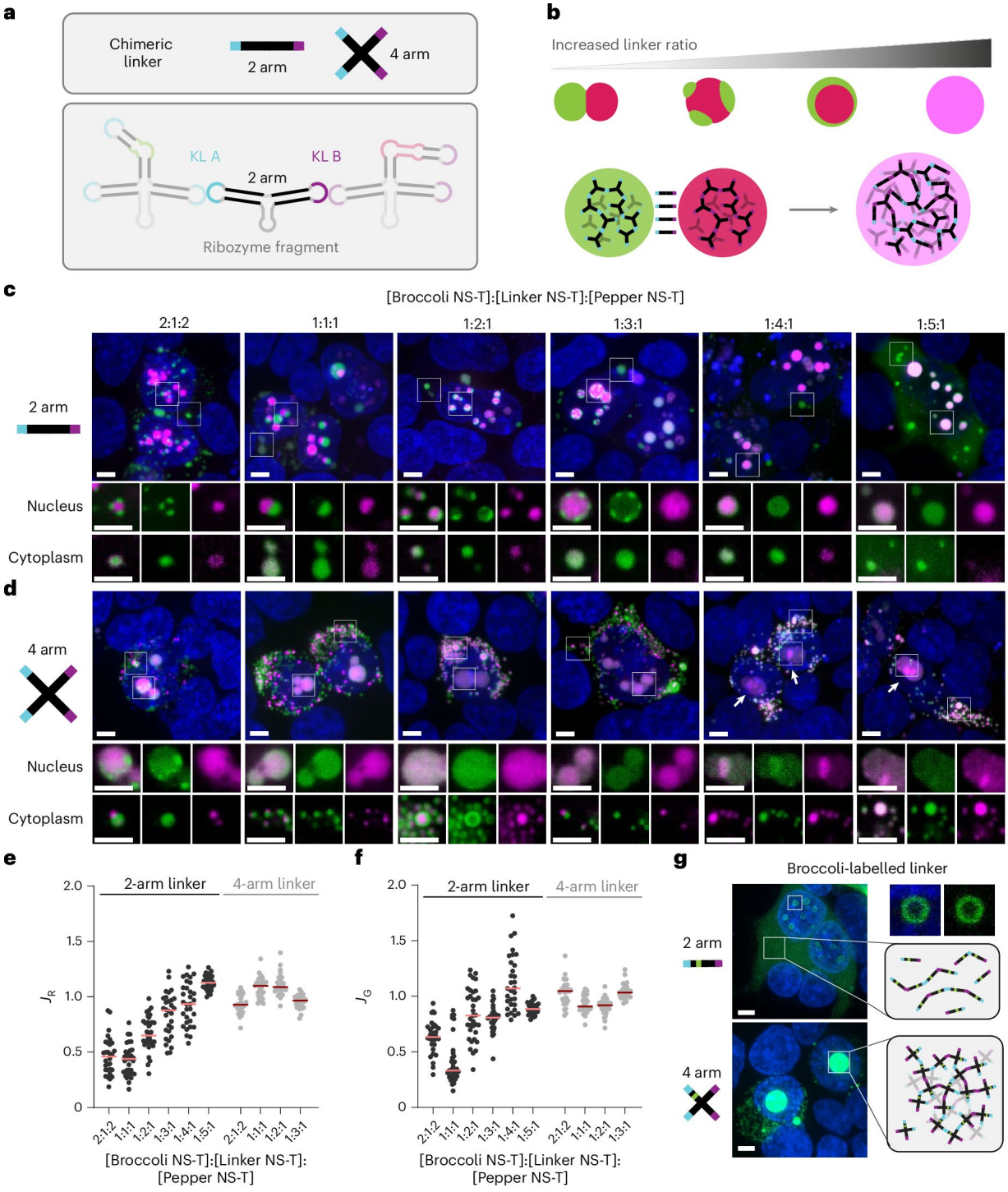

Figure 2-5. Chimeric linker nanostars at different ratios yield condensates with programmable sub-compartmentalization.

a, A schematic of two-arm and four-arm chimeric linker nanostars. **b,** Increasing the ratio of chimeric linker nanostars relative to distinct nanostars enhances condensate mixing. **c,d,** Confocal micrographs of cells expressing nanostars at varying plasmid ratios ([Broccoli nanostar plasmid (NS-T)]:[Linker NS-T]:[Pepper NS-T]) using two-arm (**c**) or four-arm (**d**) linkers. Top panels show larger fields of view (z-projections) and bottom panels show zoomed-in sections. White arrows indicate non-homogeneous mixing, probably owing to clustering of the four-arm linkers. **e,f,** Quantification of mixing for two-arm and four-arm linkers. For two-arm linkers, mixing indices J_R (**e**) and J_G (**f**) increase with linker ratio. Four-arm linkers exhibit higher mixing indices consistent with increased valency. **g,** Broccoli-labelled two-arm linkers do not form condensates on their own, whereas four-arm linkers self-assemble into condensates. Cells were stained with Hoechst (nuclei), DFHBI (Broccoli) and HBC620 (Pepper). Images were acquired 48 h after transfection. All experiments were performed in three independent replicates. Scale bars, 5 μm.

The degree of mixing between the two phases of nuclear condensates was quantified through mixing indices J_R and J_G that measured the normalized fraction of red in green, and green in red condensates[80] (**Fig. 2-5e,f**). Compared with J_R, index J_G showed more fluctuation owing to a lower signal-to-noise ratio of Broccoli compared with Pepper (**Fig. 2-52**). To our surprise, Broccoli-labelled four-arm linkers formed condensates when expressed individually (**Fig. 2-5g**), suggesting that the non-homogeneous mixing observed in **Fig. 2-5d** (white arrows) probably resulted from the local clustering of non-fluorescently labelled linkers.

2.2.6 Recruitment of target RNAs in *trans*

One unique advantage of RNA nanostars is their ability to recruit specific target RNA through base pairing. To demonstrate this, we first built a model RNA target that included a single stem–loop domain with a KL complementary to the nanostar KL. This target was successfully colocalized with the condensates (**Fig. 2-6a**), as indicated by the PCC and the partition coefficient (**Fig. 2-6c** and **Fig. 2-53i**). By contrast, we found no colocalization when the correct KL sequence was missing on either the nanostar or the target RNA (**Fig. 2-6b** and **Fig. 2-53d,e**). While successful, this approach requires modification of the target RNA, which may be undesirable. To bypass this constraint, we modified nanostars to carry a dedicated hybridization domain complementary to the target RNA (**Fig. 2-6d)**. This is a sequence-specific recruitment strategy applicable in principle to any RNA transcript, provided that the intermolecular hybridization outcompetes local secondary structures. As a proof of concept, we used an arbitrary 21-nt sequence as the recruitment domain. Colocalization was observed only when this domain matched the target RNA sequence (**Fig. 2-6e,f** and **Fig. 2-53f–h,j**). To quantify colocalization, we provided Manders' overlap coefficients, which assess the fraction of overlapping independent of signal intensities, as well as PCC values, whose low values are because of the low expression levels of target RNA molecules. Although the long hybridization domain slightly reduced condensate formation, probably owing to steric hindrance, recruitment was unaffected, and condensation could be improved by increasing the nanostar-to-target RNA ratio (**Fig. 2-53c**).

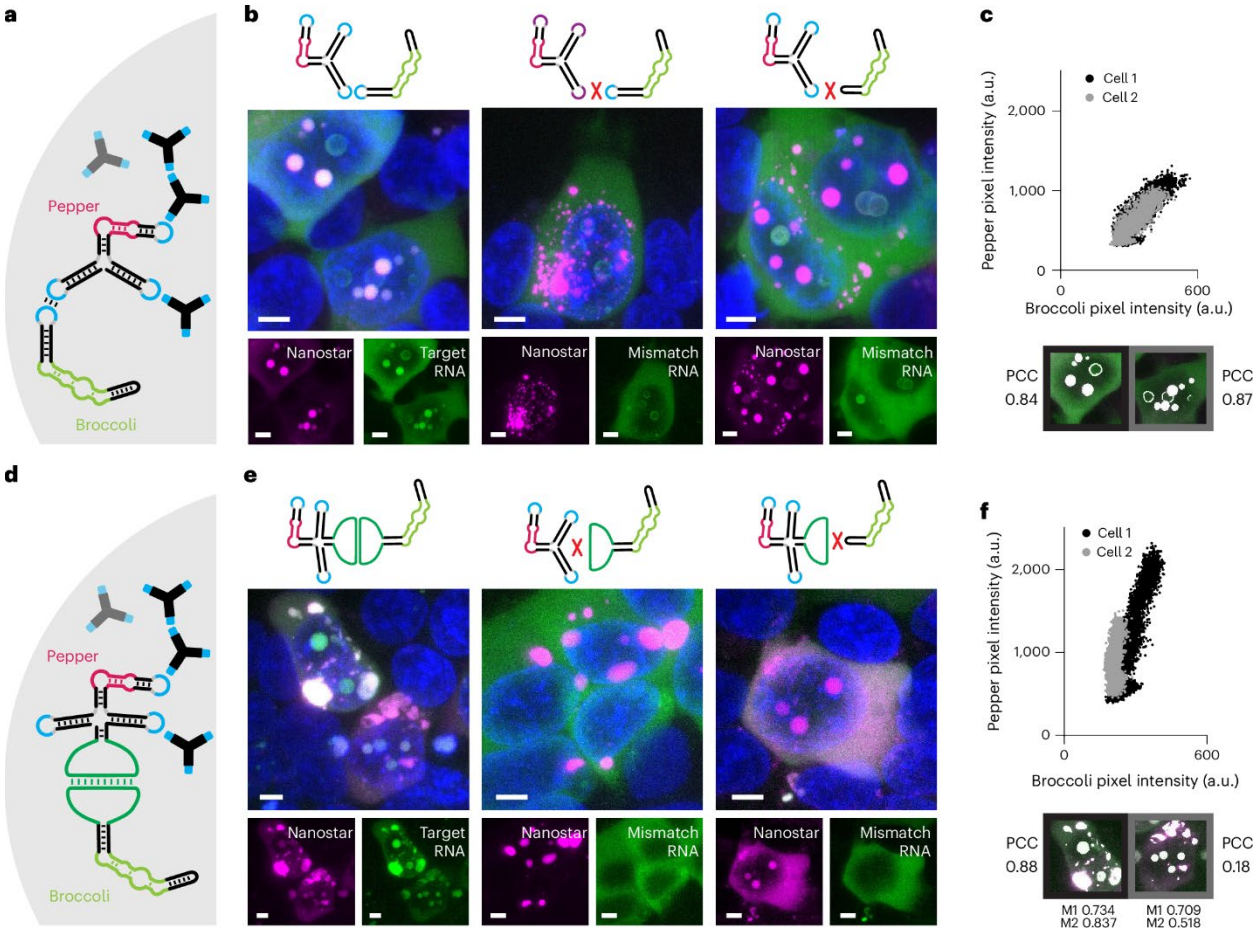

Figure 2-6. RNA nanostar condensates recruit cellular RNA molecules through sequence-specific interactions.

a, A schematic illustrating the recruitment of Broccoli-labelled RNA molecules to condensates formed by Pepper-labelled nanostars through shared KL sequences. **b**, Confocal micrographs showing colocalization only when both the nanostar and target RNA contain matching KL sequences. **c**, Scatter plots of Broccoli and Pepper pixel intensities within the indicated regions of interest, with corresponding PCCs. **d**, A schematic illustrating the recruitment of Broccoli-labelled target RNAs to condensates formed by Pepper-labelled nanostars engineered with a complementary recruitment domain. **e**, Confocal micrographs showing colocalization only when both the nanostar and target RNA contain matching recruitment domains. **f**, Scatter plots of Broccoli and Pepper pixel intensities within the indicated regions of interest, with corresponding PCC values. In cell 2, low target RNA expression reduces signal-to-noise and lowers the PCC despite visible overlap. Manders' overlap coefficients are provided to quantify the

fraction of overlapping signal. Cells were stained with Hoechst (nuclei), DFHBI (Broccoli) and HBC620 (Pepper). Control PCC analyses are shown in Fig. 2-53. All experiments were performed in three independent replicates. Images are confocal z-projections. Scale bars, 5 μm.

2.3 Conclusion

We have demonstrated a simple yet highly programmable strategy to build RNA condensates in living mammalian cells from short ssRNAs that fold into star-shaped motifs. Leveraging advances in DNA and RNA nanotechnology[19,23,27,98–100], our work establishes that sequence-specific RNA interactions can act as a structural and functional driver of condensate formation, enabling precise control of condensate material properties and cellular localization through rational sequence design[5,13,48,101–104].

A major contribution of this study is the demonstration that synthetic RNA condensates can spatially localize small molecules, proteins and other RNAs through sequence design independently of any cellular localization signals and allows tuning of the nuclear-to-cytoplasmic ratio. Because most cellular reactions occur in specific subcellular compartments, the ability to programme condensate localization provides a powerful means to modulate intracellular pathways. Another unique feature of RNA-based condensates is their ability to form discrete, multicomponent compartments solely through rationally designed KL interactions. This capability is difficult to achieve with synthetic protein-based condensates, which typically rely on intrinsically disordered regions that lack the base-pairing programmability of RNA[105]. Previously, recruitment of target RNAs into condensates relied on engineered recognition tags on the target RNA[12,106]. Here, we introduce a more general approach: direct sequence-specific

hybridization between nanostars and target RNA sequences. This strategy eliminates the need for target RNA modification and may be applied to arbitrary transcripts, providing means to control native RNAs and pathways such as rRNA processing and mRNA translation[89,107,108].

Overexpression of structured circular RNAs may contribute to metabolic stress, as suggested by our immunostaining results. This could be improved by inducible expression. Shell-like structures also warrant further investigation: they may originate from weak intermolecular interactions, such as G-quadruplex formation within fluorescent aptamers[109], or from metabolic pathways associated with circular RNAs, as indicated by their interaction with G3BP1 (ref. [92]). Alternatively, they could represent another form of condensate, akin to previously reported anisosomes[93]. With the growing recognition of RNA as a central player in cellular phase separation, we anticipate that future versions of this technology will achieve greater selectivity and adaptability, ultimately enabling the construction of synthetic organelles with tailored and novel biological functions.

2.4 Methods

2.4.1 Sequence design

Nanostars were designed using NUPACK[26] based on published *in vitro* results[79]. For each design, 10 NUPACK trials were run, the one that generated the lowest defect score was selected. Broccoli, Pepper, Mango and MS2 aptamer sequences were taken from the literature[85,87,97,110]. All sequences are listed in a separate Table 2-5 and 2-6.

2.4.2 Design of nanostar stem sequences and inclusion of aptamer domains

The stem sequence used in nanostar variant 15nt-3A-Br (Fig. 2-1 of the manuscript) was adapted from Stewart *et al*. (Stem 1 design)[79]. We used NUPACK scripts to generate the sequence of 10 and 20 nt-long stems de novo, as summarized in Supplementary Note 2-1. The 25 nt-long stem sequence was adapted from Fabrini *et al*[80]. Stem sequences were modified to insert Broccoli and Pepper aptamer as part of one of the arms, assuming that nanostar folding assists with correct aptamer folding. We adapted the length of aptamer-including stems to remain comparable with the other nanostar arms. For 10nt-/15nt-/20nt- long arms, we respectively used 4bp+4bp/6bp+6bp/8bp+8bp long domains to flank aptamers. For the 25nt-arm, 8bp+8bp domains were used to flank aptamers due to limitations in DNA synthesis. The sequence of the arm with aptamers was optimized using the NUPACK script in Supplementary Note 2-2. Because Mango and MS2 aptamers include a functional loop, they cannot be inserted into an arm. For this reason, we included them as an additional arm at the 3' end of their nanostar. We chose the 3' end to prioritize nanostar transcription and folding relative to aptamer folding. Broccoli, Pepper, and Mango aptamers were selected to demonstrate orthogonality because 1) they have non overlapping emission spectra; 2) their fluorescence does not require aptamer dimerization, which would introduce undesired interactions between nanostars. To develop orthogonal nanostars (Fig. 2-4 and 5 of the manuscript), the stem of 15nt-3A-Br was modified to minimize interactions between nanostars. Using a script similar to the one in Supplementary Note 2-1, we generated multiple 15nt-long stems. We selected two presenting the lowest defect scores and minimal interaction with the 15nt-3A-Br nanostar, and we modified them to include Pepper and Mango aptamers.

2.4.3 Design of nanostar kissing loop sequences

All kissing loops are 9 nt long and include a 6 nt interaction sequence flanked by 3 unpaired adenine residues, 2 upstream and 1 downstream of the interaction sequence (5'-AA…A-3'). The wild-type kissing loop (5'-GCGCGC) was adapted from the HIV-1 palindromic kissing loop sequence8. Orthogonal kissing loops 5'-UCGCGA, 5'-GUCGAC, and 5'-GGUACC were taken from Fabrini *et al*. [80] Kissing loops 5'-GUAUAC and 5'-UAUAUA were designed by simply replacing GC pairs with AU pairs. Non-palindromic kissing loops were adapted from the 3sβ set designed by Stewart *et al*[79].

2.4.4 RNA synthesis for *in vitro* characterization

All RNA strands for *in vitro* experiments were transcribed from custom DNA templates synthesized by Integrated DNA Technologies as LabReady resuspension, standard desalt purification. We annealed non-coding DNA templates with a 21-nt complement including the T7 promoter region and a 4 nt sealing domain (5'-GCGC). These templates were annealed in 1X TE/50 mM NaCl from 90°C to RT at -1°C/min at 5 μM for storage and used at 0.01 μM during *in vitro* transcription. RNA strands were transcribed *in vitro* at 37 °C using 7.5% (v/v) T7 polymerase from the AmpliScribe T7-Flash transcription kit (ASF3507, Biosearch Technologies), and transcription buffer prepared in-house: 40 mM of Tris-HCl, 10 mM of NaCl, 30 mM $MgCl_2$, 2 mM spermidine, 7.5 mM each NTP, 10 mM DTT.

2.4.5 Plasmid development

The highly stable nanostar stem-loop domains facilitate polymerase dissociation. As a result, polymerase chain reactions (PCR) of nanostar DNA templates generate products with incorrect lengths and sequences. For this reason, inserts were directly

purchased from Integrated DNA Technologies as two single-stranded, 5’ phosphorylated oligonucleotides containing the sequence of interest, flanked by NotI and SacII restriction sites. The two strands were annealed in 50 mM NaCl and 1x TE buffer using a heat treatment protocol including a 5-minute melt at 90°C, followed by a slow temperature ramp at -1°C/min, and held at 20°C. The resulting products were double-stranded DNA fragments with sticky ends ready for ligation. After annealing, strands were purified with a DNA cleanup kit (NEB T1030). The DNA encoding the nanostar sequences was inserted in the pAV-U6+27-Tornado-Broccoli (Addgene 261587) plasmid. Plasmids were prepared by (1) digestion with NotI-HF (NEB R3189S) (2 µL for 20 µL reactions) at 37°C for 1 hour; (2) purification with the DNA cleanup kit; (3) digestion with SacII (NEB R0157S) (2 µL for 20 µL reactions) at 37°C for 1 hour; and (4) purification with a 0.8% 1x TAE agarose gel to select the product with the correct size. Digested backbones were finally purified using a gel extraction kit (Qiagen 28704). Digested backbone and inserts were ligated at a 1:10 molecular ratio by overnight incubation with T4 DNA ligase (NEB M0202S) at 4°C. Ligated plasmids were transformed into 50 µL DF5Hα competent cells (Thermofisher EC0112 and 18258012) following the manufacturer’s protocol. We then extracted plasmid DNA using a Miniprep kit (Qiagen 27106) following the manufacturer’s protocol. Extracted plasmids were finally sequenced by Eurofins Genomics (whole plasmid sequencing service). The plasmid expressing MCP-mCherry was purchased from Addgene (207668).

2.4.6 Cell culture and maintenance

HEK293T (ATCC® CRL-3216™), HeLa (ATCC® CCL-2™), and U-2 OS (ATCC® HTB-96™) cells were grown in Dulbecco Modified Eagle’s Medium (DMEM), high

glucose, pyruvate (ThermoFisher 11995065) containing 10% Fetal Bovine Serum (FBS) and 100 U/ml Penicillin/Streptomycin (Thermo Fisher) and maintained at 37 °C with 5% CO2 in a humidified incubator. Cells used for imaging were cultured in µ-Slide 8 Well high slides (Ibidi GmbH).

2.4.7 Transfection

Seeding density was adapted across cell types to achieve ~70% confluence at transfection. Three wells were seeded as replicates for each condition tested. Lipofectamine 2000 (ThermoFisher 11668019) was used for transfecting HEK293T cells. FuGene HD (Promega E2311) was used for transfecting HeLa and U-2 OS cells as it demonstrated less cytotoxicity (additional details below).

For experiments involving the expression of multiple nanostars, the total amount of plasmid DNA used in each experiment was kept constant, with an equal proportion of each nanostar variant. For experiments involving the co-delivery of plasmids expressing nanostars and MCP-mCherry, the total amount of plasmid DNA also remained constant. The plasmids encoding nanostars and MCP-mCherry were mixed and delivered in a 9:1 ratio.

Transfection using Lipofectamine 2000

HEK293T cells were seeded at $5*10^5$ cells/mL, 500 µL/well into 24 well plates one day before transfection. Transfection was performed following the manufacturer's protocol, with a 500 ng final plasmid concentration and a 2 µL final Lipofectamine 2000 volume per well. The DNA-lipid complex was incubated with cells for 4-6 hours and then aspirated and changed to complete DMEM as mentioned above. Cells were reseeded into µ-Slide 8 Well high slides (Ibidi GmbH) the following day at $5*10^5$ cells/mL for

imaging. Slides were pre-coated by incubating with 0.001% poly-L-lysine for at least 30 minutes, followed by washing once with PBS before the addition of cells. We incubated reseeded cells overnight and imaged them the next day.

Transfection using FuGene HD

HeLa cells were seeded at 1.5*10^5/mL; U-2 OS cells were seeded at 4*105/mL, 500 µL/well into 24 well plates one day before transfection. Transfection was performed by mixing 1.65 µg of plasmid with OptiMEM to a total volume of 78 µL. The mixture was vortexed for 1-2 s and centrifuged down. Then we added 4.95 µL Fugene HD to the mixture, vortexed for 1 s, centrifuged down, and incubated at room temperature for 15 minutes. For HeLa and U-2 OS cells, a 15 µL mixture was added to each well. Media change was performed the next day before reseeding. Cells were reseeded into 8-well Ibidi slides following the same protocol as HEK293 cells using the seeding density mentioned at the beginning of this paragraph.

2.4.8 Total RNA extraction

Cells were transfected in 24 well plates. We changed the media 24 hours after transfection, and collected cells 48 hours after transfection. For collection, we aspirated media, washed with PBS, and trypsinized the cells. After trypsinization, cells were resuspended in PBS, lysed, and RNA was purified using the Monarch® Total RNA Miniprep Kit (NEB T2010S). RNA concentration was estimated using a Nanodrop 2000c by measuring absorption at 260 nm.

2.4.9 Fluorescence microscopy and live cell imaging

Live cell staining

The culture medium from overnight incubation was aspirated and replaced with fresh medium supplemented with 2 drops of NucBlue Live reagent (Hoechst 33342 nuclear dye, Thermo Fisher R37605) per mL of media, along with the appropriate staining dyes according to experimental conditions. For conditions involving the Broccoli aptamer, we used 40 μM of 3,5-Difluoro-4-hydroxybenzylidene imidazolinone (DFHBI) (Lucerna, 400-5mg); for experiments involving the Pepper aptamer, we supplied 10 nM of (4-((2-hydroxyethyl)(methyl)amino)-benzylidene)-cyanophenylacetonitrile 620 (HBC620) (MedChemExpress, HY-133520). Live cells were then incubated for at least 15 minutes at 37°C before imaging. Cells were imaged in the presence of dyes.

Fixed cell staining and immunostaining

Mouse anti-Coilin (Cajal body colocalization) was purchased from Abcam (ab11822, 1:1900, 1 μg/mL). Mouse anti-SC35 (nuclear speckle colocalization) was purchased from Abcam (ab11826, 1:200, 5 μg/mL). Mouse anti-fibrillarin (nucleolus colocalization) was purchased from Antibodies.com (A85370, 1:200). Mouse anti-G3BP1 (stress granules colocalization) was purchased from Thermo Fisher (66486-1-IG, 1:200, 5 μg/mL). Mouse anti-DCP1A (P body colocalization) was purchased from Novus biological (H00055802-M06, 1:200).

Before fixation, cell culture media were removed and cells were rinsed with PBS (Thermo Fisher 10010023). Cells were then fixed in PBS buffer (Thermo Fisher 14190144) containing 4% paraformaldehyde (Thermo Fisher 043368.9M) for 10 minutes at room temperature, and washed with the PBS buffer three times, each for 5

minutes. Next, we permeabilized cells with 0.5% Triton X-100 (Sigma Aldrich 9002-93-1) in the PBS buffer for 10 minutes and washed them three times. For imaging condensates involving the Mango aptamer, we added PBS supplemented with NucBlue reagent (Thermo Fisher R37605) and 200 nM of TO1-Biotin (TO1-B) (ABM, G955). Cells were incubated in the buffer for 15 minutes before imaging. For experiments involving immunostaining, cells were further blocked using 3% BSA (w/v, Sigma Aldrich 9048-46-8) in the PBS buffer for 1 hour, and washed three times. Then, cells were stained with corresponding primary antibodies diluted to the above-mentioned concentrations with 3% BSA in the PBS buffer and incubated at 4°C overnight. The next day, primary antibodies were removed and cells were washed three times before the addition of secondary antibodies (Thermo Fisher A-21236, 1:1000 in 3% BSA in PBS buffer). We incubated cells in secondary antibodies for 1 hour before removing the buffer and washing them three times with PBS. For the final wash, PBS was supplemented with 40 μM DFHBI and NucBlue reagent. Cells were incubated in the buffer for 15 minutes before imaging.

Microscopy

FRAP and fusion experiments were performed with epifluorescence imaging using a Nikon Eclipse TI-E inverted microscope and a 60x oil immersion objective. Z-stack confocal images were acquired using a Nikon Ti microscope equipped with an NL5+ camera. Images in Figure 2-4D and 4K were captured using a Yokogawa CSU X1 spinning disk confocal on an inverted Zeiss stand. Hoechst (NucBlue staining) signals were detected in the UV channel (Ex 405 nm). Broccoli aptamer fluorescence was measured using the GFP channel (Ex 488 nm). Mango aptamer fluorescence was

measured using the YFP channel (Ex 514 nm). Pepper aptamer, CY3, and mCherry fluorescence was detected using the RFP channel (Ex 561 nm). Finally, Alexa Fluor™ 647-labeled secondary antibody fluorescence was detected using the 647 nm channel (Ex 647 nm).

2.4.10 Image processing

Confocal micrographs in the manuscript figures are max-pixel-intensity Z projections, unless otherwise specified in the figure caption. We chose to use Z projections rather than single-plane images because they provide a more comprehensive view of condensate signals across all planes. Midplane images are provided in the Supplementary Figures.

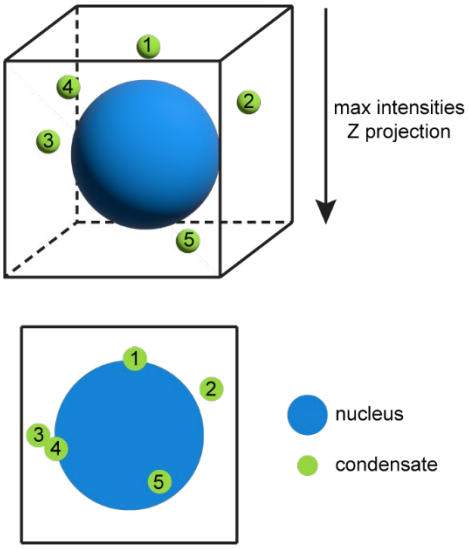

Figure 2-7. Max intensities Z projections distort the volume and localization of objects.

It is well known that Z projections distort the actual volume and localization of objects. For example, condensates in different planes may appear to overlap (as shown for condensates 3 and 4 in the schematic on the right). Condensates located above or below the nucleus, or within the nuclear indentation, may appear to be inside the nucleus itself (as shown for condensates 1 and 5 on the left). These artifacts might

cause confusion about the actual cellular localization of condensates. All confocal scans were processed to obtain careful estimates of condensate location and volume, as explained in the following subsections.

Measuring the volume and number of condensates in the cytoplasm and in the nucleus

Cells expressing condensates were cropped into small regions of interest (ROI). At least 50 expressing cells were selected for each nanostar structure. For each ROI, condensates were segmented using Labkit, a machine learning-based plugin for ImageJ, by manually providing labels followed by a training step9. The plugin generates masks where condensates in the nucleus and in the cytoplasm are classified into different groups, manifested as distinct pixel intensities. The masks were transformed into Imaris files (Imaris 10.1, Oxford Instruments), and reconstructed into 3D surfaces using Imaris (Supplementary Figure S28 and S36). Condensates in the nucleus and in the cytoplasm generated separate surfaces. Any surface object with a volume smaller than 0.015 μm3 (~ two voxels) was considered noise and excluded from our dataset. Adjacent surfaces connected to one object by the software algorithm were manually eliminated. Individual condensates were assigned to different cells manually by comparing reconstruction results and cropped ROIs. Surface volumes were exported for each ROI and pooled into one dataset for each nanostar variant.

Calculating nuclear volume with or without nanostar expression

Nuclear volumes were calculated using the surface tool in Imaris (Oxford Instruments). Before processing, we prepared a cropped ROI when large areas in the field of view lack condensate-expressing cells. Surfaces were generated using the machine learning segmentation tool. A general training algorithm was saved, and the

same training classifier was applied to each image. Once machine learning segmentation is implemented, a watershed algorithm of 8 μm is applied to split touching nuclei. We removed surfaces with a high average intensity (likely apoptotic), near the border of the field of view, and volumes smaller than 450 μm (likely segmentation noise). The thresholds for intensity and volume cutoff were adjusted slightly for each image. Manual cleaning of the dataset was done by removing nuclei cut in the z-axis, apoptotic nuclei, and by splitting any touching nuclei. We removed nuclei stacked on top of each other, a frequent event in HEK293T cells. Touching nuclei were removed when Imaris failed to split touching nuclei due to errors in the cut surface. Multiple touching nuclei, or nuclei with a border difficult to distinguish, were removed as well. Cleaned datasets were further processed to identify two classes of nuclei, either expressing or non-expressing condensates. We examined multiple fields of views in multiple samples, gathering data for at least 50 condensate-expressing cells and hundreds of non-expressing cells for each nanostar structure. The volume of each nucleus was normalized by the average volume of all non-expressing nuclei for every sample group.

Partition coefficients for linked condensates

Linked condensates were detected and segmented using FIJI and Python3 scripts adapted from previous work by Fabrini *et al*[80]. The pipeline included preparing cropped ROI, image enhancement and mask generation, and partition coefficients calculation. ROI were defined from single plane confocal microscopic images with two channels (Em 488 nm and Em 561 nm, corresponding to Broccoli and Pepper channels) acquired with 60x lens and multiple FOVs per sample from three replicates. Cropped ROIs were segmented in FIJI using a macro: for each channel, denoising via a

Gaussian Blur (sigma = 1.5), sliding paraboloid background subtraction (smoothing disabled, radius = 10), contrast enhancement (saturated = 0.35), and finally convert to binary masks using the Li and Otsu masks. Because these two segmentation methods can over- or under-segment, the final partition coefficients were calculated as the average of results generated from both methods. Fluorescence images were analyzed using a Python-based pipeline leveraging libraries such as numpy, pandas, and skimage. For each image, green and red fluorescence channels were normalized to a [0,1] scale, and masks were applied to extract mean fluorescence intensities from regions of interest. In Figure 2-5 we report the quantities I_G^G, I_G^R, I_R^R, and I_R^G, where I_X^Y is the average intensity of channel X within the binary mask of channel Y; G stands for the Green channel and R stands for the Red channel. To calculate these quantities we used two approaches, based on the nature of mixing patterns, partial or complete. For 2 arm linkers, ratios ≥ 1:4:1 were considered as complete mixing; for 4 arm linkers, ratios ≥ 1:2:1 were considered as complete mixing due to doubled linker valency. Discussion about the effect of mixing type selection can be found at Fig 2-52. For partial mixing, non-overlapping regions of the masks were identified by subtracting their intersection (nonoverlapping_mask). For complete mixing, the union of the masks was used (union_mask). Mean fluorescence intensities from these regions for both channels were used to compute overlap strengths, represented as J-values, which quantify the ratio of cross-masked to self-masked intensities. J_R was defined as I_R^G/I_R^R, and J_G was defined as I_G^R/I_G^G. J-values were calculated separately for masks generated by Li and Otsu methods, with the final values averaged between the two.

All partition coefficients were calculated using a Python script (see code availability) as:

$$Partition\ coefficient = \frac{Fluor.density_{condensed}}{Fluor.density_{dilute}}$$

Where $Fluor.density_{condensed}$ were calculated separately for nuclear and cytoplasmic condensates from z-stacked confocal microscopy images by 1) extracting background fluorescence as the minimal voxel intensity across the field of view, 2) masking condensates region, 3) subtracting background fluorescence for all voxels, 4) summing all non-zero voxel intensities. Then:

$$Fluor.density_{dilute} = \frac{\sum background\ subtracted\ voxel\ intensities}{number\ of\ voxels}$$

$Fluor.density_{dilute}$ were calculated by 1) extracting background fluorescence as the minimal voxel intensity across the field of view, 2) cropping 10*10*10 voxels separately from the dilute phases within the nucleus and cytoplasm, 3) subtracting background fluorescence for all voxels, and finally computing:

$$Fluor.density_{dilute} = mean\ Fluor.intensity$$

Pearson correlation coefficient (PCC) and Manders' overlap coefficient

All PCC were calculated using ImageJ. Masks of nuclear or cytoplasmic condensates were generated using Labkit and converted to ROIs. Then correlations within the ROI between the two channels were calculated using the plugin Colocalization Finder.

As pointed out by Dunn *et al.*[111], Pearson correlation coefficients "depend upon a simple linear relationship, they will be depressed if measured over a field of cells with heterogeneous expression or uptake of the target molecules, thus under-representing

the degree of correlation". For this reason, it is recommended to use a region of interest (ROI) for PCC calculation. In our experiment, we saw distinct linear relationships between cytoplasmic and nuclear condensates due to different preferences of cellular localization due to the Broccoli or Pepper tagging. Nuclear condensates turn to have stronger Broccoli signals, while cytoplasmic condensates turn to have stronger Pepper signals (Figure 2-4A, bottom). These differences can also be seen on scatter plots shown in Figure 2-4B, bottom.

In Fig. 2-5F, cell 2 expressed a low level of target RNA molecule, and the low signal-to-noise ratio resulted in low PCC value although the colocalization is visually apparent. To resolve this, we include Manders' overlap coefficients as they are independent of the intensities of each channel, focusing instead on the proportional overlap of signals where both are present. M1 measures the fraction of the first channel's intensity that overlaps with the second, and M2 measures the fraction of the second channel's intensity that overlaps with the first. The thresholding and Manders coefficient calculation was done by the JaCoP plugin (v2.1.4) on ImageJ.

2.4.11 Fluorescence recovery after photobleaching (FRAP)

FRAP experiments were performed using a Nikon Eclipse TI-E inverted microscope with a temperature control unit. Temperatures were maintained at 37 °C for all experiments. For *in vitro* experiments, RNA strands were transcribed at 37°C using 7.5% (v/v) T7 polymerase from the AmpliScribe T7-Flash transcription kit (ASF3507, Biosearch Technologies), and a customized transcription buffer: 40mM Tris-HCl, 10 mM NaCl, 30 mM $MgCl_2$, 2 mM spermidine, 7.5 mM each NTP, 10 mM DTT. We supplied 1% CY3-labeled UTP (ENZ-42505). After three hours, transcription samples were

diluted 10 times using our customized transcription buffer, to reduce background fluorescence caused by excess CY3-UTP. Samples for FRAPing Broccoli aptamer were diluted in transcription buffer with DFHBI to a final concentration of 40 μM. *In vitro* samples were loaded into a house-made chamber and sealed with epoxy (Gorilla, 5-minute set) for imaging. For *in vivo* experiments, cells were stained using the protocol described in section 2.4.6.

Condensates were bleached with a 488 nm laser for 200 ms. For *in vitro* samples, imaging was captured once before bleaching and every 5 seconds for 10 min after bleaching. For *in vivo* samples, imaging was captured once before bleaching and every 200 ms for 2 min after bleaching or every 1.5 s for 5 min after bleaching. Images were analyzed by extracting time-dependent average intensities within the bleached area and unbleached area. Normalization was performed to correct photobleaching caused by repetitive imaging using the equation below:

$$\frac{I_{bleach,t}/I_{bleach,max}}{I_{unbleach,t}/I_{unbleach,max}}$$

where I denotes the mean pixel intensity in the bleached or unbleached area, t denotes the time point, max denotes the highest pixel intensity within the area among all time points. FRAP plots report the mean ± error bar from N=3 (one region of interest from one replicate was quantified, total three replicates). Mean fluorescence intensities are fitted to an exponential curve:

$$Y = Y_0 + (Y_\infty - Y_0) * \left(1 - e^{-\frac{t}{\tau}}\right)$$

2.4.12 Time-dependent coalescence analysis

For *in vitro* experiments, RNA strands were transcribed, labeled with 1% CY3-UTP, diluted 10 times with transcription buffer, and sealed in a chamber with epoxy, following the same protocol as FRAP experiments. Samples were imaged every 5 minutes for the first 4 hours, then every 20 minutes until 10 hours. We monitored condensate fusion events using a Nikon Eclipse TI-E inverted microscope with a temperature control unit. The temperature was maintained at 37°C for all experiments.

For *in vivo* fusion experiments, we imaged cells (in media supplemented with 40 μM DFHBI and 2 drops/mL NucBlue) every 5 minutes for 60 minutes under the confocal microscope. The temperature was maintained at 37°C. Fusion events were identified manually. Data processing was performed using a script in Python3 described in our previous work1. To summarize, each fusion event was identified manually and segmented using Otsu thresholding. The binary mask was then labeled to extract the centroid position, major and minor axis lengths, and orientation. Best-fit-ellipses were generated based on the extracted data. The aspect ratio was calculated as the major-to-minor axes ratio and used for curve fitting. The time constant was calculated by fitting the Aspect Ratio vs time profiles with an exponential decay with the formula

$$1 + Ae^{(-t/\tau)}$$

2.4.13 Flow cytometry

Flow cytometry experiments were performed using a BD FACSAria flow cytometer. Cells were transfected in 24 well plates, as described in section 1.6. We changed the media 24 hours after transfection, and collected cells 48 hours after transfection. For collection, we aspirated media, washed with PBS, and trypsinized the cells. After trypsinization, cells were resuspended in PBS supplemented with 10% FBS

and dyes and filtered through the 40μm cell strainer (Fisher Scientific Cat.# 22363547) for flow cytometry. Hoechst was detected using a laser with Ex 405 nm and a 450/50 nm filter; DFHBI was detected using a laser with Ex 488 nm and a 530/30 nm filter.

2.4.14 qPCR

Reverse transcription was carried out with equal amounts of RNA using the Protoscript II First Strand cDNA Synthesis Kit and random hexamers (New England Biolabs). RT-qPCR was then performed using ten-fold diluted cDNA and the Luna Universal qPCR Master Mix (New England Biolabs) in the CFX Real-Time PCR system (Bio-Rad), courtesy of the UCLA Virology Core. qPCR conditions used as previously described[112,113]. Target transcript levels were determined by normalizing the CT (cycle threshold) value of the target transcript to that of the housekeeping gene RPS11 transcript. Fold change was calculated using this normalized value relative to lipofectamine control expression levels. For RT-qPCR primers, see **Table 2-4**.

2.4.15 PAGE gel electrophoresis

Gel premix was prepared by adding 42 g of urea to nanopure water, the mixture was then heated until the urea completely dissolved. This mixture was allowed to cool to room temperature, and then a 40% (v/v) 19:1 acrylamide/bis-acrylamide solution was added in the appropriate volume for the desired percentage (final volume 100 mL). To start polymerization, 8 mL of pre-mix was added in appropriate ratios with TBE and nanopure water, ammonium persulfate (APS), and tetramethylethylenediamine (TEMED). Gels were cast in 8 × 8 cm, 1 mm thick disposable mini gel cassettes (Thermo Scientific, #NC2010) and allowed to polymerize for 30 minutes before electrophoresis. After curing, the gel was pre-run in a 1X TBE buffer for 30 minutes. Wells were washed

carefully to remove excessive urea. Samples and low-range ssRNA ladder (NEB, N0364S) were prepared by mixing individual strands with denaturing RNA loading dye (NEB, B0363S), then heated at 70 °C for 10 minutes and immediately placed on ice. Due to the low expression of exogenous RNA in mammalian cells, 5 µg of total RNA extraction was loaded onto each well. Gels were run at room temperature at 100 V in 1X TBE unless otherwise noted. After electrophoresis, the gels were washed three times, each for 5 minutes, with nanopure water, then stained with DFHBI-1T staining buffer (10µM DFHBI-1T, 40mM HEPES, 100mM KCl, and 1mM $MgCl_2$) for 15 minutes. After staining, gels were imaged using the Bio-Rad Gel Imaging Systems. Then, gels were washed three times, each for 5 minutes again to remove the DFHBI-1T and stained in 1xSYBR Gold Nucleic Acid Gel Stain for 15 minutes and imaged again.

2.4.16 Data availability

All the data that support the findings of this study are available within the article and its Supplementary Information. Additional data are available via Zenodo at https://doi.org/10.5281/zenodo.17823527. Source data are provided with this paper.

2.4.17 Code Availability

The data analysis code used in this article is available via GitHub at https://github.com/FrancoLabUCLA/Li-2025-RNA-condensate.

2.5 References

1. Shin, Y. & Brangwynne, C. P. Liquid phase condensation in cell physiology and disease. *Science* **357**, eaaf4382 (2017).

2. Hyman, A. A., Weber, C. A. & Jülicher, F. Liquid-liquid phase separation in biology. *Annu. Rev. Cell Dev. Biol.* **30**, 39–58 (2014).

3. Alberti, S. Phase separation in biology. *Curr. Biol.* **27**, R1097–R1102 (2017).

4. Kato, M., Zhou, X. & McKnight, S. L. How do protein domains of low sequence complexity work? *RNA* **28**, 3–15 (2022).

5. Rhine, K., Vidaurre, V. & Myong, S. RNA Droplets. *Annu. Rev. Biophys.* **49**, 247–265 (2020).

6. Bevilacqua, P. C., Williams, A. M., Chou, H.-L. & Assmann, S. M. RNA multimerization as an organizing force for liquid-liquid phase separation. *RNA* **28**, 16–26 (2022).

7. Courchaine, E. M., Lu, A. & Neugebauer, K. M. Droplet organelles? *EMBO J.* **35**, 1603–1612 (2016).

8. Hirose, T., Ninomiya, K., Nakagawa, S. & Yamazaki, T. A guide to membraneless organelles and their various roles in gene regulation. *Nat. Rev. Mol. Cell Biol.* **24**, 288–304 (2023).

9. Alberti, S. & Hyman, A. A. Biomolecular condensates at the nexus of cellular stress, protein aggregation disease and ageing. *Nat. Rev. Mol. Cell Biol.* **22**, 196–213 (2021).

10. Alberti, S. & Dormann, D. Liquid-liquid phase separation in disease. *Annu. Rev. Genet.* **53**, 171–194 (2019).

11. Schuster, B. S. & others. Controllable protein phase separation and modular recruitment to form responsive membraneless organelles. *Nat. Commun.* **9**, 2985 (2018).

12. Reinkemeier, C. D., Girona, G. E. & Lemke, E. A. Designer membraneless organelles enable codon reassignment of selected mRNAs in eukaryotes. *Science* **363**, eaaw2644 (2019).

13. Dai, Y. & others. Programmable synthetic biomolecular condensates for cellular control. *Nat. Chem. Biol.* **19**, 518–528 (2023).

14. van der Lee, R. & others. Classification of intrinsically disordered regions and proteins. *Chem. Rev.* **114**, 6589–6631 (2014).

15. Jain, A. & Vale, R. D. RNA phase transitions in repeat expansion disorders. *Nature* **546**, 243–247 (2017).

16. Guo, H. & others. Spatial engineering of E. coli with addressable phase-separated RNAs. *Cell* **185**, 3823-3837.e23 (2022).

17. Sato, Y., Sakamoto, T. & Takinoue, M. Sequence-based engineering of dynamic functions of micrometer-sized DNA droplets. *Sci. Adv.* **6**, eaba3471 (2020).

18. Biffi, S. & others. Phase behavior and critical activated dynamics of limited-valence DNA nanostars. *Proc. Natl. Acad. Sci. U. S. A.* **110**, 15633–15637 (2013).

19. Jeon, B.-J., Nguyen, D. T. & Saleh, O. A. Sequence-Controlled adhesion and microemulsification in a two-phase system of DNA liquid droplets. *J. Phys. Chem. B* **124**, 8888–8895 (2020).

20. Gong, J., Tsumura, N. & Sato, Y. Computational DNA droplets recognizing miRNA sequence inputs based on liquid-liquid phase separation. *Adv. Funct. Mater.* **32**, 2270206 (2022).

21. Chworos, A. & others. Building programmable jigsaw puzzles with RNA. *Science* **306**, 2068–2072 (2004).

22. Guo, P. The emerging field of RNA nanotechnology. *Nat. Nanotechnol.* **5**, 833–842 (2010).

23. Conrad, N., Chang, G., Fygenson, D. K. & Saleh, O. A. Emulsion imaging of a DNA nanostar condensate phase diagram reveals valence and electrostatic effects. *J. Chem. Phys.* **157**, 234203 (2022).

24. McRae, E. K. S. & others. Structure, folding and flexibility of co-transcriptional RNA origami. *Nat. Nanotechnol.* **18**, 808–817 (2023).

25. Fabrini, G. & others. Co-transcriptional production of programmable RNA condensates and synthetic organelles. *bioRxiv* https://doi.org/10.1101/2023.10.06.561174 (2024) doi:10.1101/2023.10.06.561174.

26. Zadeh, J. N. & others. NUPACK: analysis and design of nucleic acid systems. *J. Comput. Chem.* **32**, 170–173 (2011).

27. Nguyen, D. T. & Saleh, O. A. Tuning phase and aging of DNA hydrogels through molecular design. *Soft Matter* **13**, 5421–5427 (2017).

28. Xiao, C.-D., Ishizuka, T. & Xu, Y. Antiparallel RNA G-quadruplex formed by human telomere RNA containing 8-bromoguanosine. *Sci. Rep.* **7**, 6695 (2017).

29. Cheong, C. & Moore, P. B. Solution structure of an unusually stable RNA tetraplex containing G- and U-quartet structures. *Biochemistry* **31**, 8406–8414 (1992).

30. Gu, J., Wang, J. & Leszczynski, J. Hydrogen bonding in 5-bromouracil-adenine-5-bromouracil-adenine (T+AT+A) tetrads. *J. Phys. Chem. B* **108**, 9277–9286 (2004).

31. Falkenberg, C. V., Blinov, M. L. & Loew, L. M. Pleomorphic ensembles: formation of large clusters composed of weakly interacting multivalent molecules. *Biophys. J.* **105**, 2451–2460 (2013).

32. Levitz, P. Off-lattice reconstruction of porous media: critical evaluation, geometrical confinement and molecular transport. *Adv. Colloid Interface Sci.* **76–77**, 71–106 (1998).

33. Levitz, P. Toolbox for 3D imaging and modeling of porous media: relationship with transport properties. *Cem. Concr. Res.* **37**, 351–359 (2007).

34. Testard, V., Berthier, L. & Kob, W. Influence of the glass transition on the liquid-gas spinodal decomposition. *Phys. Rev. Lett.* **106**, 125702 (2011).

35. Di Michele, L. & others. Multistep kinetic self-assembly of DNA-coated colloids. *Nat. Commun.* **4**, 2007 (2013).

36. Clever, J. L., Wong, M. L. & Parslow, T. G. Requirements for kissing-loop-mediated dimerization of human immunodeficiency virus RNA. *J. Virol.* **70**, 5902–5908 (1996).

37. Agarwal, S., Osmanovic, D., Klocke, M. A. & Franco, E. The growth rate of DNA condensate droplets increases with the size of participating subunits. *ACS Nano* **16**, 11842–11851 (2022).

38. Zhang, F. & others. Function of hexameric RNA in packaging of bacteriophage φ29 DNA in vitro. *Mol. Cell* **2**, 141–147 (1998).

39. Stoev, I. D. & others. On the role of flexibility in linker-mediated DNA hydrogels. *Soft Matter* **16**, 990–1001 (2020).

40. Brangwynne, C. P. & others. Germline P granules are liquid droplets that localize by controlled dissolution/condensation. *Science* **324**, 1729–1732 (2009).

41. Brangwynne, C. P., Mitchison, T. J. & Hyman, A. A. Active liquid-like behavior of nucleoli determines their size and shape in Xenopus laevis oocytes. *Proc. Natl. Acad. Sci. U. S. A.* **108**, 4334–4339 (2011).

42. Elbaum-Garfinkle, S. & others. The disordered P granule protein LAF-1 drives phase separation into droplets with tunable viscosity and dynamics. *Proc. Natl. Acad. Sci. U. S. A.* **112**, 7189–7194 (2015).

43. Alshareedah, I. & others. Interplay between short-range attraction and long-range repulsion controls reentrant liquid condensation of ribonucleoprotein-RNA complexes. *J. Am. Chem. Soc.* **141**, 14593–14602 (2019).

44. Jeon, B.-J. & others. Salt-dependent properties of a coacervate-like, self-assembled DNA liquid. *Soft Matter* **14**, 7009–7015 (2018).

45. Dey, S. & others. DNA origami. *Nat. Rev. Methods Primer* **1**, 1–24 (2021).

46. Wadsworth, G. M. & others. RNAs undergo phase transitions with lower critical solution temperatures. *Nat. Chem.* **15**, 1693–1704 (2023).

47. Rossi-Gendron, C. & others. Isothermal self-assembly of multi-component and evolutive DNA nanostructures. *Nat. Nanotechnol.* https://doi.org/10.1038/s41565-023-01468-2 (2023) doi:10.1038/s41565-023-01468-2.

48. Poudyal, R. R., Sieg, J. P., Portz, B., Keating, C. D. & Bevilacqua, P. C. RNA sequence and structure control assembly and function of RNA condensates. *RNA* **27**, 1589–1601 (2021).

49. Song, W. & others. Imaging RNA polymerase III transcription using a photostable RNA-fluorophore complex. *Nat. Chem. Biol.* **13**, 1187–1194 (2017).

50. Filonov, G. S., Song, W. & Jaffrey, S. R. Spectral tuning by a single nucleotide controls the fluorescence properties of a fluorogenic aptamer. *Biochemistry* **58**, 1560–1564 (2019).

51. Leppek, K. & Stoecklin, G. An optimized streptavidin-binding RNA aptamer for purification of ribonucleoprotein complexes identifies novel ARE-binding proteins. *Nucleic Acids Res.* **42**, e13 (2014).

52. Austin, R. J., Xia, T., Ren, J., Takahashi, T. T. & Roberts, R. W. Differential modes of recognition in N peptide-boxB complexes. *Biochemistry* **42**, 14957–14967 (2003).

53. Yamaoki, Y., Nagata, T., Mashima, T. & Katahira, M. Development of an RNA aptamer that acquires binding capacity against HIV-1 Tat protein via G-quadruplex formation in response to potassium ions. *Chem. Commun.* **53**, 7056–7059 (2017).

54. Dundas, C. M., Demonte, D. & Park, S. Streptavidin-biotin technology: improvements and innovations in chemical and biological applications. *Appl. Microbiol. Biotechnol.* **97**, 9343–9353 (2013).

55. Ma, H. & others. Multiplexed labeling of genomic loci with dCas9 and engineered sgRNAs using CRISPRainbow. *Nat. Biotechnol.* **34**, 528–530 (2016).

56. Rizzuti, M., Nizzardo, M., Zanetta, C., Ramirez, A. & Corti, S. Therapeutic applications of the cell-penetrating HIV-1 Tat peptide. *Drug Discov. Today* **20**, 76–85 (2015).

57. Lai, D., Proctor, J. R. & Meyer, I. M. On the importance of cotranscriptional RNA structure formation. *RNA* **19**, 1461–1473 (2013).

58. Milburn, S. C., Goldrick, M. & Winkler, M. Compositions and methods for increasing the yields of in vitro RNA transcription and other polynucleotide synthetic reactions. (1993).

59. Shimizu, Y. & others. Cell-free translation reconstituted with purified components. *Nat. Biotechnol.* **19**, 751–755 (2001).

60. Banani, S. F., Lee, H. O., Hyman, A. A. & Rosen, M. K. Biomolecular condensates: organizers of cellular biochemistry. *Nat. Rev. Mol. Cell Biol.* **18**, 285–298 (2017).

61. Guo, P. & Afonin, K. A. *RNA Nanotechnology and Therapeutics*. (CRC Press, 2022).

62. Boeynaems, S. & others. Spontaneous driving forces give rise to protein-RNA condensates with coexisting phases and complex material properties. *Proc. Natl. Acad. Sci.* **116**, 7889–7898 (2019).

63. Cakmak, F. P., Choi, S., Meyer, M. O., Bevilacqua, P. C. & Keating, C. D. Prebiotically-relevant low polyion multivalency can improve functionality of membraneless compartments. *Nat. Commun.* **11**, 5949 (2020).

64. Choi, S., Meyer, M. O., Bevilacqua, P. C. & Keating, C. D. Phase-specific RNA accumulation and duplex thermodynamics in multiphase coacervate models for membraneless organelles. *Nat. Chem.* **14**, 1110–1117 (2022).

65. Huang, Z., Kangovi, G. N., Wen, W., Lee, S. & Niu, L. An RNA aptamer capable of forming a hydrogel by self-assembly. *Biomacromolecules* **18**, 2056–2063 (2017).

66. Xue, Z. & others. Targeted RNA condensation in living cells via genetically encodable triplet repeat tags. *Nucleic Acids Res.* **51**, 8337–8347 (2023).

67. Wu, J. & others. Self-assembly of intracellular multivalent RNA complexes using dimeric corn and beetroot aptamers. *J. Am. Chem. Soc.* **144**, 5471–5477 (2022).

68. Locatelli, E., Handle, P. H., Likos, C. N., Sciortino, F. & Rovigatti, L. Condensation and demixing in solutions of DNA nanostars and their mixtures. *ACS Nano* **11**, 2094–2102 (2017).

69. Xing, Z., Ness, C., Frenkel, D. & Eiser, E. Structural and linear elastic properties of DNA hydrogels by coarse-grained simulation. *Macromolecules* **52**, 504–512 (2019).

70. Tao, J. & Frankel, A. D. Specific binding of arginine to TAR RNA. *Proc. Natl. Acad. Sci. U. S. A.* **89**, 2723–2726 (1992).

71. Geary, C., Grossi, G., McRae, E. K. S., Rothemund, P. W. K. & Andersen, E. S. RNA origami design tools enable cotranscriptional folding of kilobase-sized nanoscaffolds. *Nat. Chem.* **13**, 549–558 (2021).

72. Tan, R. & Frankel, A. D. Structural variety of arginine-rich RNA-binding peptides. *Proc. Natl. Acad. Sci. U. S. A.* **92**, 5282–5286 (1995).

73. Yamamoto, R. & others. A novel RNA motif that binds efficiently and specifically to the Ttat protein of HIV and inhibits the trans-activation by Tat of transcription in vitro and in vivo. *Genes Cells* **5**, 371–388 (2000).

74. Linear Stack Alignment with SIFT. (2012).

75. Dzuricky, M., Rogers, B. A., Shahid, A., Cremer, P. S. & Chilkoti, A. De novo engineering of intracellular condensates using artificial disordered proteins. *Nat. Chem.* **12**, 814–825 (2020).

76. Ji, R. *et al.* RNA Condensate as a Versatile Platform for Improving Fluorogenic RNA Aptamer Properties and Cell Imaging. *J. Am. Chem. Soc.* **146**, 4402–4411 (2024).

77. Banani, S. F. & others. Compositional control of phase-separated cellular bodies. *Cell* **166**, 651–663 (2016).

78. Li, P. & others. Phase transitions in the assembly of multivalent signalling proteins. *Nature* **483**, 336–340 (2012).

79. Stewart, J. M. *et al.* Modular RNA motifs for orthogonal phase separated compartments. *Nat. Commun.* **15**, 6244 (2024).

80. Fabrini, G. *et al.* Co-transcriptional production of programmable RNA condensates and synthetic organelles. *Nat. Nanotechnol.* **19**, 1665–1673 (2024).

81. Litke, J. L. & Jaffrey, S. R. Highly efficient expression of circular RNA aptamers in cells using autocatalytic transcripts. *Nat. Biotechnol.* **37**, 667–675 (2019).

82. Tan, E., Chin, C. S. H., Lim, Z. F. S. & Ng, S. K. HEK293 Cell Line as a Platform to Produce Recombinant Proteins and Viral Vectors. *Front. Bioeng. Biotechnol.* **9**, 796991 (2021).

83. DuBridge, R. B. & others. Analysis of mutation in human cells by using an Epstein-Barr virus shuttle system. *Mol. Cell. Biol.* https://doi.org/10.1128/mcb.7.1.379-387.1987 (1987) doi:10.1128/mcb.7.1.379-387.1987.

84. Bereiter, R. & others. Engineering covalent small molecule-RNA complexes in living cells. *Nat. Chem. Biol.* https://doi.org/10.1038/s41589-024-01801-3 (2025) doi:10.1038/s41589-024-01801-3.

85. Johansson, H. E., Liljas, L. & Uhlenbeck, O. C. RNA recognition by the MS2 phage coat protein. *Semin. Virol.* **8**, 176–185 (1997).

86. Li, X., Wu, J. & Jaffrey, S. R. Engineering fluorophore recycling in a fluorogenic RNA aptamer. *Angew. Chem. Int. Ed.* **133**, 24355–24363 (2021).

87. Chen, X. & others. Visualizing RNA dynamics in live cells with bright and stable fluorescent RNAs. *Nat. Biotechnol.* **37**, 1287–1293 (2019).

88. Molliex, A. & others. Phase separation by low complexity domains promotes stress granule assembly and drives pathological fibrillization. *Cell* **163**, 123–133 (2015).

89. Feric, M. & others. Coexisting liquid phases underlie nucleolar subcompartments. *Cell* **165**, 1686–1697 (2016).

90. Parker, D. M., Tauber, D. & Parker, R. G3BP1 promotes intermolecular RNA-RNA interactions during RNA condensation. *Mol. Cell* **85**, 571–584 (2025).

91. Zhou, W.-Y. & others. Circular RNA: metabolism, functions and interactions with proteins. *Mol. Cancer* **19**, 172 (2020).

92. Fischer, J. W., Busa, V. F., Shao, Y. & Leung, A. K. L. Structure-mediated RNA decay by UPF1 and G3BP1. *Mol. Cell* **78**, 70–84 (2020).

93. Yu, H. & others. HSP70 chaperones RNA-free TDP-43 into anisotropic intranuclear liquid spherical shells. *Science* **371**, eabb4309 (2021).

94. Timney, B. L. & others. Simple rules for passive diffusion through the nuclear pore complex. *J. Cell Biol.* **215**, 57–76 (2016).

95. Arzt, M. & others. LABKIT: labeling and segmentation toolkit for big image data. *Front. Comput. Sci.* **4**, 777728 (2022).

96. Lee, D. S. W. & others. Size distributions of intracellular condensates reflect competition between coalescence and nucleation. *Nat. Phys.* **19**, 586–596 (2023).

97. Cawte, A. D., Unrau, P. J. & Rueda, D. S. Live cell imaging of single RNA molecules with fluorogenic Mango II arrays. *Nat. Commun.* **11**, 1283 (2020).

98. Udono, H. & others. Programmable computational RNA droplets assembled via kissing-loop interaction. *ACS Nano* **18**, 15477–15486 (2024).

99. Agarwal, S., Osmanovic, D., Dizani, M., Klocke, M. & Franco, E. Dynamic control of DNA condensation. *Nat. Commun.* **15**, 1915 (2024).

100. Malouf, L. & others. Sculpting DNA-based synthetic cells through phase separation and phase-targeted activity. *Chem* https://doi.org/10.1016/j.chempr.2023.10.004 (2023) doi:10.1016/j.chempr.2023.10.004.

101. Roden, C. & Gladfelter, A. S. RNA contributions to the form and function of biomolecular condensates. *Nat. Rev. Mol. Cell Biol.* **22**, 183–195 (2021).

102. Garcia-Jove Navarro, M. & others. RNA is a critical element for the sizing and the composition of phase-separated RNA-protein condensates. *Nat. Commun.* **10**, 3230 (2019).

103. Bose, M., Rankovic, B., Mahamid, J. & Ephrussi, A. An architectural role of specific RNA-RNA interactions in oskar granules. *Nat. Cell Biol.* **26**, 1934–1942 (2024).

104. Langdon, E. M. & others. mRNA structure determines specificity of a polyQ-driven phase separation. *Science* **360**, 922–927 (2018).

105. Welles, R. M. & others. Determinants that enable disordered protein assembly into discrete condensed phases. *Nat. Chem.* **16**, 1062–1072 (2024).

106. Kim, T. H. & others. Phospho-dependent phase separation of FMRP and CAPRIN1 recapitulates regulation of translation and deadenylation. *Science* **365**, 825–829 (2019).

107. Dai, Y., You, L. & Chilkoti, A. Engineering synthetic biomolecular condensates. *Nat. Rev. Bioeng.* **1**, 466–480 (2023).

108. Kim, J. & Franco, E. RNA nanotechnology in synthetic biology. *Curr. Opin. Biotechnol.* **63**, 135–141 (2020).

109. Rostain, W. Engineering of RNA sensors and actuators in living cells. (University of Warwick, 2017).

110. Filonov, G. S., Moon, J. D., Svensen, N. & Jaffrey, S. R. Broccoli: rapid selection of an RNA mimic of green fluorescent protein by fluorescence-based selection and directed evolution. *J. Am. Chem. Soc.* **136**, 16299–16308 (2014).

111. Dunn, K. W., Kamocka, M. M. & McDonald, J. H. A practical guide to evaluating colocalization in biological microscopy. *Am. J. Physiol.-Cell Physiol.* **300**, C723–C742 (2011).

112. Yang, E. *et al.* Elucidation of TRIM25 ubiquitination targets involved in diverse cellular and antiviral processes. *PLOS Pathog.* **18**, e1010743 (2022).

113. Huang, S. *et al.* Positive selection analyses identify a single WWE domain residue that shapes ZAP into a more potent restriction factor against alphaviruses. *PLOS Pathog.* **20**, e1011836 (2024).

2.6 Supplementary Information

2.6.1 Supplementary Note

SUPPLEMENTARY NOTE 1

NUPACK script for 20nt-3WT stem sequence design. A similar script was used for the 10 nt long stem designs.

---

material = rna1999

temperature = 37

trials = 10

structure NS= U1 D20 U9 U2 D20 U9 U2 D20 U9

domain arm1= N20AAGCGCGCAN20AA

domain arm2= N20AAGCGCGCAN20AA

domain arm3= N20AAGCGCGCAN20

NS.seq = arm1 arm2 arm3

prevent = AAAA, CCCC, GGGG, UUUU, KKKKKK, MMMMMM, RRRRRR, SSSSSS, WWWWWW, YYYYYY

SUPPLEMENTARY NOTE 2

NUPACK Script for 15nt-3A-Br stem sequence optimization

—----------

material = rna1999

temperature = 37

trials = 10

DU+ notation

structure NS= U41 D6 (U12 D6 (U9) U17) U2 U39

Broccoli aptamer sequence underlined

domain arm1= GCGAGAGCGCUGCCCAAUCGCGAAGGGCAGCGCUCUCGCAA

domain arm2=
N6ACGGUCGGGUCCN6AAUCGCGAAN6GUCGAGUAGAGUGUGGGN6AA

domain arm3= GCGUUCACACUGACCAAUCGCGAAGGUCAGUGUGAACGC

NS.seq = arm1 arm2 arm3

prevent = AAAA, CCCC, GGGG, UUUU, KKKKKK, MMMMMM, RRRRRR, SSSSSS, WWWWWW, YYYYYY

2.6.2 Supplementary Figures

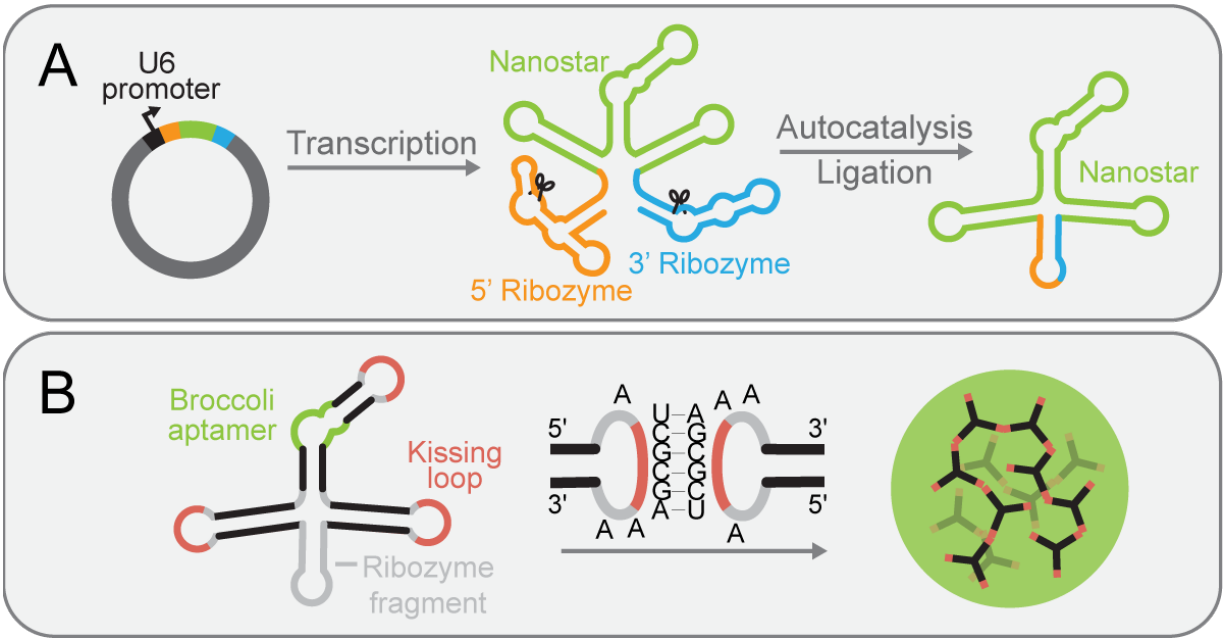

Figure 2-8. Autocatalytic circularization of RNA nanostar and condensate formation.

A, We adopted an expression system in which each nanostar sequence (in green) is flanked by 5'- (in orange) and 3'- (in blue) self-cleaving ribozymes designed by Litke *et al*. Once transcribed, ribozymes autocatalyse and generate functional groups on the new RNA ends. The RNA molecule then becomes a substrate for an endogenous RNA ligase, and becomes circularized before ligation. **B**, After endogenous circularization an RNA nanostar includes three stems (in black), three identical and self-complementary kissing loops (in orange), a ribozyme fragment (in gray, at the bottom), and other adenine spacers (in gray). Phase separation is induced by inter-molecular hybridization between kissing loops.

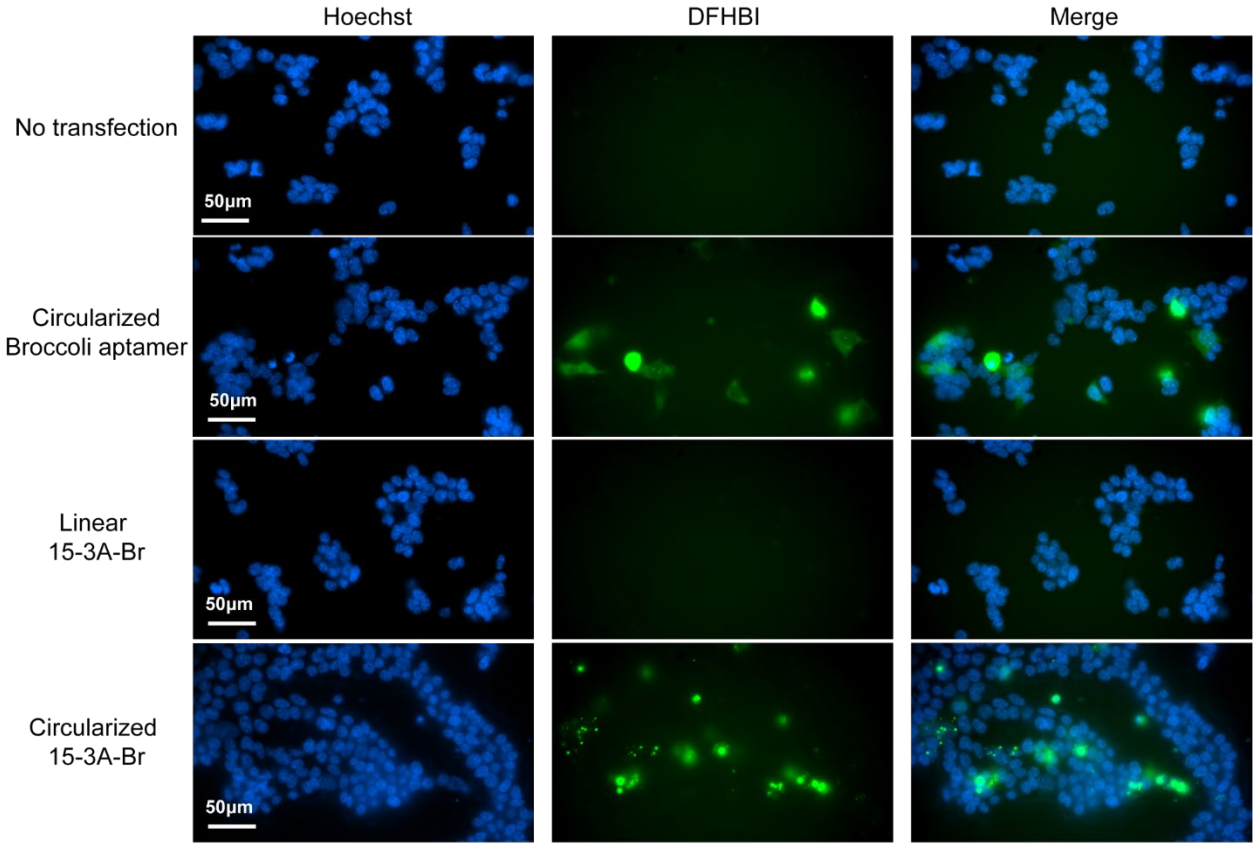

Figure 2-9. Circularization significantly enhances RNA accumulation.

Representative images showing fluorescence from HEK293T cells with no transfection, transfected with plasmids expressing circular Broccoli, linear, or circularized nanostars presenting three 15 nucleotide arms carrying the Broccoli aptamer (15nt-3A-Br). Linear 15nt-3A-Br was expressed using the same vector, but without the 3'- and 5'- ribozyme sequence. Without circularization, fluorescence signals were barely detectable. Images are representative of three replicates taken 48 hours after transfection. All images were taken using the same exposure time. Scale bar, 50 μm.

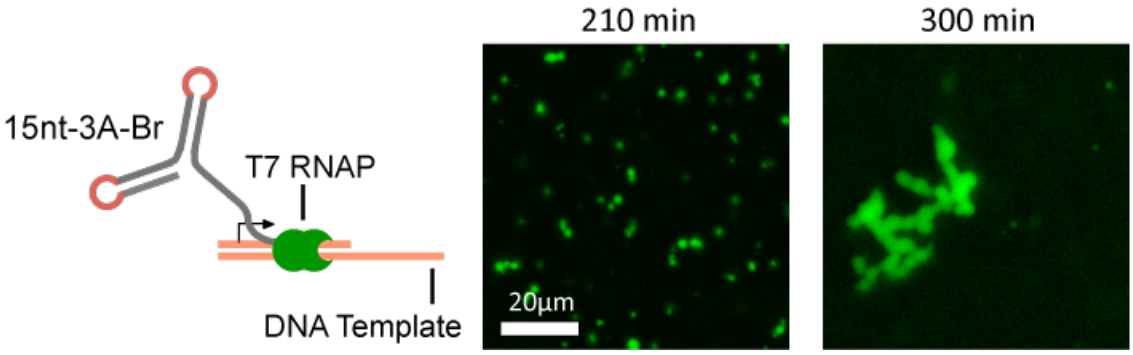

Figure 2-10. Cotranscriptional formation and growth of 15nt-3A-Br condensates *in vitro*.

Condensate formation during *in vitro* transcription. DNA templates are partially annealed to have a double-stranded promoter. RNA strands were transcribed *in vitro* at 37°C using 7.5% (v/v) T7 polymerase and transcription buffer and stained by 40 μM DFHBI. Images are representative from three independent experimental replicates.

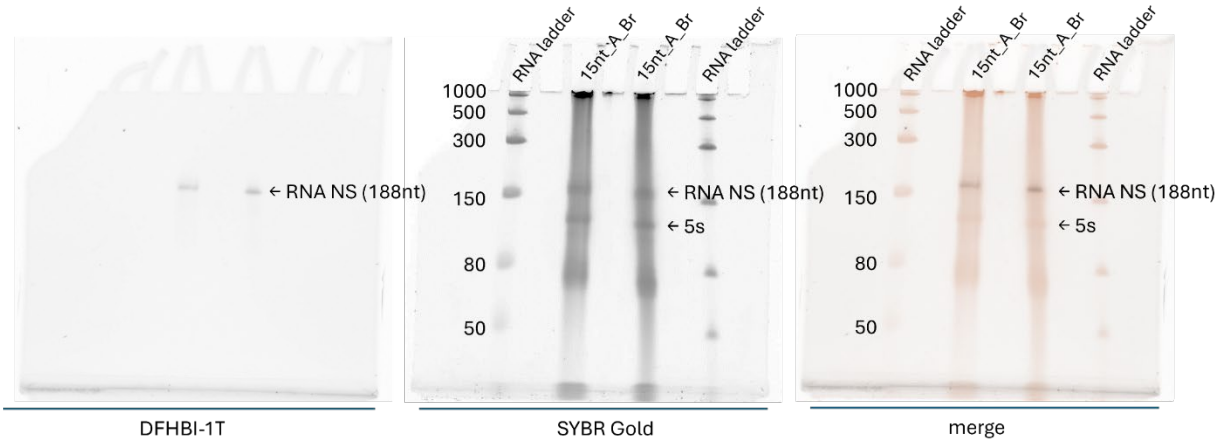

Figure 2-11. In-gel staining of Broccoli-tagged RNA nanostar in HEK293T cells.

HEK293T cells were transfected with a plasmid encoding 15nt-3A-Br. After 48 hours of expression, total RNA was isolated, separated by denaturing PAGE, and stained with DFHBI-1T and 1x SYBR Gold. RNA nanostars tagged with Broccoli aptamer are clearly detectable. Circularized RNA nanostars migrated faster than ssRNA ladder strands of the same length, consistent with previous observations[81].

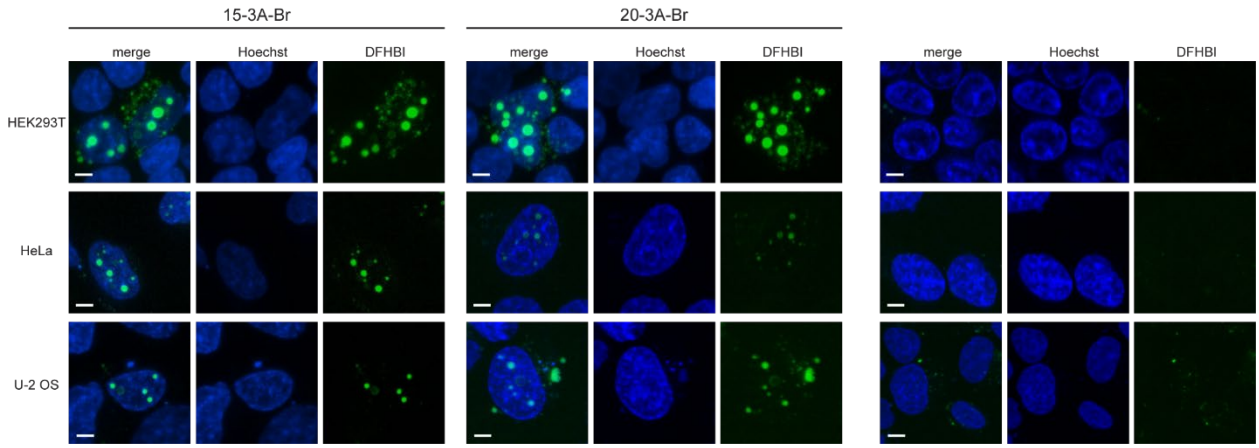

Figure 2-12. RNA nanostars form condensates in HEK293T, HeLa, and U-2 OS cells.

Cells are stained with NucBlue reagent and 40μM DFHBI. Expression level is higher in HEK293T cells as the presence of T antigen facilitates plasmid replication. We tested two variants of our nanostar design: one with 15-nucleotide-long arms (15nt-3A-Br, left) and another with 20-nucleotide-long arms (20-3A-Br, middle), compared to non-transfected cells (right). Images are representative from three independent biological replicates. Scale bar, 5 μm.

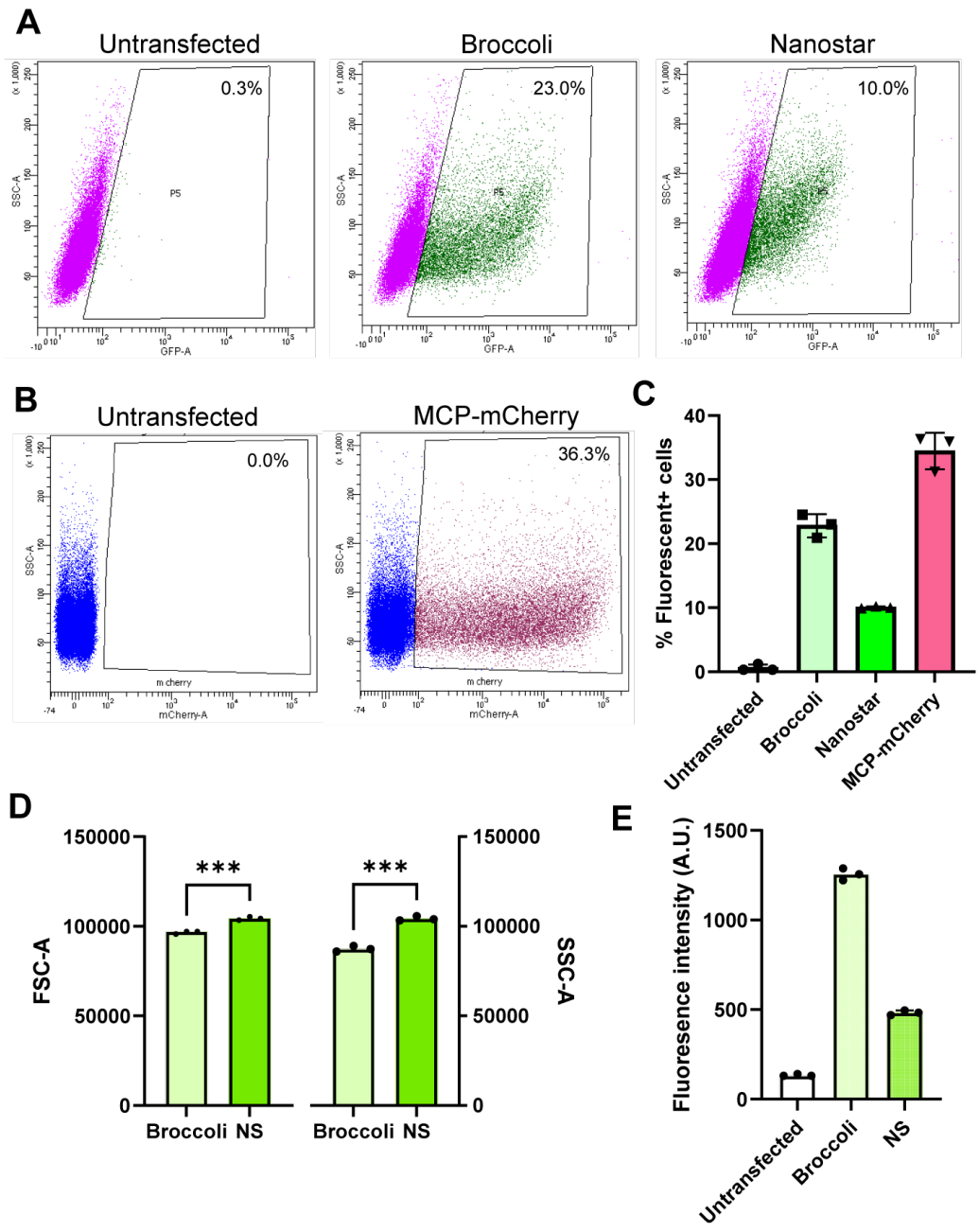

Figure 2-13. Flow cytometry plots and quantification comparing untransfected cells with cells expressing circularized Broccoli aptamer, circularized Broccoli-tagged RNA nanostars, or MCP-mCherry.

In general, cells expressing circularized RNA showed lower transfection efficiency than those expressing mCherry, as shown in **B** and **C**. This may also reflect the detection limit of the flow cytometer, since Broccoli fluorescence is much weaker than mCherry. Among circularized RNA constructs, cells

expressing nanostars showed lower transfection efficiency (**C**), larger size, higher granularity (**D**), and lower fluorescence intensity (**E**) compared to those expressing Broccoli alone. Cells were analyzed 24 hours post-transfection. SSC-A, side scatter amplitude; FSC-A, forward scatter amplitude. Significance was determined by unpaired two-tailed t-test; ***p < 0.001. P values are 0.0004 for FSC-A and 0.0001 for SSC-A. Data are presented as mean values +/- SD. All experiments were performed in three independent replicates.

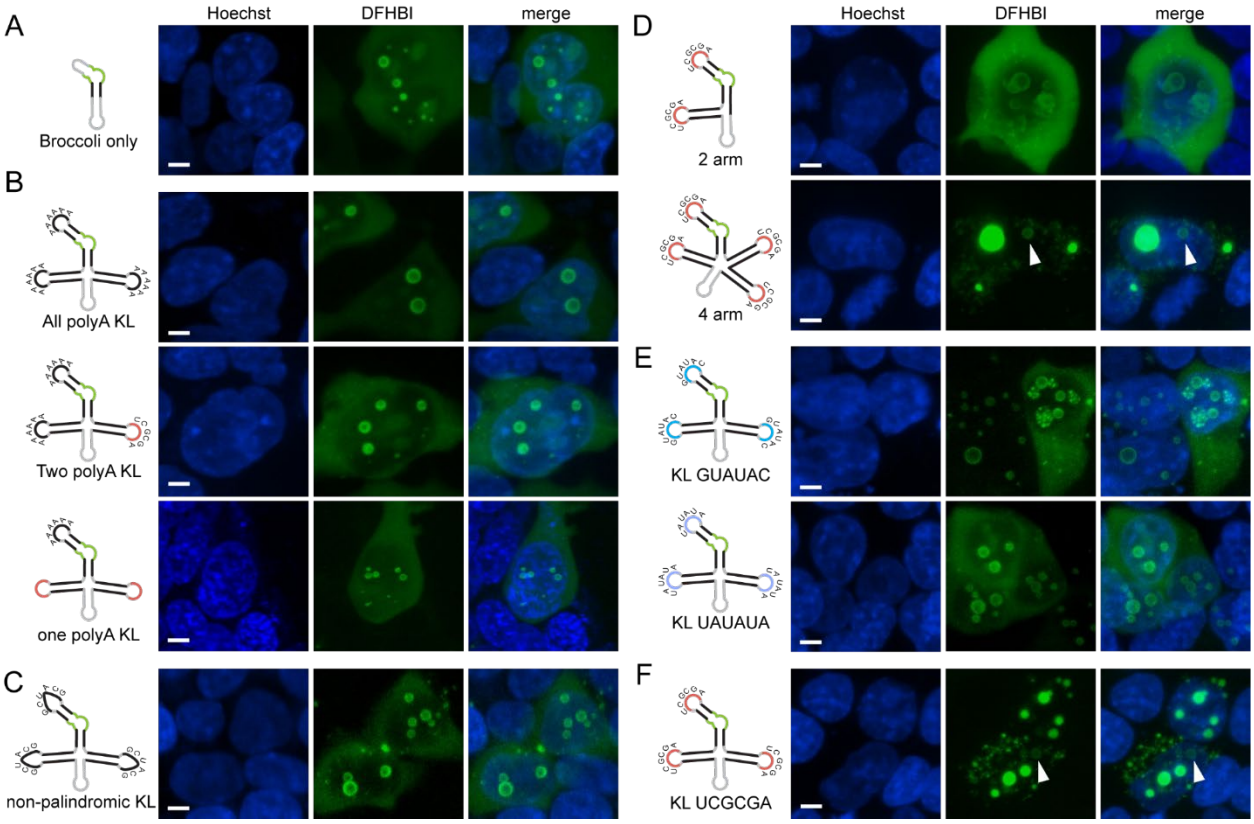

Figure 2-14. Shells emerge in cells expressing circularized RNA and a variety of control nanostars, regardless of their capability to form condensates.

A, Expression of circularized Broccoli yield diffused fluorescence in the cytoplasm and formed shells in the nucleus. **B,** Replacing kissing loops with polyadenine domains disrupted condensate formation and generated shells. Changing one kissing loop was sufficient to disrupt condensate formation. **C,** Expression of nanostar with a non-palindromic kissing loop formed shells in the nucleus. **D,**

Eliminating one arm from the nanostar formed exclusively nuclear shells (top). Addition of one arm formed big, bright condensates and shells in the nucleus and small puncta in the cytoplasm. **E,** Motifs designed to have weak nanostar-nanostar interactions formed abundant nuclear shells. **F,** shells formed in the nucleus of cells expressing nanostar 15nt-3A-Br. Cells were stained with NucBlue reagents and 40 μM DFHBI. Images are all z projections, and are representative from three independent biological replicates. Scale bar, 5 μm.

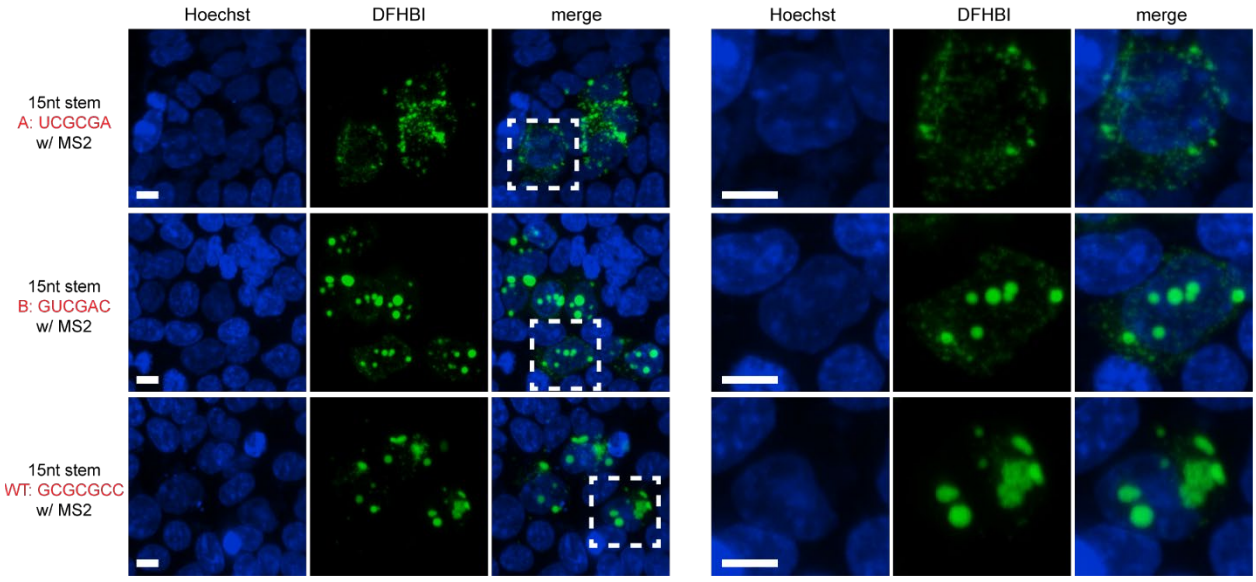

Figure 2-15. Nanostars including the MS2 aptamer form condensates when adopting different kissing loops with varying strength.

Representative images (left) and zoomed-in views (right) of the white-squared area showing cells transfected with nanostars that include an MS2 domain and differ by kissing loop sequence (A/B/WT). The strength of kissing loop interactions increases as GC content increases from top to bottom, resulting in more nuclear retention and more aggregate-like condensates in the cytoplasm. Cells were stained with NucBlue reagents and 40 μM DFHBI. Images are all z projections, and are representative from three independent biological replicates. Scale bar, 10 μm.

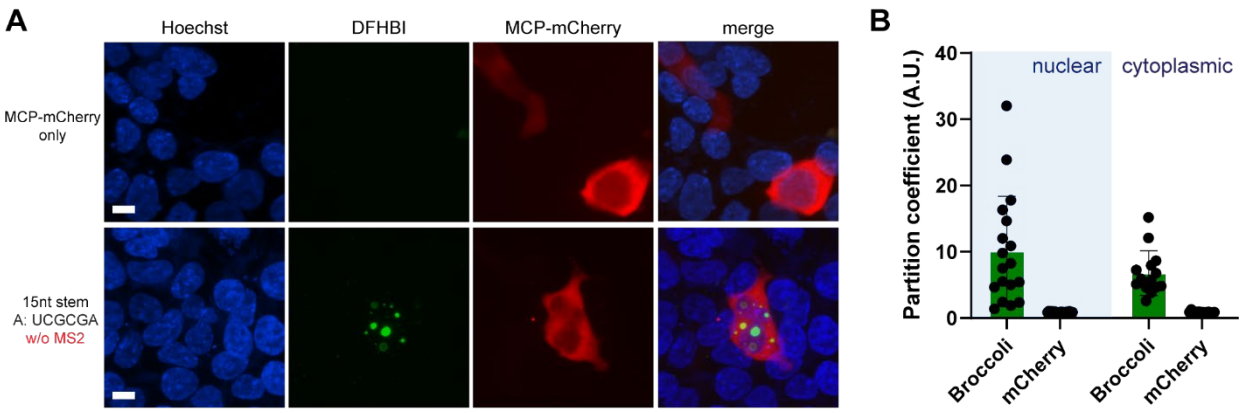

Figure 2-16. RNA nanostars lacking the MS2 domain do not recruit mCherry.

A, Representative images showing transfection of plasmids expressing MCP-mCherry (top) and co-transfection plasmids expressing MCP-mCherry and nanostars (bottom). MCP-mCherry expression in cells leads to a homogenous distribution of fluorescent signals across cells. Protein concentration in the cytoplasm is higher than in the nucleus. Without MS2 aptamer, nanostars form condensates that do not colocalize with MCP-mCherry. **B,** Partition coefficients of cells co-expressing nanostars that lack MS2 aptamer, in the presence of MCP-mCherry. Broccoli-tagged nanostars demonstrating slightly higher nuclear partition coefficients than the cytoplasmic ones. Partition coefficients of mCherry for both nuclear or cytoplasmic condensates averaged around 1, indicating no recruitment. Data are presented as mean values +/- SD. Images are all z projections, and are representative from three independent biological replicates. Scale bar, 10 μm.

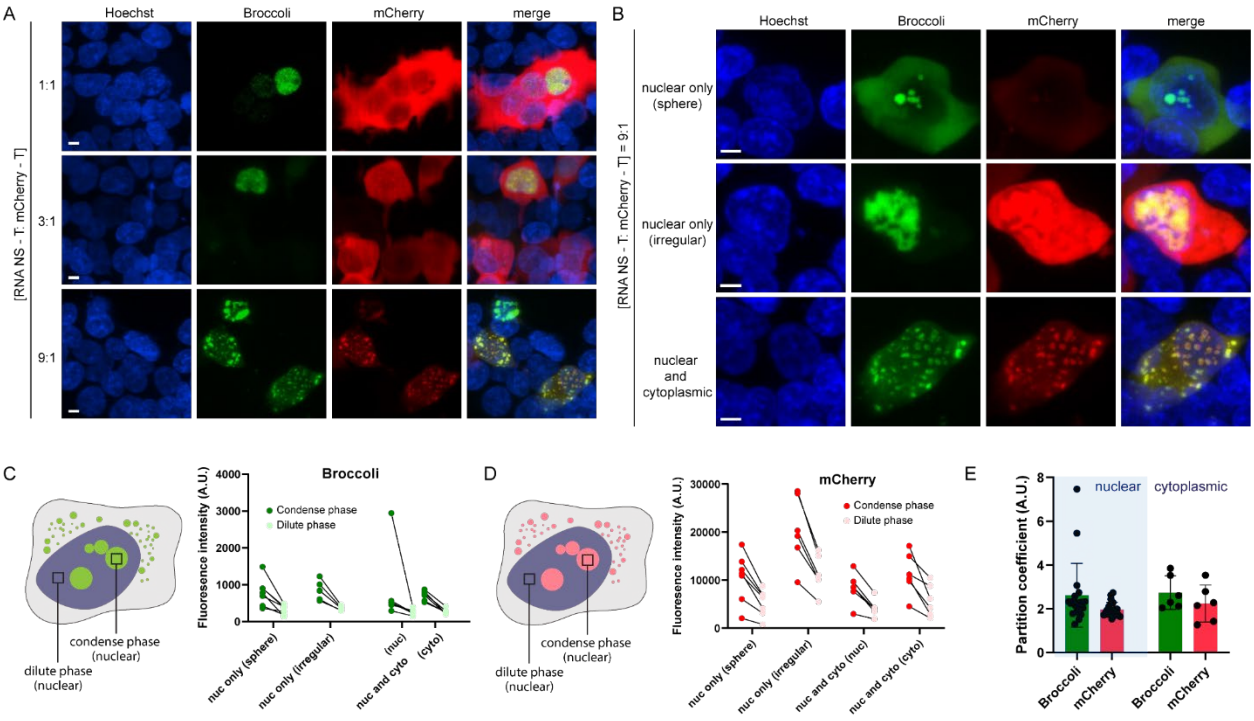

Figure 2-17. Condensate morphology is influenced by both the overall expression levels of mCherry and RNA and their relative expression.

A, Example confocal images of cells co-transfected with mCherry and RNA nanostar plasmids at different transfection ratios (mCherry:RNA = 1:1, 1:3, 1:9). Excess mCherry binding to nanostars causes irregularly shaped aggregates, while higher RNA ratios promote spherical condensates. **B,** Example images at 1:9 transfection ratio, normalized to the same brightness range (brighter indicates higher expression), confirm that excessive mCherry expression correlates with irregular aggregate formation. **C,** Quantification of mean fluorescence intensity reveals that RNA (Broccoli) expression remains constant across spherical and irregularly shaped condensates, whereas **D,** mCherry levels increase in irregularly shaped aggregates, both in the dilute and condensed phases. In cells exhibiting both cytoplasmic and nuclear condensates, mCherry localizes primarily to the cytoplasm (lacking an NLS signal), and results in slightly higher fluorescence intensity in both dilute and condensed phases when compared to the nucleus. **E,** Partition coefficient analysis shows consistent values (~2) for RNA and mCherry across condensates in the nucleus and in the cytoplasm. The Broccoli partition coefficient is 3-4 fold lower when compared to RNA condensates that do not recruit mCherry (Fig. S9), indicating that the presence of cargo molecules

has a significant impact on the composition of the dense phase. Each dot represents one cell. Data are presented as mean values +/- SD. Images are all z projections, and are representative from three independent biological replicates. Scale bar, 5 μm.

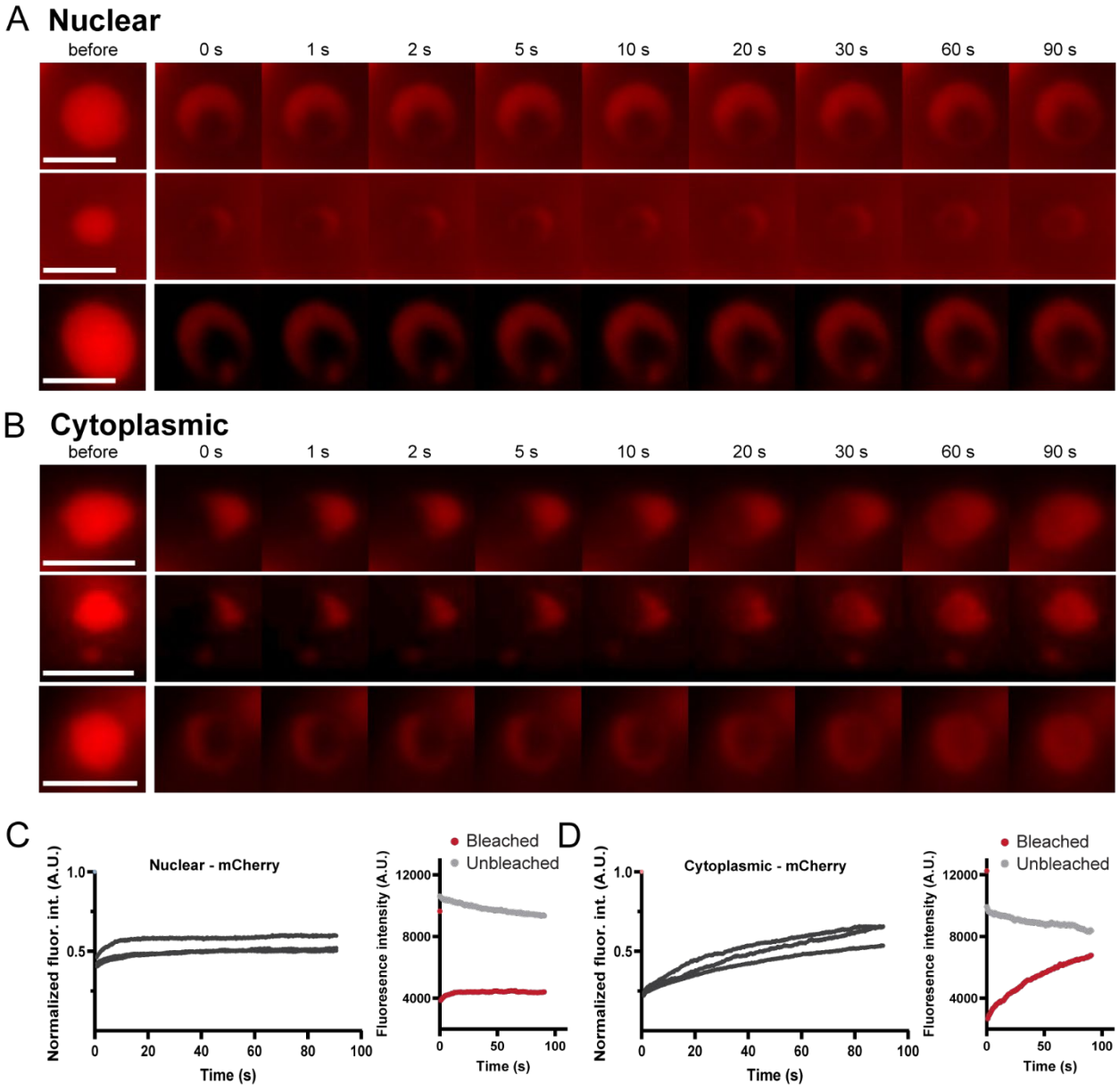

Figure 2-18. FRAP of MCP-mCherry recruited to nuclear and cytoplasmic condensates formed by MS2-modified nanostars shown in Figure 2-1E.

A and B, Representative images showing FRAP behavior of MCP-mCherry cargo recruited through the MS2 domain on nanostars. C and D, Left: Normalized fluorescence intensities change after bleaching. The normalization was done as described in section 1.9 to address bleaching caused by repetitive imaging. Right: Examples of unnormalized data. Scale bar, 5 μm.

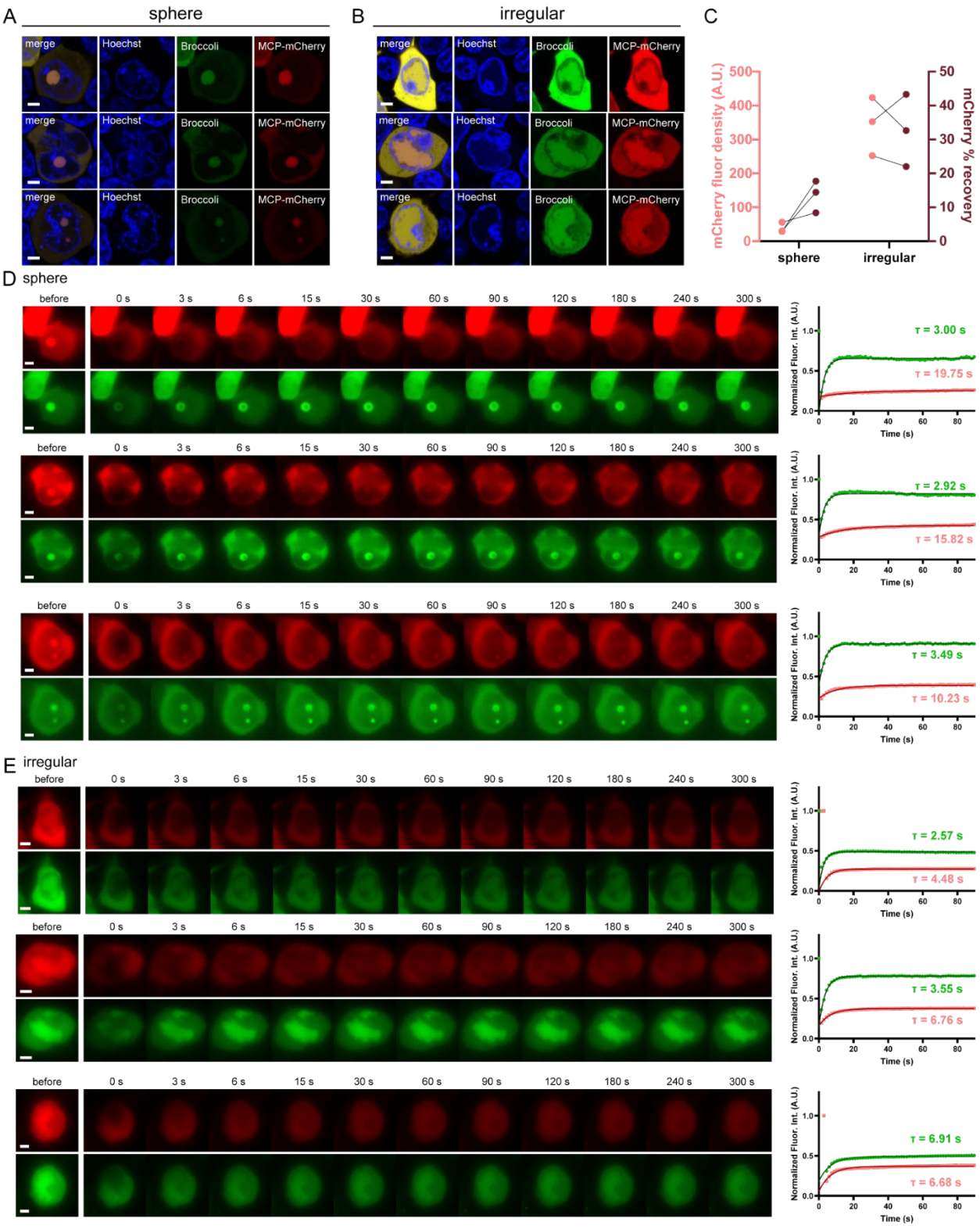

Figure 2-19. Irregularly shaped aggregates show faster and greater mCherry recovery after photobleaching compared to spherical condensates.

A, B, Split-channel confocal images of cells forming spherical condensates (A) or irregularly shaped aggregates (B) (more discussion of the two morphologies can be found in Fig. S10B-D). All confocal images were normalized to the same visualization range (brighter indicates higher expression). As shown in Figure S10, irregular aggregates exhibit excessive mCherry expression relative to spherical condensates. **C,** Correlation between mCherry fluorescence density within condensates and percentage of mCherry recovery after photobleaching shown in D and E. Higher mCherry fluorescence density corresponds to a higher percentage of mCherry recovery. **D, E,** Dual-channel FRAP results for spherical condensates (D) and irregularly shaped aggregates (E). Quantification shows that while Broccoli recovery remains similar, mCherry recovery is consistently faster in irregular aggregates. This is likely because mCherry, as a bulky cargo that does not directly participate in condensation, loosens the RNA condensate network and increases its diffusivity. Dots represent mean fluorescence intensity at each time point, and lines represent fitted recovery curves $Y = Y_0 + (Y_\infty - Y_0) * \left(1 - e^{-\frac{t}{\tau}}\right)$. Due to cellular movement, condensates drift along the z-axis during long observation periods, leading to apparent fluorescence increases after the plateau and affecting fitting parameters. To ensure consistency, curve fitting was performed using the first 90 s of data. Micrographs in (A) and (B) are mid-plane confocal images, and are representative from three independent biological replicates. Scale bar, 5 μm.

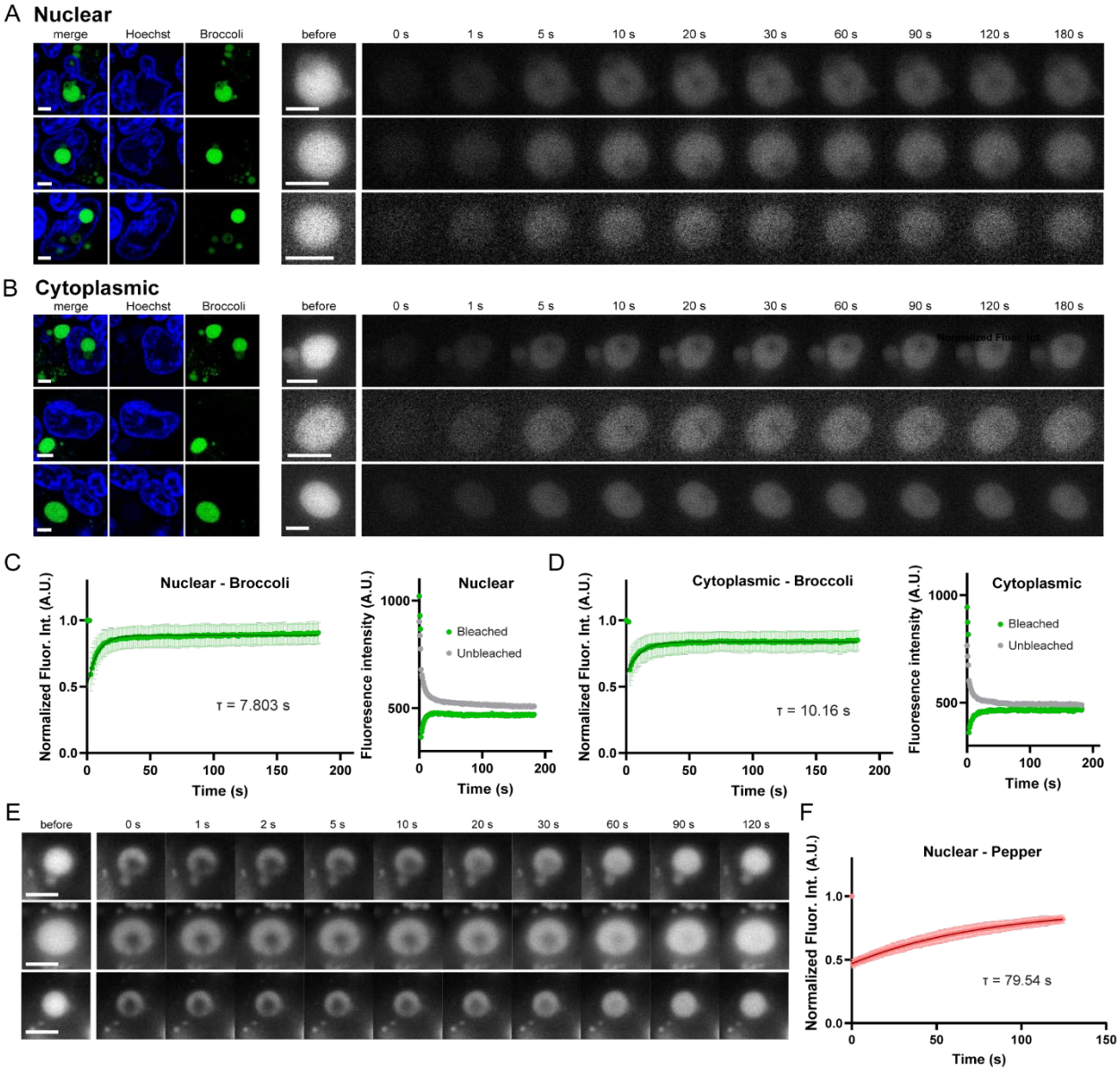

Figure 2-20. FRAP of nuclear condensates formed by nanostars labeled with Broccoli (15nt-3A-Br) and Pepper (15nt-3B-Pp) aptamers.

A, B, Condensates' cellular location were confirmed by mid plane confocal images (left). Representative images (right) showing FRAP behavior of 15nt-3A-Broccoli. **C, D,** Left: Normalized fluorescence intensities change after bleaching. The normalization was done as described in section 1.9 to address bleaching caused by repetitive imaging. Right: Examples of unnormalized data. Dots indicate mean intensity at the corresponding time point. Error bars indicate standard deviation. Line indicates the

fitted curve from equation $Y = Y_0 + (Y_\infty - Y_0) * \left(1 - e^{-\frac{t}{\tau}}\right)$. **E, F,** representative images (E) and quantification (F) of 15-3A-Pepper. Representative Micrographs in (A) and (B) are mid-plane confocal images. Data are presented as mean values +/- SD. All experiments were performed in three independent replicates. Scale bar, 5 μm.

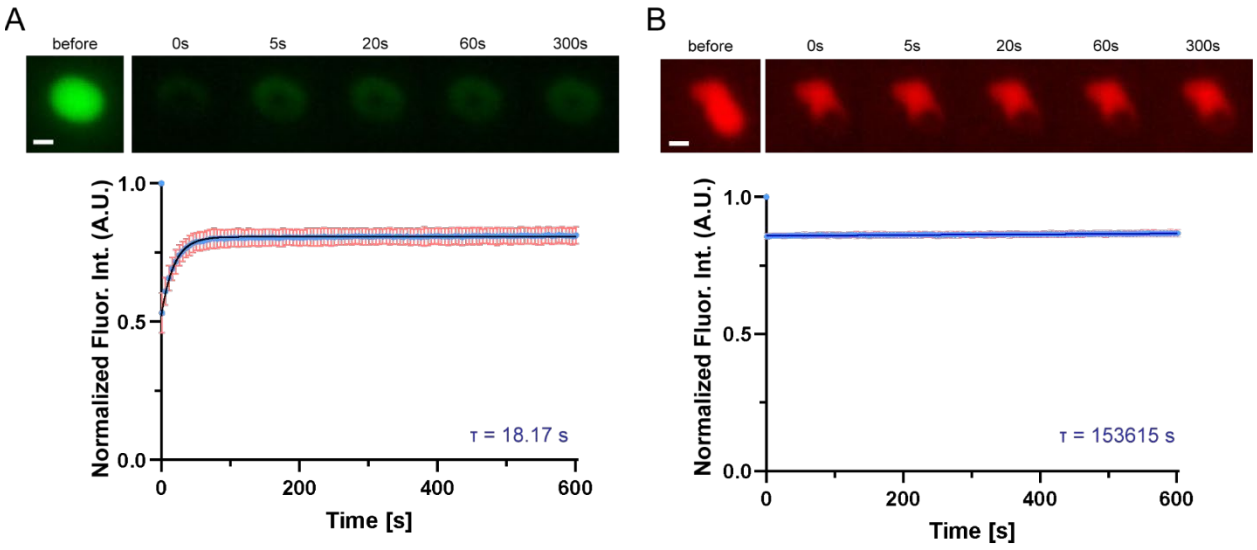

Figure 2-21. FRAP of condensates (15nt-3A-Br nanostar) produced during *in vitro* transcription targeting Broccoli aptamer or Cy3.

Representative images (top) and plots of normalized fluorescence intensity showing FRAP behavior of Broccoli aptamer (**A**) and CY3-labeled RNA (**B**). The *in vitro* transcription reaction was supplied with 1% CY3-labeled UTP, and diluted 10x using 1x transcription buffer and DFHBI (final concentration 40 μM) before imaging to reduce strong background fluorescence caused by free Cy3-UTP. No recovery in the Cy3 channel might be attributed to the dilution, leaving little to no Cy3-labeled RNA in the dilute phase available for recovery. Images are captured in GFP channels for A and RFP channels for B. Blue dots indicate mean intensity at the corresponding time point. Orange error bars indicate standard deviation. The dark blue line indicates the fitted equation $Y = Y_0 + (Y_\infty - Y_0) * \left(1 - e^{-\frac{t}{\tau}}\right)$. Data are presented as mean values +/- SD. All experiments were performed in three independent replicates. Scale bar, 1 μm.

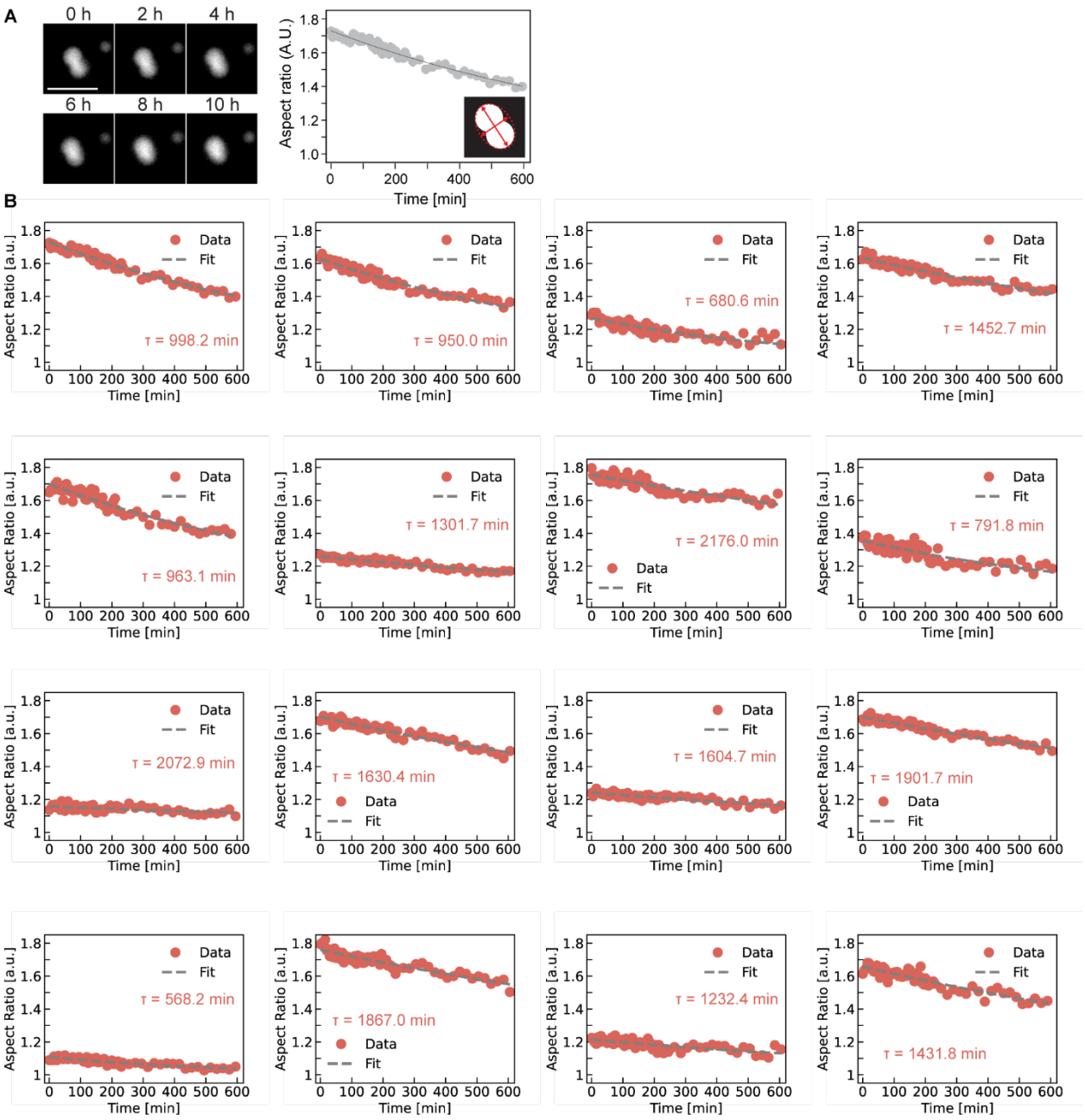

Figure 2-22. Time-dependent coalescence of condensates produced during *in vitro* transcription of nanostar 15nt-3A-Br.

A, Example micrographs of one fusion event. Schematic shows the definition of aspect ratio as the major and minor axes ratio from the best-fit-ellipses. **B,** Analysis results tracking 16 condensate fusion events measured within one field of view from one sample. Nanostars were transcribed using 1% CY3-

UTP for labeling; condensates were monitored in a sealed chamber, and imaged on a heat stage at 37°C. The dashed line is a fit of the exponential function $1 + Ae^{(-t/\tau)}$. Scale bar, 5 μm.

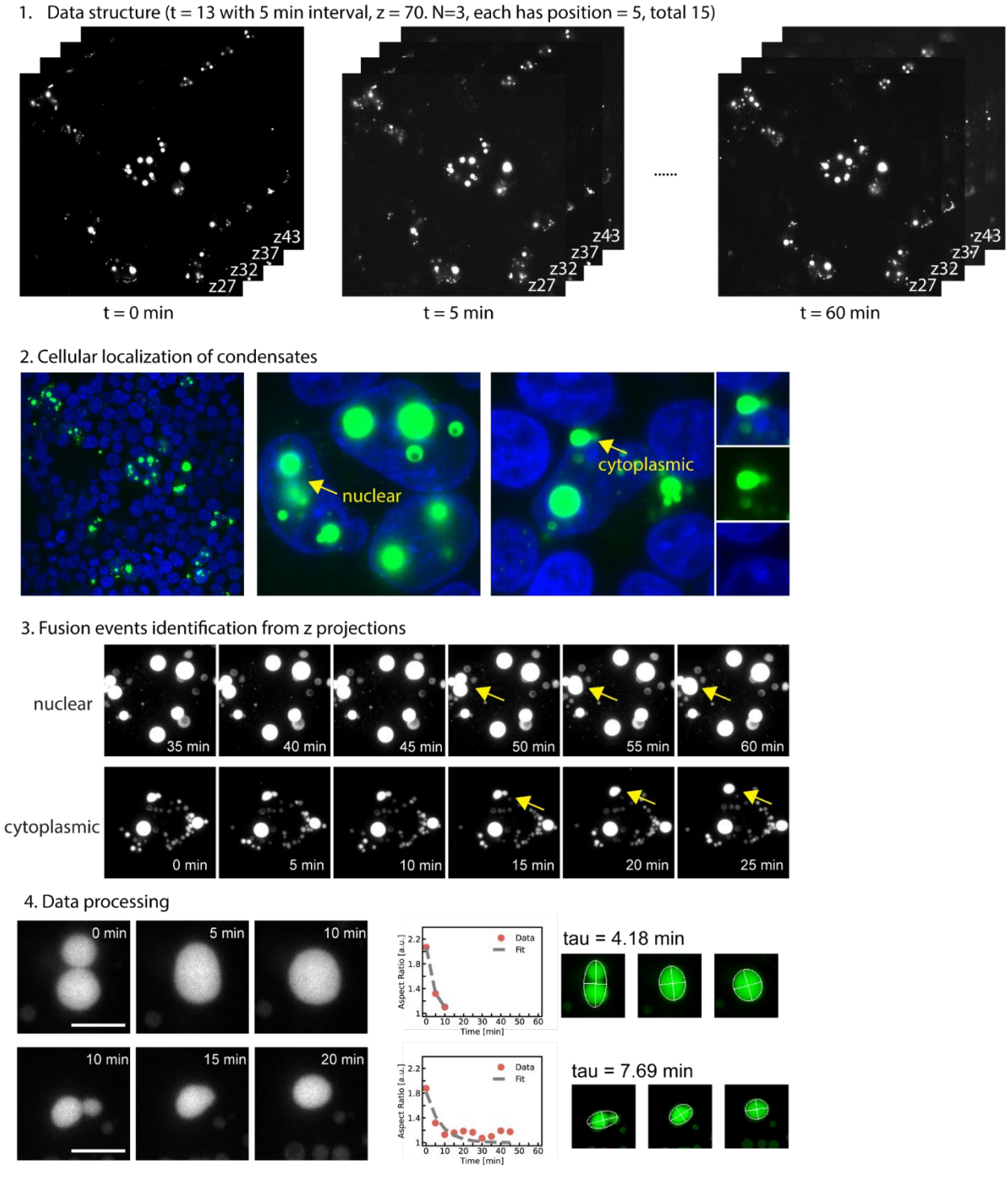

Figure 2-23. *In vivo* fusion data processing workflow.

Cells were transfected to express 15nt-3A-Broccoli for 48 hours, and stained with DFHBI for Broccoli (green) and Hoechst for the nuclei (blue) before imaging. 1) Time-lapse images were collected using confocal microscopy as z-stacks every five minutes, across five positions per replicate and three biological replicates. 2) A single mid-plane image was selected to determine the cellular localization of condensates while minimizing phototoxicity. 3) Fusion events were manually identified. 4) A Python script was used to extract aspect ratios. Scale bar, 5 μm.

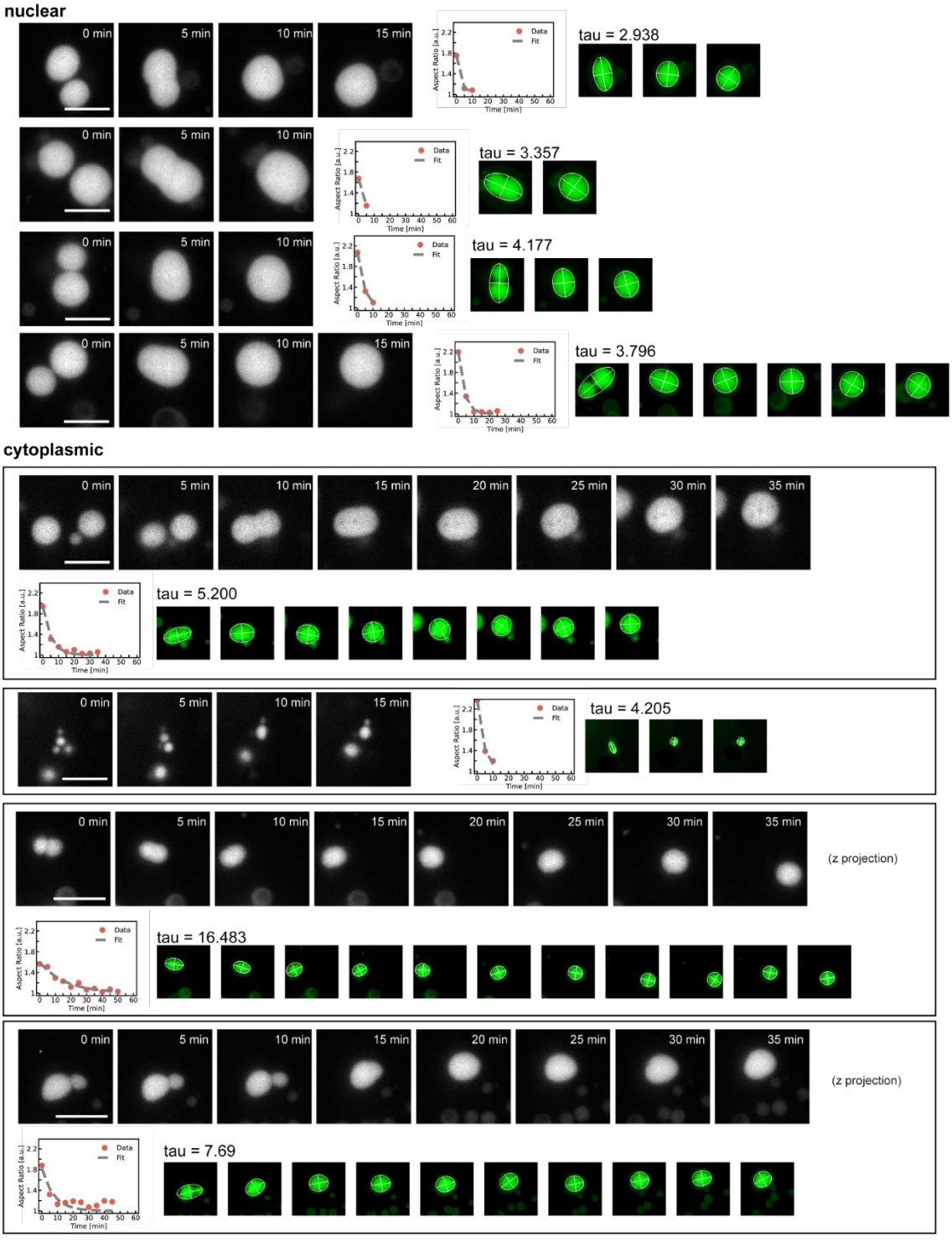

Figure 2-24. Time-dependent coalescence of condensates in cells transfected to produce nanostar 15nt-3A-Br.

Mid plane confocal images show four nuclear and two cytoplasmic fusion events. Z projections show two cytoplasmic events with condensates on different z levels. Aspect ratios were calculated as the ratio of the major to minor axes from best-fit ellipses, as shown in the green micrographs. The dashed lines are fits of the exponential function $1 + Ae^{(-t/\tau)}$. Scale bar, 5 μm.

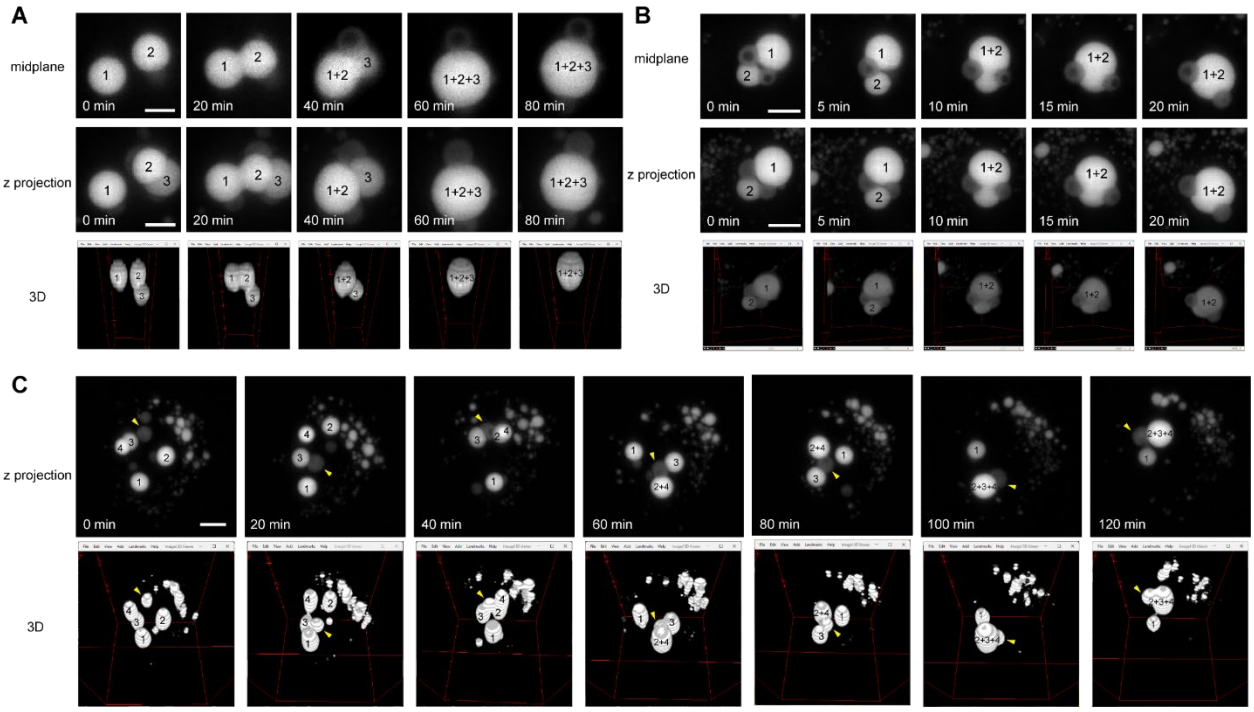

Figure 2-25. Three complex fusion events in three dimensions.

Fusion events can involve multiple condensates and appear to be affected by the shells (as shown in the second and third events), where condensates fused but the shells remained distinct. Scale bar, 5 μm.

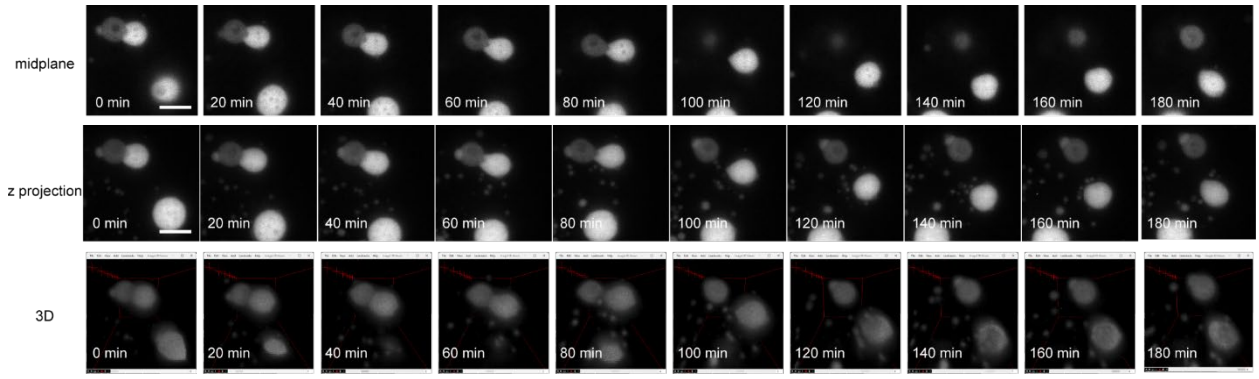

Figure 2-26. Example splitting event.

Confocal images show a splitting event between a shell and a condensate. Scale bar, 5 μm.

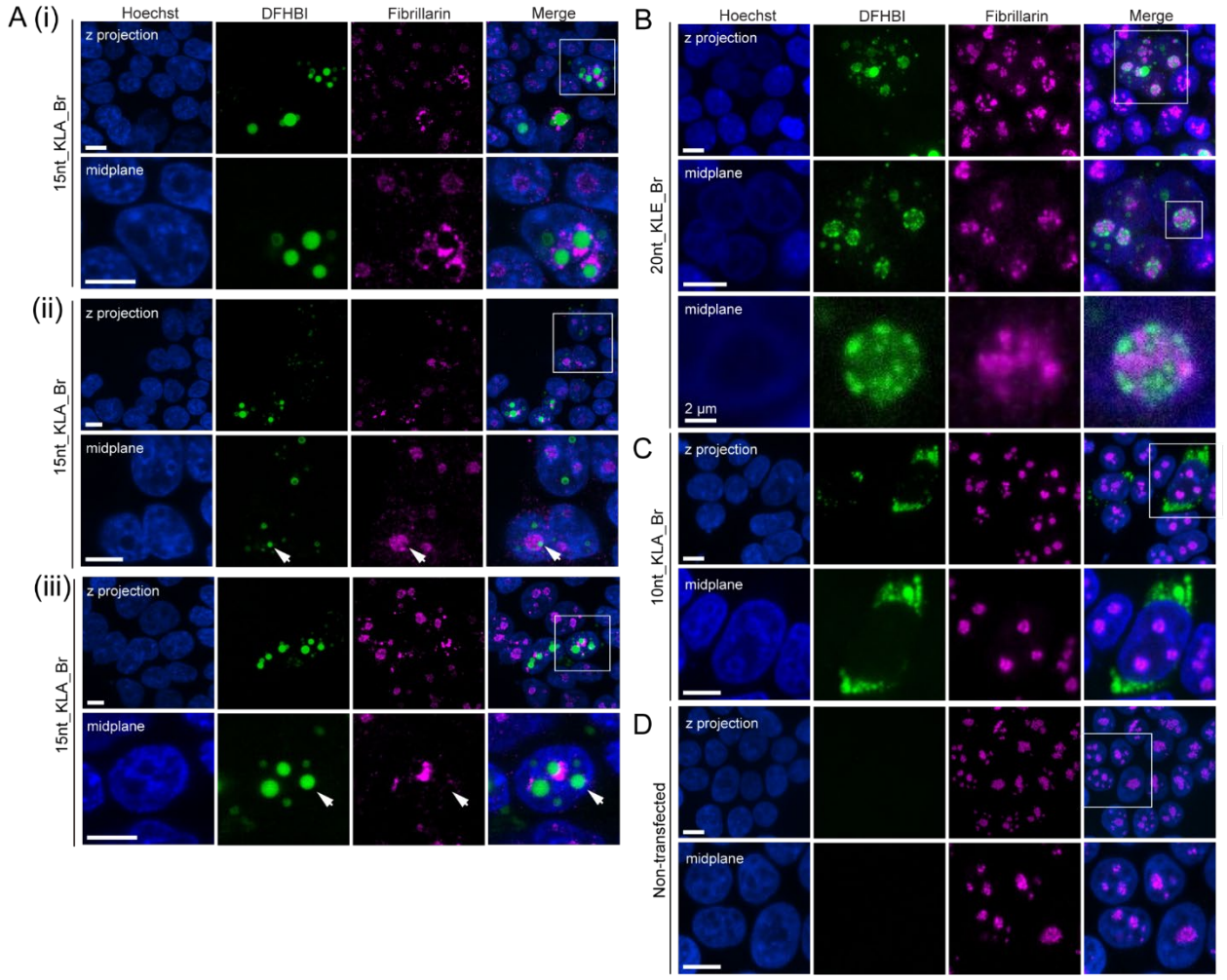

Figure 2-27. RNA nanostars forming nuclear condensates colocalize with the nucleolus and exclude fibrillarin.

We tested nanostar designs that differ by arm length (10, 15 or 20 nucleotides) and kissing loop sequence (designs A or E). **A**, Z-projection and midplane confocal images of 15nt-A-Br showing condensates colocalizing with the nucleolus. In both high (i) and low (ii) expressing cells, condensates exclude fibrillarin, forming dark regions with reduced signal. Most nuclear condensates show fibrillarin accumulation on the surface but are not exclusively nucleolar, as in (iii) (white arrows). **B**, 20nt-E-Br nanostars form small puncta inside the nucleolus that exclude fibrillarin, similar to A(ii). **C**, 10nt-A-Br nanostars, which do not form nuclear condensates, show no change in fibrillarin localization. **D**, Fibrillarin distribution in non-transfected HEK293T cells. Representative images from three replicates. Scale bar, 10 μm.

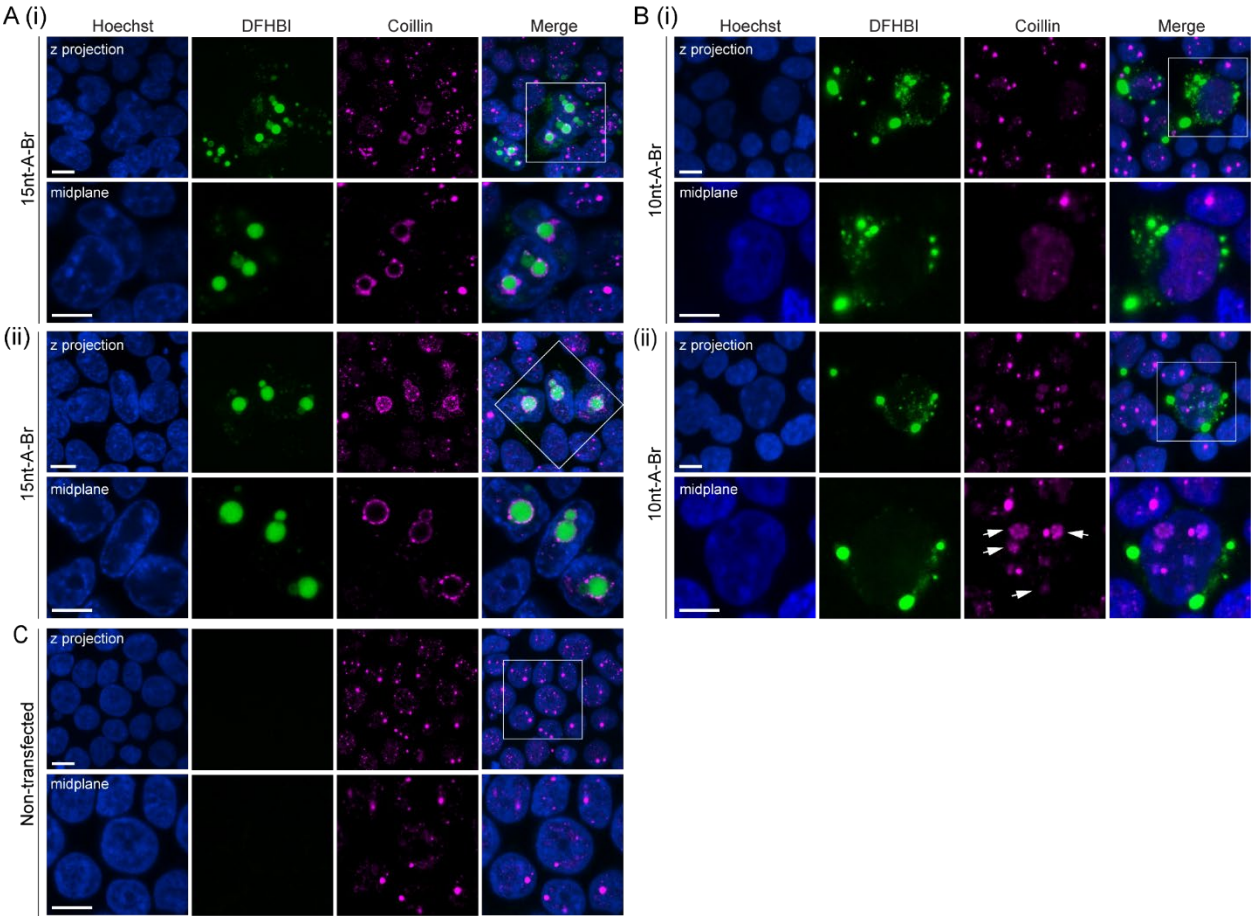

Figure 2-28. Cajal bodies cluster on the surface of large nuclear condensates.

We tested nanostar designs that differ by arm length (10, 15 or 20 nucleotides) and kissing loop sequence (designs A or E). **A,** Z-projection (top row) and single-slice confocal image (bottom row, white square in Z-projection) showing Cajal bodies clustered on the surface of condensates inside of nuclei. In both fields of view (i) and (ii), Coilin localizes at the surface of nuclear condensates. **B (i)**, RNA nanostars that form exclusively cytoplasmic condensates (10 nt arm length, see Fig. 2 of the manuscript) did not change Coilin localization in most nanostar-expressing cells. However, in some cases, localization of Coilin appeared altered (**B (ii)**). **C**, Cajal body in non-transfected HEK293T cells. Representative images from three replicates. Scale bar, 10 μm.

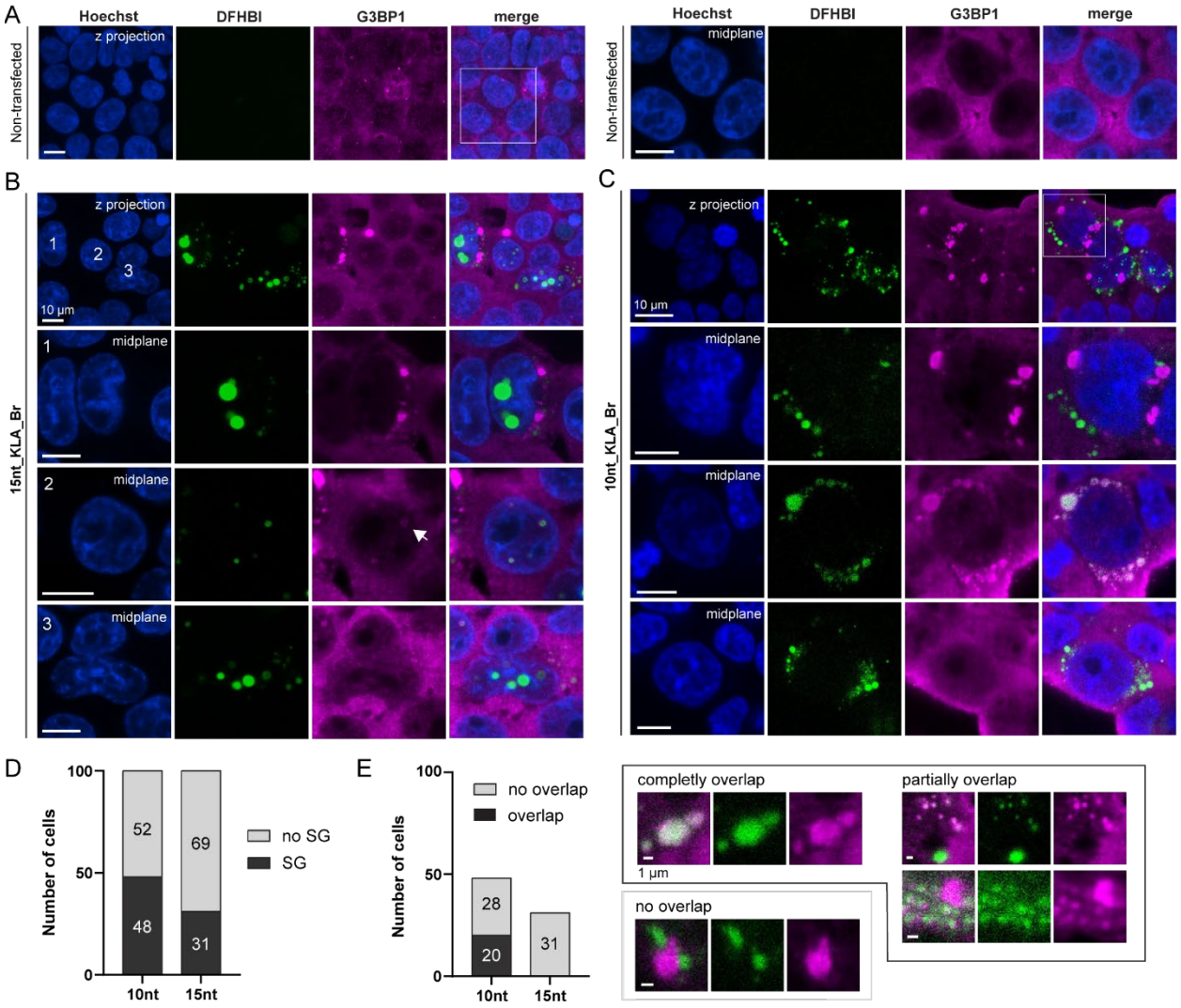

Figure 2-29. The formation of abundant cytoplasmic condensates increases the likelihood of stress granule (SG) formation.

A, Z-projection (left) and zoom-in mid-plane confocal images (right) of untreated HEK293T cells stained with G3BP1 showing no SG formation. **B,** Z-projection (top row) and mid-plane images (bottom rows) of cells transfected with plasmids expressing 15-A-Br and stained with G3BP1. RNA condensation may correlate with SG formation without colocalizing with G3BP1, as in cell 1; this is not observed in all cells, as seen in cell 3. In cell 2, nanostars form shells that colocalize with G3BP1 (see Figure S23 for discussion). **C,** Z-projection (top row) and mid-plane images (bottom rows) of cells transfected with 10-A-Br and stained with G3BP1, showing examples of SG formation without colocalization (first row), with

colocalization (second row, different FOV), and without SG formation (third row, different FOV). **D,** 10-A-Br nanostars show a higher tendency to trigger SG formation compared with 15-A-Br. **E,** Bar plot (left) showing that among cells with SG formation, only 10-A-Br displayed overlap between condensate and G3BP1 signals. Representative micrographs demonstrate the observed overlap patterns. Scale bar, 10 µm.

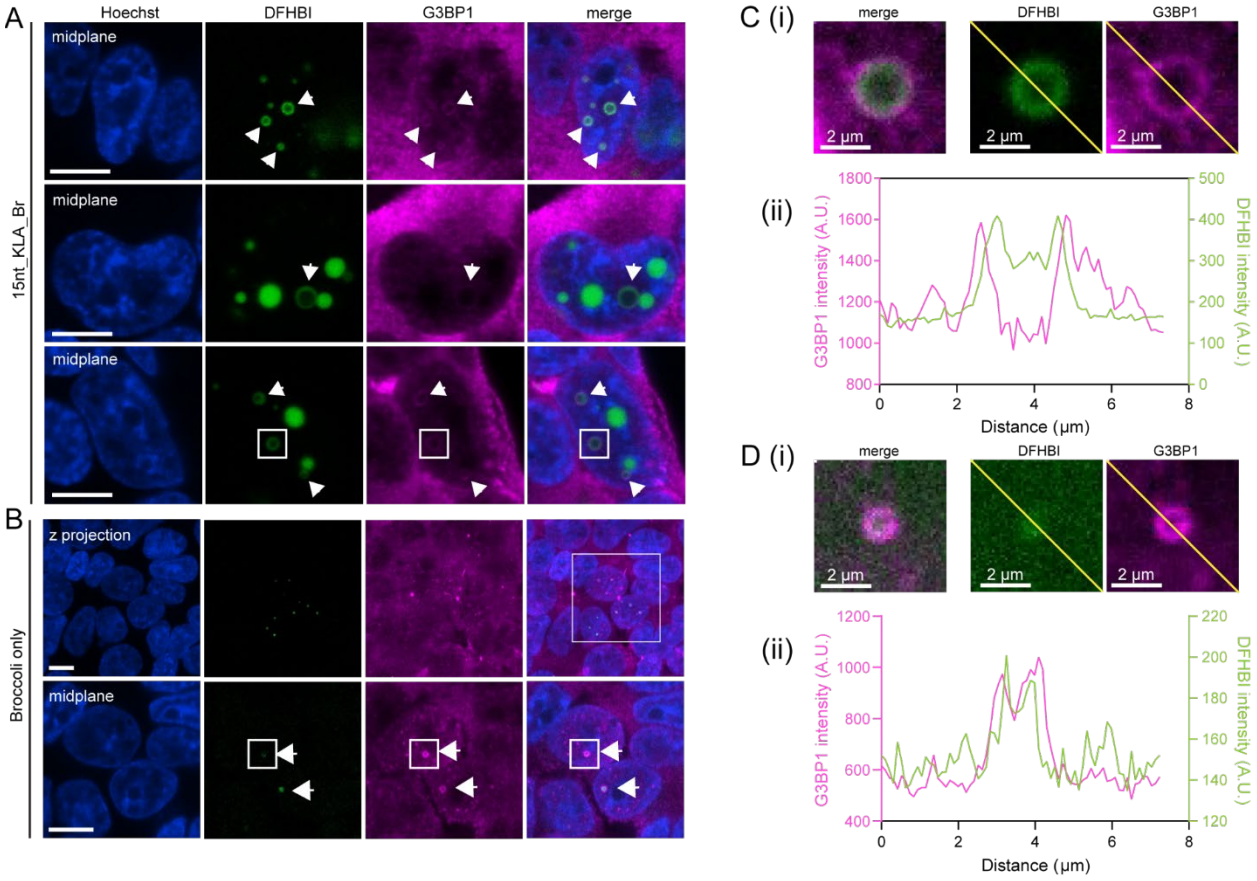

Figure 2-30. Shells are consistently observed across different fields of view in cells expressing RNA nanostars (A) or circularized Broccoli (B).

G3BP1 colocalizes with shells but not with nuclear condensates, likely due to structure-mediated RNA decay. **C, D,** Pixel intensity profile of shells from nanostar-expressing cells (C, white square in A), or Broccoli-expressing cells (D, white square in B) illustrating its layered organization. Scale bar, 10 µm.

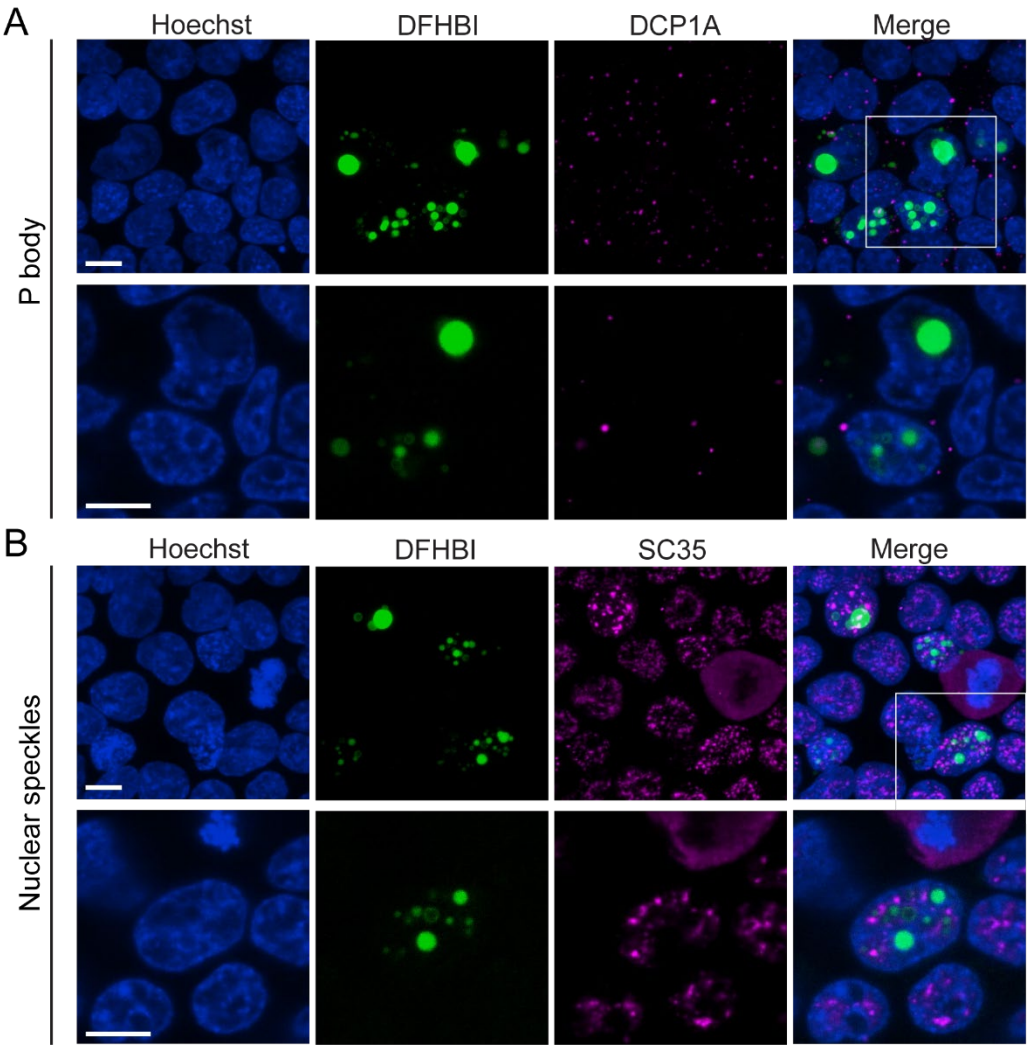

Figure 2-31. Nuclear speckles (A) and P bodies (B) do not colocalize with RNA condensates.

Z-projection (top row) and single-slice (bottom row, white square in Z-projection) confocal images of cells were fixed 48 hours post-transfection. Images are representative of three replicates. Scale bar: 10 μm.

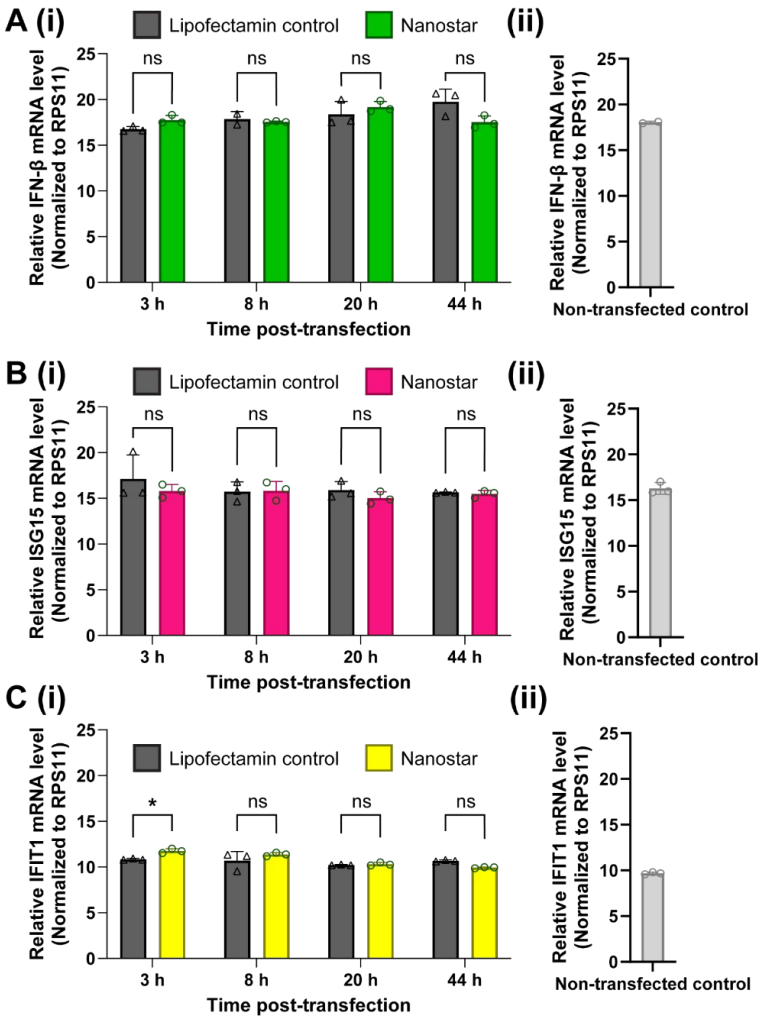

Figure 2-32. Quantitative PCR (qPCR) analysis of interferon-stimulated gene (ISG) expression.

Expression levels of IFN-β (A), ISG15 (B), and IFIT1 (C) were measured and normalized to RPS11 in cells transfected with 15nt-3A-Br or treated with Lipofectamine alone at 3, 8, 20, and 44 hours post-transfection. (ii) Expression levels of the same genes in untreated cells are shown for comparison. All experiments were performed in three independent biological replicates. Data are presented as mean values +/- SD. Statistical significance was determined by two-way ANOVA followed by multiple comparison tests.

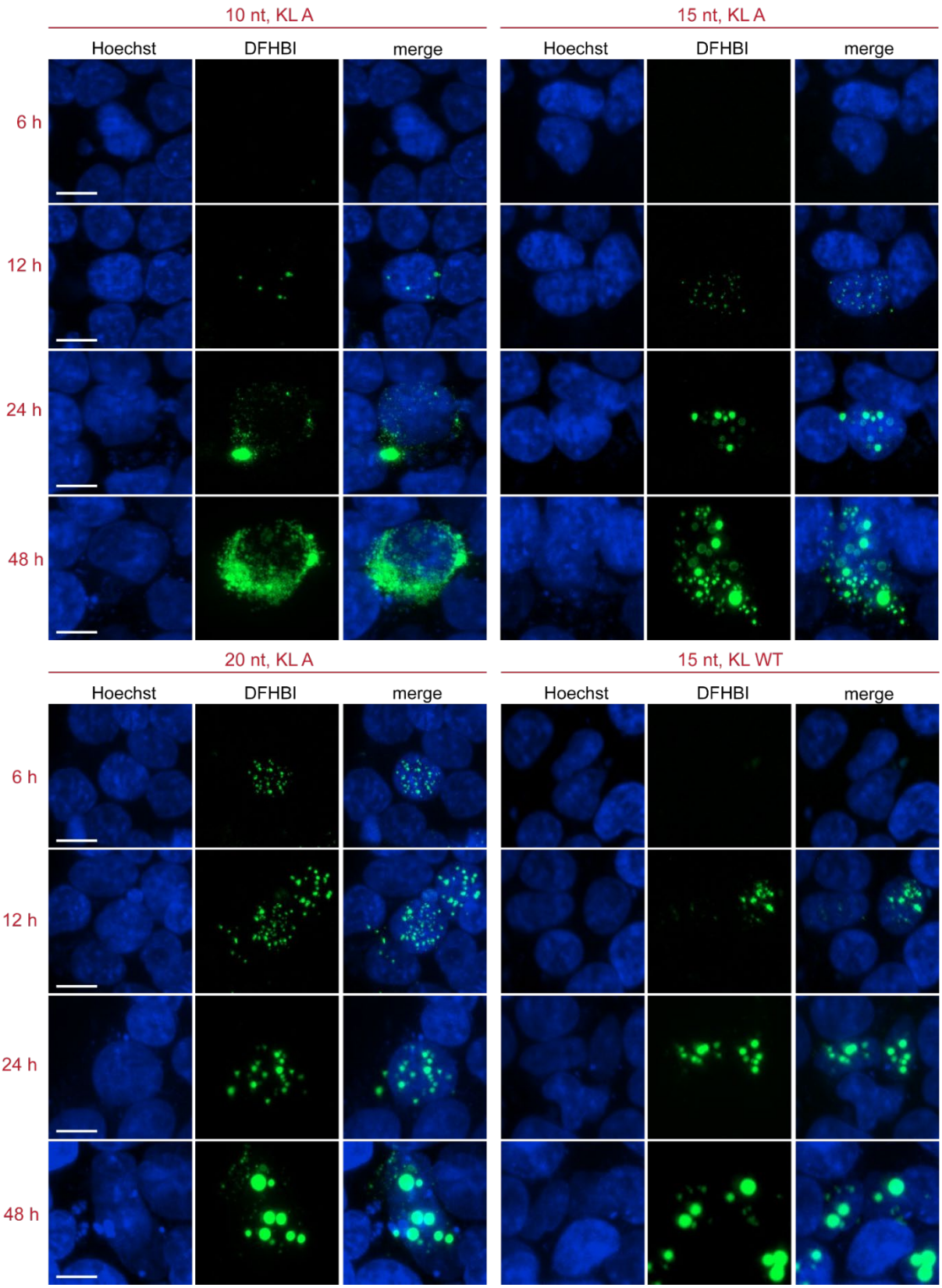
10 nt, KL A
15 nt, KL A
20 nt, KL A
15 nt, KL WT
Hoechst
DFHBI
merge
6 h
12 h
24 h
48 h

Figure 2-33. Split-channel images of the micrographs shown in Figure 2-2.

Scale bar, 10 μm.

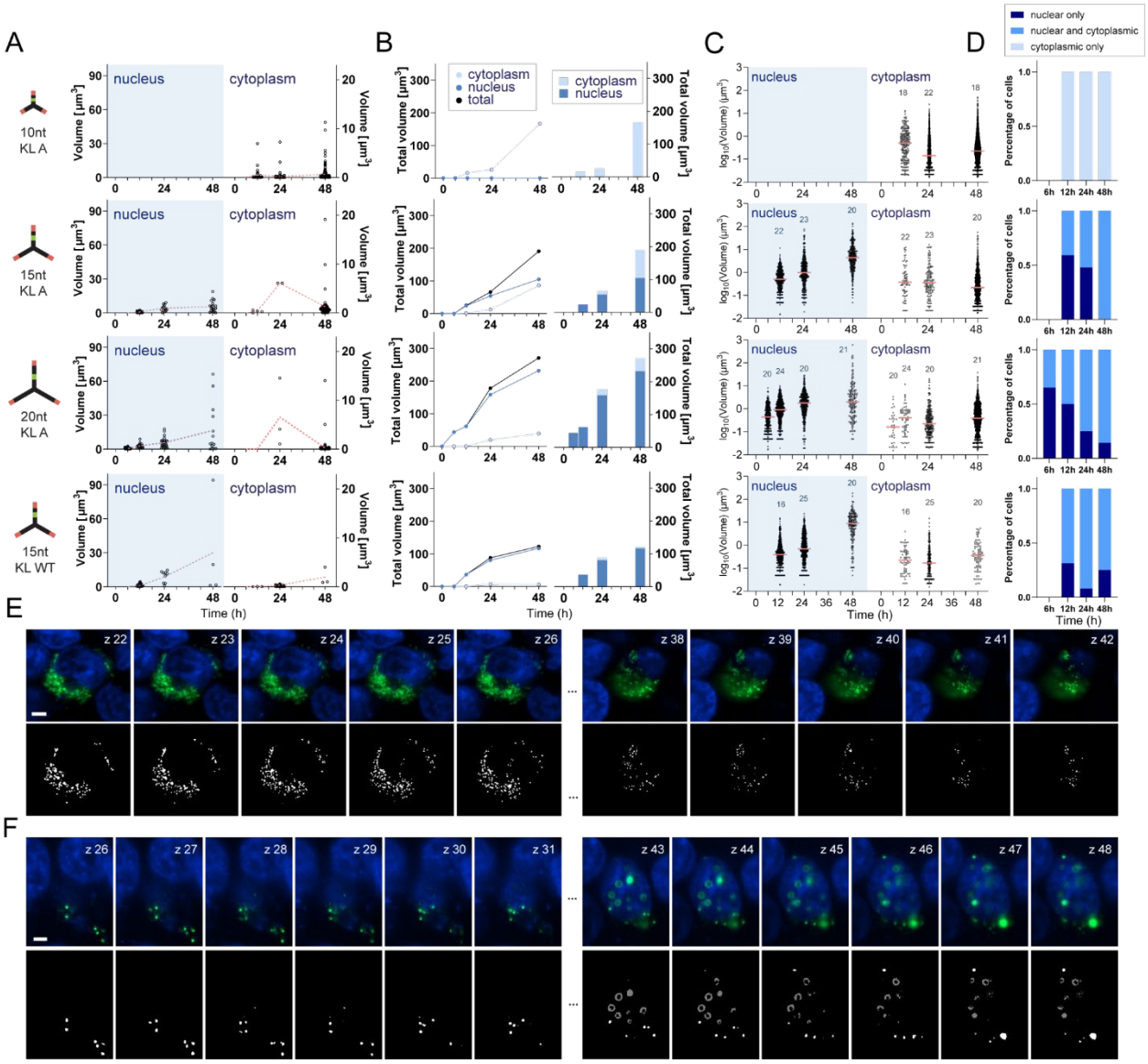

Figure 2-34. Individual and total condensate volume of a representative cell.

A, Dot plots showing individual condensate volume at each time point. Dashed lines represent change of the mean volume. **B,** Line plots and grouped bar plots showing the change of total volume over time. Plots in B and C are for condensate volumes collected for an individual cell tracked over time in the corresponding row of A, indicated by white arrows. **C,** Dot plots showing temporal evolution of individual condensate volume (nuclear and cytoplasmic). Above each dot plot, we report the number of sampled

cells at each time point, across multiple fields of view, from three replicates. **D,** Bar plots reporting the fraction of cells showing exclusively nuclear, nuclear and cytoplasmic, and exclusively cytoplasmic condensates at each time point. **E, F,** Single plane images (top) and the corresponding masks (bottom) for 10 nt KLA (E) and 15 nt KLA (F) at 48 hours. In the masks, cytoplasmic condensates are in white, while nuclear condensates are in gray. Increasing in slice number indicating intersecting from bottom to top of the cell. The masks were then reconstructed into 3D based on slice thickness for condensate volume quantification. Scale bar, 5 μm.

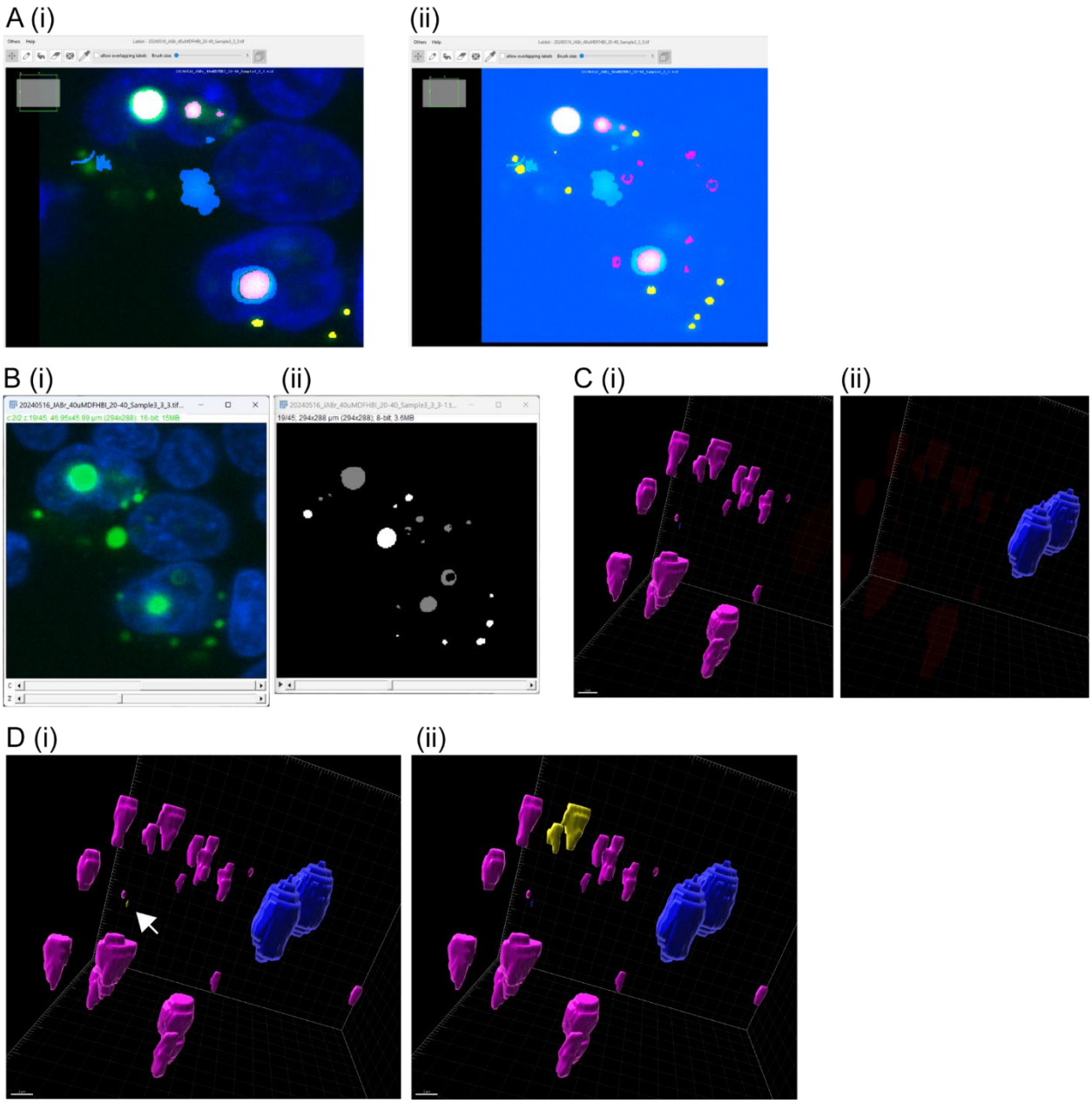

Figure 2-35. Condensate volume quantification workflow.

A, For each confocal image, regions containing condensate-expressing cells were cropped and we manually labeled nuclear and cytoplasmic condensates (**i**) to generate a machine-learning segmentation pipeline using Labkit, an ImageJ plugin[9]. (ii). **B,** Comparison between a region of interest containing three condensate-expressing cells (i) and its mask (ii) that had condensates inside of the nucleus (gray) and the cytoplasm (white). **C,** Masks were analyzed in IMARIS to create surfaces for

condensate populations inside (ii) and outside (i) of the nucleus. **D,** Data cleaning was performed to exclude single-voxel signals (i). Neighboring condensates that were fused were cropped manually. Statistics like condensate volume and number were automatically calculated by IMARIS and output for further analysis.

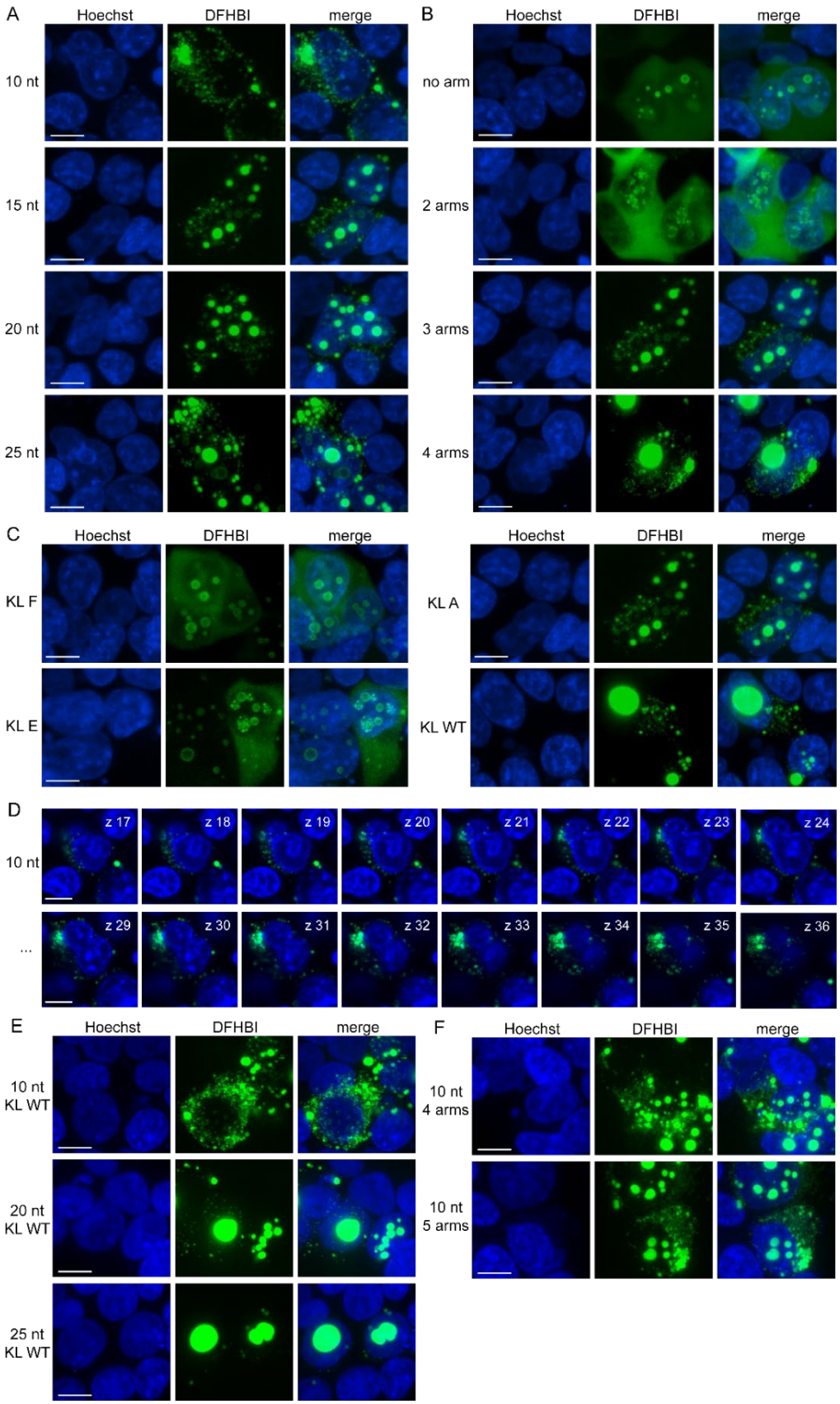
A
Hoechst
DFHBI
merge
10 nt
15 nt
20 nt
25 nt
B
Hoechst
DFHBI
merge
no arm
2 arms
3 arms
4 arms
C
Hoechst
DFHBI
merge
KL F
KL E
KL A
KL WT
D
10 nt
...
z 17
z 18
z 19
z 20
z 21
z 22
z 23
z 24
z 29
z 30
z 31
z 32
z 33
z 34
z 35
z 36
E
Hoechst
DFHBI
merge
10 nt KL WT
20 nt KL WT
25 nt KL WT
F
Hoechst
DFHBI
merge
10 nt 4 arms
10 nt 5 arms

Figure 2-36. Split-channel images (A, B, C, E, and F) of the micrographs shown in Figure 2-3 and single midplane images (D) showing 10nt nanostar forming exclusively cytoplasmic condensates.

Scale bar, 10 μm.

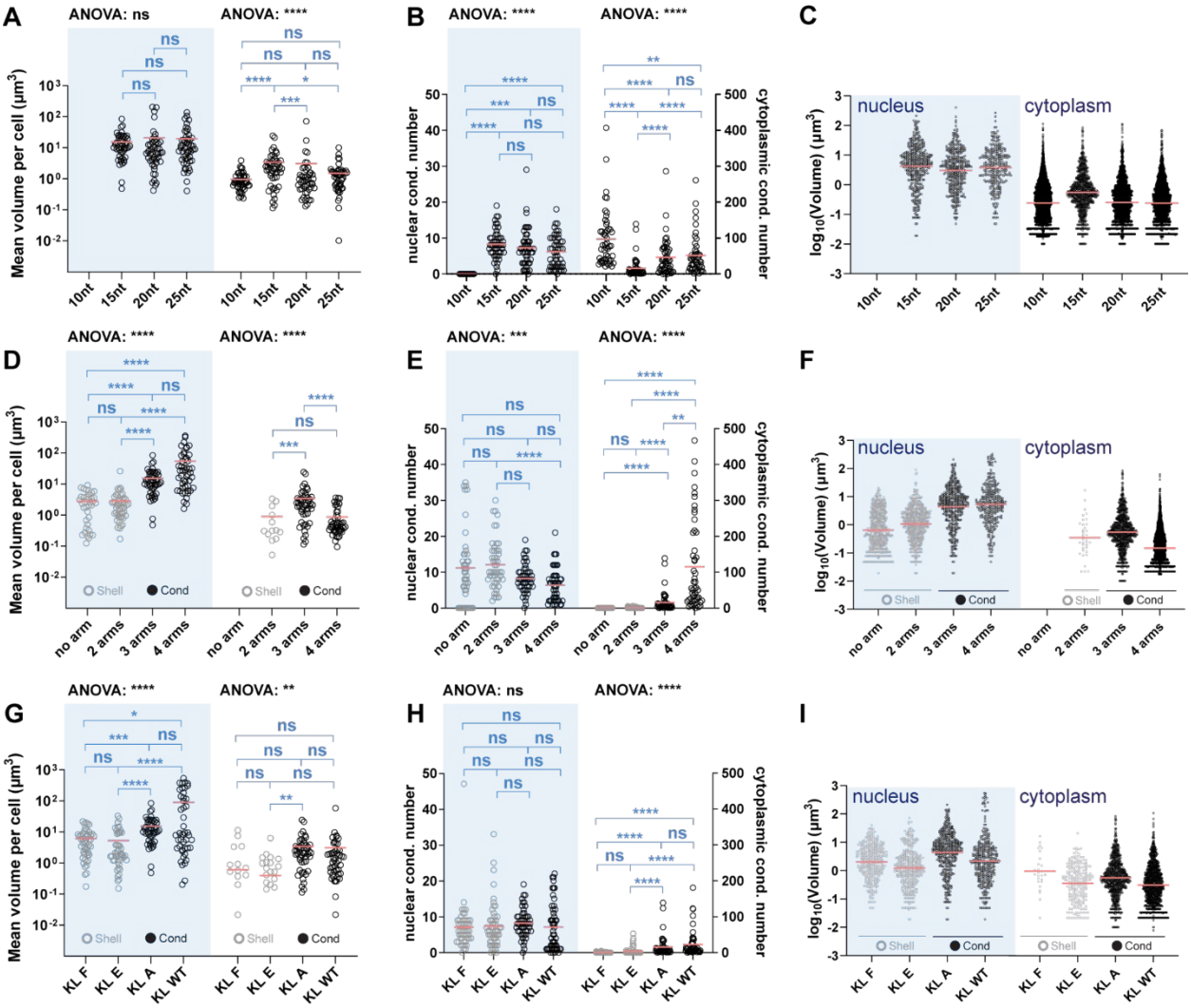

Figure 2-37. Data shown in Figure 2-3 annotated with statistical significance. Distributions of condensate volume in the nucleus and cytoplasm comparing different arm lengths (A–C), arm numbers (D–F), and kissing loop sequences (G–I).

A, D, G, Average condensate volume per cell, where each dot represents a cell. **B, E, H,** Condensate number per cell, where each dot represents a cell. **C, F, I,** Individual condensate volumes,

where each dot represents a condensate. Red lines indicate the mean. Cells with no nuclear or cytoplasmic condensates were assigned to have average condensate volume and condensate number per cell as zero. Significance was determined by non-parametric one-way ANOVA test (Kruskal-Wakkus test) followed by Dunn's multiple comparisons test. P value summary on the top compares all four groups while comparisons of individual groups were reported below. P-values are provided in Supplementary Table 3. *p < 0.05; **p < 0.01; ***p < 0.001; ****p < 0.0001; ns, not significant.

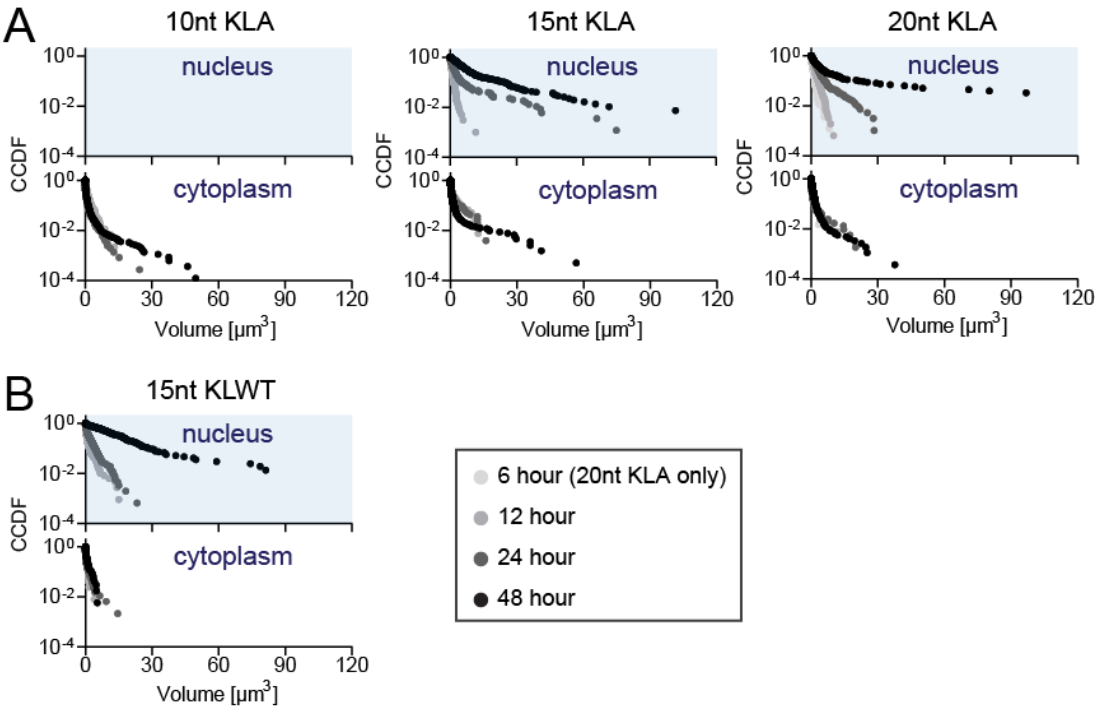

Figure 2-38. Complementary cumulative distributions of condensate volume at different time points post-transfection.

Data in Fig. 2-2 and 2-34. To generate cumulative distribution functions (CCDFs) of condensate volumes, condensates were individually segmented in three dimensions and rescaled by the mean condensate volume in each cell. After rescaling, data from all cells were pooled and plotted collectively. Each dot represents a condensate.

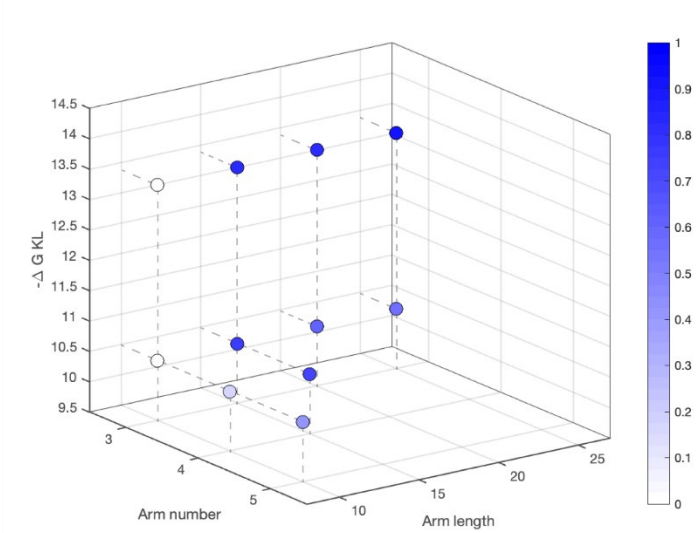

Figure 2-39. Fraction of nuclear condensates as a function of design parameters.

This is a version of Figure 2-3J based on retrieved data. ΔG values were predicted by NUPACK using kissing loop RNA sequences assuming 37 °C, 1M strand concentration, 1M Na^+. The color map shows normalized percentages of nuclear condensates over total condensate volume measured from 50 expressing cells. A cutoff effect was observed, as constructs with 10 nt arms formed exclusively cytoplasmic condensates, likely due to their smaller size relative to the nuclear pore complex. Overall, the ratio of nuclear condensates increases with longer arm length, higher arm number, or stronger kissing loop interactions.

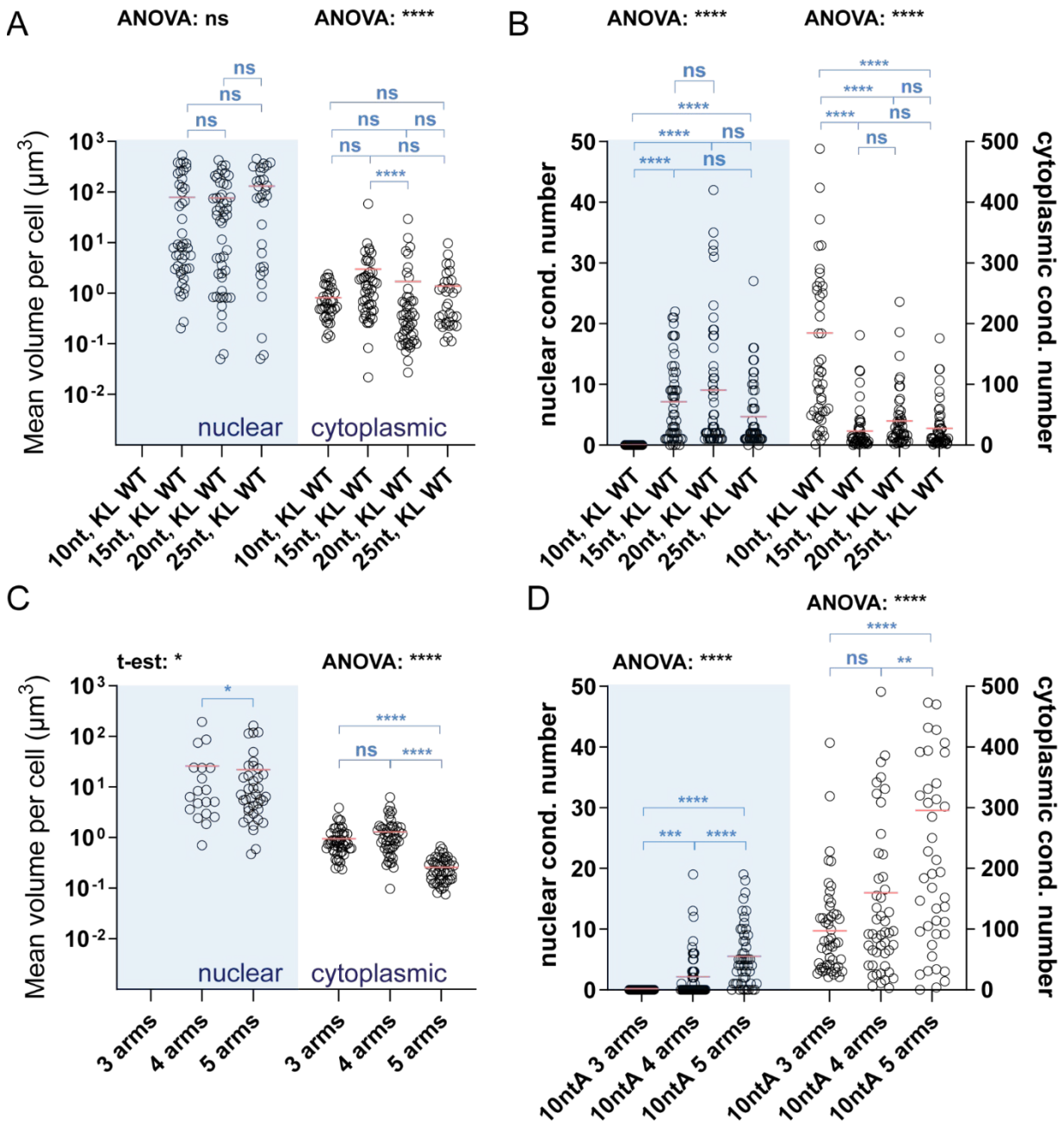

Figure 2-40. Condensate volume quantification of nanostar designs shown in Fig. 2-3K and L.

A, C, Average condensates' volume in the nucleus and cytoplasm of individual cells on a log scale. **B, D,** Number of condensates in the nucleus or cytoplasm measured in individual cells. Each black circle represents one cell. Red lines indicate the mean. Cells with no nuclear or cytoplasmic condensates were assigned to have average condensate volume and condensate number per cell as zero.

Significance was determined by non-parametric one-way ANOVA test (Kruskal-Wakkus test) followed by Dunn's multiple comparisons test or non-parametric unpaired two-tailed t-test (Mann-Whitney test) for panel C since only two groups are compared. P value summary on the top compares all four groups while comparisons of individual groups were reported below. P-values are provided in Table 2-3. *p < 0.05; **p < 0.01; ***p < 0.001; ****p < 0.0001; ns, not significant.

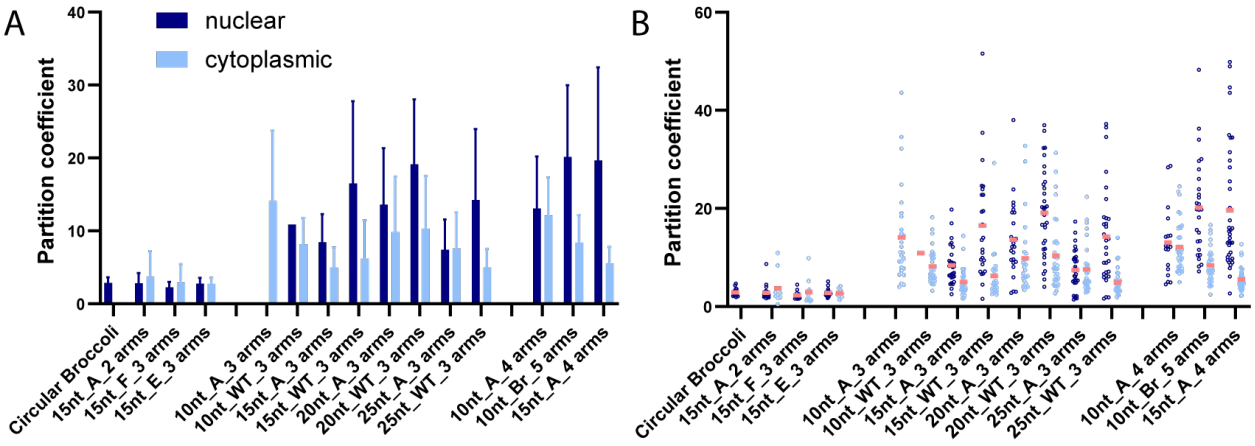

Figure 2-41. Partition coefficients of all nanostar designs.

Partition coefficients, defined as the ratio of fluorescence intensity in the condensed phase to that in the dilute phase, are shown for each construct. A shows a summary plot of the individual data points presented in B. Nanostars forming only shells exhibit low partition coefficients (left four groups). In general, partition coefficients vary widely across cells. Nuclear condensates display higher mean partition coefficients than cytoplasmic condensates. Increasing nanostar arm length, kissing loop strength (from A to WT), or the number of arms (right three groups) all lead to higher mean partition coefficients in nuclear condensates. Data in (A) are presented as mean values +/- SD. All experiments were performed in three independent replicates.

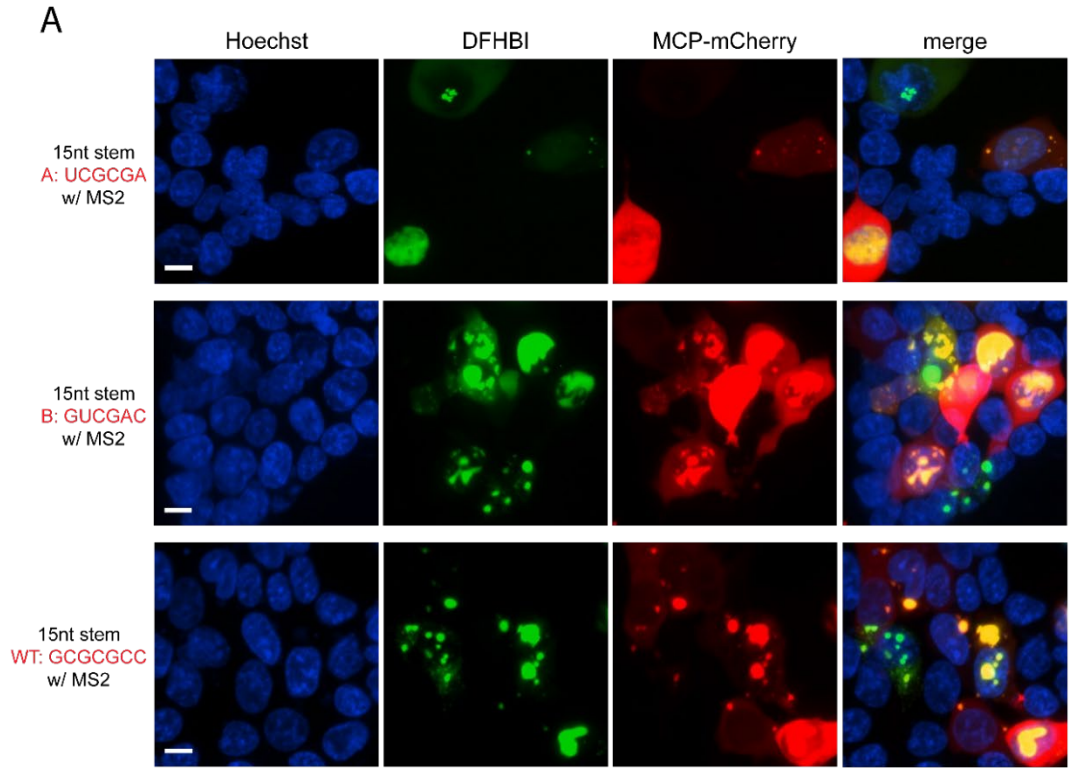
A
Hoechst
DFHBI
MCP-mCherry
merge
15nt stem
A: UCGCGA
w/ MS2
15nt stem
B: GUCGAC
w/ MS2
15nt stem
WT: GCGCGCC
w/ MS2

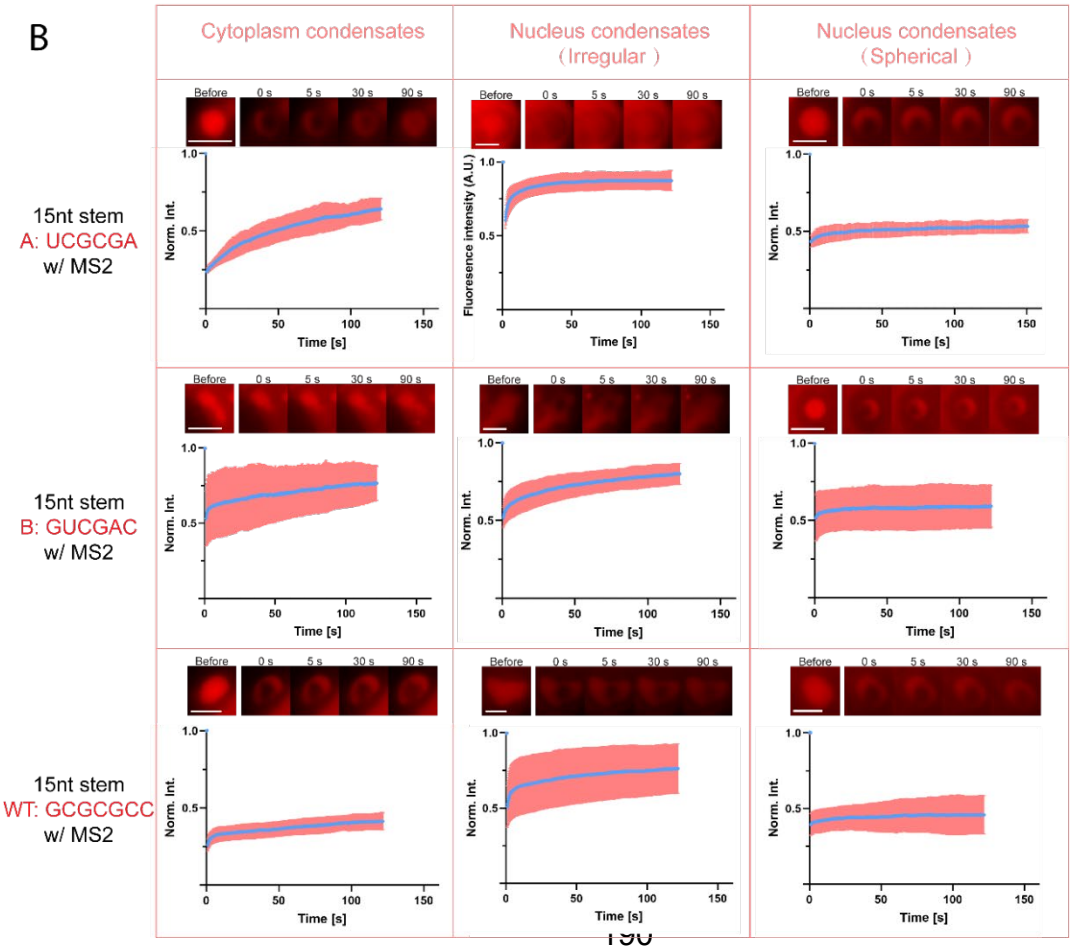
B
Cytoplasm condensates
Nucleus condensates
(Irregular)
Nucleus condensates
(Spherical)
Before
0 s
5 s
30 s
90 s
Norm. Int.
Fluoresence intensity (A.U.)
Time [s]
15nt stem
A: UCGCGA
w/ MS2
15nt stem
B: GUCGAC
w/ MS2
15nt stem
WT: GCGCGCC
w/ MS2

Figure 2-42. mCherry recruitment to condensates is maintained across nanostar kissing loops of increasing strength, however protein diffusivity decreases.

A, Condensates formed from three different types of kissing loops can recruit MCP-mCherry. Plasmids expressing MCP-mCherry and RNA nanostar are transfected in a 1:9 ratio. The stoichiometry of plasmids delivered varies between individual cells, leading to diverse expression profiles. **B**, FRAP was performed on condensates colocalized with mCherry fluorescence, observed in panel A, including condensates located in the cytoplasm, and condensates located in the nucleus presenting a spherical or an irregular shape. Blue dots indicate mean values at the corresponding time point. Shaded areas indicate the standard deviation. The dark blue line indicates the fitted curve to the mean values from equation $Y = Y_0 + (Y_\infty - Y_0) * \left(1 - e^{-\frac{t}{\tau}}\right)$. Data are presented as mean values +/- SD. All experiments were performed in three independent replicates. Scale bars in A indicate 10 μm, in B indicate 5 μm.

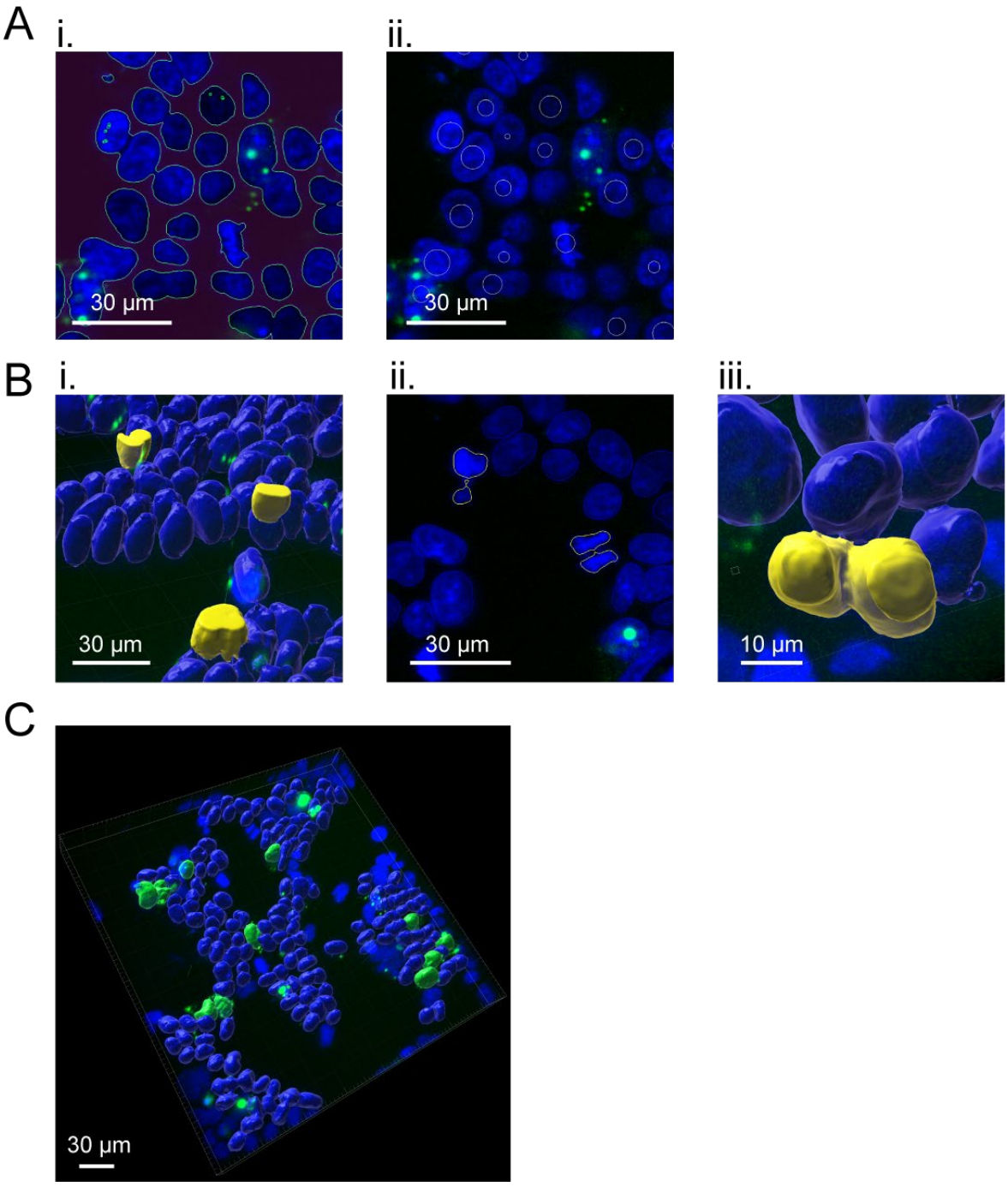

Figure 2-43. Nucleus volume quantification workflow with IMARIS.

A, Example images showing the automated segmentation. We trained a machine learning model by manually labeling the nuclei and background on slices. The same model was applied to all confocal images and generated primary segmentation results as the example image showing in (i). To split

touching nuclei, we applied a watershed method with estimated object size = 8 μm (ii), where circles indicate seed positions. **B**, Example images showing the data cleaning process. Nuclei split along the z-axis due to incomplete imaging (i) and nuclei with abnormally high pixel intensities indicating apoptosis or mitosis cells (ii) were manually excluded. Nuclei that failed to be split using the watershed algorithm were cut manually using the cutting tool in Imaris software to ensure proper segmentation of all nuclei (iii). Touching nucleus or nuclei without a distinguishable border were also removed. **C**, Example image showing classification results, where nuclei of condensate-expressing cells were highlighted in green and nuclei of non-expressing cells were in blue.

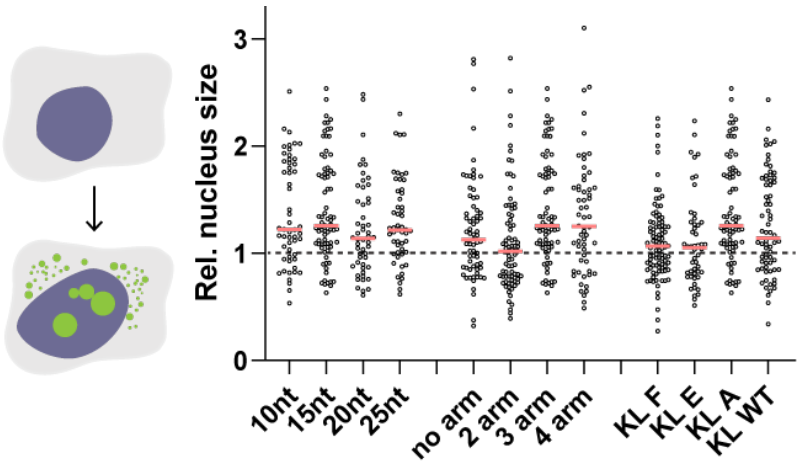

Figure 2-44. Nucleus volume quantification for nanostar-expressing cells.

Nuclei of cells expressing nanostars exhibit an average volume that is consistently enlarged when compared to non-expressing cells (dashed line). The expression of condensate-forming nanostars seem to cause more nucleus enlargement, characterized by increased mean volume and by a shift in the overall volume distribution. This may be related to increased osmotic pressure within the nucleus caused by excessive production of circularized RNA. This analysis corresponds to data shown in Fig. 2-3 of the manuscript, imaged 48 hours after transfection. Each dot represents the nucleus volume from a nanostar-expressing cell that is normalized to the average nucleus volume of non-expression cells in the same experiment. Red lines indicate the mean.

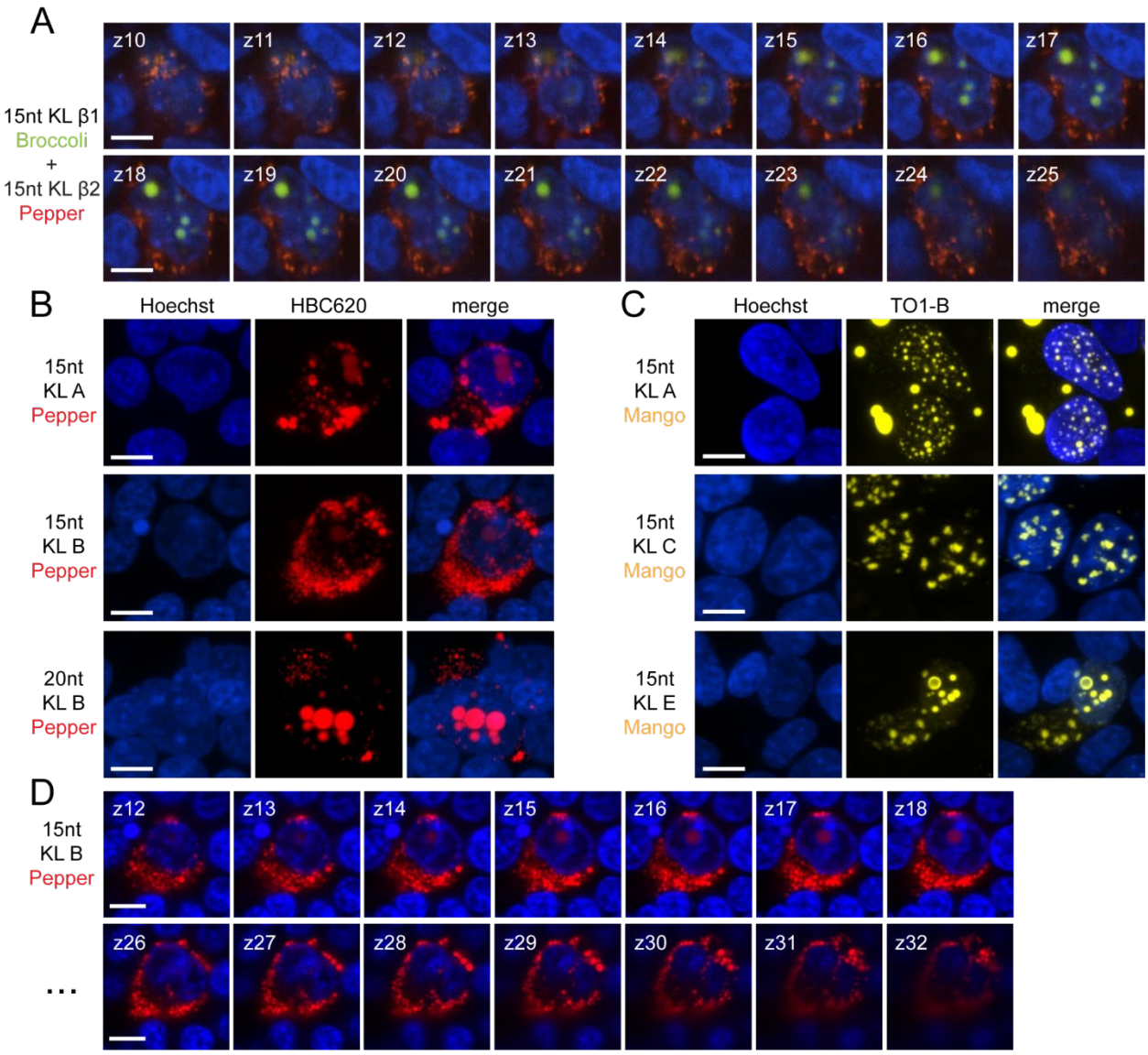

Figure 2-45. Single midplane images and Split-channel images of the micrographs shown in Figure 2-4.

A, Single midplane images for the cell shown in Fig. 4A. **B,** Split channel images of nanostars tagged with Pepper. **C,** Split channel images of nanostars tagged with Mango. **D,** Single midplane images for the cell shown in Fig. 2-4C. 15nt KL B Pepper nanostars form primarily cytoplasmic condensates**.** Scale bar, 5 μm.

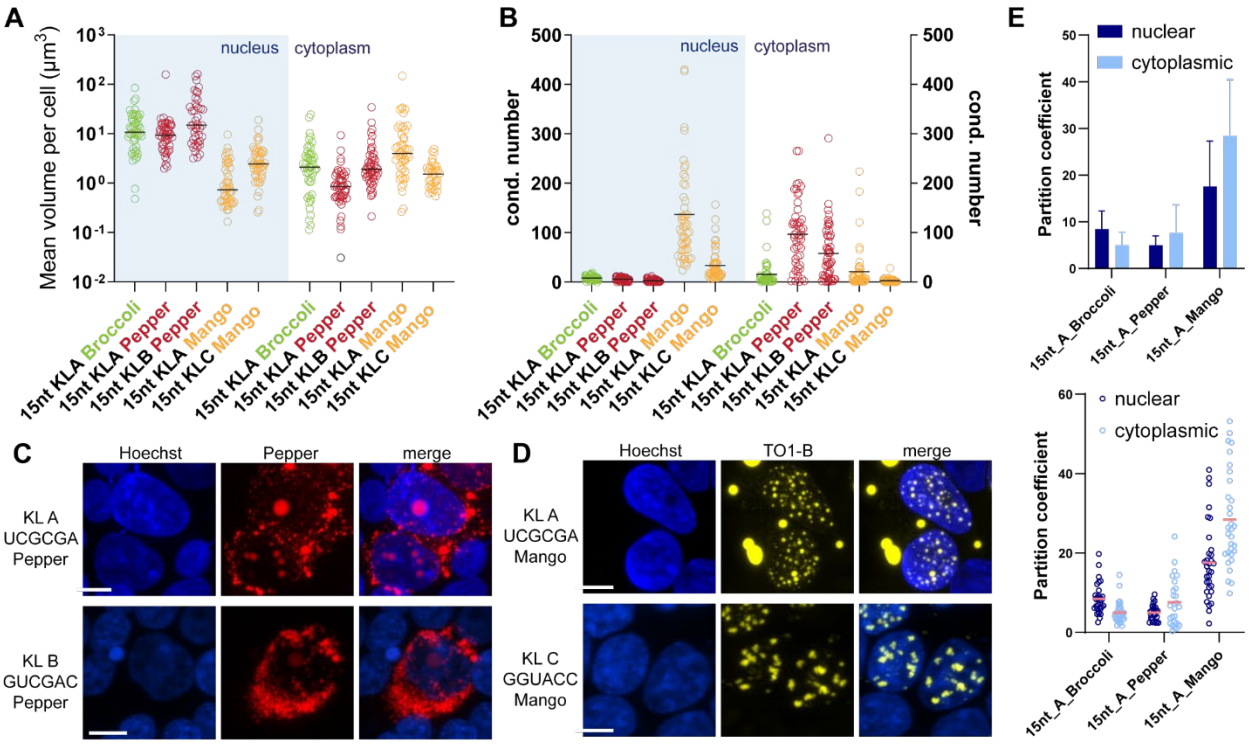

Figure 2-46. The choice of fluorogenic aptamer influences nanostar condensation behavior.

A, Average condensate volume in the nucleus and cytoplasm of individual cells (log scale). **B,** Number of condensates in the nucleus or cytoplasm per cell. Each black circle represents one cell; red lines indicate the mean. **C, D,** Representative images of Pepper (C) and Mango (D) nanostars with different kissing loops. Although sharing the same stem (15 nt, KL A), nanostars display distinct localization and morphology depending on the aptamer used. Placement of UA base pairs alters kissing loop strength (KL A < KL B < KL C), leading to larger nuclear condensates for 15-B-Pp compared to 15-A-Pp, and larger, more nuclear-localized, and more irregular condensates for 15-C-Mango compared to 15-A-Mango. **E,** Bar plot (top) and its corresponding dot plot (bottom) showing partition coefficients of nanostars tagged with different aptamers. Each dot represents one cell. Data are presented as mean values +/- SD. Images are representative from three independent biological replicates. Scale bar: 10 μm.

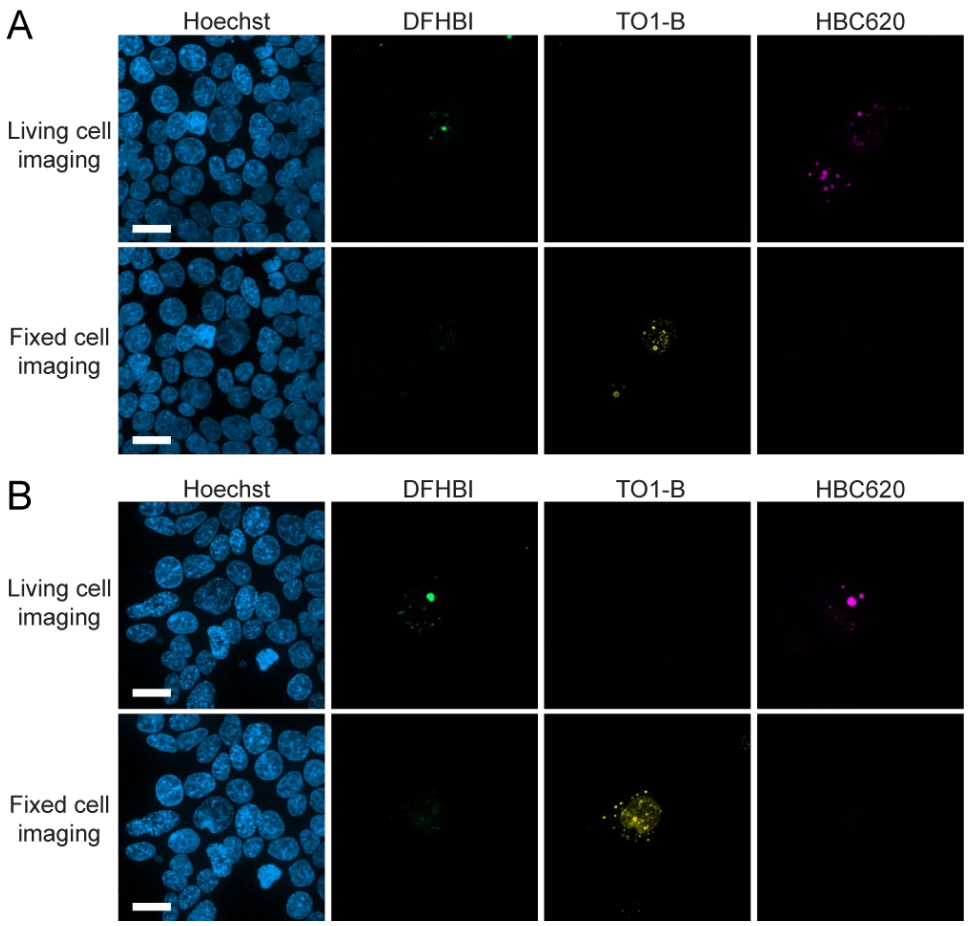

Figure 2-47. Tri-color images were acquired by live cell imaging followed by on-stage fixation and fixed imaging at the same field of view.

A, Split channel images of condensates shown in Fig. 2-4D. **B**, Split channel images of condensates shown in Fig. 2-4K. For fixed cell imaging results, strong Mango signals in the yellow channel spillover into the green channel, resulting in weak green signals that colocalize with the yellow signal. All experiments are replicated three times. Scale bar, 20 μm.

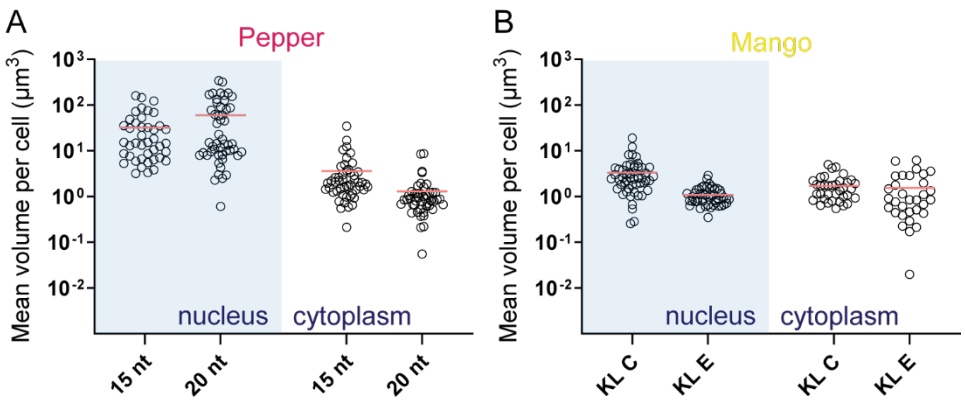

Figure 2-48. Average condensates' volume in the nucleus and cytoplasm of Pepper and Mango expressing cells on a log scale.

Each black circle represents one cell. Red lines indicate the mean.

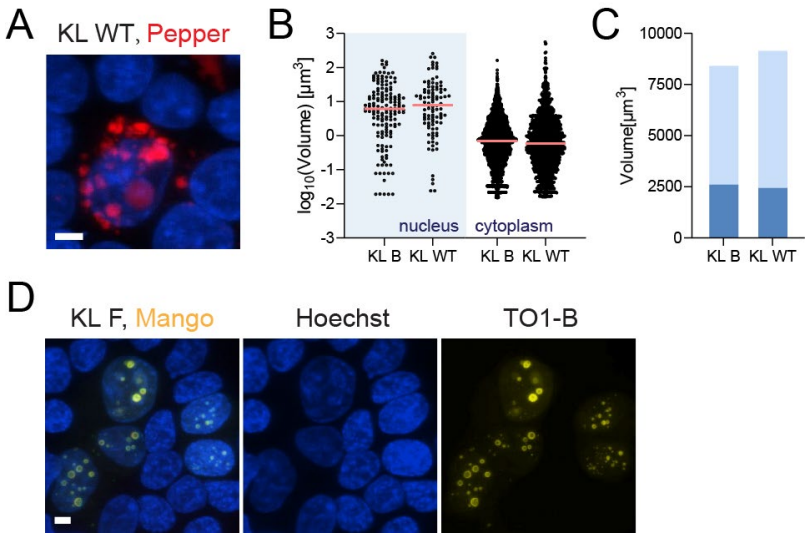

Figure 2-49. Pepper and Mango-labelled condensates.

A, Z-projection of confocal microscopy images showing that Pepper-labeled nanostars (Fig. 2-4) with a WT kissing loop (GCGCGC) produce condensates that lose spherical shape, appearing as aggregates of smaller condensates. **B, C,** The cellular localization of the Pepper-WT nanostars does not change when compared to Pepper-B nanostars (Fig. 2-4). **D,** Z-projection of confocal microscopy images showing that Mango-tagged nanostars (Fig. 2-4) with kissing loop (AUAUAU) yields nuclear shells and

diffusive Mango fluorescence in the cytoplasm, but not condensates were found. All experiments are conducted in triplicate. Scale bar, 5 μm.

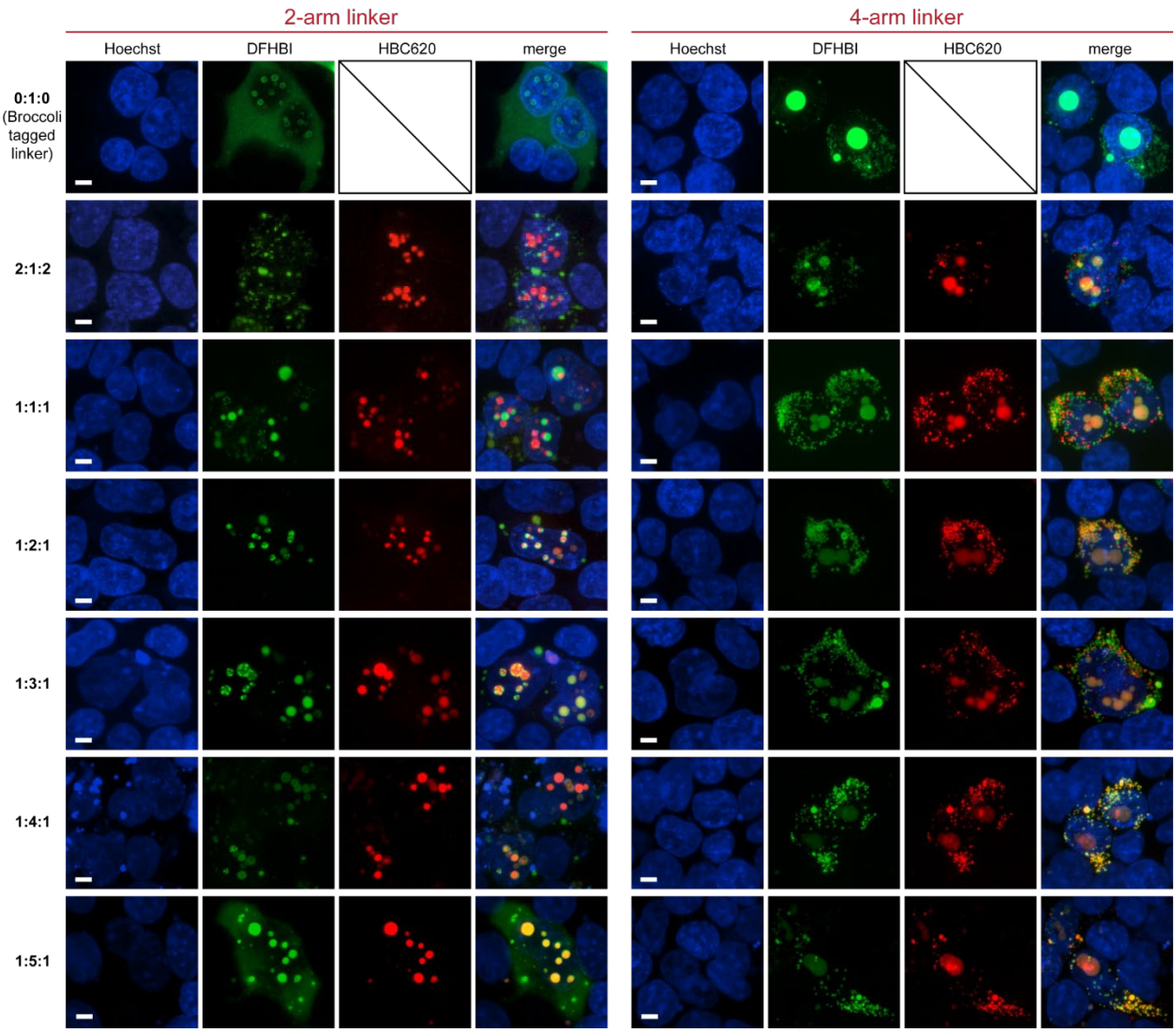

Figure 2-50. Split-channel images of the micrographs shown in Figure 2-5.

Scale bar, 5 μm.

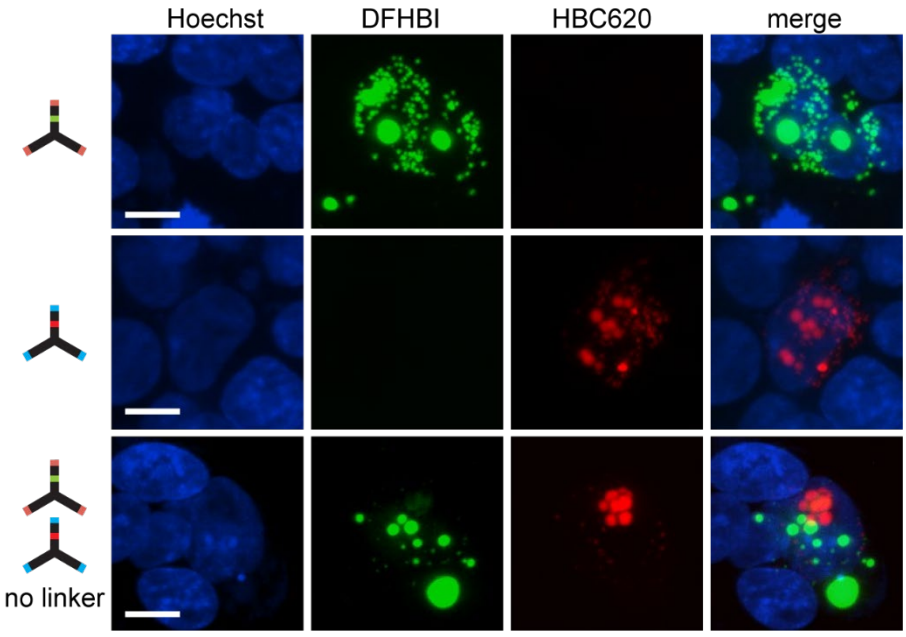

Figure 2-51. Broccoli- and Pepper-labeled nanostars form orthogonal condensates in the absence of RNA linkers.

Nanostars with 20nt long arm and orthogonal kissing loops form non-mixing condensates. Images are representative of three replicates. Scale bar, 10 μm.

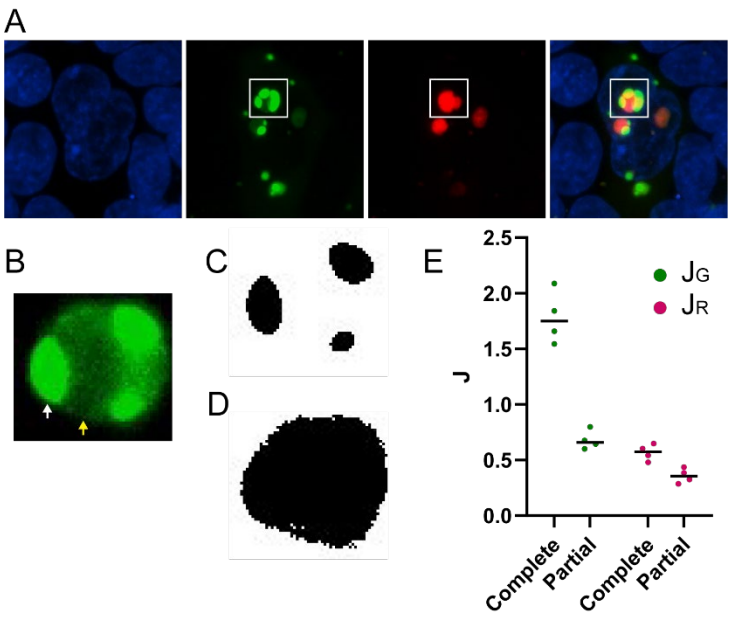

Figure 2-52. Mixing index is influenced by non-uniform mixing.

A, Representative z-projection image showing a cell transfected with nanostars with kissing loops A and B, and RNA linker at 1:4:1 plasmid ratio. **B,** Image showing the Broccoli signal (nanostar A) at a single slice, indicating a non-uniform mixing in which we can identify a high signal region (white arrow) and low signal region (yellow arrow). Classifying this droplet as partial (with mask generated in **C**) or complete (with mask generated in **D**) mixing leading to significantly different mixing index, as shown in **E**. In the manuscript, all droplets from 1:4:1 ratio are defined as complete mixing.

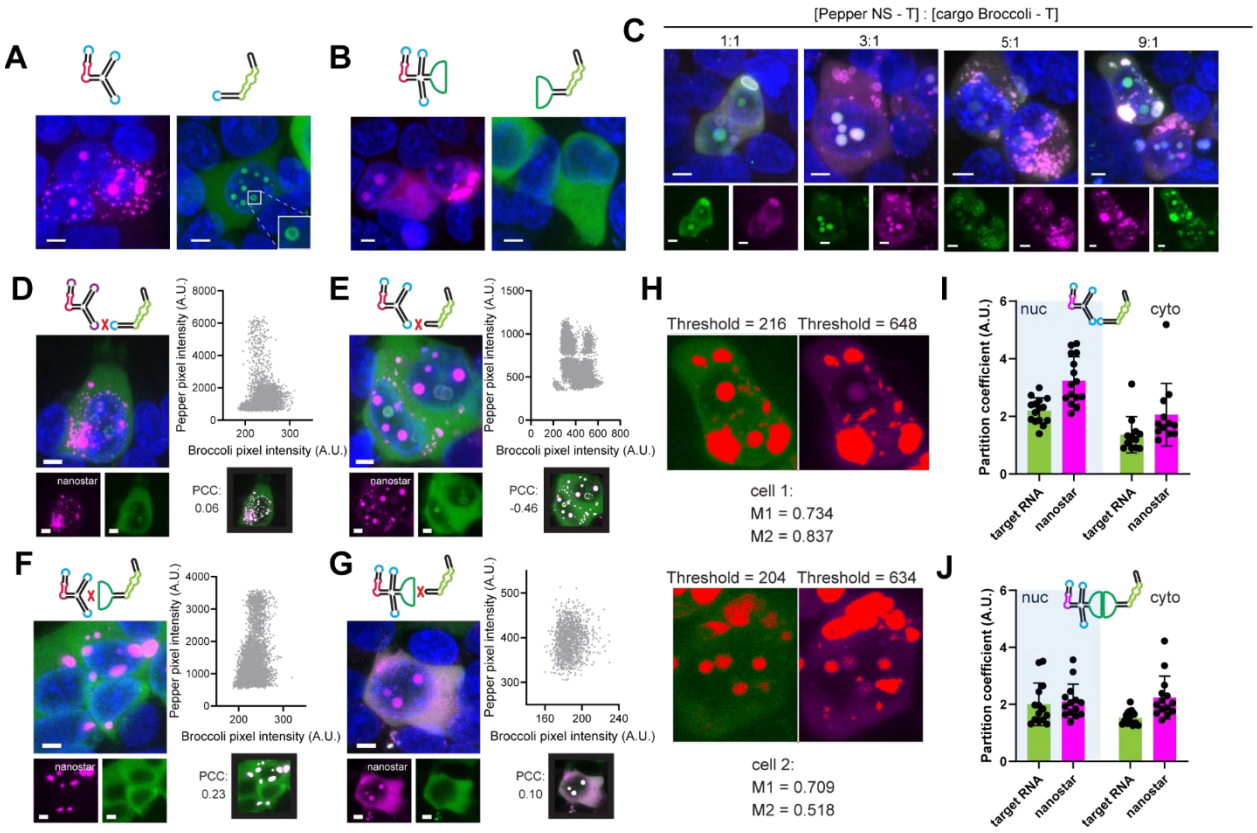

Figure 2-53. RNA nanostar condensates recruit cellular RNA molecules through sequence-specific interactions.

A, B, Confocal images of Pepper-labeled nanostars and Broccoli-labeled RNA molecules transfected individually. **C,** Confocal images of cells co-transfected with nanostar and RNA cargo plasmids at different transfection ratios. Steric hindrance from hybridization may impede condensate formation; therefore, a higher nanostar-to-cargo ratio is required for condensation. **D-G,** Micrographs and scatter plots showing control experiments in Fig. 6. Pearson correlation coefficients (PCC) show no colocalization between Pepper-labeled nanostars and Broccoli-labeled RNA molecules with absence of matched sequences. **H,** Thresholded images (highlighted in red) of cells 1 and 2 in Fig. 6F and their corresponding M1 and M2 coefficients confirmed colocalization between nanostars labeled with Pepper in magenta and the target RNA labeled with Broccoli in green. Although visual colocalization was evident, the low Broccoli signal intensity in cell 2 produced a low PCC value of 0.18 in Fig. 6F. Manders' colocalization coefficients, which quantify the fraction of overlapping signal, help resolve this issue. **I, J,**

Partition coefficient of nanostars (pink) and target RNA (green) when adding a kissing loop (I) or complementary recruitment domain (J) for recruitment. Each dot represents one cell. Data are presented as mean values +/- SD. Images are representative from three independent biological replicates. Scale bar, 5 μm.

2.6.3 Supplementary Tables

Table 2-1. Elements in the expression cassette using the TORNADO expression system.

Caption	Sequence
Yellow is the U6+27 promoter. Teal is the 5' ribozyme sequence. Cyan is the 3' ribozyme sequence. The ^ symbols represent cleavage sites catalyzed by ribozymes and mark the circularized expression product sequence. Green is the RNA sequence of interest (15nt-KLA-Br, here). The [] symbols mark an arm. The <> symbols mark a kissing loop (KL A, here). Red is the U6 terminator. Sites used for cloning (underlined): SalI (GTCTAC) and XbaI (TCTAGA), inserting using this pair generates linear RNA nanostar (As demonstrated in Supplementary Fig. 2) NotI (GCGGCCGC) and SacII (CCGCGG), inserting	RNA sequence GAGGGCCUAUUUCCCAUGAUUCCUUCAUAUUUGC AUAUACGAUACAAGGCUGUUAGAGAGAUAAUUAGA AUUAAUUUGACUGUAAACACAAAGAUAUUAGUACA AAAUACGUGACGUAGAAAGUAAUAAUUUCUUGGGU AGUUUGCAGUUUUAAAAUUAUGUUUUAAAAUGGAC UAUCAUAUGCUUACCGUAACUUGAAAGUAUUUCGA UUUCUUGGCUUUAUAUAUCUUGUGGAAAGGACGA AACACCGUGCUCGCUUCGGCAGCACAUAUACUAG UCGACGGGCCGCACUCGCCGGUCCCAAGCCCGGA UAAAAUGGGAGGGGGCGGGAAACCGCCU^AACCAU GCCGAGUGCGGCCGC[GCGAGAGCGCUGCCC<AA UCGCGAA>GGGCAGCGCUCUCGC]AA[GGAUGGAC GGUCGGGUCCGAGGGC<AAUCGCGAA>GCCCUCG UCGAGUAGAGUGUGGGCCAUCC]AA[GCGUUCACA CUGACC<AAUCGCGAA>GGUCAGUGUGAACGC]CC GCGGUCGGCGUGGACUGUAG^AACACUGCCAAUG CCGGUCCCAAGCCCGGAUAAAAGUGGAGGGUACA GUCCACGCUCUAGAGCGGACUUCGGUCCGCUUUU U DNA sequence (Template strand) GAGGGCCTATTTCCCATGATTCCTTCATATTTGCATA TACGATACAAGGCTGTTAGAGAGATAATTAGAATTA ATTTGACTGTAAACACAAAGATATTAGTACAAAATAC GTGACGTAGAAAGTAATAATTTCTTGGGTAGTTTGC AGTTTTAAAATTATGTTTTAAAATGGACTATCATATG CTTACCGTAACTTGAAAGTATTTCGATTTCTTGGCTT TATATATCTTGTGGAAAGGACGAAACACCGTGCTCG CTTCGGCAGCACATATACTAGTCGACGGGCCGCAC

using this pair generates circularized RNA nanostar	TCGCCGGTCCCAAGCCCGGATAAAATGGGAGGGG GCGGGAAACCGCCT^AACCATGCCGAGTGCGGCCG C[GCGAGAGCGCTGCCC<AATCGCGAA>GGGCAGC GCTCTCGC]AA[GGATGGACGGTCGGGTCCGAGGG C<AATCGCGAA>GCCCTCGTCGAGTAGAGTGTGGG CCATCC]AA[GCGTTCACACTGACC<AATCGCGAA>G GTCAGTGTGAACGC]CCGCGGTCGGCGTGGACTGT AG^AACACTGCCAATGCCGGTCCCAAGCCCGGATA AAAGTGGAGGGTACAGTCCACGCTCTAGAGCGGAC TTCGGTCCGCTTTTT

Table 2-2. Nomenclature of kissing loops used in the manuscript.

Kissing loop nomenclature	Sequence
A	5’ - AA UCGCGA A - 3’
B	5’ - AA GUCGAC A - 3’
C	5’ - AA GGUACC A - 3’
E	5’ - AA GUAUAC A - 3’
F	5’ - AA UAUAUA A - 3’
WT	5’ - AA GCGCGC A - 3’
Beta 1 (non-palindromic)	5’ - AA GCUACG A - 3’
Beta 2 (non-palindromic)	5’ - AA CGUAGC A - 3’

Table 2-3. P-values in Figure 2-3.

Significance was determined by non-parametric one-way ANOVA test (Kruskal-Wallis test) followed by Dunn’s multiple comparisons test for comparing more than two groups, or non-parametric

unpaired two-tailed t-test (Mann-Whitney test) for comparing two groups. *p < 0.05; **p < 0.01; ***p < 0.001; ****p < 0.0001; ns, not significant.

Panel	Plot	Cellular localization	ANOVA results	Multiple comparison					
				10 vs 15	10 vs 20	10 vs 25	15 vs 20	15 vs 25	20 vs 25
B, arm length	Average volume per cell	nucleus	0.1199				0.1189	>0.9999	0.7902
		cytoplasm	<0.001	<0.0001	>0.9999	0.6396	0.0009	0.0264	>0.9999
	Condensate number per cell	nucleus	<0.001	<0.0001	<0.0001	<0.0001	>0.9999	0.382	>0.9999
		cytoplasm	<0.001	<0.0001	0.0004	0.0039	<0.0001	<0.0001	>0.9999
				0 vs 2	0 vs 3	0 vs 4	2 vs 3	2 vs 4	3 vs 4
D, arm number	Average volume per cell	nucleus	<0.001	>0.9999	<0.0001	<0.0001	<0.0001	<0.0001	0.4704
		cytoplasm	<0.001				0.0009	>0.9999	<0.0001
	Condensate number per cell	nucleus	0.0001	0.114	>0.9999	0.1919	0.0634	<0.0001	0.319
		cytoplasm	<0.0001	0.8846	<0.0001	<0.0001	<0.0001	<0.0001	0.0037
				F vs E	F vs A	F vs WT	E vs A	E vs WT	A vs WT
F, KL strength	Average volume per cell	nucleus	<0.001	0.8746	0.0005	0.015	<0.0001	<0.0001	>0.9999
		cytoplasm	0.007	>0.9999	0.3758	>0.9999	0.0067	0.3801	0.3334

	Condensate number per cell	nucleus	0.0837	>0.9999	0.328	>0.9999	0.2857	>0.9999	0.1123
		cytoplasm	<0.0001	0.9504	<0.0001	<0.0001	<0.0001	<0.0001	>0.9999
				10 vs 15	10 vs 20	10 vs 25	15 vs 20	15 vs 25	20 vs 25
K, arm length	Average volume per cell	nucleus	0.2614				>0.9999	0.6225	0.3311
		cytoplasm	<0.0001	0.1861	0.1344	>0.9999	<0.0001	0.1921	0.2213
	Condensate number per cell	nucleus	<0.0001	<0.0001	<0.0001	<0.0001	>0.9999	>0.9999	0.4766
		cytoplasm	<0.0001	<0.0001	<0.0001	<0.0001	0.0794	>0.9999	0.6451
				3 vs 4	3 vs 5	4 vs 5			
L, arm number	Average volume per cell	nucleus	0.0122 (t test)			0.0122			
		cytoplasm	<0.0001	0.7686	<0.0001	<0.0001			
	Condensate number per cell	nucleus	<0.0001	0.0007	<0.0001	<0.0001			
		cytoplasm	<0.0001	0.4296	<0.0001	0.0046			

Table 2-4. RT-qPCR primer sequences.

Target Gene	Orientation	Sequence (5'-3')
ISG15	Forward	GGCTGGGAGCTGACGGTGAAG
	Reverse	GCTCCGCCCGCCAGGCTCTGT
IFIT1	Forward	TTGATGACGATGAAATGCCTGA
	Reverse	CAGGTCACCAGACTCCTCAC
OASL	Forward	CCATTGTGCCTGCCTACAGAG
	Reverse	CTTCAGCTTAGTTGGCCGATG
RPS11	Forward	GCCGAGACTATCTGCACTAC
	Reverse	ATGTCCAGCCTCAGAACTTC
IFN-β	Forward	GTC AGA GTG GAA ATC CTA AG
	Reverse	ACA GCA TCT GCT GGT TGA AG

Table 2-5. RNA sequences. Blue denotes stem, gray denotes spacers, orange denotes kissing loops, underline denotes aptamers, green denotes hybridization domains.

Structure Name		RNA Sequence
	15nt-KL A-Broccoli	GCGAGAGCGCUGCCCAAUCGCGAAGGGCAGCGCUCUCGCAAGGAUGGACGGUCGGG UCCGAGGGCAAUCGCGAAGCCCUCGUCGAGUAGAGUGUGGGCCAUCCAAGCGUUCAC ACUGACCAAUCGCGAAGGUCAGUGUGAACGC
Varying arm number (Fig. 2-3)	Circular Broccoli	GAGACGGUCGGGUCCAGAUAUUCGUAUCUGUCGAGUAGAGUGUGGGCUCGUGG
	15nt-KL A-Broccoli-2 arm	GCGAGAGCGCUGCCCAAUCGCGAAGGGCAGCGCUCUCGCAAGGAUGGACGGUCGGG UCCGAGGGCAAUCGCGAAGCCCUCGUCGAGUAGAGUGUGGGCCAUCC

	15nt-KL A-Broccoli-4 arm	GCGAGAGCGCUGCCCAAUCGCGAAGGGCAGCGCUCUCGCAAGGAUG GACGGUCGGGUCCGAGGGCAAUCGCGAAGCCCUCGUCGAGUAGAGU GUGGGCCAUCCAAGCGUUCACACUGACCAAUCGCGAAGGUCAGUGU GAACGCAAGAUGUAUUCAAGUCCAAUCGCGAAGGGCUUGAGUACGU C
	10nt-KL A-Broccoli-4 arm	GACGCUCAGCAAUCGCGAAGCUGAGCGUC AA GGAGACGGUCGGGUCCCUGCAAUCGCGAAGCAGGUCGAGUAGAGUGUGGGCUCC AA GCUCCACGUCAAUCGCGAAGAUGUGGAGC AA GCUUGCGUGCAAUCGCGAAGCACGCAAGC
	10nt-KL A-Broccoli-5 arm	GCUGGCAGCCAAUCGCGAAGGCUGCCAGC AA GACGCUCAGCAAUCGCGAAGCUGAGCGUC AA GGAGACGGUCGGGUCCCUGCAAUCGCGAAGCAGGUCGAGUAGAGUGUGGGCUCC AA GCUCCACGUCAAUCGCGAAGAUGUGGAGC AA GCUUGCGUGCAAUCGCGAAGCACGCAAGC
Varying arm length (Fig. 2-2, 3)	10nt-KL A-Broccoli	GACGCUCAGCAAUCGCGAAGCUGAGCGUCAAGGAGACGGUCGGGUCCCUGCAAUCGC GAAGCAGGUCGAGUAGAGUGUGGGCUCCAAGCUCCACGUCAAUCGCGAAGAUGUGG AGC
	10nt-KL WT-Broccoli	GACGCUCAGCAAGCGCGCAGCUGAGCGUCAAGGAGACGGUCGGGUCCCUGCAAGCGC GCAGCAGGUCGAGUAGAGUGUGGGCUCCAAGCUCCACGUCAAGCGCGCAGAUGUGG AGC
	20nt-KL A-Broccoli	GCGACGUGUUACGGCGAGGCAAUCGCGAAGCCUCGCCGUAACACGUCGCAAGGGCGA GGACGGUCGGGUCCGAGCGGUCAAUCGCGAAGACCGCUCGUCGAGUAGAGUGUGGG CCUCGCCCAAGCUCCGCUCCCAGUGGGCUCAAUCGCGAAGAGCCCACUGGGAGCGGA GC
	20nt-KL WT-Broccoli	GCGACGUGUUACGGCGAGGCAAGCGCGCAGCCUCGCCGUAACACGUCGCAAGGGCGA GGACGGUCGGGUCCGAGCGGUCAAGCGCGCAGACCGCUCGUCGAGUAGAGUGUGGG CCUCGCCCAAGCUCCGCUCCCAGUGGGCUCAAGCGCGCAGAGCCCACUGGGAGCGGA GC
	25nt-KL A-Broccoli	GCACAGUGUCUGUGCGACUGCACCCAAUCGCGAAGGGUGUAGUCGCAUAGACAUUG UGCAACCGUCGCGACGGUCGGGUCCGCAGCUCAAUCGCGAAGAGCUGCGUCGAGUAG AGUGUGGGCGCGACGGAACACUCGUAGCAUUGUGCCUGUCUCCAAUCGCGAAGGAG AUAGGCACAGUGCUAUGAGUG
	25nt-KL WT-Broccoli	GCACAGUGUCUGUGCGACUGCACCCAAGCGCGCAGGGUGUAGUCGCAUAGACAUUG UGCAACCGUCGCGACGGUCGGGUCCGCAGCUCAAGCGCGCAGAGCUGCGUCGAGUAG AGUGUGGGCGCGACGGAACACUCGUAGCAUUGUGCCUGUCUCCAAGCGCGCAGGAG AUAGGCACAGUGCUAUGAGUG
Varying kissing loop sequence (Fig. 2-2, 3)	15nt-KL WT-Broccoli	GCGAGAGCGCUGCCCAAGCGCGCAGGGCAGCGCUCUCGCAAGGAUGGACGGUCGGGU CCGAGGGCAAGCGCGCAGCCCUCGUCGAGUAGAGUGUGGGCCAUCCAAGCGUUCACA CUGACCAAGCGCGCAGGUCAGUGUGAACGC
	15nt-KL E-Broccoli	GCGAGAGCGCUGCCCAAGAUAUCAGGGCAGCGCUCUCGCAAGGAUGGACGGUCGGG UCCGAGGGCAAGAUAUCAGCCCUCGUCGAGUAGAGUGUGGGCCAUCCAAGCGUUCAC ACUGACCAAGAUAUCAGGUCAGUGUGAACGC

	15nt-KL F-Broccoli	GCGAGAGCGCUGCCCAAUAUAUAAGGGCAGCGCUCUCGCAAGGAUGGACGGUCGGGUCCGAGGGCAAUAUAUAAGCCCUCGUCGAGUAGAGUGUGGGCCAUCCAAGCGUUCACACUGACCAAUAUAUAAGGUCAGUGUGAACGC
Varying aptamer fluorescent (Fig. 2-4)	15nt-KL A-Pepper	GCGAGAGCGCUGCCCAAUCGCGAAGGGCAGCGCUCUCGCAACCGGGACCAAUCGUGGCGUGUCGGCAGGGCAAUCGCGAAGCCCUGCACUGGCGCCGUCCCGGAAGCGUUCACACUGACCAAUCGCGAAGGUCAGUGUGAACGC
	15nt-KLA-Mango	GCGAGAGCGCUGCCCAAUCGCGAAGGGCAGCGCUCUCGCAAGCGAUGAACGUAGGGAAUCGCGAACCCUACGUUCAUCGCAAGCGUUCACACUGACCAAUCGCGAAGGUCAGUGUGAACGCAAGGCACGUACGAAGGAGAGGAGAGGAAGAGGAGAGUACGUGCC
	15nt-KL B-Pepper	GGGACGAGGGUCGGCAAGUCGACAGCUGACCCUCGUCCCAAGGCUGACCAAUCGUGGCGUGUCGGCAGAGCAAGUCGACAGCUCUGCACUGGCGCCGUCAGCCAAGCGCUCGCCCUCGCCAAGUCGACAGGUGAGGGCGAGUGC
	15nt-KL C-Mango	GCUCGAUUGACGGGCAAGGUACCAGCCCGUCAAUCGAGCAACCUAGCGGCUUACUCAAGGUACCAGGGUAGGCUGCUAGGAAGCGCCAUUCAUUGUAAAGGUACCAUACAAUGAGUGGCGCAAGGCACGUACGAAGGAGAGGAGAGGAAGAGGAGAGUACGUGCC
	15nt-KL WT-Pepper	GGGACGAGGGUCGGCAAGCGCGCAGCUGACCCUCGUCCCAAGGCUGACCAAUCGUGGCGUGUCGGCAGAGCAAGCGCGCAGCUCUGCACUGGCGCCGUCAGCCAAGCGCUCGCCCUCGCCAAGCGCGCAGGUGAGGGCGAGUGC
	15nt-KL E-Mango	GCUCGAUUGACGGGCAAGAUAUCAGCCCGUCAAUCGAGCAACCUAGCGGCUUACUCAAGAUAUCAGGGUAGGCUGCUAGGAAGCGCCAUUCAUUGUAAAGAUAUCAUACAAUGAGUGGCGCAAGGCACGUACGAAGGAGAGGAGAGGAAGAGGAGAGUACGUGCC
	15nt-KL F-Mango	GCUCGAUUGACGGGCAAUAUAUAAGCCCGUCAAUCGAGCAACCUAGCGGCUUACUCAAUAUAUAAGGGUAGGCUGCUAGGAAGCGCCAUUCAUUGUAAAUAUAUAAUACAAUGAGUGGCGCAAGGCACGUACGAAGGAGAGGAGAGGAAGAGGAGAGUACGUGCC
	20nt-KL B-Pepper	GCGACGUGUUACGGCGAGGCAAGUCGACAGCCUCGCCGUAACACGUCGCAAGACCCGGACCAAUCGUGGCGUGUCGGCCUCCGGCAAGUCGACAGCCGGAGGCACUGGCGCCGUCCGGGUCAAGCUCCGCUCCCAGUGGGCUCAAGUCGACAGAGCCCACUGGGAGCGGAGC
Non-palindromic Kissing loop (Fig. 2-4A, B)	15nt-KL β1-Broccoli	GCGAGAGCGCUGCCCAAGCUACGAGGGCAGCGCUCUCGCAAGGAUGGACGGUCGGGUCCGAGGGCAAGCUACGAGCCCUCGUCGAGUAGAGUGUGGGCCAUCCAAGCGUUCACACUGACCAAGCUACGAGGUCAGUGUGAACGC
	15nt-KL β2-Pepper	GCGAGAGCGCUGCCCAACGUAGCAGGGCAGCGCUCUCGCAACCGGGACCAAUCGUGGCGUGUCGGCAGGGCAACGUAGCAGCCCUGCACUGGCGCCGUCCCGGAAGCGUUCACACUGACCAACGUAGCAGGUCAGUGUGAACGC
Peptide recruitment (Fig. 2-1)	15nt-KL A-Broccoli-MS2	GCGAGAGCGCUGCCCAAUCGCGAAGGGCAGCGCUCUCGCAAGGAUGGACGGUCGGGUCCGAGGGCAAUCGCGAAGCCCUCGUCGAGUAGAGUGUGGGCCAUCCAAGCGUUCACACUGACCAAUCGCGAAGGUCAGUGUGAACGCAAACAUGAGGAUCACCCAUGU
	15nt-KL B-Broccoli-MS2	GCGAGAGCGCUGCCCAAGUCGACAGGGCAGCGCUCUCGCAAGGAUGGACGGUCGGGUCCGAGGGCAAGUCGACAGCCCUCGUCGAGUAGAGUGUGGGCCAUCCAAGCGUUCACACUGACCAAGUCGACAGGUCAGUGUGAACGCAAACAUGAGGAUCACCCAUGU
	15nt-KL WT-	GCGAGAGCGCUGCCCAAGCGCGCAGGGCAGCGCUCUCGCAAGGAUGGACGGUCGGGUCCGAGGGCAAGCGCGCAGCCCUCGUCGAGUAGAGUGUGGGCCAUCCAAGCGUUCACACUGACCAAGCGCGCAGGUCAGUGUGAACGCAAACAUGAGGAUCACCCAUGU

	Broccoli-MS2	
Linker (Fig. 2-5)	15nt-KLAB-Linker-2arm	GCGAGAGCGCUGCCCAAUCGCGAAGGGCAGCGCUCUCGCAAGCGAUGAACGUAGGGAAGUCGACACCCUACGUUCAUCGC
	15nt-KLAB-Linker-4arm	GCGAGAGCGCUGCCCAAUCGCGAAGGGCAGCGCUCUCGCAAGCGAUGAACGUAGGGAAUCGCGAACCCUACGUUCAUCGCAAGCGUUCACACUGACCAAGUCGACAGGUCAGUGUGAACGCAAGAUGUAUUCAAGUCCAAGUCGACAGGGCUUGAGUACGUC
	15nt-KLAB-Linker-2arm-Broccoli	GCGAGAGCGCUGCCCAAUCGCGAAGGGCAGCGCUCUCGCAAGGAUGGACGGUCGGGUCCGAGGGCAAGUCGACAGCCCUCGUCGAGUAGAGUGUGGGCCAUCC
	15nt-KLAB-Linker-4arm-Broccoli	GCGAGAGCGCUGCCCAAUCGCGAAGGGCAGCGCUCUCGCAAGGAUGGACGGUCGGGUCCGAGGGCAAUCGCGAAGCCCUCGUCGAGUAGAGUGUGGGCCAUCCAAGCGUUCACACUGACCAAGUCGACAGGUCAGUGUGAACGCAAGAUGUAUUCAAGUCCAAGUCGACAGGGCUUGAGUACGUC
Sequence-specific RNA recruitment (Fig. 2-6)	Broccoli_1A	GCGGAGACGGUCGGGUCCAGAUAUUCGUAUCUGUCGAGUAGAGUGUGGGCUCCGCAA GCGAGAGCGCUGCCC AAUCGCGAA GGGCAGCGCUCUCGC
	Broccoli_GFPSc	GCGGAGACGGUCGGGUCCAGAUAUUCGUAUCUGUCGAGUAGAGUGUGGGCUCCGCAA GGUGUCCC AA AGAUUAGGUGAUUGGAGCGGA A GGGACGCC
	15nt-KL B-Pepper-GFPSc	GGGACGAGGGUCGGCAAGUCGACAGCUGACCCUCGUCCCAAGGCUGACCAAUCGUGGCGUGUCGGCAGAGCAAGUCGACAGCUCUGCACUGGCGCCGUCAGCCAAGCGCUCGCCCUCGCCAAGUCGACAGGUGAGGGCGAGUGCAAGGCACUA AA UCCGCUCCAAUCACCUAAUCU A UAGUGCC
Eliminating Kissing-loop (Fig. 2-14)	20nt-KL A-1polyA-Broccoli	GCGACGUGUUACGGCGAGGCAAAAAAAAAGCCUCGCCGUAACACGUCGCAAGGGCGAGGACGGUCGGGUCCGAGCGGUCAAUCGCGAAGACCGCUCGUCGAGUAGAGUGUGGGCCUCGCCCAAGCUCCGCUCCCAGUGGGCUCAAUCGCGAAGAGCCCACUGGGAGCGGAGC
	20nt-KL A-2polyA-Broccoli	GCGACGUGUUACGGCGAGGCAAAAAAAAAGCCUCGCCGUAACACGUCGCAAGGGCGAGGACGGUCGGGUCCGAGCGGUCAAUCGCGAAGACCGCUCGUCGAGUAGAGUGUGGGCCUCGCCCAAGCUCCGCUCCCAGUGGGCUCAAAAAAAAAGAGCCCACUGGGAGCGGAGC
	20nt-KL A-3polyA-Broccoli	GCGACGUGUUACGGCGAGGCAAAAAAAAAGCCUCGCCGUAACACGUCGCAAGGGCGAGGACGGUCGGGUCCGAGCGGUCAAAAAAAAAGACCGCUCGUCGAGUAGAGUGUGGGCCUCGCCCAAGCUCCGCUCCCAGUGGGCUCAAAAAAAAAGAGCCCACUGGGAGCGGAGC

Table 2-6. DNA template sequences.

DNA template name		DNA Insert Sequence (Template strand/Coding strand)
	15nt-KL A-Broccoli	5'-GCGTTCACACTGACCTTCGCGATTGGTCAGTGTGAACGCTTGGATGGCCCACACTCTACTC

		GACGAGGGCTTCGCGATTGCCCTCGGACCCGACCGTCCATCCTTGCGAGAGCGCTGCCCT TCGCGATTGGGCAGCGCTCTCGC / 5'- GCGAGAGCGCTGCCCAATCGCGAAGGGCAGCGCTCTCGCAAGGATGGACGGTCGGGTCC GAGGGCAATCGCGAAGCCCTCGTCGAGTAGAGTGTGGGCCATCCAAGCGTTCACACTGA CCAATCGCGAAGGTCAGTGTGAACGC
Varying arm number (Fig. 2-3)	Circular Broccoli	purchased plasmid from Addgene #261587
	15nt-KL A-Broccoli-2 arm	5'- GGATGGCCCACACTCTACTCGACGAGGGCTTCGCGATTGCCCTCGGACCCGACCGTCCAT CCTTGCGAGAGCGCTGCCCTTCGCGATTGGGCAGCGCTCTCGC / 5'- GCGAGAGCGCTGCCCAATCGCGAAGGGCAGCGCTCTCGCAAGGATGGACGGTCGGGTCC GAGGGCAATCGCGAAGCCCTCGTCGAGTAGAGTGTGGGCCATCC
	15nt-KL A-Broccoli-4 arm	5'- GACGTACTCAAGCCCTTCGCGATTGGACTTGAATACATCTTGCGTTCACACTGACCTTCGC GATTGGTCAGTGTGAACGCTTGGATGGCCCACACTCTACTCGACGAGGGCTTCGCGATTG CCCTCGGACCCGACCGTCCATCCTTGCGAGAGCGCTGCCCTTCGCGATTGGGCAGCGCTCT CGC / 5'- GCGAGAGCGCTGCCCAATCGCGAAGGGCAGCGCTCTCGCAAGGATGGACGGTCGGGTCC GAGGGCAATCGCGAAGCCCTCGTCGAGTAGAGTGTGGGCCATCCAAGCGTTCACACTGA CCAATCGCGAAGGTCAGTGTGAACGCAAGATGTATTCAAGTCCAATCGCGAAGGGCTTGA GTACGTC
	10nt-KL A-Broccoli-4 arm	5'- GCTTGCGTGCTTCGCGATTGCACGCAAGCTTGCTCCACATCTTCGCGATTGACGTGGAGCT TGGAGCCCACACTCTACTCGACCTGCTTCGCGATTGCAGGGACCCGACCGTCTCCTTGACG CTCAGCTTCGCGATTGCTGAGCGTC / 5'- GACGCTCAGCAATCGCGAAGCTGAGCGTCAAGGAGACGGTCGGGTCCCTGCAATCGCGA AGCAGGTCGAGTAGAGTGTGGGCTCCAAGCTCCACGTCAATCGCGAAGATGTGGAGCAA GCTTGCGTGCAATCGCGAAGCACGCAAGC
	10nt-KL A-Broccoli-5 arm	5' - GCTTGCGTGCTTCGCGATTGCACGCAAGCTTGCTCCACATCTTCGCGATTGACGTGGAGCT TGGAGCCCACACTCTACTCGACCTGCTTCGCGATTGCAGGGACCCGACCGTCTCCTTGACG CTCAGCTTCGCGATTGCTGAGCGTCTTGCTGGCAGCCTTCGCGATTGGCTGCCAGC / 5' - GCTGGCAGCCAATCGCGAAGGCTGCCAGCAAGACGCTCAGCAATCGCGAAGCTGAGCGT CAAGGAGACGGTCGGGTCCCTGCAATCGCGAAGCAGGTCGAGTAGAGTGTGGGCTCCAA GCTCCACGTCAATCGCGAAGATGTGGAGCAAGCTTGCGTGCAATCGCGAAGCACGCAAG C
	10nt-KL A-Broccoli	5'- GCTCCACATCTTCGCGATTGACGTGGAGCTTGGAGCCCACACTCTACTCGACCTGCTTCGC

Varying arm length (Fig. 2-2, 3)		GATTGCAGGGACCCGACCGTCTCCTTGACGCTCAGCTTCGCGATTGCTGAGCGTC/ 5'- GACGCTCAGCAATCGCGAAGCTGAGCGTCAAGGAGACGGTCGGGTCCCTGCAATCGCGA AGCAGGTCGAGTAGAGTGTGGGCTCCAAGCTCCACGTCAATCGCGAAGATGTGGAGC
	10nt-KL WT-Broccoli	5' - GCTCCACATCTGCGCGCTTGACGTGGAGCTTGGAGCCCACACTCTACTCGACCTGCTGCGC GCTTGCAGGGACCCGACCGTCTCCTTGACGCTCAGCTGCGCGCTTGCTGAGCGTC / 5' - GACGCTCAGCAAGCGCGCAGCTGAGCGTCAAGGAGACGGTCGGGTCCCTGCAAGCGCGC AGCAGGTCGAGTAGAGTGTGGGCTCCAAGCTCCACGTCAAGCGCGCAGATGTGGAGC
	20nt-KL A-Broccoli	5'- GCTCCGCTCCCAGTGGGCTCTTCGCGATTGAGCCCACTGGGAGCGGAGCTTGGGCGAGG CCCACACTCTACTCGACGAGCGGTCTTCGCGATTGACCGCTCGGACCCGACCGTCCTCGCC CTTGCGACGTGTTACGGCGAGGCTTCGCGATTGCCTCGCCGTAACACGTC 5'- GACGTGTTACGGCGAGGCAATCGCGAAGCCTCGCCGTAACACGTCGCAAGGGCGAGGAC GGTCGGGTCCGAGCGGTCAATCGCGAAGACCGCTCGTCGAGTAGAGTGTGGGCCTCGCC CAAGCTCCGCTCCCAGTGGGCTCAATCGCGAAGAGCCCACTGGGAGCGGAGC
	20nt-KL WT-Broccoli	5'- GCTCCGCTCCCAGTGGGCTCTGCGCGCTTGAGCCCACTGGGAGCGGAGCTTGGGCGAGG CCCACACTCTACTCGACGAGCGGTCTGCGCGCTTGACCGCTCGGACCCGACCGTCCTCGCC CTTGCGACGTGTTACGGCGAGGCTGCGCGCTTGCCTCGCCGTAACACGTC/ 5'- GACGTGTTACGGCGAGGCAAGCGCGCAGCCTCGCCGTAACACGTCGCAAGGGCGAGGAC GGTCGGGTCCGAGCGGTCAAGCGCGCAGACCGCTCGTCGAGTAGAGTGTGGGCCTCGCC CAAGCTCCGCTCCCAGTGGGCTCAAGCGCGCAGAGCCCACTGGGAGCGGAGC
	25nt-KL A-Broccoli	5'- CACTCATAGCACTGTGCCTATCTCCTTCGCGATTGGAGACAGGCACAATGCTACGAGTGTT CCGTCGCGCCCACACTCTACTCGACGCAGCTCTTCGCGATTGAGCTGCGGACCCGACCGTC GCGACGGTTGCACAATGTCTATGCGACTACACCCTTCGCGATTGGGTGCAGTCGCACAGA CACTGTGC/ 5'- GCACAGTGTCTGTGCGACTGCACCCAATCGCGAAGGGTGTAGTCGCATAGACATTGTGCA ACCGTCGCGACGGTCGGGTCCGCAGCTCAATCGCGAAGAGCTGCGTCGAGTAGAGTGTG GGCGCGACGGAACACTCGTAGCATTGTGCCTGTCTCCAATCGCGAAGGAGATAGGCACA GTGCTATGAGTG
	25nt-KL WT-Broccoli	5' - CACTCATAGCACTGTGCCTATCTCCTGCGCGCTTGGAGACAGGCACAATGCTACGAGTGTT CCGTCGCGCCCACACTCTACTCGACGCAGCTCTGCGCGCTTGAGCTGCGGACCCGACCGT CGCGACGGTTGCACAATGTCTATGCGACTACACCCTGCGCGCTTGGGTGCAGTCGCACAG ACACTGTGC / 5' - GCACAGTGTCTGTGCGACTGCACCCAAGCGCGCAGGGTGTAGTCGCATAGACATTGTGCA

		ACCGTCGCGACGGTCGGGTCCGCAGCTCAAGCGCGCAGAGCTGCGTCGAGTAGAGTGTG GGCGCGACGGAACACTCGTAGCATTGTGCCTGTCTCCAAGCGCGCAGGAGATAGGCACA GTGCTATGAGTG
Varying kissing loop sequence (Fig. 2-2, 3)	15nt-KL WT-Broccoli	5'- GCGTTCACACTGACCTGCGCGCTTGGTCAGTGTGAACGCTTGGATGGCCCACACTCTACTC GACGAGGGCTGCGCGCTTGCCCTCGGACCCGACCGTCCATCCTTGCGAGAGCGCTGCCCT GCGCGCTTGGGCAGCGCTCTCGC/ 5'- GCGAGAGCGCTGCCCAAGCGCGCAGGGCAGCGCTCTCGCAAGGATGGACGGTCGGGTC CGAGGGCAAGCGCGCAGCCCTCGTCGAGTAGAGTGTGGGCCATCCAAGCGTTCACACTG ACCAAGCGCGCAGGTCAGTGTGAACGC
	15nt-KL E-Broccoli	5'- GCGTTCACACTGACCTGATATCTTGGTCAGTGTGAACGCTTGGATGGCCCACACTCTACTC GACGAGGGCTGATATCTTGCCCTCGGACCCGACCGTCCATCCTTGCGAGAGCGCTGCCCT GATATCTTGGGCAGCGCTCTCGC/ 5'- GCGAGAGCGCTGCCCAAGATATCAGGGCAGCGCTCTCGCAAGGATGGACGGTCGGGTCC GAGGGCAAGATATCAGCCCTCGTCGAGTAGAGTGTGGGCCATCCAAGCGTTCACACTGAC CAAGATATCAGGTCAGTGTGAACGC
	15nt-KL F-Broccoli	5'- GCGTTCACACTGACCTTATATATTGGTCAGTGTGAACGCTTGGATGGCCCACACTCTACTC GACGAGGGCTTATATATTGCCCTCGGACCCGACCGTCCATCCTTGCGAGAGCGCTGCCCTT ATATATTGGGCAGCGCTCTCGC/ 5'- GCGAGAGCGCTGCCCAATATATAAGGGCAGCGCTCTCGCAAGGATGGACGGTCGGGTCC GAGGGCAATATATAAGCCCTCGTCGAGTAGAGTGTGGGCCATCCAAGCGTTCACACTGAC CAATATATAAGGTCAGTGTGAACGC
Varying aptamer fluorescent (Fig. 2-4)	15nt-KL A-Pepper	5' - GCGTTCACACTGACCTTCGCGATTGGTCAGTGTGAACGCTTCCGGGACGGCGCCAGTGCA GGGCTTCGCGATTGCCCTGCCGACACGCCACGATTGGTCCCGGTTGCGAGAGCGCTGCCC TTCGCGATTGGGCAGCGCTCTCGC / 5' - GCGAGAGCGCTGCCCAATCGCGAAGGGCAGCGCTCTCGCAACCGGGACCAATCGTGGCG TGTCGGCAGGGCAATCGCGAAGCCCTGCACTGGCGCCGTCCCGGAAGCGTTCACACTGAC CAATCGCGAAGGTCAGTGTGAACGC
	15nt-KLA-Mango	5' - GGCACGTACTCTCCTCTTCCTCTCCTCTCCTTCGTACGTGCCTTGCGTTCACACTGACCTTCG CGATTGGTCAGTGTGAACGCTTGCGATGAACGTAGGGTTCGCGATTCCCTACGTTCATCG CTTGCGAGAGCGCTGCCCTTCGCGATTGGGCAGCGCTCTCGC / 5' - GCGAGAGCGCTGCCCAATCGCGAAGGGCAGCGCTCTCGCAAGCGATGAACGTAGGGAAT CGCGAACCCTACGTTCATCGCAAGCGTTCACACTGACCAATCGCGAAGGTCAGTGTGAAC GCAAGGCACGTACGAAGGAGAGGAGAGGAAGAGGAGAGTACGTGCC

	15nt-KL B-Pepper	5'- GCACTCGCCCTCACCTGTCGACTTGGCGAGGGCGAGCGCTTGGCTGACGGCGCCAGTGCA GAGCTGTCGACTTGCTCTGCCGACACGCCACGATTGGTCAGCCTTGGGACGAGGGTCAGC TGTCGACTTGCCGACCCTCGTCCC/ 5'- GGGACGAGGGTCGGCAAGTCGACAGCTGACCCTCGTCCCAAGGCTGACCAATCGTGGCG TGTCGGCAGAGCAAGTCGACAGCTCTGCACTGGCGCCGTCAGCCAAGCGCTCGCCCTCGC CAAGTCGACAGGTGAGGGCGAGTGC
	15nt-KL C-Mango	5'- GGCACGTACTCTCCTCTTCCTCTCCTCTCCTTCGTACGTGCCTTGCGCCACTCATTGTATGGT ACCTTTACAATGAATGGCGCTTCCTAGCAGCCTACCCTGGTACCTTGAGTAAGCCGCTAGG TTGCTCGATTGACGGGCTGGTACCTTGCCCGTCAATCGAGC / 5'- GCTCGATTGACGGGCAAGGTACCAGCCCGTCAATCGAGCAACCTAGCGGCTTACTCAAGG TACCAGGGTAGGCTGCTAGGAAGCGCCATTCATTGTAAAGGTACCATACAATGAGTGGCG CAAGGCACGTACGAAGGAGAGGAGAGGAAGAGGAGAGTACGTGCC
	15nt-KL WT-Pepper	5'- GCACTCGCCCTCACCTGCGCGCTTGGCGAGGGCGAGCGCTTGGCTGACGGCGCCAGTGC AGAGCTGCGCGCTTGCTCTGCCGACACGCCACGATTGGTCAGCCTTGGGACGAGGGTCA GCTGCGCGCTTGCCGACCCTCGTCCC / 5'- GGGACGAGGGTCGGCAAGCGCGCAGCTGACCCTCGTCCCAAGGCTGACCAATCGTGGCG TGTCGGCAGAGCAAGCGCGCAGCTCTGCACTGGCGCCGTCAGCCAAGCGCTCGCCCTCGC CAAGCGCGCAGGTGAGGGCGAGTGC
	15nt-KL E-Mango	5'- GGCACGTACTCTCCTCTTCCTCTCCTCTCCTTCGTACGTGCCTTGCGCCACTCATTGTATGAT ATCTTTACAATGAATGGCGCTTCCTAGCAGCCTACCCTGATATCTTGAGTAAGCCGCTAGG TTGCTCGATTGACGGGCTGATATCTTGCCCGTCAATCGAGC / 5'- GCTCGATTGACGGGCAAGATATCAGCCCGTCAATCGAGCAACCTAGCGGCTTACTCAAGA TATCAGGGTAGGCTGCTAGGAAGCGCCATTCATTGTAAAGATATCATACAATGAGTGGCG CAAGGCACGTACGAAGGAGAGGAGAGGAAGAGGAGAGTACGTGCC
	15nt-KL F-Mango	5'- GGCACGTACTCTCCTCTTCCTCTCCTCTCCTTCGTACGTGCCTTGCGCCACTCATTGTATTAT ATATTTACAATGAATGGCGCTTCCTAGCAGCCTACCCTTATATATTGAGTAAGCCGCTAGG TTGCTCGATTGACGGGCTTATATATTGCCCGTCAATCGAGC / 5'- GCTCGATTGACGGGCAATATATAAGCCCGTCAATCGAGCAACCTAGCGGCTTACTCAATAT ATAAGGGTAGGCTGCTAGGAAGCGCCATTCATTGTAAATATATAATACAATGAGTGGCGC AAGGCACGTACGAAGGAGAGGAGAGGAAGAGGAGAGTACGTGCC
	20nt-KL B-Pepper	5'- GCTCCGCTCCCAGTGGGCTCTGTCGACTTGAGCCCACTGGGAGCGGAGCTTGACCCGGAC GGCGCCAGTGCCTCCGGCTGTCGACTTGCCGGAGGCCGACACGCCACGATTGGTCCGGG

		TCTTGCGACGTGTTACGGCGAGGCTGTCGACTTGCCTCGCCGTAACACGTCGC / 5'- GCGACGTGTTACGGCGAGGCAAGTCGACAGCCTCGCCGTAACACGTCGCAAGACCCGGA CCAATCGTGGCGTGTCGGCCTCCGGCAAGTCGACAGCCGGAGGCACTGGCGCCGTCCGG GTCAAGCTCCGCTCCCAGTGGGCTCAAGTCGACAGAGCCCACTGGGAGCGGAGC
Non-palindromic Kissing loop (Fig. 2-4A, B)	15nt-KL β1-Broccoli	5'- GCGTTCACACTGACCTCGTAGCTTGGTCAGTGTGAACGCTTGGATGGCCCACACTCTACTC GACGAGGGCTCGTAGCTTGCCCTCGGACCCGACCGTCCATCCTTGCGAGAGCGCTGCCCT CGTAGCTTGGGCAGCGCTCTCGC / 5'- GCGAGAGCGCTGCCCAAGCTACGAGGGCAGCGCTCTCGCAAGGATGGACGGTCGGGTCC GAGGGCAAGCTACGAGCCCTCGTCGAGTAGAGTGTGGGCCATCCAAGCGTTCACACTGA CCAAGCTACGAGGTCAGTGTGAACGC
	15nt-KL β2-Pepper	5'- GCGTTCACACTGACCTGCTACGTTGGTCAGTGTGAACGCTTCCGGGACGGCGCCAGTGCA GGGCTGCTACGTTGCCCTGCCGACACGCCACGATTGGTCCCGGTTGCGAGAGCGCTGCCC TGCTACGTTGGGCAGCGCTCTCGC / 5'- GCGAGAGCGCTGCCCAACGTAGCAGGGCAGCGCTCTCGCAACCGGGACCAATCGTGGCG TGTCGGCAGGGCAACGTAGCAGCCCTGCACTGGCGCCGTCCCGGAAGCGTTCACACTGAC CAACGTAGCAGGTCAGTGTGAACGC
Peptide recruitment (Fig. 2-1)	15nt-KL A-Broccoli-MS2	5'- ACATGGGTGATCCTCATGTTTGCGTTCACACTGACCTTCGCGATTGGTCAGTGTGAACGCT TGGATGGCCCACACTCTACTCGACGAGGGCTTCGCGATTGCCCTCGGACCCGACCGTCCA TCCTTGCGAGAGCGCTGCCCTTCGCGATTGGGCAGCGCTCTCGC / 5'- GCGAGAGCGCTGCCCAATCGCGAAGGGCAGCGCTCTCGCAAGGATGGACGGTCGGGTCC GAGGGCAATCGCGAAGCCCTCGTCGAGTAGAGTGTGGGCCATCCAAGCGTTCACACTGA CCAATCGCGAAGGTCAGTGTGAACGCAAACATGAGGATCACCCATGT
	15nt-KL B-Broccoli-MS2	5'- ACATGGGTGATCCTCATGTTTGCGTTCACACTGACCTGTCGACTTGGTCAGTGTGAACGCT TGGATGGCCCACACTCTACTCGACGAGGGCTGTCGACTTGCCCTCGGACCCGACCGTCCA TCCTTGCGAGAGCGCTGCCCTGTCGACTTGGGCAGCGCTCTCGC / 5'- GCGAGAGCGCTGCCCAAGTCGACAGGGCAGCGCTCTCGCAAGGATGGACGGTCGGGTCC GAGGGCAAGTCGACAGCCCTCGTCGAGTAGAGTGTGGGCCATCCAAGCGTTCACACTGA CCAAGTCGACAGGTCAGTGTGAACGCAAACATGAGGATCACCCATGT
	15nt-KL WT-Broccoli-MS2	5'- ACATGGGTGATCCTCATGTTTGCGTTCACACTGACCTGCGCGCTTGGTCAGTGTGAACGCT TGGATGGCCCACACTCTACTCGACGAGGGCTGCGCGCTTGCCCTCGGACCCGACCGTCCA TCCTTGCGAGAGCGCTGCCCTGCGCGCTTGGGCAGCGCTCTCGC / 5'- GCGAGAGCGCTGCCCAAGCGCGCAGGGCAGCGCTCTCGCAAGGATGGACGGTCGGGTC

		CGAGGGCAAGCGCGCAGCCCTCGTCGAGTAGAGTGTGGGCCATCCAAGCGTTCACACTG ACCAAGCGCGCAGGTCAGTGTGAACGCAAACATGAGGATCACCCATGT
Linker (Fig. 2-5)	15nt-KLAB-Linker-2arm	5'- GCGATGAACGTAGGGTGTCGACTTCCCTACGTTCATCGCTTGCGAGAGCGCTGCCCTTCG CGATTGGGCAGCGCTCTCGC / 5'- GCGAGAGCGCTGCCCAATCGCGAAGGGCAGCGCTCTCGCAAGCGATGAACGTAGGGAA GTCGACACCCTACGTTCATCGC
	15nt-KLAB-Linker-4arm	5'- GACGTACTCAAGCCCTGTCGACTTGGACTTGAATACATCTTGCGTTCACACTGACCTGTCG ACTTGGTCAGTGTGAACGCTTGCGATGAACGTAGGGTTCGCGATTCCCTACGTTCATCGCT TGCGAGAGCGCTGCCCTTCGCGATTGGGCAGCGCTCTCGC / 5'- GCGAGAGCGCTGCCCAATCGCGAAGGGCAGCGCTCTCGCAAGCGATGAACGTAGGGAAT CGCGAACCCTACGTTCATCGCAAGCGTTCACACTGACCAAGTCGACAGGTCAGTGTGAAC GCAAGATGTATTCAAGTCCAAGTCGACAGGGCTTGAGTACGTC
	15nt-KLAB-Linker-2arm-Broccoli	5'- GGATGGCCCACACTCTACTCGACGAGGGCTGTCGACTTGCCCTCGGACCCGACCGTCCAT CCTTGCGAGAGCGCTGCCCTTCGCGATTGGGCAGCGCTCTCGC / 5'- GCGAGAGCGCTGCCCAATCGCGAAGGGCAGCGCTCTCGCAAGGATGGACGGTCGGGTCC GAGGGCAAGTCGACAGCCCTCGTCGAGTAGAGTGTGGGCCATCC
	15nt-KLAB-Linker-4arm-Broccoli	5'- GACGTACTCAAGCCCTGTCGACTTGGACTTGAATACATCTTGCGTTCACACTGACCTGTCG ACTTGGTCAGTGTGAACGCTTGGATGGCCCACACTCTACTCGACGAGGGCTTCGCGATTG CCCTCGGACCCGACCGTCCATCCTTGCGAGAGCGCTGCCCTTCGCGATTGGGCAGCGCTCT CGC / 5'- GCGAGAGCGCTGCCCAATCGCGAAGGGCAGCGCTCTCGCAAGGATGGACGGTCGGGTCC GAGGGCAATCGCGAAGCCCTCGTCGAGTAGAGTGTGGGCCATCCAAGCGTTCACACTGA CCAAGTCGACAGGTCAGTGTGAACGCAAGATGTATTCAAGTCCAAGTCGACAGGGCTTGA GTACGTC
Sequence-specific RNA recruitment (Fig. 2-6)	Broccoli_1KL A	5' - GCGAGAGCGCTGCCCTTCGCGATTGGGCAGCGCTCTCGCTTGCGGAGCCCACACTCTACT CGACAGATACGAATATCTGGACCCGACCGTCTCCGC / 5' - GCGGAGACGGTCGGGTCCAGATATTCGTATCTGTCGAGTAGAGTGTGGGCTCCGCAAGC GAGAGCGCTGCCCAATCGCGAAGGGCAGCGCTCTCGC
	Broccoli_GFPSc	5' - GGCGTCCCTTCCGCTCCAATCACCTAATCTTTGGGACACCTTGCGGAGCCCACACTCTACTC GACAGATACGAATATCTGGACCCGACCGTCTCCGC / 5' -

		GCGGAGACGGTCGGGTCCAGATATTCGTATCTGTCGAGTAGAGTGTGGGCTCCGCAAGG TGTCCCAAAGATTAGGTGATTGGAGCGGAAGGGACGCC
	15nt-KL B-Pepper-GFPSc	5' - GGCACTATAGATTAGGTGATTGGAGCGGATTTAGTGCCTTGCACTCGCCCTCACCTGTCGA CTTGGCGAGGGCGAGCGCTTGGCTGACGGCGCCAGTGCAGAGCTGTCGACTTGCTCTGC CGACACGCCACGATTGGTCAGCCTTGGGACGAGGGTCAGCTGTCGACTTGCCGACCCTCG TCCC / 5' - GGGACGAGGGTCGGCAAGTCGACAGCTGACCCTCGTCCCAAGGCTGACCAATCGTGGCG TGTCGGCAGAGCAAGTCGACAGCTCTGCACTGGCGCCGTCAGCCAAGCGCTCGCCCTCGC CAAGTCGACAGGTGAGGGCGAGTGCAAGGCACTAAATCCGCTCCAATCACCTAATCTATA GTGCC
Eliminating Kissing-loop (Fig. 2-14)	20nt-KL A-1polyA-Broccoli	5'- GCTCCGCTCCCAGTGGGCTCTTCGCGATTGAGCCCACTGGGAGCGGAGCTTGGGCGAGG CCCACACTCTACTCGACGAGCGGTCTTCGCGATTGACCGCTCGGACCCGACCGTCCTCGCC CTTGCGACGTGTTACGGCGAGGCTTTTTTTTTGCCTCGCCGTAACACGTCGC / 5'- GCGACGTGTTACGGCGAGGCAAAAAAAAAGCCTCGCCGTAACACGTCGCAAGGGCGAGG ACGGTCGGGTCCGAGCGGTCAATCGCGAAGACCGCTCGTCGAGTAGAGTGTGGGCCTCG CCCAAGCTCCGCTCCCAGTGGGCTCAATCGCGAAGAGCCCACTGGGAGCGGAGC
	20nt-KL A-2polyA-Broccoli	5'- GCTCCGCTCCCAGTGGGCTCTTTTTTTTTGAGCCCACTGGGAGCGGAGCTTGGGCGAGGC CCACACTCTACTCGACGAGCGGTCTTCGCGATTGACCGCTCGGACCCGACCGTCCTCGCCC TTGCGACGTGTTACGGCGAGGCTTTTTTTTTGCCTCGCCGTAACACGTCGC / 5'- GCGACGTGTTACGGCGAGGCAAAAAAAAAGCCTCGCCGTAACACGTCGCAAGGGCGAGG ACGGTCGGGTCCGAGCGGTCAATCGCGAAGACCGCTCGTCGAGTAGAGTGTGGGCCTCG CCCAAGCTCCGCTCCCAGTGGGCTCAAAAAAAAAGAGCCCACTGGGAGCGGAGC
	20nt-KL A-3polyA-Broccoli	5'- GCTCCGCTCCCAGTGGGCTCTTTTTTTTTGAGCCCACTGGGAGCGGAGCTTGGGCGAGGC CCACACTCTACTCGACGAGCGGTCTTTTTTTTTGACCGCTCGGACCCGACCGTCCTCGCCCT TGCGACGTGTTACGGCGAGGCTTTTTTTTTGCCTCGCCGTAACACGTCGC / 5'- GCGACGTGTTACGGCGAGGCAAAAAAAAAGCCTCGCCGTAACACGTCGCAAGGGCGAGG ACGGTCGGGTCCGAGCGGTCAAAAAAAAAGACCGCTCGTCGAGTAGAGTGTGGGCCTCG CCCAAGCTCCGCTCCCAGTGGGCTCAAAAAAAAAGAGCCCACTGGGAGCGGAGC